UNIVERSITA' DEGLI STUDI DI PADOVA

Sede Amministrativa: Università degli Studi di Padova

Dipartimento di Fisica Tecnica

SCUOLA DI DOTTORATO DI RICERCA IN INGEGNERIA INDUSTRIALE
INDIRIZZO FISICA TECNICA
CICLO XXI

TWO-PHASE HEAT TRANSFER IN MINICHANNEL HEAT EXCHANGERS: HEAT PUMP APPLICATIONS, DESIGN, MODELLING

Direttore della Scuola : Ch.mo Prof. Paolo Bariani
Supervisore : Ch.mo Prof. Alberto Cavallini
Co-Supervisore : Ing. Davide Del Col

Dottorando : Enrico Da Riva

Abstract

Refrigerant charge minimization is one of the most important targets for heating and air conditioning applications when using natural refrigerants like hydrocarbons or ammonia to cope with the new environmental challenges.

Some applications of minichannels for charge minimization in heat pumps are presented and discussed in this thesis.

The design of an innovative condenser, an evaporator and an internal heat exchanger is presented. These devices are shell-and-tube heat exchangers using 2 mm i.d. minichannels and realized for the use with propane. Computational procedures based on empirical correlations available in the literature and a simplified model of the heat transfer and pressure drop processes have been developed and used for the design. Experimental performance data of the heat exchangers when using R22 and propane is reported and compared against the predictions given by the computational procedures.

The shell-and-tube minichannel heat exchangers have been installed in a 100 kW heat pump using propane as the refrigerant. The unit has been designed for laboratory tests and the minichannel shell-and-tube heat exchangers have been installed in the facility together with a conventional plate condenser and an evaporator. Different configurations have been tested in order to quantify the advantages of operating the heat pump using the low charge heat exchangers, with regard to both energy performance and propane charge. In particular, the experimental performance when using the minichannel condenser is compared to the one obtained when using the plate condenser, and the influence of the internal heat exchanger on the performance of the equipment is measured and discussed. Experimental data about the efficiency with propane of the semihermetic compressor installed in the heat pump is also reported.

Besides empirical correlations to predict the global thermal performance, a more complete understanding of the two-phase flow and heat transfer in minichannels is needed for the design and optimization of heat exchangers.

Some CFD simulations are presented in this thesis using the innovative Volume Of Fluid (VOF) method, which is able to directly compute multiphase flows without using any empirical closure law to model the interaction between the phases.

In order to assess the capability of the method to compute the motion of the gas-liquid interface, which is crucial for two-phase flow and heat transfer, simulations of the adiabatic churn flow regime of air-water mixture at different pipe diameters and liquid and gas superficial velocities have been initially performed. A comparison of the numerical results with experimental visualizations is reported and a simplified theoretical model of the wave levitation process has been developed and used to explain the numerical results. The VOF simulations were then extended to the study of condensation of R134a inside a minichannel with 1 mm internal diameter. Computational results about the evolution of the vapour-liquid interface and the heat transfer coefficient along the channel are reported.

Riassunto

La riduzione della carica di refrigerante nelle applicazioni di condizionamento e riscaldamento è uno dei vincoli di progetto principali quando vengono utilizzati, per motivi di carattere ambientale, refrigeranti naturali come idrocarburi ed ammoniaca.

Alcune applicazioni dei minicanali per la minimizzazione della carica nelle pompe di calore vengono presentate e discusse nella presente tesi.

Viene presentato il progetto di un condensatore, un evaporatore ed uno scambiatore di calore rigenerativo innovativi. Questi componenti sono degli scambiatori di calore a fascio tubiero utilizzanti minicali del diametro di 2 mm e progettati per l'uso con propano. Delle procedure di calcolo basate su di correlazioni disponibili in letteratura ed un modello semplificato del processo di scambio termico sono state utilizzate per il progetto. Le prestazioni sperimentali degli scambiatori con R22 e propano vengono riportate e confrontate con le stime fornite dalle procedure di calcolo.

Gli scambiatori di calore sono stati installati in una pompa di calore della capacità termica di 100 kW utilizzante propano come fluido frigorigeno. Nell'impianto della pompa di calore, destinata a test di laboratorio, sono stati installati anche un condensatore ed un evaporatore a piastre convenzionali. In questo modo è stato possibile confrontare diverse configurazioni al fine di quantificare in via sperimentale i vantaggi apportati dall'utilizzo degli scambiatori a minicanali, in termini sia di prestazioni energetiche, sia di carica di propano richiesta. In particolare, le prestazioni delle configurazioni utilizzanti il condensatore a minicanali vengono confrontate con quelle delle configurazioni utilizzanti lo scambiatore a piastre, e l'influenza sulle prestazioni energetiche dello scambiatore rigenerativo viene misurata e discussa. Vengono inoltre riportati dati sperimentali relativi all'efficienza con propano del compressore semiermetico installato nella pompa di calore.

Oltre a correlazioni empiriche in grado di stimare le prestazioni termiche globali, il progetto e l'ottimizzazione di scambiatori di calore richiede una più approfondita conoscenza del deflusso e dello scambio termico all'interno di minicanali.

Vengono presentate in questa tesi delle simulazioni di termofluidodinamica computazionale tramite l'innovativo metodo VOF (Volume Of Fluid) in grado di simulare direttamente deflussi multifase senza la necessità di utilizzare correlazioni empiriche per la modellazione dell'interazione tra le fasi.

Al fine di validare l'efficacia di questo metodo nel calcolare il moto dell'interfaccia gas-liquido, il quale è un aspetto cruciale nello scambio termico bifase, sono state in un primo momento eseguite delle simulazioni del regime di deflusso "churn flow" per una miscela aria-acqua nel caso di un tubo liscio verticale adiabatico, a differenti valori di diametro del tubo e di velocità superficiale delle due fasi. I risultati sono stati confrontati con visualizzazioni sperimentali ed un modello teorico semplificato del processo di levitazione delle onde è stato sviluppato ed utilizzato per commentare i risultati numerici.

Le simulazioni con il metodo VOF sono state in un secondo momento estese allo studio della condensazione di R134a all'interno di un minicanale del diametro di 1 mm. Vengono riportati risultati computazionali relativi all'evoluzione dell'interfaccia vapore-liquido e dei coefficienti di scambio termico lungo il minicanale.

Contents

List of figures

List of tables

Chapter 1.

Introduction

Minichannel heat exchangers are nowadays widely used and studied in a number of different applications. In the case of condensers for automotive air-conditioning applications, for example, extruded aluminium multi-port minichannel tubing is a technology that has become common.

One of the advantages given by the use of minichannels is the reduction of the size of the device. For this reason, minichannel heat exchangers are studied in the field of electronic applications, where the increasing demand for higher performance requires the adoption of miniaturized heat sinks able to provide high heat flux removal.

The focus of the present work is on the minimization of the refrigerant charge, which can be considered one of the most important targets for heating ventilation and air conditioning applications (HVAC) to cope with the new environmental challenges.

As a consequence of the phase out of CFCs and HCFCs refrigerants because of their negative influence on the ozone layer, hydrofluorocarbons (HFCs) are nowadays being used. Since these fluids are in most cases strong greenhouse gases, the environmental impact of the atmospheric emissions during the whole lifetime of equipment cannot be considered negligible. For this reason, natural fluids with no environmental impact on the ozone layer and very low impact on the greenhouse effect like hydrocarbons, ammonia and carbon dioxide have been suggested as substitutes for synthetic refrigerants. Even not considering the global warming issue, the adoption of natural fluids, which are much better known than man-made ones, also provides some kind of intrinsic safety against potential unknown negative effects of man-made substances.

Charge minimization is a major design objective for equipment using hydrocarbons or ammonia because the possible hazard when dealing with toxic or flammable fluids is proportional to the total amount of refrigerant trapped in the system. The same restriction should be adopted, in any case, in systems operating with halogenated fluids when trying to reduce emissions for environmental reasons. Since most of the charge in HVAC equipment is trapped in the heat exchangers, and especially in the condenser, the first step in order to minimize the refrigerant charge is the optimization of these devices, and minichannels technology appears to be a very good opportunity to obtain this target.

Some applications of minichannels for charge minimization in heat pumps are presented and discussed in this thesis.

A condenser, an evaporator and an internal heat exchanger have been designed and manufactured in collaboration between the University of Padova and Onda SpA in

the framework of the European project SHERHPA, dealing with the development of heat pumps in compliance with the future environmental regulations. These heat exchangers are segmentally baffled shell-and-tube heat exchangers using 2 mm i.d. copper minichannels designed for charge minimization and the use with propane. Computational procedures based on a simplified model of the heat transfer and pressure drop processes have been developed and used for the design. The experimental performance of the minichannel heat exchangers when using R22 and propane is reported in this thesis and compared against the predictions given by the computational procedures.

Furthermore, a heat pump with around 100 kW heating capacity using propane as the refrigerant and devoted to laboratory tests has been designed and realized in collaboration between the University of Padova and Hiref SpA in the framework of the same project. The major design constraint was the minimization of the refrigerant charge while maintaining high energy efficiency. It has been chosen to design a water-to-water heat pump, because roof top chillers and heat pumps using a hydronic system to distribute chilled or hot water are an ideal solution to the safety problem.

The three minichannel heat exchangers have been installed in the heat pump along with a conventional brazed plate condenser and a brazed plate evaporator in order to compare different configurations and quantify the advantages of operating the unit using the minichannel heat exchangers, with regard both to performance and propane charge.

The design and experimental data of energy efficiency and total refrigerant charge are reported in this thesis. In particular, the performance when using the minichannel condenser is compared to the one obtained when using the brazed plate condenser, and the influence of the minichannel internal heat exchanger on the performance of the equipment is measured and discussed. Experimental data about the efficiency with propane of the semihermetic compressor installed in the heat pump is also reported.

Besides the development and validation of empirical correlations able to predict the global thermal performances, a more complete understanding of the two-phase flow and heat transfer processes in minichannels is needed for the design and optimization of heat exchangers. The study of two-phase heat transfer in minichannels, however, is very complex, mainly because of the presence of a vapour-liquid interface and different flow regimes and spatial distributions of the phases which have a very strong influence on the heat transfer.

While in the past CFD simulations were not suitable for the study of such kind of complex phenomena, a number of different methods are nowadays available for the direct simulation of multiphase flows because of the increased computational capabilities. These new techniques can be very useful, in particular when trying to extend the investigation to new minichannel geometries for which a lack of experimental data or correlations exists. Some simulations are presented in this thesis using the Volume Of Fluid (VOF) method, which is able to compute multiphase flows of immiscible fluids, tracking the motion of the interface between them without using any empirical closure law to model the interaction between the phases.

The VOF method implemented in the commercial code FLUENT was first used to perform a numerical simulation of the adiabatic churn flow regime of air-water mixture in a vertical pipe at different liquid and gas superficial velocities and different pipe diameters, focusing on the process of formation and levitation of the interfacial flooding-type waves. This work is not directly linked to the study concerning minichannel heat exchangers, however it was important in order to assess the capability

of the method used to compute the motion of the gas-liquid interface, which is crucial to characterize two-phase flow and heat transfer.

The model was then extended to the study of condensation of R134a inside a minichannel with 1 mm internal diameter at low mass flux (i.e. G = 200 $kgm^{-2}s^{-1}$). This study was performed at the Cooling Technologies Research Center (CTRC) of the Purdue University, West Lafayette, Indiana, USA under the supervision of Prof. Suresh Garimella and Prof. Jayathi Murthy.

The preliminary results about this study are reported in this thesis, showing the evolution of the vapour-liquid interface and the heat transfer coefficient along the channel.

The manuscript is organized as follows:

- Chapter 1 – Introduction: Background and purpose of the present study.
- Chapter 2 – Shell-and-tube minichannel heat exchangers: Design, experimental performance and computational procedures for the minichannel shell-and-tube heat exchangers.
- Chapter 3 – Propane heat pump: Design, experimental energy efficiency and refrigerant charge for different configurations of the unit. Performance of the compressor is also discussed.
- Chapter 4 – VOF simulation of condensation in minichannel.
- Chapter 5 – VOF simulation of churn flow.
- Chapter 6 – Conclusions.

Chapter 2.

Shell-and-tube minichannel heat exchangers

2.1 Introduction

Several reasons can lead to the adoption of minichannel heat exchangers. In particular, minichannel heat exchangers are widely studied specially in the case of electronic applications, where miniaturized heat sinks with high heat flux removal capabilities are required. Conventional air cooling solutions are not suitable in this case, and heat sinks with embedded microchannels, both for the case of single-phase liquid cooling and flow boiling, are widely studied.

While in a large number of cases minichannels are studied to reduce the size of heat removal devices, the focus of the present work is on the reduction of the refrigerant charge, while maintaining the energy efficiency. Clearly, the reduction of charge is obtained mainly by minimizing the volume of the refrigerant side of the heat exchanger, but it should be stressed here that the target of charge minimization is quite different from the one of the miniaturization of the heat exchanger itself. As will be shown in this chapter, for example, the minichannel heat exchangers here presented display a much smaller internal charge as compared to conventional plate heat exchangers, however, from the point of view of the overall dimensions, they are bigger, since no constraints on the dimension of the secondary fluid side volume were required.

While the heat exchanger miniaturization is very important for electronic applications, or in order to reduce the amount of material adopted during the manufacturing process, the refrigerant charge minimization can be considered one of the most important targets for heating ventilation and air conditioning applications (HVAC) to cope with the new environmental challenges.

The worldwide alert about the greenhouse effect has led to an increasing interest on new HVAC technologies with low environmental impact. The energy efficiency of equipment must increase, in order to reduce the energy consumption and the consequent carbon dioxide emissions caused by the electricity production. However, also the direct effect due to the atmospheric emissions of refrigerants must be considered.

As a consequence of the phase out of chlorinated refrigerants (i.e. CFCs and HCFCs) because of their negative influence on the ozone layer, hydrofluorocarbons (HFCs) containing no chlorine are nowadays being used by the HVAC industry in newer equipment. These fluids display null ODP, but in most cases are strong greenhouse gases (e.g. GWP_{R134a} = 1300, GWP_{R407C} = 1520, GWP_{R410A} = 1720). Therefore, as a general consideration, the environmental impact of the atmospheric

emissions during the whole lifetime of equipment, from manufacture to dismantling, cannot be considered negligible.

It should also be also remembered that chlorofluorocarbons (CFCs) were invented in the ‘30s as completely inert and harmless fluids. Only 50 years later, in 1974, their effect on the ozone layer destruction was discovered. Since HFCs nowadays being used are quite new man-made fluids (like CFCs were when first introduced into the market) their potential negative effects cannot be completely known.

A future environmental legislation concerning refrigerants in relation to the greenhouse effect is expected. Within the EU, for example, in mobile air conditioning systems, the gradual phase out of fluids with GWP higher than 150 starting from 1st January 2011 has been regulated by the directive 2006/40/EC. In some countries (e.g. Austria, Switzerland, Denmark) new legislations have already been approved for a global phase out of HFCs. Furthermore, even if no agreement has been achieved yet, regulations on greenhouse refrigerants are discussed within the Kyoto protocol and later amendments.

For these reasons, part of the scientific community has suggested that natural fluids with no environmental impact on the ozone layer and very low impact on the greenhouse effect like hydrocarbons (HCs), ammonia and carbon dioxide should be used as substitutes for synthetic refrigerants. Furthermore, the adoption of natural fluids, which are much better known than man-made ones, should provide some kind of intrinsic safety against potential unknown negative effects of man-made substances.

Among the natural fluids suggested, hydrocarbons refrigerants are chemically related to the halogenated ones and their use would not involve major changes in equipment design, since their thermodynamic properties and materials compatibility are similar to those of traditionally used synthetic fluids. The main problem of the use of HCs as refrigerants is their flammability which has prevented from using them in a more extensive way. Regarding ammonia, this refrigerant is toxic and flammable, mainly together with traces of oil. Since the possible hazard when dealing with toxic or flammable fluids can be considered proportional to the total amount of refrigerant trapped in the system, the charge minimization is a major design objective for equipment using HCs or ammonia.

It is interesting to notice that, since also the total amount of atmospheric emissions from equipment, from manufacture to dismantling, is proportional to the total amount of refrigerant trapped in the system, the same restriction should be adopted in systems operating with halogenated fluids.

For all these reasons, it is clear that the refrigerant charge minimization can be considered one of the most important targets for HVAC applications to cope with the new environmental challenges.

In order to address charge reduction in HVAC equipment, one should analyze the location of the refrigerant charge in the facility.

In a paper by Harms *et. al.* (2003), the charge inventory distribution among the components of three unitary air conditioners with capacity varying from 9 kW to 26 kW and using R22 and R407C as refrigerant has been estimated. Most of the heat exchangers used standard microfin tubes, with internal diameter varying from 6 mm to 9 mm. According to their results, most of the charge was expected to be trapped in the exchangers; in particular the computed charge in the condenser varied from 30% up to 70% of the total amount, while the charge in the evaporator was about 15%.

In a paper by Palm (2007), most of the charge in a 5 kW capacity water-to-water heat pump adopting brazed plate heat exchangers and using propane was experimentally measured to be trapped in the heat exchangers, and mainly in the condenser, where about 40 % of the total charge was found.

Similar results have been obtained in an estimation by Corberán and Martínez (2008a) of the charge inventory distribution among the components of a water-to-water propane heat pump using plate heat exchangers (PHEs): 50% of the total charge is expected to be found in the condenser, while about 15% should be trapped in the evaporator.

Since most of the charge in HVAC equipment is trapped in the heat exchangers, the first step in order to get a reduction of the refrigerant charge is the optimization of these devices, especially of the condenser, and minichannels technology appears to be a very good opportunity to obtain this target.

Nevertheless, minichannels could represent also a solution to the high pressure challenge when using carbon dioxide as a refrigerant.

Internal volume, and consequently charge, decreases with the square of diameter reduction, while the heat transfer area decreases with the diameter. This is definitely an advantage of minichannels, because the ratio of heat transfer area over volume increases when decreasing the channel diameter.

Besides, in the case of shear stress dominated condensation, the reduction of the channel diameter increases the heat transfer coefficient. This second advantage, however, could be negligible in heating and air conditioning applications, since the refrigerant side is not usually the thermal controlling side in a heat exchanger. As an example, Fig. 2.1 reports the heat transfer coefficient during condensation of R134a, propane (R290) and isobutane (R600a) at mass flux G = 400 kg/(m^{2}s^2), vapour quality x = 0.5 and 40°C saturation temperature inside tubes with diameter varying from 10 mm down to 1mm. Heat transfer coefficients have been computed using the model by Cavallini *et al.* (2006).

On the other hand, when reducing the hydraulic diameter, the refrigerant pressure drop increases for the same mass flux. The graph in Fig. 2.2 depicts the pressure gradient for R134a, R290 and R600a at mass flux G = 400 kg/(m^{2}s^2), vapour quality x = 0.5 and 40°C saturation temperature inside tubes with diameter varying from 10 mm down to 1mm. The reported pressure gradients have been computed using the model by Cavallini *et al.* (2008a).

The graph in Fig. 2.2 suggests that it could be not convenient, from an energetic point of view, to decrease the channel beyond a certain value due to the increase of the pressure drop and the possible penalty on the COP. This is particularly important in evaporators in comparison to condensers, since the lower the temperature, the higher the saturation temperature drop. Nevertheless, this issue can be easily mitigated by increasing the number of tubes fed in parallel, in order to reduce the mass flux. However, in particular in the case of an evaporator, where a two-phase mixture is present at the inlet of the heat exchanger, this approach opens another important issue, which is the distribution of the refrigerant.

Ammonia and hydrocarbons have some advantages as compared to conventional refrigerants, with regard to charge reduction, such as the low liquid density. A comparison between refrigerants aiming to show the opportunities for charge reduction in a condenser has been performed by Hrnjak (2005).

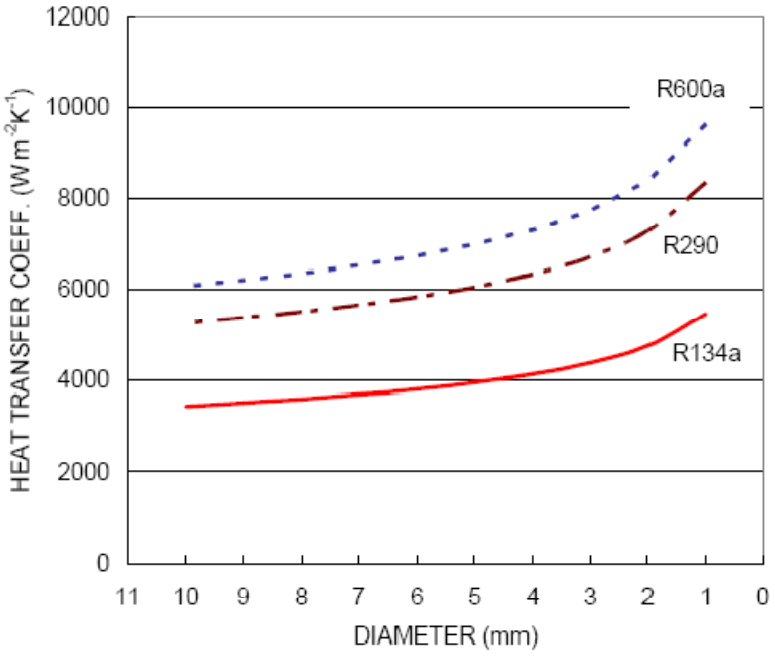

Fig. 2.1. Condensation heat transfer coefficient at mass velocity 400 kg/(m^{2}s), 0.5 vapour quality, 40°C saturation temperature. Values were predicted using the model by Cavallini *et al.* (2006).

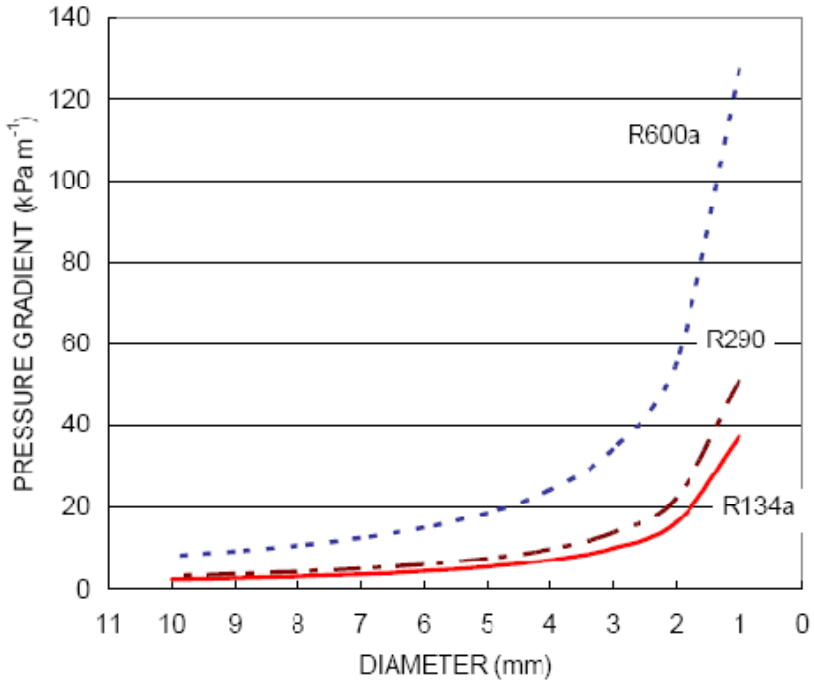

Fig. 2.2. Pressure gradient at mass velocity 400 kg/(m^{2}s), 0.5 vapour quality, 40°C saturation temperature. Values were predicted using the model by Cavallini *et al.* (2008a).

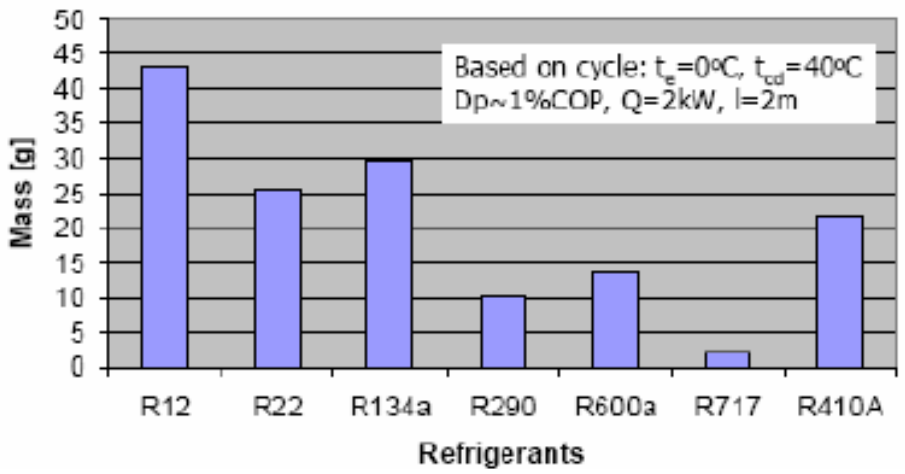

Fig. 2.3. Estimation of condenser charge with different refrigerants by Hrnjak (2005).

The results are represented in Fig. 2.3: the charge represents the mass in the tubes assuming homogeneous void fraction, 2 kW capacity, length of the tubes equal to 2 m, evaporating and condensing temperatures of 0°C and 40°C and variable cross section which was reduced, for each refrigerant, down to the point where pressure drop reduces COP by 1%. Regardless of some simplifications, these results show the opportunities for charge reduction in minichannels for ammonia and HCs as compared to some other refrigerants.

Air-to-propane prototype heat exchangers employing minichannels have been developed and installed in a 2 kW cooling capacity refrigeration system at the University of Illinois, Urbana-Champaign, by Hrnjak and Hoehne (2004). Fig. 2.4 shows the breakdown of propane charge in the equipment studied by Hrnjak and Hoehne. Since the charge in the heat exchangers has been minimized, the major contribution to charge, in this case, is due to the compressor, then to the condenser and to the evaporator. The authors state that the use of microchannels tubes has reduced the total system charge from approximately 0.2 kg in conventional systems to less than 0.13kg.

The benefits of using minichannels heat exchangers for ammonia were shown in Hrnjak (2005). A chiller using minichannel condenser was realized and tested, leading to a system charge of 18 grams per kW evaporator capacity.

As compared to air-to-refrigerant heat exchangers, liquid-to-refrigerant heat exchangers can further minimize the charge by exploiting the better heat transfer properties of the liquid. It should be considered, however, that the additional secondary fluid loop introduces an extra temperature difference between the refrigeration system and the heat source and heat sink, which may reduce the overall performance.

Liquid-to-propane prototypes heat exchangers, using flat multiport 1.4 mm hydraulic diameter aluminium tubes, have been realized at the KTE, Stockholm, and installed in a 5 kW heat pump (Fernando *et al.*, 2004, Palm, 2007). An evaluation of the heat transfer performances of these prototypes minichannel heat exchangers during

single phase flow, evaporation and condensation can be found, respectively, in Fernando *et al.* (2008a), Fernando *et al.* (2008b) and Fernando *et al.* (2008c).

The prototype minichannel heat exchangers described in this thesis were designed for the use with propane in collaboration between the University of Padova and Onda SpA in the framework of the European project SHERHPA. These minichannel heat exchangers have been installed in a water-to-water heat pump using propane having a heating capacity of about 100 kW and designed for laboratory tests.

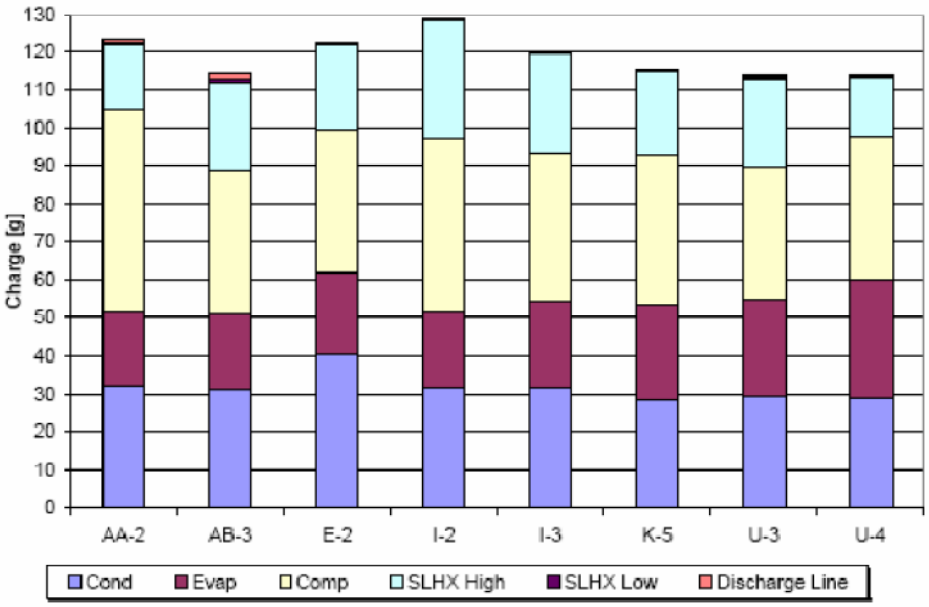

Fig. 2.4 Experimental charge breakdown measured by Hrnjak and Hoehne (2004). The charge is divided in the following components: condenser, evaporator, compressor, internal heat exchanger (high pressure and low pressure), discharge line.

2.2 Design of minichannel shell-and-tube heat exchangers

A condenser, an evaporator and an internal heat exchanger have been designed and realized in collaboration between the University of Padova and Onda SpA. These prototypes have been designed for the installation in a heat pump using propane as refrigerant and the major design constraint was the minimization of the refrigerant charge, while maintaining the energy efficiency. The design and the experimental performance of the condenser and the evaporator when using R22 are reported, respectively, in Cavallini *et al.* (2008b) and Del Col *et al.* (2008).

The three heat exchangers are segmentally baffled shell-and-tube heat exchangers using 2 mm i.d. copper minichannels instead of conventional microfin tubes. In order to reduce the refrigerant side internal volume, in the case of the condenser and the evaporator propane flows inside the tubes and water flows on the shell side. In the case of the internal heat exchanger, since the density of the superheat vapour is very low in comparison to the density of the subcooled liquid (i.e. at saturation conditions T = 2°C, ρ_G = 11 kg/m^3; at saturation conditions T = 50°C, ρ_L = 449 kg/m^3), the liquid propane flows inside the tubes, while the vapour flows on the shell side.

For all the three prototypes it has been adopted a single shell pass with two tube passes by using a U-tube bundle. The refrigerant flow is horizontal and propane enters from the top in the condenser and the internal heat exchanger and from the bottom in the evaporator.

The outside diameter of the minichannels adopted is 4 mm, while the inside diameter is 2 mm. It can be noted here that these heat exchangers could therefore represent a solution to the high pressure challenge when using carbon dioxide, provided that an appropriate design of the header is given.

The general features and dimensions of the heat exchangers are given in Table 2.1, while the overall dimensions are shown in Fig. 2.5, Fig. 2.6 and Fig. 2.7 for the condenser, the evaporator and the internal heat exchanger, respectively. The same outside shell dimensions have been used for the condenser and the evaporator, while the internal heat exchanger is clearly smaller.

Table 2.1. Minichannel heat exchangers specifications.

	Condenser	Evaporator	IHX
Tubes	U-type, smooth	U-type, smooth	U-type, smooth
Tube inside diameter	0.002 m	0.002 m	0.002 m
Tube outside diameter	0.004 m	0.004 m	0.004 m
Tube layout pattern	30° triangular	30° triangular	30° triangular
Tube length	1.1 m	1.1 m	0.35 m
Shell internal diameter	0.265 m	0.265 m	0.133 m
Tube pitch	0.008 m	0.006 m	0.006 m
Number of tubes	564	1248	226
Number of baffles	11	15	4
Baffle type	Segmental	Segmental	Segmental
Baffle spacing	0.084 m	0.059 m	0.070 m
Baffle cut	24 %	26 %	25 %
Tube side volume	2.9 L	5.8 L	0.5 L

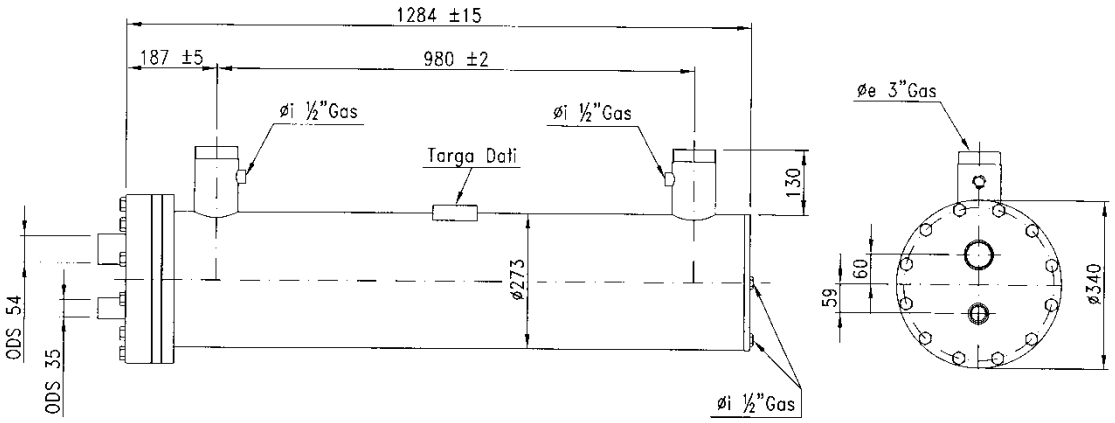

Fig. 2.5. Condenser overall dimensions.

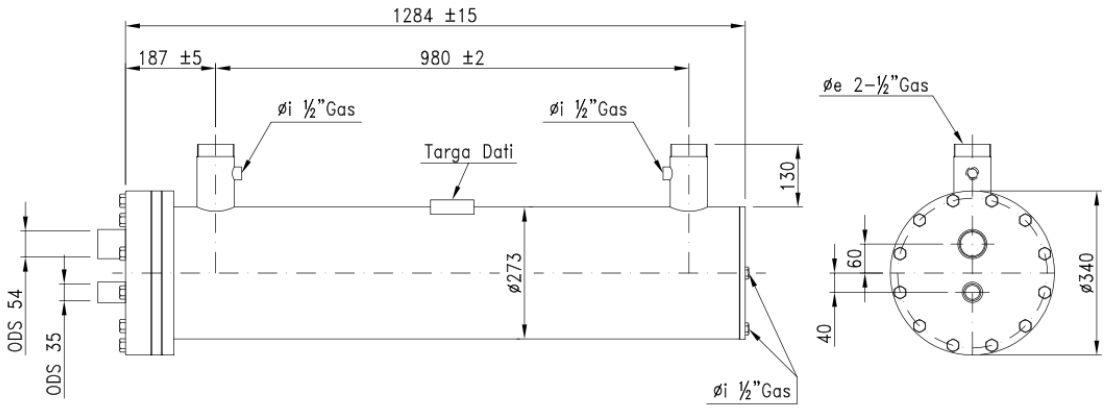

Fig. 2.6. Evaporator overall dimensions.

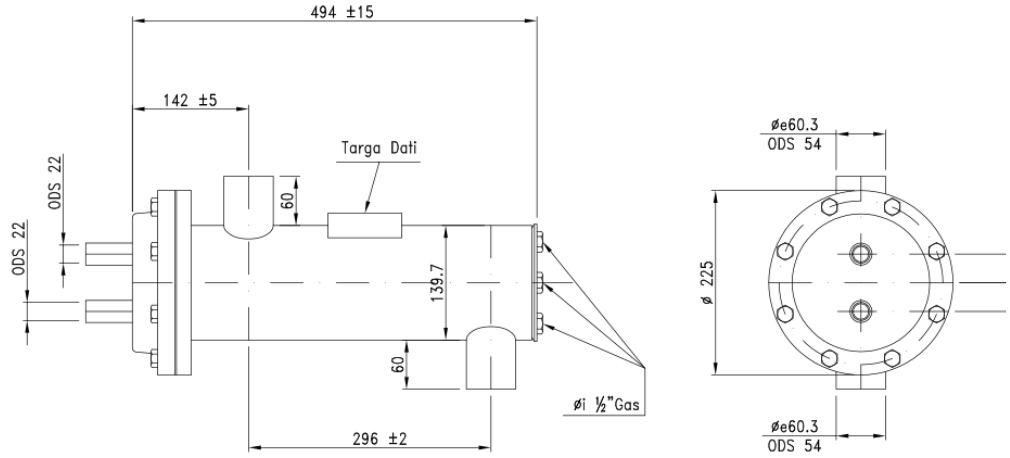

Fig. 2.7. Internal heat exchanger overall dimensions.

The condenser has been designed in order to provide, when using propane as the refrigerant, around 100 kW heating capacity, with around 50°C condensing temperature, when the inlet and outlet water temperature at the shell side are 40°C and 45°C.

The evaporator has been designed in order to provide 80 kW cooling capacity, with around 2°C evaporating temperature and 5 K outlet superheating, when the inlet vapour quality is around 0.25 and the inlet and outlet water temperature at the shell side are 12°C and 7°C.

The use of an internal heat exchanger is suggested by the manufacturer of the compressor used in the heat pump in order to reduce the solubility of propane in the oil and avoid problems due to the decrease of the lubricant viscosity (Bitzer, 1997). At least 20 K vapour superheat at the compressor suction and discharge are suggested by Bitzer. The internal heat exchanger has been designed in order to provide around 20K additional vapour superheat when the liquid propane enters at the design conditions corresponding to the condenser outlet (i.e. 50°C saturation temperature) and the vapour propane enters at the design conditions corresponding to the evaporator outlet (i.e. 2°C saturation temperature and 5K superheat).

Computational procedures based on a simplified model of the heat transfer and pressure drop processes in the heat exchangers have been used for the design the prototypes. These models will be described in detail in section 2.4.

Since the amount of refrigerant that can be trapped in the headers is not negligible, a special design has been developed to reduce the internal volume of the headers where liquid propane is present. The condenser header, evaporator header and internal heat exchanger header are shown in Fig. 2.8, Fig. 2.9 and Fig. 2.10. As one can see, the volume of the outlet condenser header and of both the inlet and outlet headers of the internal heat exchanger has been minimized.

The refrigerant pressure drop always reduces the thermal performance of a condenser or an evaporator by reducing the saturation temperature and increases the energy consumption of the compressor. One disadvantage of using minichannel is that when decreasing the hydraulic diameter of a pipe the pressure drop increases for the same mass flux. Therefore, the refrigerant pressure drop is a very important parameter when designing heat exchangers using minichannels.

In the condenser, the refrigerant flow is divided into 282 parallel minichannels. At nominal conditions, when operating with propane, the mass flux is G = 330 kg/(m^{2}s) and the expected design pressure drop is around Δp = 20 kPa corresponding to about 0.6 K saturation temperature drop. As one can see, the design saturation temperature drop is pretty low as compared to the temperature difference between the two fluids (i.e. 40-45°C water temperature and 50°C design condensing temperature). This may suggest to increase the mass velocity by reducing the number of parallel minichannels and adopting longer circuits. In fact, in the design of the present heat exchanger, the maximum overall length is limited and therefore, for two passes, the total length of the minichannels cannot be further increased.

The problem of the saturation temperature drop induced by the pressure drop in the refrigerant flow is much stronger in the evaporator in comparison to the condenser, mainly because the lower the temperature, the higher the saturation temperature drop. This is the reason why in the evaporator the refrigerant flow is divided into a much higher number of tubes (i.e. 624 minichannels in the evaporator and 282 minichannels in the condenser).

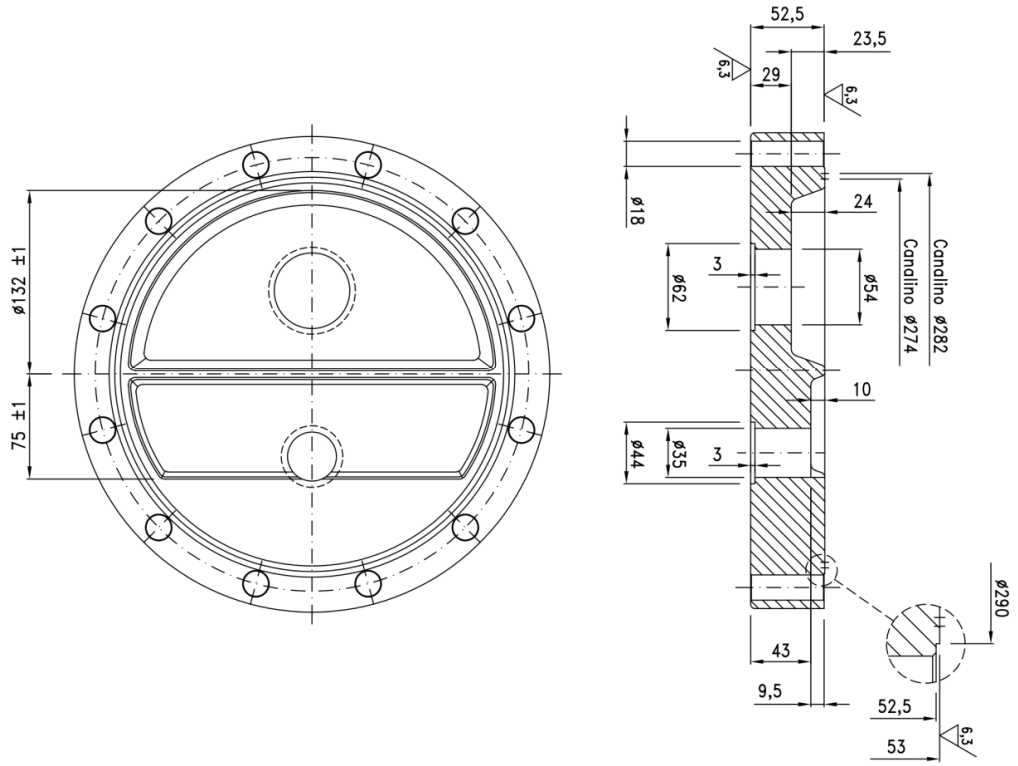

Fig. 2.8. Condenser header.

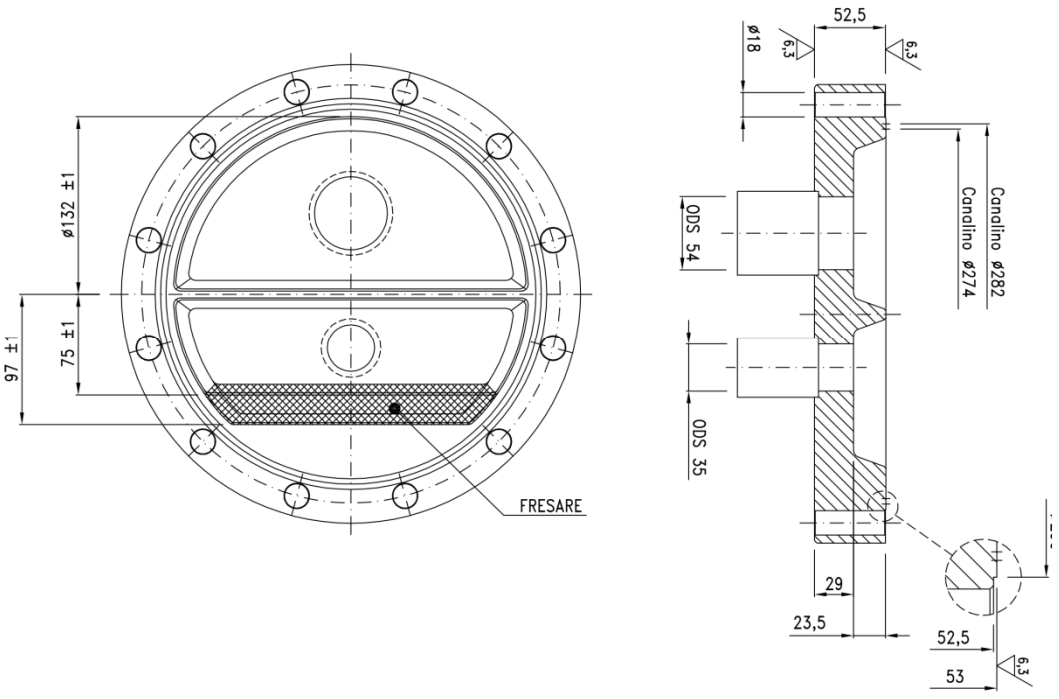

Fig. 2.9. Evaporator header.

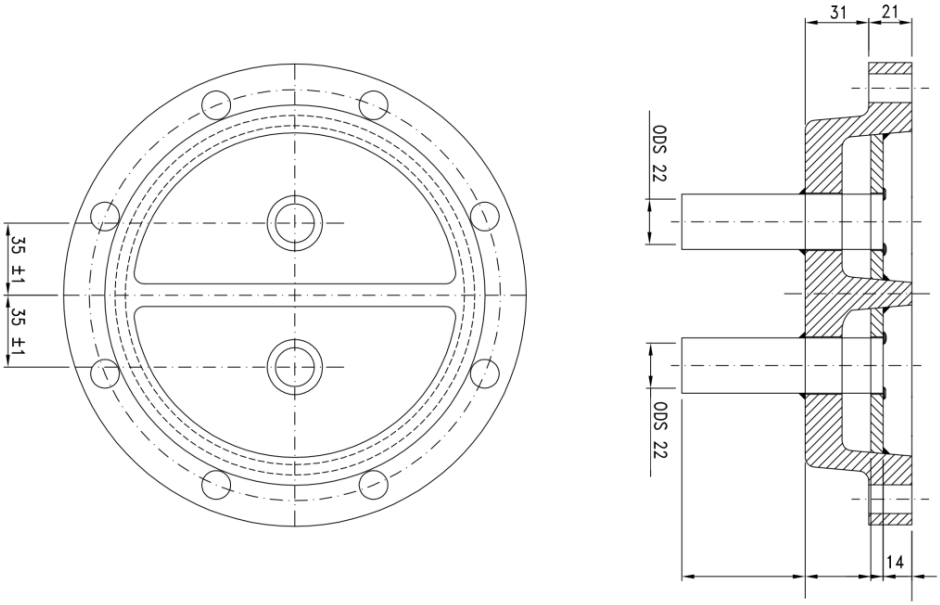

Fig. 2.10. Internal heat exchanger header.

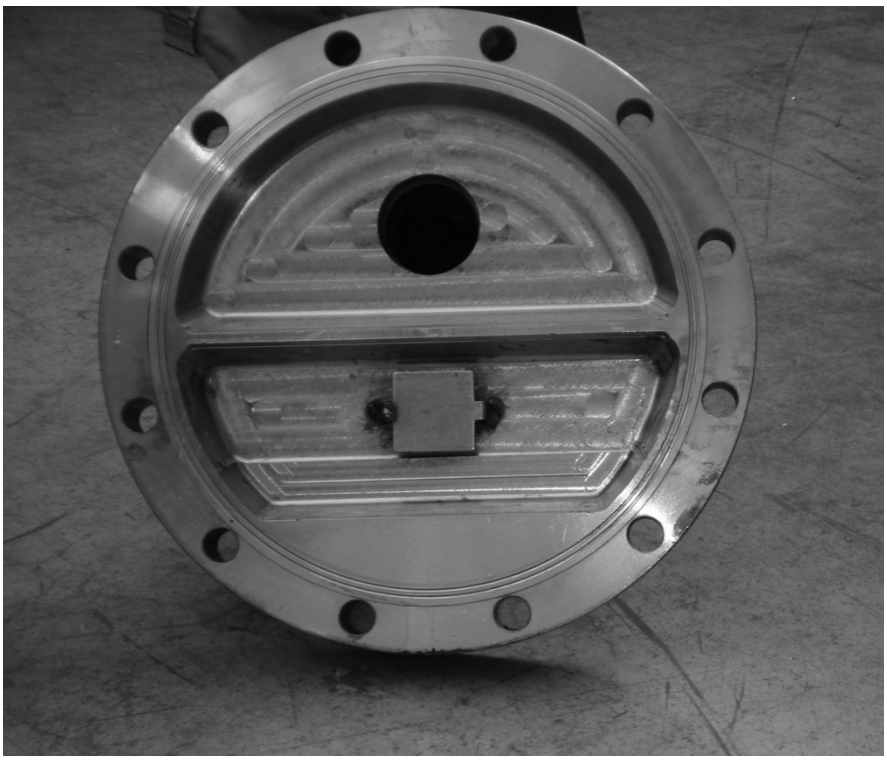

Fig. 2.11. Evaporator distributor.

The evaporator has been designed in order to get an optimal saturation temperature drop as compared to the difference between the two fluids. At nominal conditions, when operating with propane, the mass flux is around G = 150 kg/(m^{2}s) and the expected design pressure drop is about Δp = 30 kPa, corresponding to around 2 K saturation temperature drop.

Fig. 2.13 shows the evaporator tube sheet. Clearly, because of the very high number of minichannels fed in parallel, the distribution in the evaporator is a very important issue. Tests have been performed during the design process using R22 as refrigerant comparing two different distributors: a small plate put at the end of the inlet pipe and a perforated plate covering all inlet header. According to the better performance obtained in these tests, the design with the small plate was chosen. A picture of the distributor installed in the evaporator is shown in Fig. 2.11.

R22 displays a volumetric cooling capacity very similar to the propane one, therefore the velocity of the refrigerant flowing through the evaporator is around the same for both fluids. However, since the two-phase mixture is impinging on the distributor, the momentum should be the parameter ruling this kind of flow and therefore the density should have an influence on the performance of this kind of distributor. It should be stressed that the R22 density is more than double the R290 density (i.e. at 2°C saturation temperature, R290: ρ_G = 11 kg/m^3, ρ_L = 526 kg/m^3; R22: ρ_G = 23 kg/m^3, ρ_L = 1275 kg/m^3); therefore it is not really clear if the small plate is the best choice also when using propane. At the moment of writing, no experimental test with propane of the evaporator has been run.

While inside the tubes the oil return should not be a problem since a sufficient high design velocity of the refrigerant has been chosen, this issue must be considered on the shell side of the internal heat exchanger. A picture of the baffles of the internal heat exchanger is shown in Fig. 2.12. In order to assure the return of the oil to the compressor, vapour propane enters the shell from the top next to the tube sheet, and exit from the bottom. Furthermore, the two baffles covering the bottom of the shell have been perforated and the heat exchanger has been installed with some inclination.

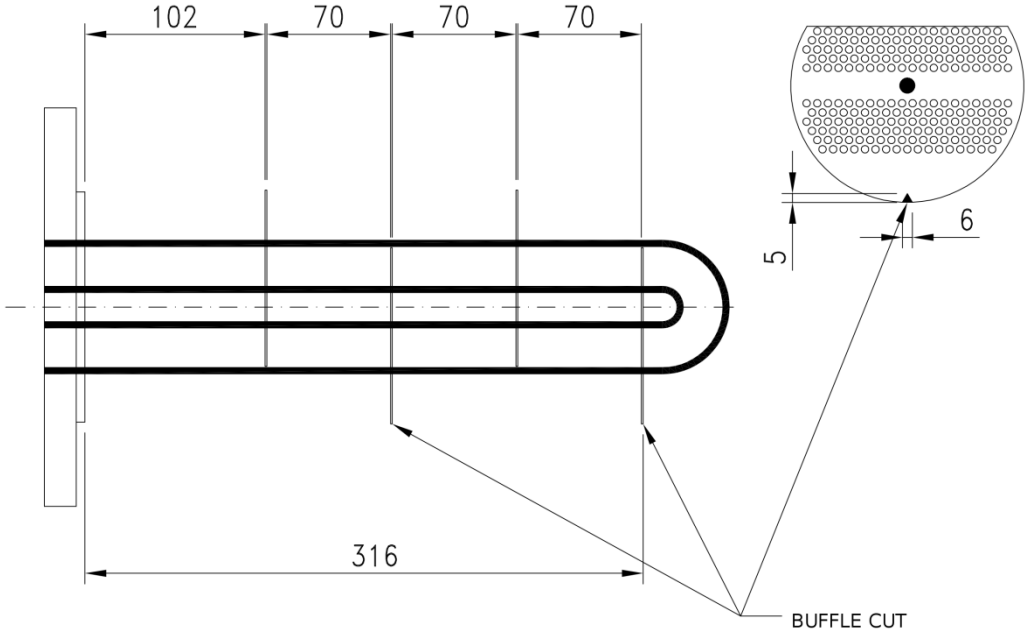

Fig. 2.12. Internal heat exchanger baffles.

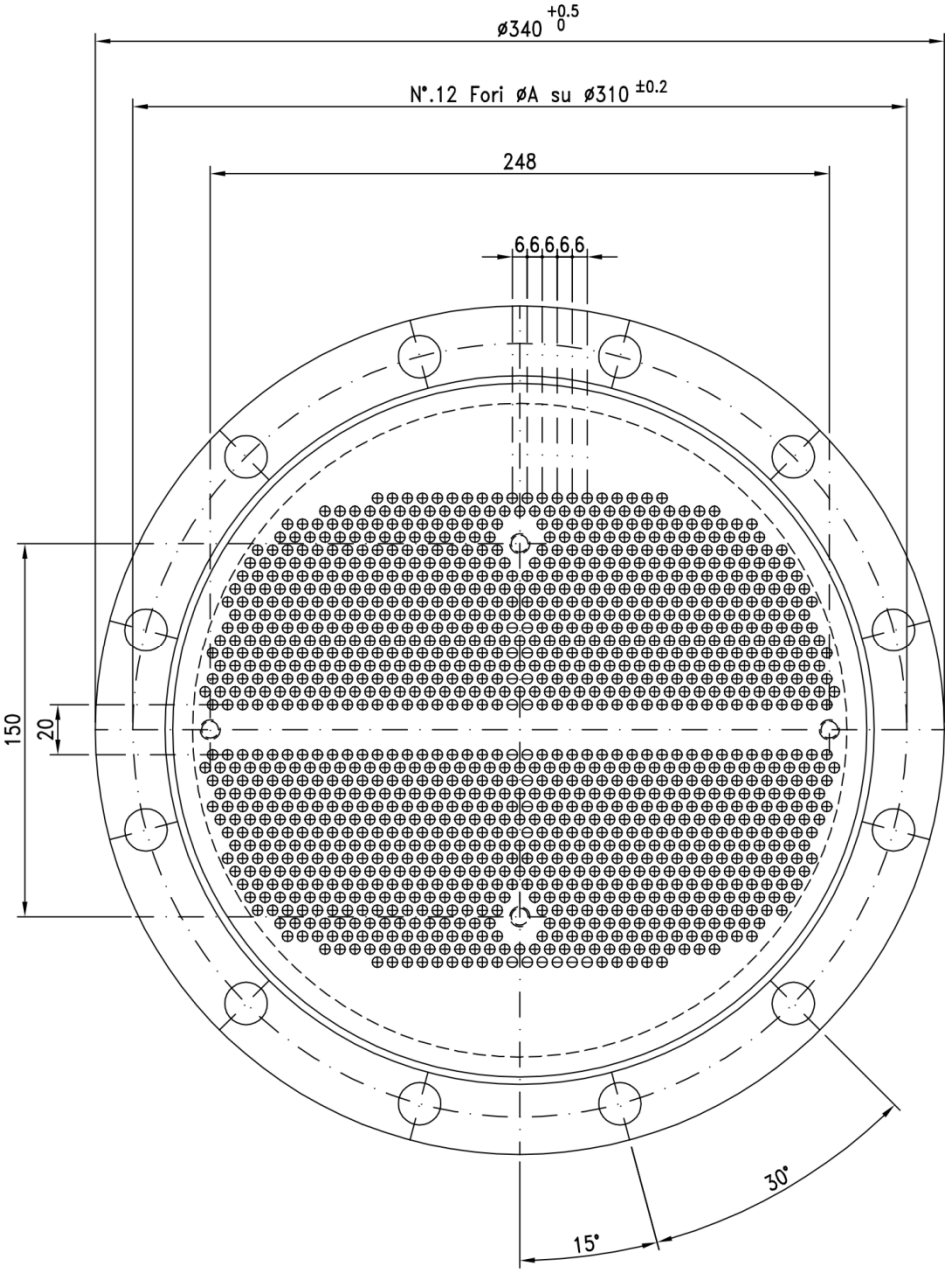

Fig. 2.13. Evaporator tube sheet.

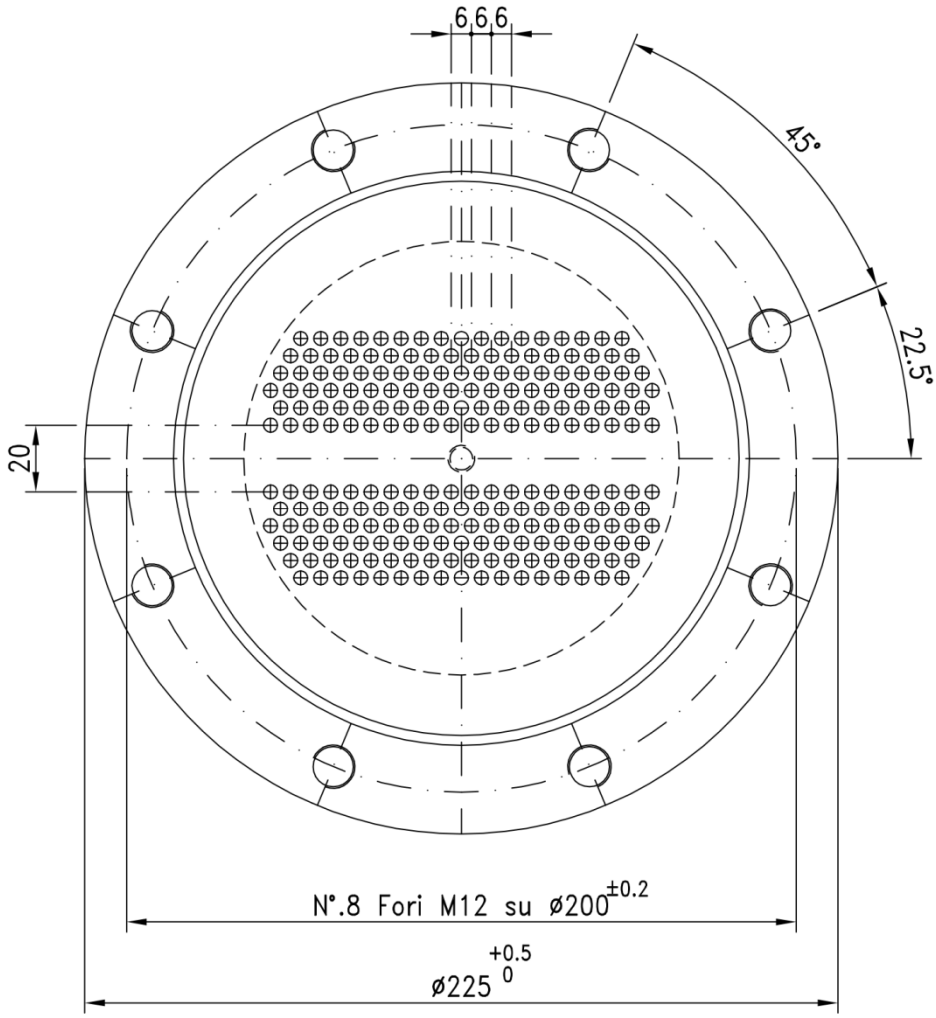

Fig. 2.14. Internal heat exchanger tube sheet.

2.3 Experimental tests with R22 and R290

The minichannel evaporator and the minichannel condenser have been tested at the facility located at the R&D laboratory of Onda SpA, before being installed in the heat pump. Refrigerant R22 has been used instead of propane to perform this first set of tests of the thermal and hydraulic performances of the prototypes. This fluid has been chosen because it presents a temperature versus pressure saturation curve and volumetric capacity values very similar to the ones of propane.

Furthermore, the minichannel condenser has also been tested with R22 during evaporating conditions, in order to obtain same experimental data for the validation of the computational procedure used to design the evaporator.

The minichannel prototypes have been installed in a heat pump using propane as the refrigerant, along with conventional brazed plate heat exchangers, in order to compare different working configurations, both in terms of energy efficiency and refrigerant charge. This second set of experimental test has been run at the Dipartimento di Fisica Tecnica, University of Padova. A description of the heat pump instrumentation can be found in Section 3.5.

In this section, experimental data about the minichannel condenser and the minichannel internal heat exchanger when using propane is reported. At the moment of writing the present thesis, no configuration using the minichannel evaporator has been tested yet.

In the facility located at the R&D laboratory of Onda SpA, the compressor is controlled by an inverter, therefore for the tests with R22 the heat flow rate could be varied continuously by varying the refrigerant flow rate.

In the propane heat pump, no inverter is used. However, the capacity control of the reciprocating compressor used allows to reduce the capacity down to 66% by switching off two cylinders out of six. For this reason, experimental points here reported for R290, are clustered around two values of the refrigerant flow rate, corresponding to the operation at 100% capacity and 66% capacity. However, some variation of the refrigerant flow rate could be obtained by varying the evaporating pressure or the superheating, thus varying the density of vapour at the compressor suction.

2.3.1 Experimental performance of the minichannel condenser with R22 and R290

The saturation temperature correspondent to the pressure measured at the inlet, when using R22, is plotted versus heat flow rate in Fig. 2.15. Data has been obtained at 40°C and 30°C water inlet temperature; in both cases the water temperature rise was 5K and the refrigerant subcooling measured at the condenser outlet was around 0.8 K. The average superheating of the vapour at the condenser inlet was around 45K.

It is interesting to point out that the condensing temperature does not change much when increasing the heat flow rate.

In the scale of the graph in Fig. 2.15 the heat flow rate ranges from 80 kW up to 120 kW. At the values of condensing temperature here considered (i.e. around 40~50°C), the corresponding values of R22 mass flow rate range from 0.4 kg/s up to 0.6 kg/s.

The experimental refrigerant pressure drop with R22 versus mass flow rate is plotted in Fig. 2.17. Data has been obtained at the same conditions as in Fig. 2.15. As one can see, the pressure drop displays a strong dependence on the refrigerant temperature: pressure drop measured at 30°C inlet water temperature (corresponding to about 40°C condensation temperature) is higher than that obtained at 40°C inlet water temperature (corresponding to about 50°C condensation temperature).

Regarding experimental data obtained with R290, the saturation temperature correspondent to the pressure measured at the condenser inlet is plotted versus heat flow rate in Fig. 2.16. Data has been obtained at 40°C, 35°C and 30°C water inlet temperature; in all cases the water temperature rise was 5K. Data has been obtained during test runs at different evaporator water temperature (i.e. 12-7°C and 10-5°C), using both the configurations with and without internal heat exchanger, at 100% and 66% compressor capacity.

The average superheating of the propane vapour at the condenser inlet was around 25 K when using the configuration without the internal heat exchanger and around 45 K when using the configuration with the internal heat exchanger. The propane subcooling at the outlet of the condenser is considered 0 K for the experimental data reported, since in the test runs here considered a slightly not complete condensation of the refrigerant was observed. This issue is further discussed in Section 3.6.

It is interesting to point out that, in order to have 100 kW heating capacity, with R22 the required mass flow rate is around 0.5 kg/s, while with R290 the required mass flow rate is around 0.3 kg/s. However, because of the different fluid densities, the required volumetric flow rate is very similar for the two fluids.

The experimental refrigerant pressure drop with R290 versus mass flow rate is plotted in Fig. 2.18. Data has been obtained at the same conditions as in Fig. 2.16. Also in this case, a very strong dependence of the pressure drop on the refrigerant temperature can be seen.

A very interesting result is shown in Fig. 2.19, where the thermal performance of the minichannel condenser when using R22 is compared to the performance obtained with R290. As one can see, the dependence of the condensing temperature on the heat flow rate display the same slope for all the cases, and the condensing temperature is lower when using R290 as compared to R22.

In the literature some data can be found about the comparison of R22 and R290 during condensation inside plate heat exchanger.

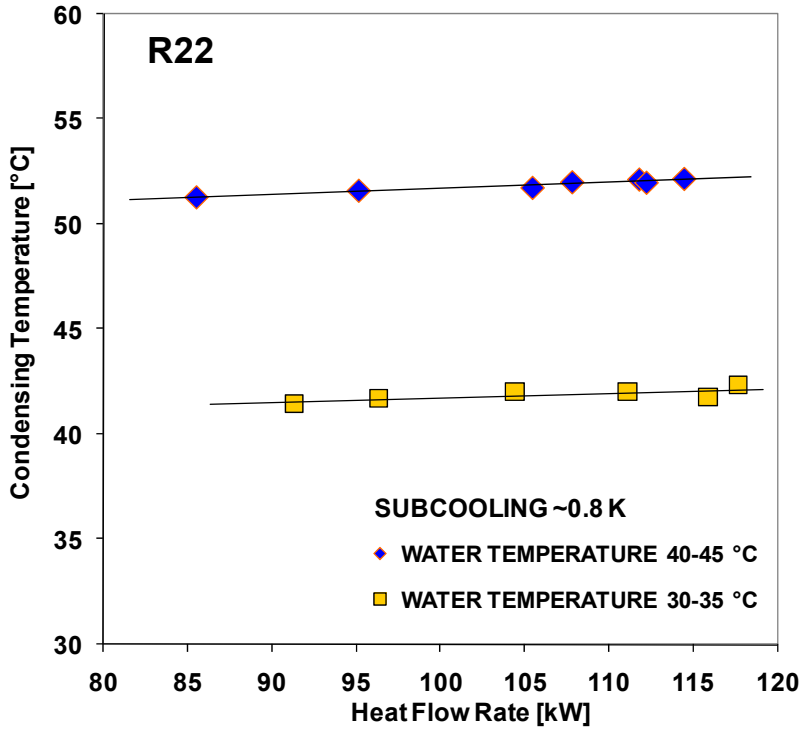

Fig. 2.15. Experimental inlet condensing temperature versus heat flow rate when using R22.

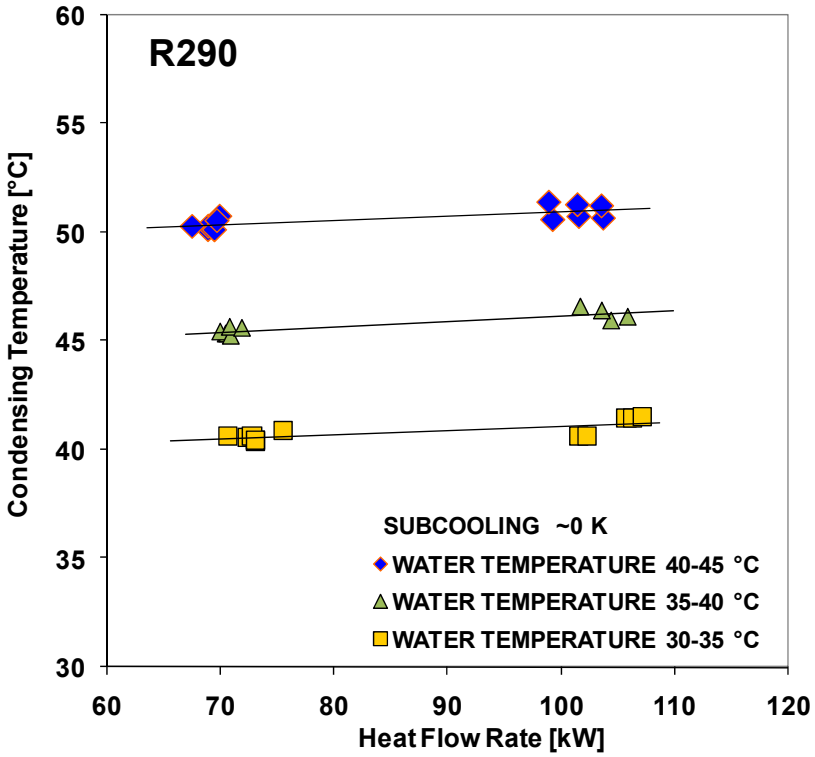

Fig. 2.16. Experimental inlet condensing temperature versus heat flow rate when using R290.

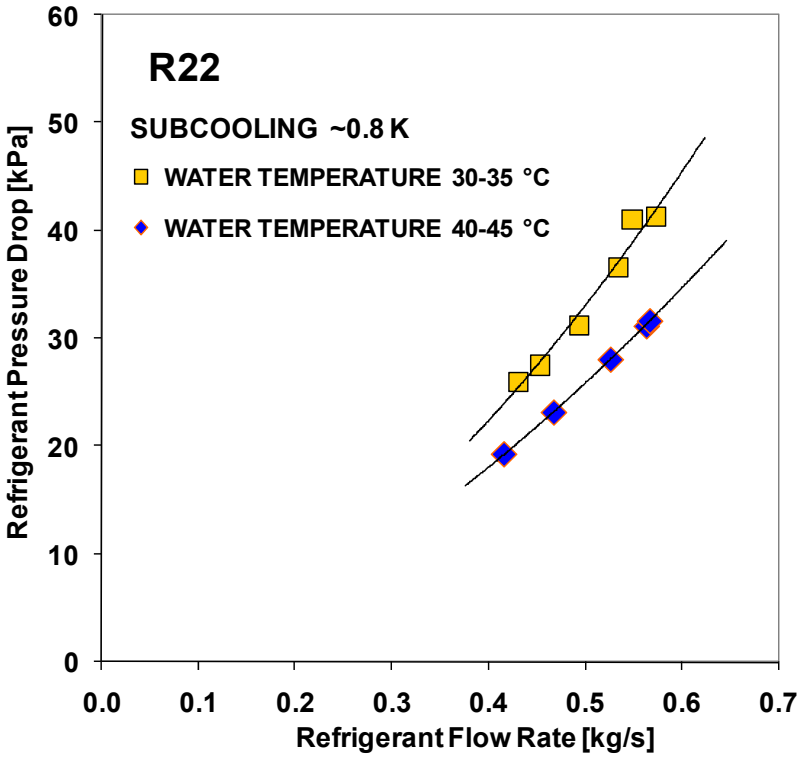

Fig. 2.17. Experimental R22 pressure drop versus mass flow rate. The corresponding values of heat flow rate range from 0 to 140 kW.

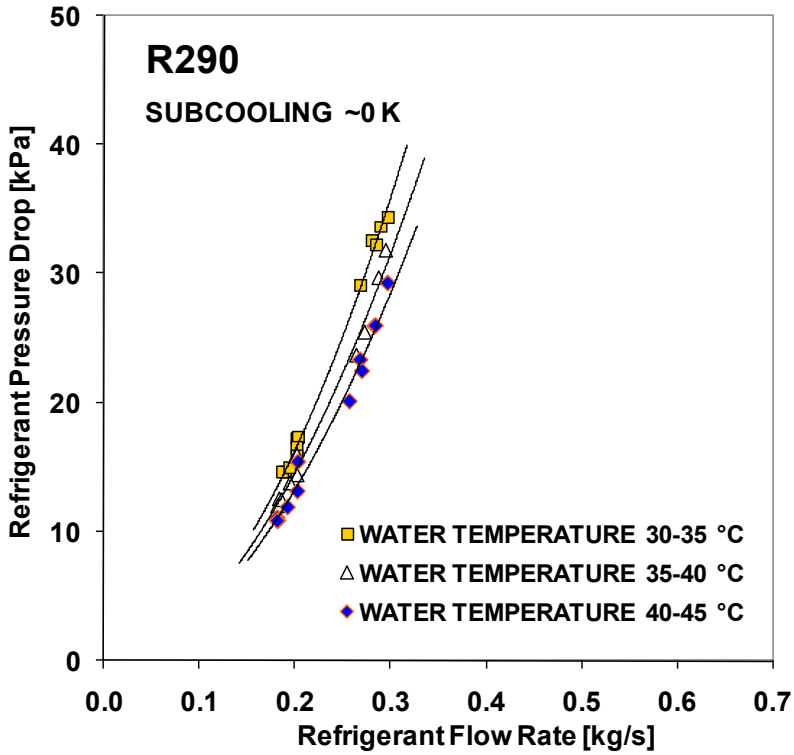

Fig. 2.18. Experimental R290 pressure drop versus mass flow rate.

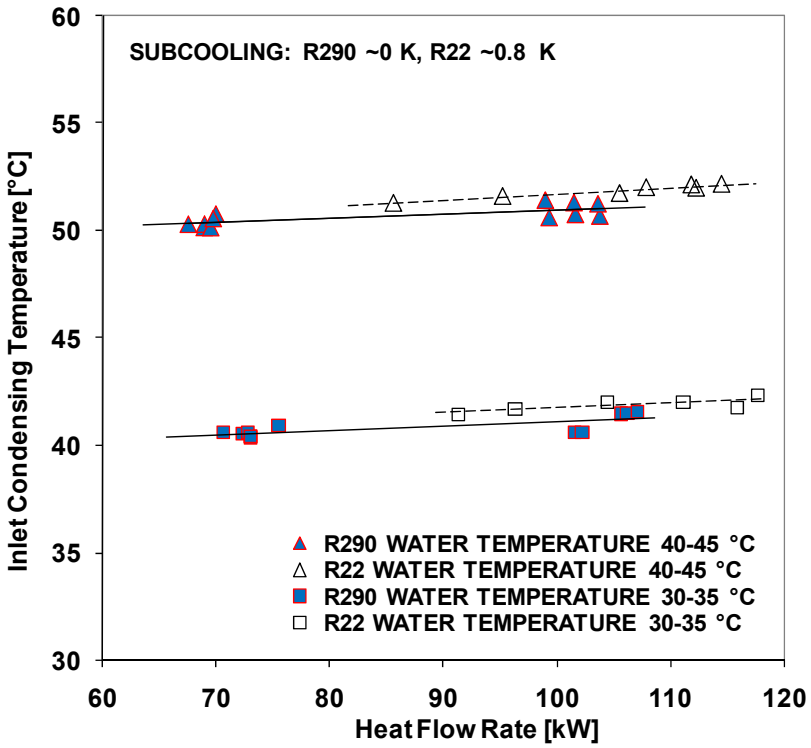

Fig. 2.19. Comparison between experimental R290 and R22 inlet condensing temperature.

Experimental data by Pelletier and Palm (1996) about condensation inside a brazed plate heat exchanger (BPHE) shows that, at the same load, the overall heat transfer coefficient is slightly lower for propane than for R22. In an analogous experimental analysis by Corberán *et. al*. (2000) similar condensation heat transfer coefficients in a BPHE have been measured for the two fluids.

It should be here remember that the process of condensation inside plate heat exchangers is pretty different from the one inside minichannels, since the former one takes place at low mass fluxes (i.e. in the order of around G = 20 kg/(m^{2}s), while the latter one takes place at much higher mass fluxes and is usually shear stress dominated (i.e. in the case of the present prototype at design condition with propane, around G = 300 kg/(m^{2}s).

The performance of the minichannel condenser with R22 and R290 can also be compared from the point of view of the pressure drop. In order to get 100 kW heating capacity, the required mass flow rate with R22 is 0.5 kg/s. At 40°C condensation temperature, the experimental pressure drop is 33 kPa, which, in terms of saturation temperature drop, corresponds to around 1 K. The corresponding mass flow rate for R290 is around 0.3 kg/s and the pressure drop is 35 kPa, corresponding to around 1 K in terms of saturation temperature drop.

Another important parameter to describe the performance of the minichannel condenser is the shell side pressure drop. In Fig. 2.20 experimental data about the water pressure versus mass flow rate obtained at 19°C is reported. At nominal condition (i.e. 100 kW heating capacity and 5 K water temperature rise), the water flow rate is 4.8 kg/s and the corresponding shell side pressure drop is around 7 kPa.

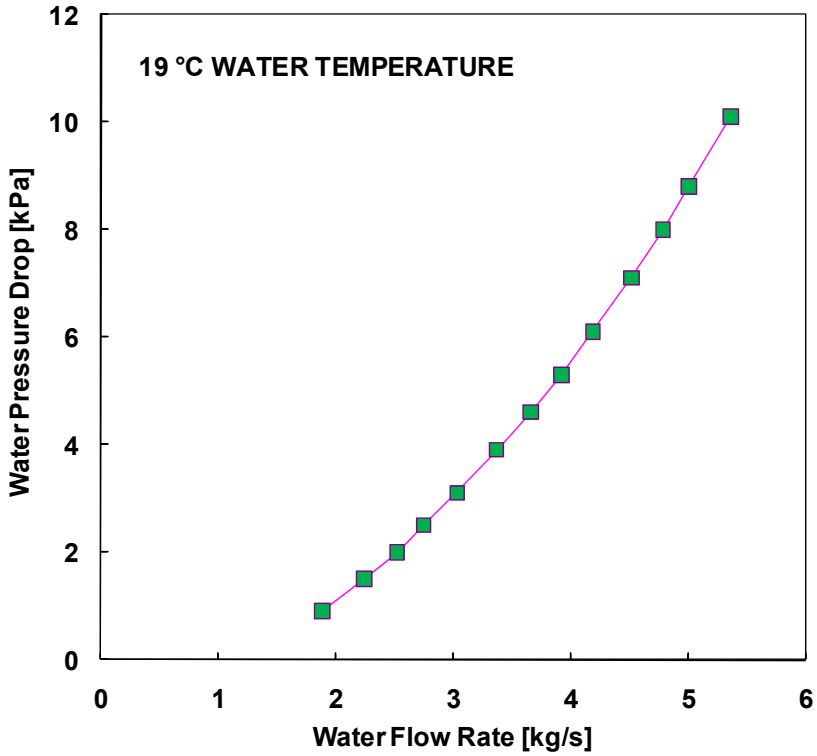

Fig. 2.20. Minichannel condenser experimental water pressure drop versus mass flow rate at 19°C.

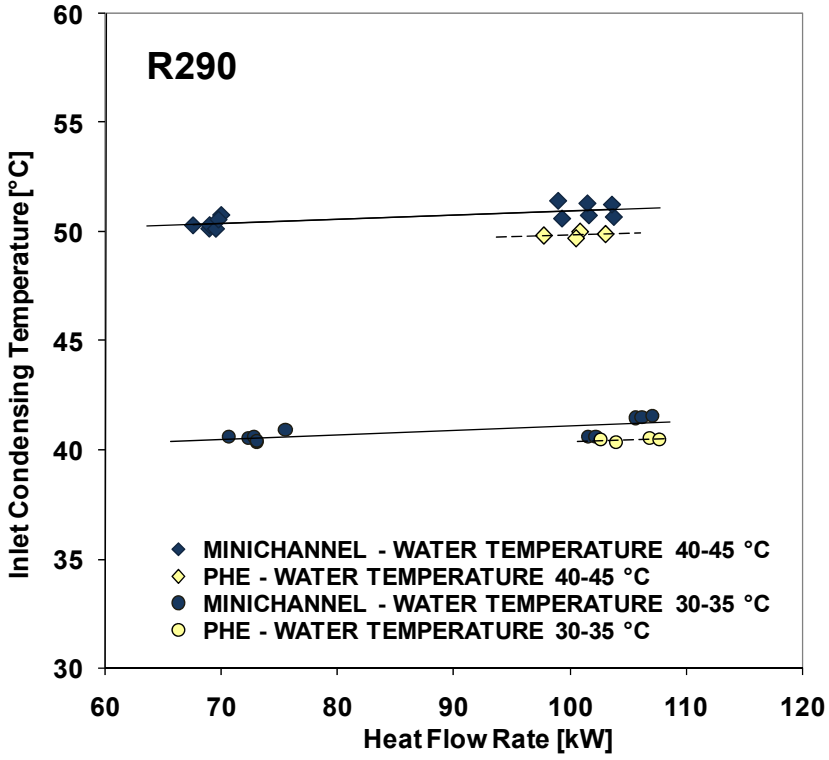

Fig. 2.21. Comparison between inlet condensing temperature for the minichannel condenser and a brazed plate heat exchanger when using R290.

Along with the minichannel condenser, a conventional brazed plate condenser has been installed in the facility of the heat pump used to obtain the experimental data here presented.

In Fig. 2.21 the thermal performances of the two condensers when using R290 are compared. As one can see, the inlet condensing temperature for the plate condenser is slightly lower at the same heat capacity. It must be stressed that the nominal heat transfer area of the plate condenser is around 7 m^2, while the propane side heat transfer area of the minichannel condenser is around 5 m^2. Furthermore, the internal volume is 2.9 L in the case of the prototype and 8.4 L in the case of the brazed plate heat exchanger; hence, 65% volume reduction has been obtained, this leading to a large reduction of the amount of refrigerant trapped in the device.

The comparison between these two condensers will be further discussed in section 3.6.2, showing how the effect of the lower performance of the minichannel condenser on the heat pump COP is negligible, while great benefits are obtained in terms of equipment charge reduction.

2.3.2 Experimental performance of the minichannel evaporator with R22

R22 has been used instead of R290 to test the thermal and hydraulic performance of the prototype evaporator.

The saturation temperature determined from the pressure measured at the outlet of the evaporator is plotted versus the heat flow rate in Fig. 2.22 and Fig. 2.23. For all the tests performed, the water temperature was 12-7°C. Data reported in Fig. 2.22 has been obtained at 3 K and 7 K superheat and fixed 0.25 inlet vapour quality. Data reported in Fig. 2.23 has been obtained at 0.2 and 0.3 inlet qualities and fixed 5 K superheat.

By increasing the vapour superheat (see Fig. 2.22), the length of the tubes occupied by superheated vapour, and thus displaying low heat transfer coefficients, increases. Hence, the global thermal performance decreases and a lower evaporating temperature is needed in order to exchange the same heat transfer rate.

When the inlet quality is reduced (see Fig. 2.23), the enthalpy change along the evaporation process increases, hence the mass flow rate required to exchange the same heat transfer rate decreases as well as the pressure drop; the consequent reduction of the saturation temperature drop explains the better thermal performance. This experimental result shows how strong is the influence of the pressure drop on the performance of the minichannel evaporator.

The experimental refrigerant pressure drop measurements corresponding to the tests of Fig. 2.22 and Fig. 2.23 are plotted versus mass flow rate in Fig. 2.24. In the same graph, the scale of the saturation temperature drop, computed at 2°C saturation temperature, is reported.

When using R22, the refrigerant mass flow rate required to obtain 80 kW cooling capacity is around 0.5 kg/s. At 12-7°C evaporator water temperature, the experimental pressure drop is 40 kPa, which, in terms of saturation temperature drop, corresponds to around 2.3 K.

In Fig. 2.25 experimental data about the water pressure drop versus mass flow rate obtained at 19°C is reported. At nominal condition (i.e. 80 kW cooling capacity and 5K water temperature drop), the required water flow rate is 3.8 kg/s and the corresponding shell side pressure drop is around 35 kPa.

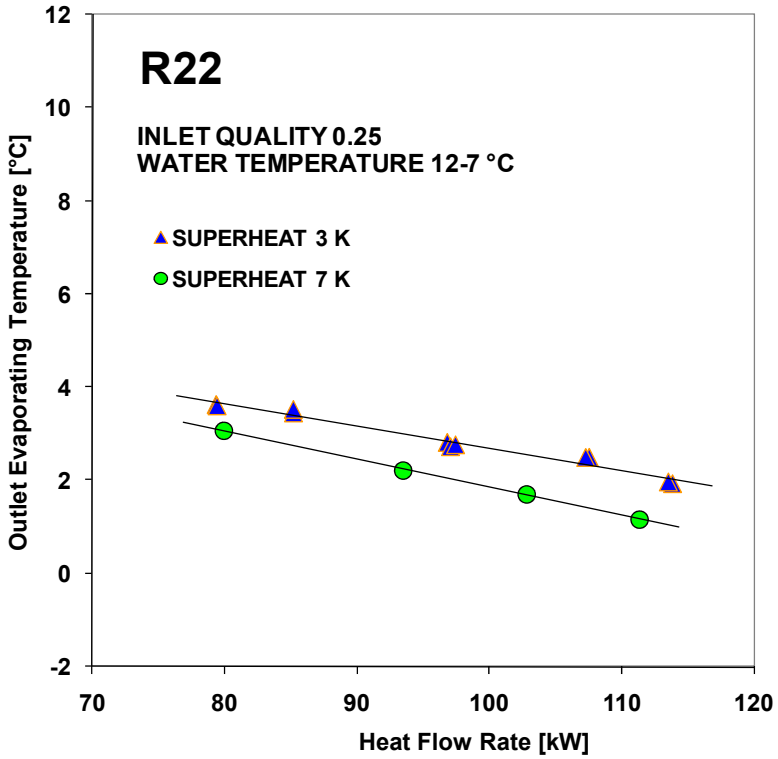

Fig. 2.22. Experimental outlet evaporating temperature versus heat flow rate at fixed inlet vapour quality.

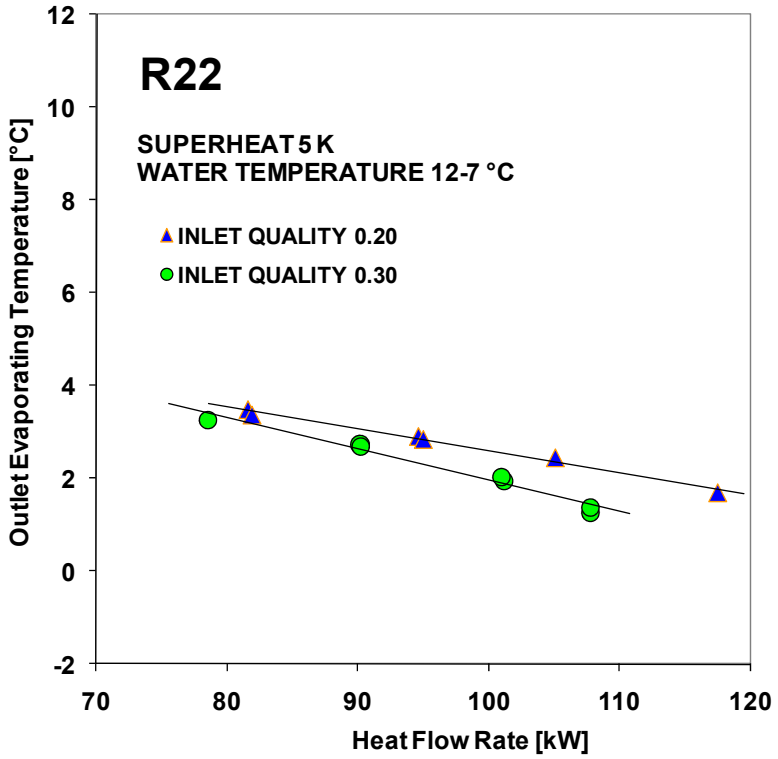

Fig. 2.23. Experimental outlet evaporating temperature versus heat flow rate at fixed superheat.

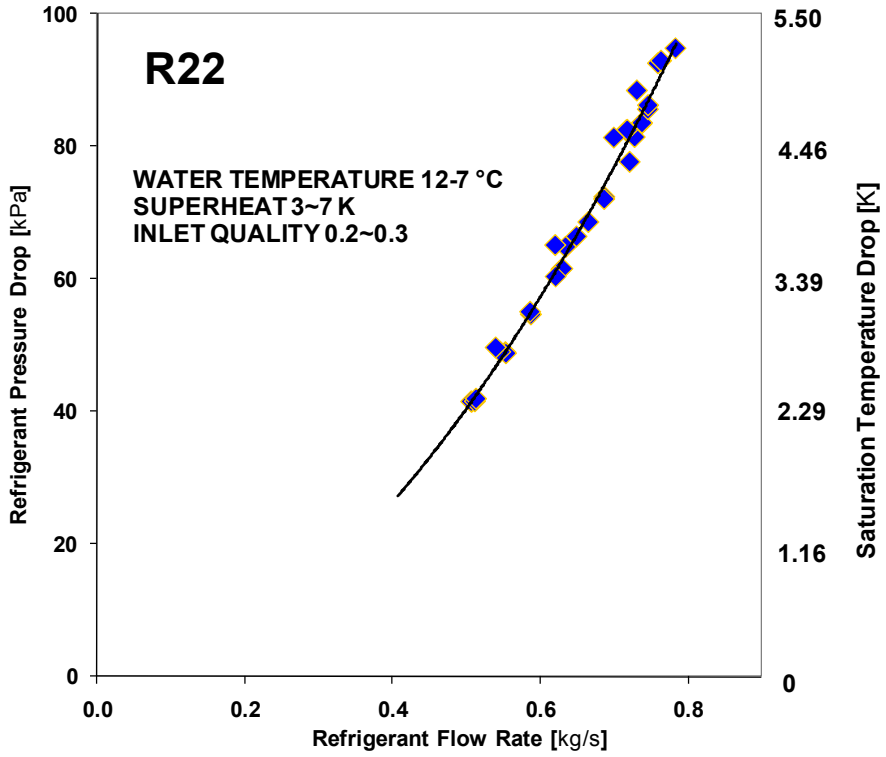

Fig. 2.24. Experimental R22 pressure drop in the minichannel evaporator versus mass flow rate. Saturation temperature drop scale is also reported.

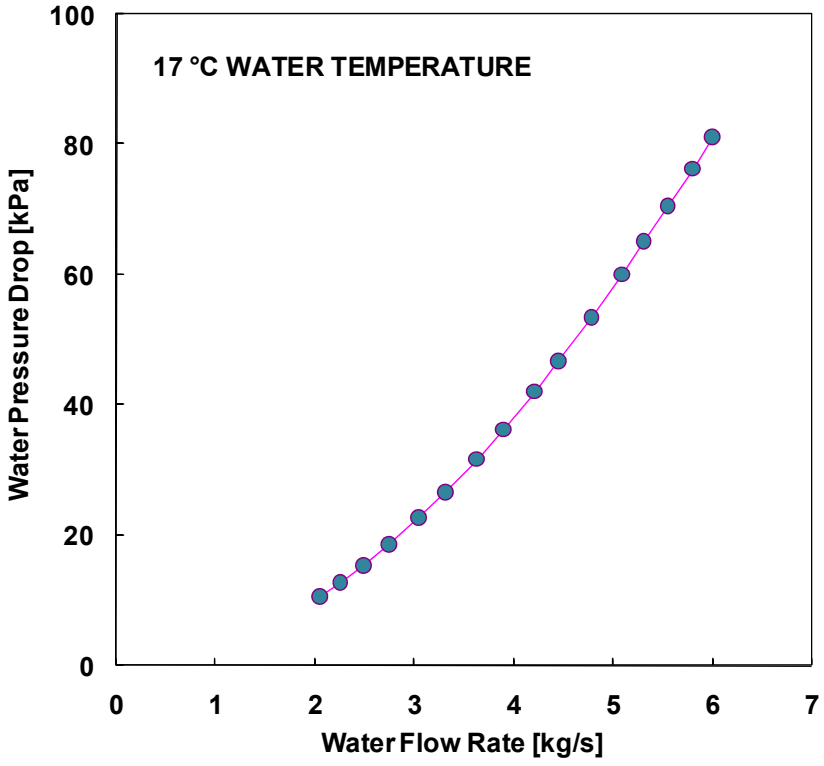

Fig. 2.25. Minichannel evaporator experimental water pressure drop versus mass flow rate at 17°C.

2.3.3 Experimental performance of the minichannel condenser during evaporation with R22

The minichannel condenser has also been tested with R22 during evaporating conditions.

The saturation temperature determined from the pressure measured at the outlet of the evaporator is plotted versus the heat flow rate in Fig. 2.26. For the four data points reported, the water temperature was 12-7°C. Data has been obtained at 3 K superheat and 0.25 inlet vapour quality. The experimental refrigerant pressure drop measurements corresponding to the tests of Fig. 2.26 are plotted versus mass flow rate in Fig. 2.27.

The number of minichannels in the evaporator is much higher than in the condenser, and the heat transfer area is around 11 m^2 in the evaporator and 5 m^2 in the condenser. In terms of refrigerant side internal volume, this is 5.8 L in the case of the evaporator and 2.9 L in the case of the condenser.

As one can see, the condenser is clearly undersized to be used as an evaporator, since a very low evaporating temperature (i.e. around -5°C) would be required to provide the design 80 kW cooling capacity with 12-7°C water temperature. In particular, the refrigerant pressure drop would be extremely high, this leading to unacceptably high saturation temperature drop.

It seems important to stress how, when looking for refrigerant charge minimization, it could be extremely important to design equipment as reversible on the secondary fluid side, instead that on the refrigerant side, so that the condenser and the evaporator can be optimized independently. In the case of the present minichannel prototypes, at example, if designing the heat pump as reversible on propane side, the condenser internal volume would be double the required value.

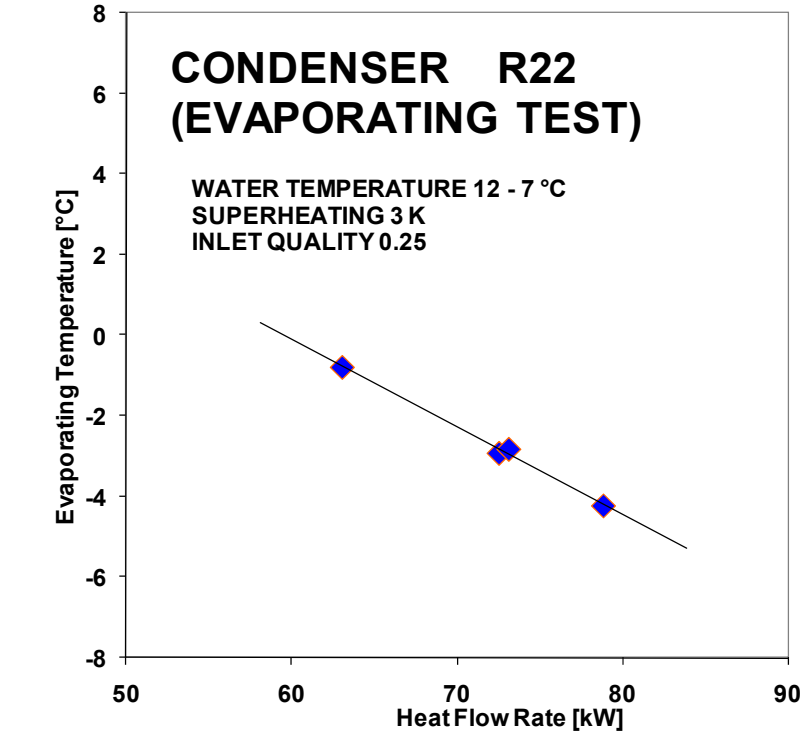

Fig. 2.26. Experimental outlet evaporating temperature versus heat flow rate for the minichannel condenser during evaporation test with R22.

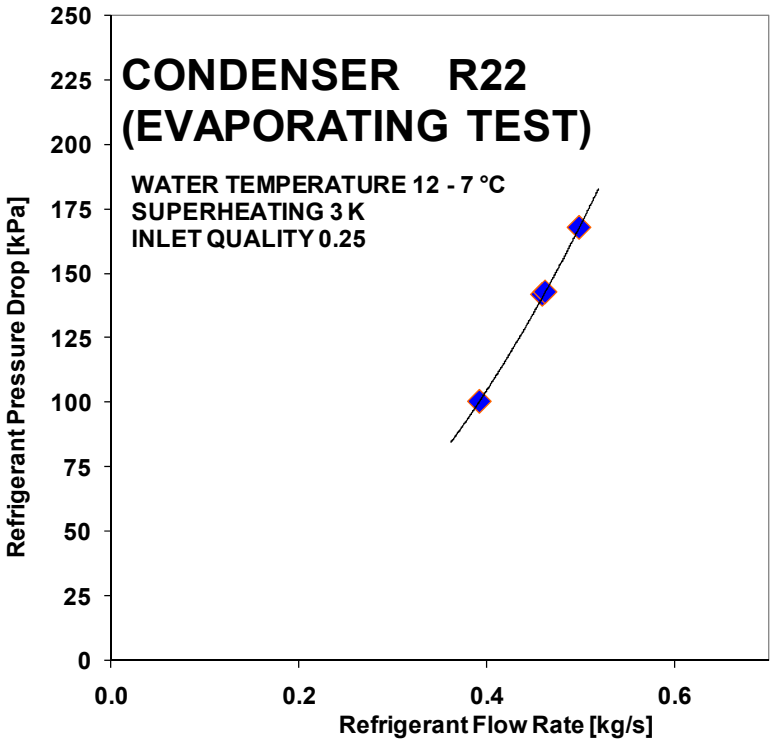

Fig. 2.27. Experimental R22 pressure drop versus mass flow rate for the minichannel condenser during evaporation test.

2.3.4 Experimental performance of the internal heat exchanger with R290

At least 20 K vapour superheat at the compressor suction and discharge are suggested by the manufacturer of the compressor used in the heat pump in order to reduce the solubility of propane in the oil and avoid problems due to the decrease of the lubricant viscosity (Bitzer, 1997).

The minichannel internal heat exchanger has been designed in order to provide around 20 K additional vapour superheat when the liquid propane enters at 50°C temperature and the vapour propane enters at the design conditions (i.e. 2°C saturation temperature and 5 K superheat).

Experimental data with R290 about the shell side vapour temperature rise versus the tube side liquid inlet temperature is reported in Fig. 2.28. Data has been obtained with vapour pressure ranging from 4.7 to 5.2 bar (the corresponding saturation temperature range from around 0°C to around 3°C). In the graph in Fig. 2.28 solid squares refer to test runs with 5~7°C inlet vapour temperature and the compressor running at 100% capacity (i.e. 0.28 kg/s mass flow rate); triangles refer to test runs at the same inlet vapour temperature, but with the compressor running at 66% capacity (i.e. 0.18 kg/s mass flow rate); finally solid circles refer to test runs at higher inlet vapour temperature (i.e. 11°C) and the compressor running at full capacity.

Clearly, when the liquid inlet temperature is increased by increasing the condensation saturation temperature, a higher additional superheat is provided by the internal heat exchanger, since an higher temperature difference between shell and tube side is available.

Comparing the first to the second data set, it is interesting to notice how no main difference is measured in the vapour temperature rise when the mass flow rate is reduced by switching the compressor capacity down to 66%. At the lowest inlet liquid temperature (obtained at 30-35°C condenser water temperature), around 17 K vapour superheating is measured; considering that the inlet superheating in that case is around 3°C, it is shown as the 20 K superheating at the IHX outlet is fulfilled.

A lower vapour temperature rise is measured for the third data set in Fig. 2.28; in that case, in terms of outlet superheating, this is compensated by the much higher superheating of the vapour at the inlet (i.e. 11 K).

In order to reduce refrigerant charge, liquid propane must flow inside the tubes. Because of the much favourable heat transfer properties of liquid as compared to fluid, the driving thermal resistance is clearly on the shell side. The thermal performance could be increased (with the consequent possibility to further decrease the size and the refrigerant charge) by increasing the velocity of the vapour on the shell side; however, this would lead to higher pressure drop.

While the pressure drop on tube side has no influence on the energy performance of heating and refrigeration equipment, since in any case the condensated liquid pressure must be reduce down to the evaporation pressure in an expansion device, the pressure drop on the shell side does decrease the overall performance, because it increases the pressure rise required to the compressor, hence increasing the energy consumption of this device.

In the facility used to get the present experimental data, no pressure transducers are present at the inlet and outlet of the internal heat exchanger, but the pressure is measured at the outlet of the evaporator and at the inlet of the compressor. Since the

vapour line is very long, these measurements cannot be used to directly get the value of pressure drop at the internal heat exchanger; however, an estimation is here attempted.

Experimental data about R290 pressure drop for the whole line from the outlet of the evaporator till the inlet of the compressor are reported in Fig. 2.29. Data has been obtained with vapour pressure ranging from 4.7 to 5.2 bar, and vapour superheating at the evaporator outlet varying from 1 up to 11K. In the facility used, test can be run using different configurations. Solid triangles in the graph in Fig. 2.29 refer to configurations not using the internal heat exchanger, while circles refer to the configuration using the internal heat exchanger. A trendline has been reduced for each data set, and the internal heat exchanger pressure drop has been estimated by subtraction one function from the other.

It could be interesting to notice how the expected shell side pressure drop is higher that the measured pressure drop in the whole suction line, which is around 8 m long for this facility.

The estimation reported is quite rough, however it can be useful to get an idea about the saturation temperature drop in the suction line induced by the internal heat exchanger. At 0.28 kg/s propane flow rate, the estimated pressure drop is around 9 kPa; at 5 bar pressure, the corresponding saturation temperature drop is around 0.6 K. At 0.18 kg/s propane flow rate, the estimated pressure drop is around 4 kPa and the corresponding saturation temperature drop is around 0.25 K.

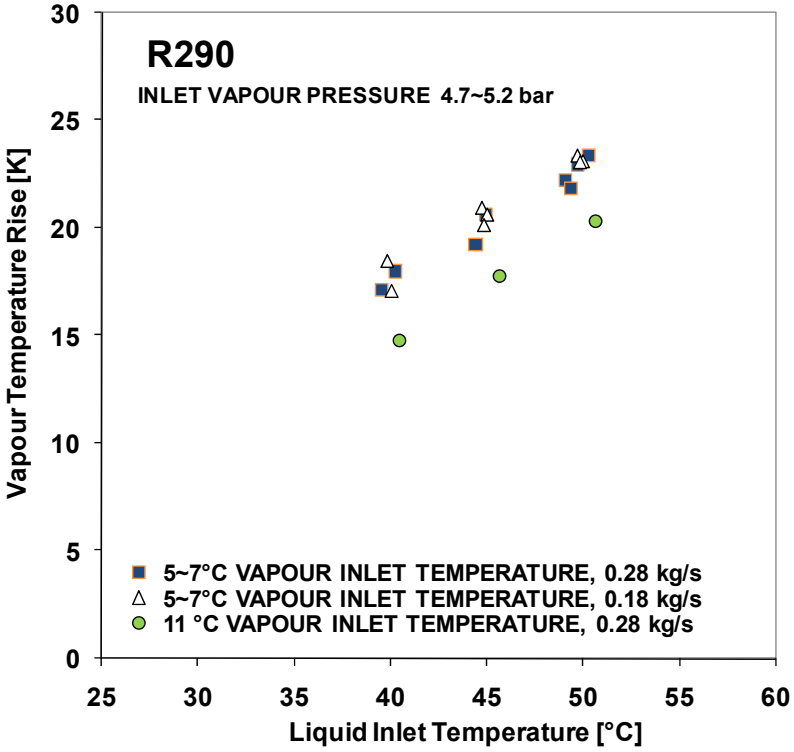

Fig. 2.28. Experimental R290 vapour temperature rise versus liquid inlet temperature for the internal heat exchanger..

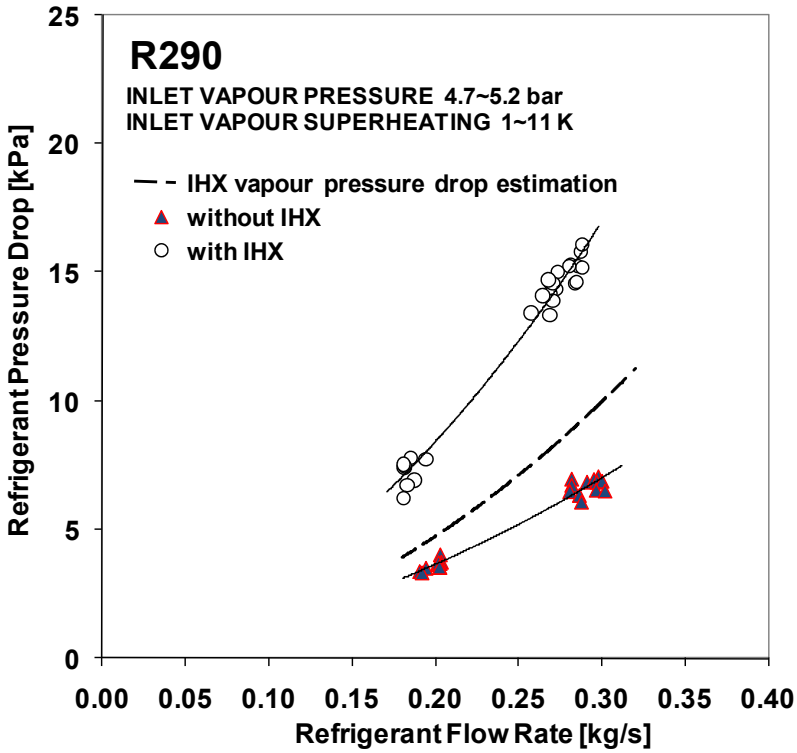

Fig. 2.29. Estimation of R290 pressure drop on the shell side of the internal heat exchanger.

2.4 Computational procedure

2.4.1 Computational procedure for the condenser design

A computational procedure based on a simplified model of the heat transfer and pressure drop processes in the condenser has been used to design this minichannel heat exchanger.

The schematization of the simplified model is depicted in Fig. 2.30. Point 2 in Fig. 2.30 corresponds to half of the tubes length, while point 3 corresponds to the saturated liquid condition.

The pressure of the refrigerant is assumed to vary linearly from points 1 to 2, 2 to 3 and 3 to 4. For each segment, a mean value of the overall heat transfer coefficient is computed. Refrigerant properties have been computed from the NIST database (NIST, 2002). The heat transfer rate, subcooling and inlet and outlet water temperatures are given as inputs to the algorithm, whilst the program output is the condensing temperature required to fulfil the imposed conditions.

The condensation heat transfer coefficient has been obtained from the Cavallini *et al.* (2006) correlation; this correlation has been developed for tubes with internal diameter $D > 3$ mm, however it was found to perform well also for minichannels.

The refrigerant pressure drop in the condensation region has been computed by the Cavallini *et al.* (2005) correlation for minichannel. The Friedel correlation (1979, 1980) for conventional tubes and the annular flow pressure drop model for minichannels by Niño (2006) have also been implemented in the program as a comparison.

In the subcooled liquid region of the minichannels, the heat transfer coefficient has been computed by the Dittus-Boelter equation (McAdams, 1942), while for the pressure drop the Blasius (1911) correlation has been used.

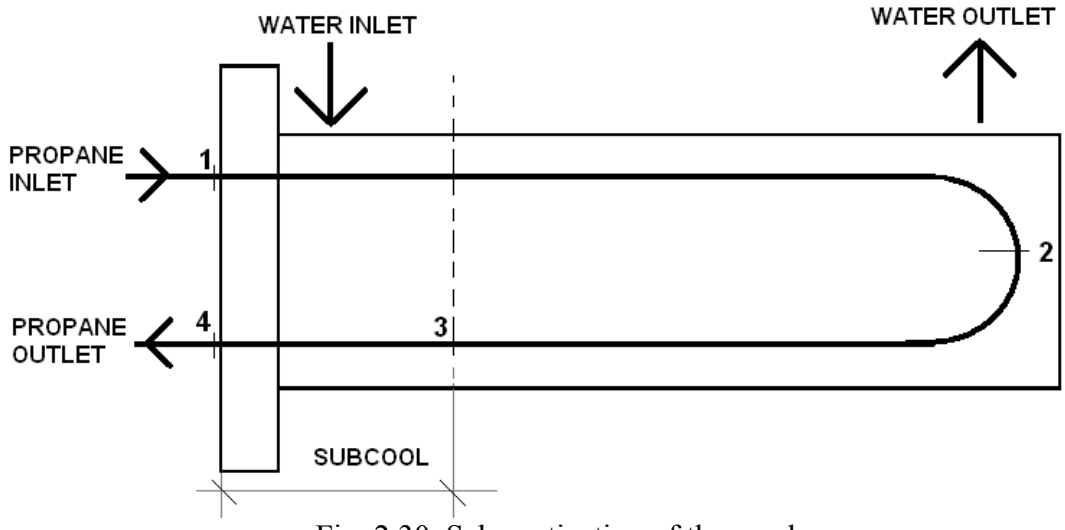

Fig. 2.30. Schematization of the condenser.

The acceleration pressure drop has been evaluated and included in the total pressure drop predictions; the void fraction required to compute the acceleration pressure drop has been computed by means of the Rouhani (1969) model as published in the Heat Exchanger Design Handbook (HEDH) (Taborek, 1983). The pressure drop due to the sudden flow expansion or contraction in the inlet and outlet headers has been computed according to Paliwoda (1992).

The overall heat transfer coefficient and pressure drop on shell side have been computed by the Bell-Delaware method (Bell, 1963) as published in the Heat Exchanger Design Handbook (Taborek, 1983). It must be noticed that the Bell-Delaware method is valid only if the ratio of the tube pitch to the outside tube diameter is kept between 1.25 and 1.5, as reported in the HEDH (Taborek, 1983), while this ratio is 2 in the case of the present condenser. Besides, the external diameter of the tubes is rather small as compared to conventional shell-and-tube heat exchangers for which the Bell-Delaware method was developed.

In Table 2.2 some results obtained by the computational procedure have been reported. The performance with R22 and R290 are compared in Table 2.2 for a reference case of 100 kW heating capacity with 3 K subcooling at the condenser outlet. The inlet and outlet water temperature are 40°C and 45°C, respectively.

Table 2.2. Performance of the condenser with R22 and R290 according to the computational procedure.

	Refrigerant	R290	R22
	Heating Capacity	100 kW	
	Subcooling	3 K	
Water side	T_{in}	40°C	
	T_{out}	45°C	
	Mass flow rate	4.8 kg/s	
	Pressure drop	9.6 kPa	
	Heat transfer coefficient	7450 $Wm^{-2}K^{-1}$	
Refrigerant side	Mass flow rate	0.294 kg/s	0.506 kg/s
	Mass flux	341 kg $m^{-2}s^{-1}$	581 kg $m^{-2}s^{-1}$
	Inlet condensing temperature	50.15°C	50.61°C
	Total pressure drop	21.1 kPa	27.3 kPa
	Inlet/outlet pressure drop	0.9 kPa	1.4 kPa
	Acceleration pressure drop	-3.2 kPa	-4.70 kPa
	Saturation temperature drop	0.57 K	0.62 K
	Heat transfer coefficient 1-2	6920 $Wm^{-2}K^{-1}$	6336 $Wm^{-2}K^{-1}$
	Heat transfer coefficient 2-3	3786 $Wm^{-2}K^{-1}$	3450 $Wm^{-2}K^{-1}$
	Heat transfer coefficient 3-4	1978 $Wm^{-2}K^{-1}$	1682 $Wm^{-2}K^{-1}$
	Inlet temperature	68°C	90°C
	Quality at point 2	0.39	0.43
	Subcooling region length	0.14 m	0.12 m
	Pressure drop 1-2	14.2 kPa	17.8 kPa
	Pressure drop 2-3	5.7 kPa	7.8 kPa
	Pressure drop 3-4	0.3 kPa	0.3 kPa

The refrigerant inlet temperature has been computed considering a reference thermodynamical cycle with 2°C evaporating temperature, 5 K superheating and 0.7 isentropic compression efficiency. It can be notice how, in this case, the compressor discharge temperature is much lower for propane (i.e. 68°C) as compared to R22 (i.e. 90°C).

The expected average heat transfer coefficient on refrigerant side is reported in Table 2.2 for each of the three regions considered in the schematization adopted. As one can see, the expected heat transfer coefficient is always higher for propane, this resulting in a lower inlet condensing temperature.

The computed average refrigerant heat transfer coefficient is very high in the first region (i.e. 1-2 in Fig. 2.30); most of the condensation process, as well as most of the pressure drop, takes place in the first half of the tubes and the expected quality at point 2 is around 0.4. While on the region 2-3 and 3-4 the driving thermal resistance is on the tube side, in the first region comparable heat transfer coefficients are computed on the water and refrigerant side.

It must be noticed that in the computational procedure here considered, the heat transfer computation in each of the three zones is based on the estimation of a heat transfer coefficient and a mean logarithmic temperature difference between the refrigerant and the water. The use of a mean logarithmic temperature difference, however, is valid only if the heat transfer coefficient can be considered constant inside the region. It is clear that this assumption is not valid in the present case, since a very big variation of the heat transfer coefficient is observed.

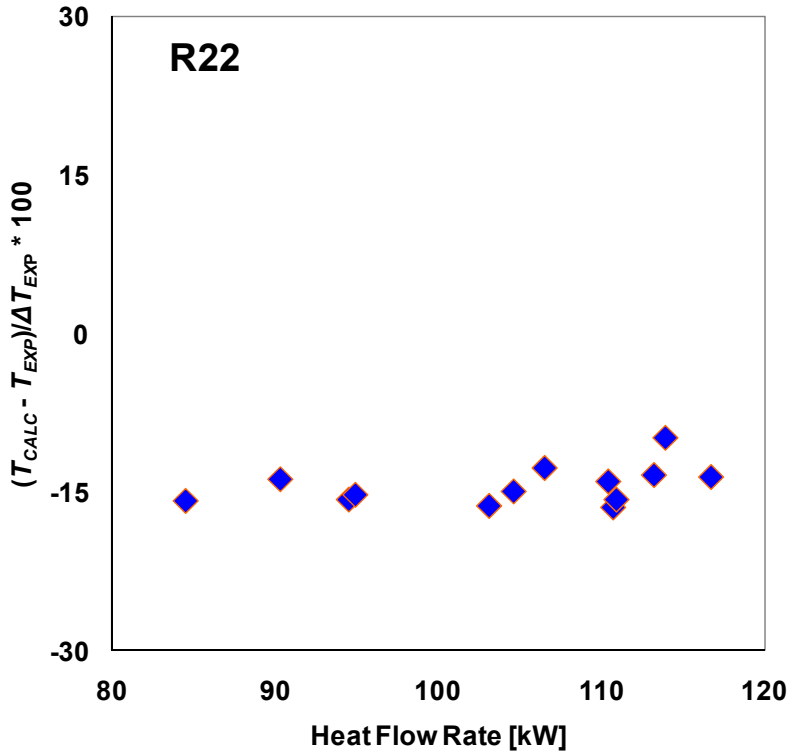

Fig. 2.31. Comparison between calculated and experimental inlet saturation temperatures (T_{CALC} and T_{EXP}) when using R22; ΔT_{EXP} is the average experimental temperature difference between the two fluids.

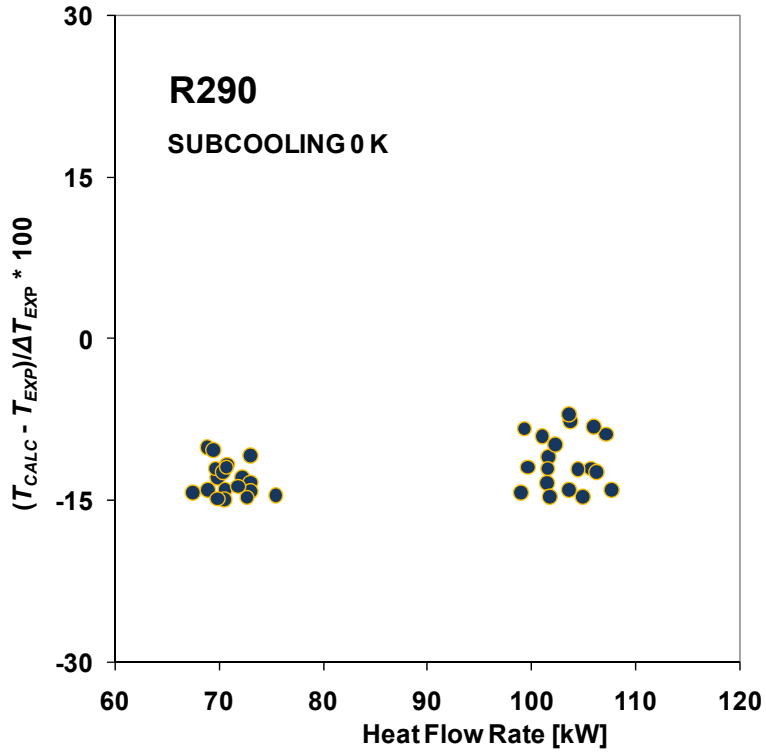

Fig. 2.32. Comparison between calculated and experimental inlet saturation temperatures (T_{CALC} and T_{EXP}) when using R290; ΔT_{EXP} is the average experimental temperature difference between the two fluids.

This clearly is the main drawback of this computational procedure. However, the results obtained by such a kind of simplified model can be useful during the design process.

By comparing the expected pressure drop, it can be seen in Table 2.2 how this is expected to be higher for R22 (i.e. 27 kPa) as compared to propane (i.e. 21 kPa). In terms of saturation temperature drop, however, the same value (i.e. around 0.6 K) is expected for both cases. In any case, such a value of saturation temperature drop is pretty low as compared to mean temperature difference between water and refrigerant (i.e. around 8 K) and the pressure drop does not have a big influence of the thermal performance.

The graphs in Fig. 2.31 and Fig. 2.32 show the comparison between the calculated and the experimental saturation temperatures (T_{CALC} and T_{EXP}) at the inlet, when using R22 and R290, respectively. ΔT_{EXP} is the average experimental temperature difference between the two fluids (i.e. 8.5 K). Data refers to the same experimental results already reported in Fig. 2.15 and Fig. 2.16. Simulations considered in Fig. 2.31 and Fig. 2.32 have been run using the Cavallini *et al.* (2005) correlation for pressure drop; however, because of the very small influence of the pressure drop on the thermal performance of the condenser, almost identical results, in terms of condensing temperature, are obtained when using the Friedel (1979, 1980) or the Niño (2006) correlations.

The thermal performance of the condenser is overpredicted by around 10~15 % (in terms of $(T_{CALC} - T_{EXP})/\Delta T_{EXP}$) for all the test conditions and both the fluid considered. It is important to notice that almost the same behavior is observed for R22 and R290.

In the computational procedure, given the values of pressure and quality at points 1, 2, 3 and 4, for every region (i.e 1-2, 2-3 and 3-4) the heat transfer coefficient and the friction factor are computed by the correlations considering a number of themodynamical points with pressure and quality evenly and linearly distributed between the values given at the extreme points. Then, the average heat transfer coefficient in each region of the condenser is computed by averaging the values obtained for these intermediate thermodynamical points.

The heat transfer coefficient during condensation depends very much on the vapour quality and it quickly decreases from inlet to outlet along the tubes. Because of that, the tube length needed to condensate the refrigerant from quality 1 to 0.9, as an example, will be shorter than the tube length needed to condensate from 0.9 to 0.8, and so on. In the computational procedure adopted, however, the average heat transfer coefficient is obtained as a simple average of the values at intermediate quality points. This schematization corresponds to considering, inside each of the three regions of the condenser, the tube lengths needed to condensate from 1 to 0.9, 0.9 to 0.8, and so on, as equal. As a consequence of this schematization, the average heat transfer coefficient is overpredicted, and this is believed to be the main reason of the disagreement between the experimental and calculated condensing temperature shown in Fig. 2.31 and Fig. 2.32.

Besides, it must be remembered that the correlations used here are applied out of their validity range. For instance, the Bell-Delaware method is not valid for the tube bundle geometrical characteristics of the present prototype and the Cavallini *et al.* (2006) correlation has been developed for tubes with internal diameter $D > 3$ mm.

Experimental data about the refrigerant pressure drop has been compared against the results given by the computational procedure with the three considered pressure drop correlations. It should be stressed that the computed values not only depend on the correlation used, but they also strongly depend on the schematization adopted.

The graphs in Fig. 2.33 and Fig. 2.34 show the comparison between the experimental refrigerant pressure drop and the values obtained from the computational procedure when using R22, with water temperature 40-45°C and 30-35°C, respectively. The graphs in Fig. 2.35, Fig. 2.36 and Fig. 2.37 show the comparison between the experimental refrigerant pressure drop and the values obtained from the computational procedure when using R290, with water temperature 40-45°C, 35-40°C and 30-35°C, respectively. The saturation pressure drop is also depicted in all the graphs.

Predictions have been computed by the Cavallini *et al.* (2005), the classical Friedel (1979, 1980) correlation and the Niño (2006) correlation. The Friedel equation has been developed for conventional tubes, while the others are given for minichannels. The pressure drop model by Niño is valid only for annular flows.

With regard to the experimental data for R22, the computational procedure when using the Cavallini *et al.* (2005) correlation is shown to predict very well the experimental data, since the maximum absolute error is about 10%, whilst when using the other two equations considered the measured data are overpredicted.

In the case of R290, different results are obtained. At low mass flow rate (i.e. data obtained with the compressor heat pump working at 66% capacity), both the Cavallini *et al.* (2005) and the Niño (2006) correlation predict very well the experimental data, but at higher mass flow rates, these correlations (and mainly the Cavallini *et al.*, 2005) underpredict experimental data, while the Friedel correlation performs well.

A global comparison between experimental and calculated refrigerant pressure drop for all the experimental points here reported for propane is shown in Fig. 2.38. The maximum absolute error is about 10% when using the Niño (2006) correlation, 15% when using the Friedel (1979, 1980) correlation and 25% when using the Cavallini *et al.* (2005) correlation.

It is very interesting to point out that for both the fluids tested the curve of pressure drop versus mass flow rate obtained when using the Niño correlation is almost parallel to the one obtained when using the Friedel equation, while the curve obtained by the Cavallini *et al.* (2005) correlation displays a lower slope. In the case of R22, the experimental slope is similar to the one given by the Cavallini *et al.* (2005) correlation (see Fig. 2.33 and Fig. 2.34), while in the case of R290 the experimental curve is steeper and the slope is more similar to the one given by the Niño and Friedel equations (see Fig. 2.35, Fig. 2.36 and Fig. 2.37).

With regard to the shell-side pressure drop, the graph in Fig. 2.39 reports the comparison between the experimental water pressure drop obtained at 19°C and the values predicted by the Bell-Delaware method (Bell, 1963). Shell side pressure drop is overpredicted by the computational procedure by about 20%.

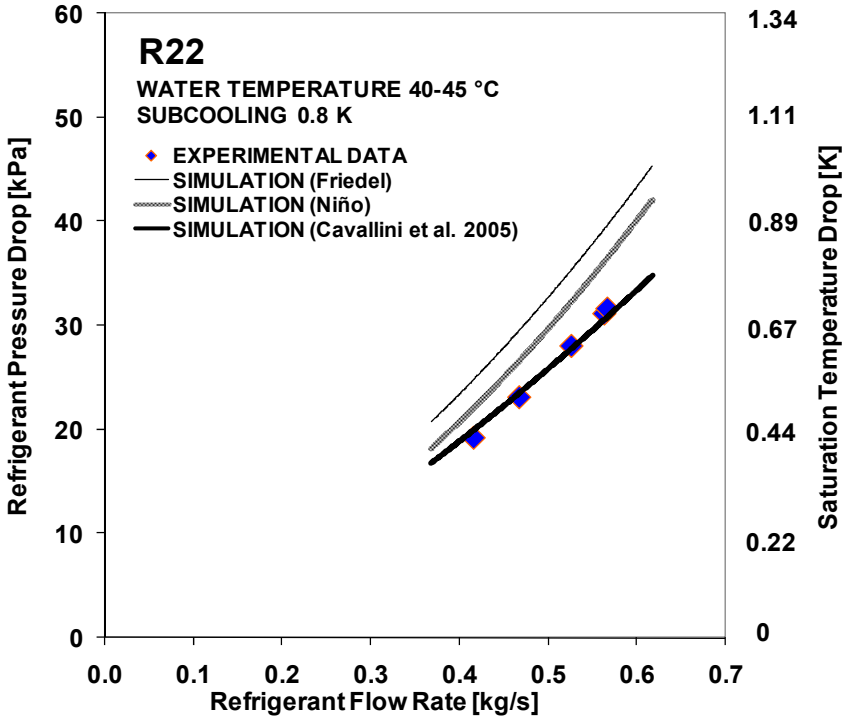

Fig. 2.33. Experimental and computed refrigerant pressure drop versus mass flow rate for R22, 40-45°C water temperature. Predictions by Cavallini *et al.* (2005), Friedel (1979, 1980) and Niño (2006). Saturation temperature drop is also depicted.

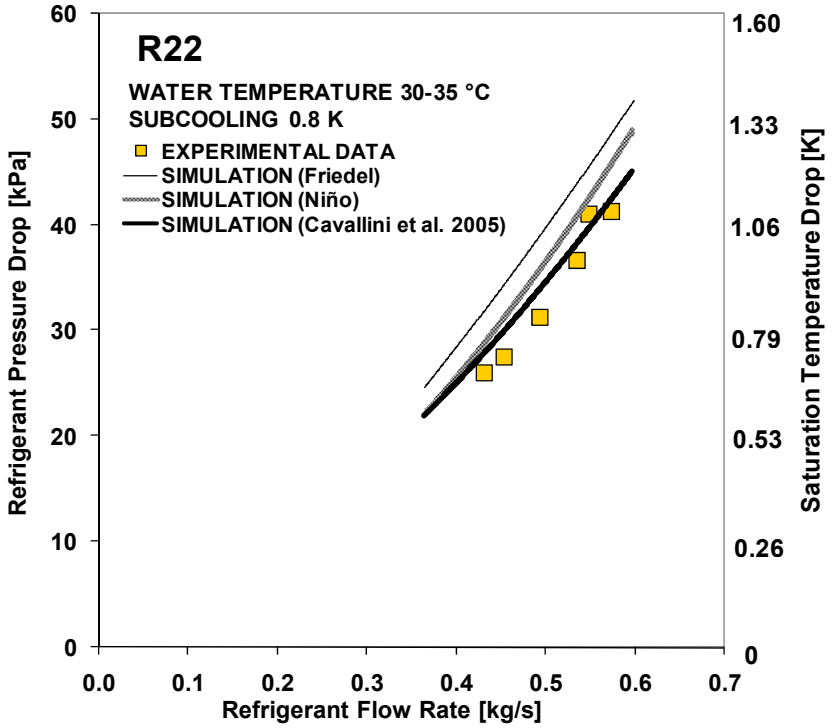

Fig. 2.34. Experimental and computed refrigerant pressure drop versus mass flow rate for R22, 30-35°C water temperature. Predictions by Cavallini *et al.* (2005), Friedel (1979, 1980) and Niño (2006). Saturation temperature drop is also depicted.

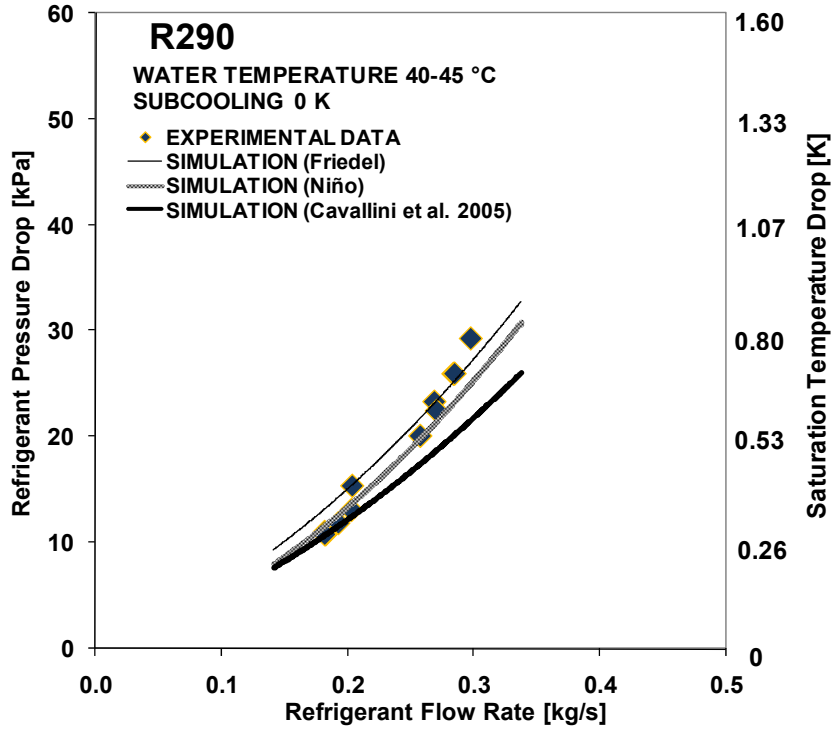

Fig. 2.35. Experimental and computed refrigerant pressure drop versus mass flow rate for R290, 40-45°C water temperature. Predictions by Cavallini *et al.* (2005), Friedel (1979, 1980) and Niño (2006). Saturation temperature drop is also depicted.

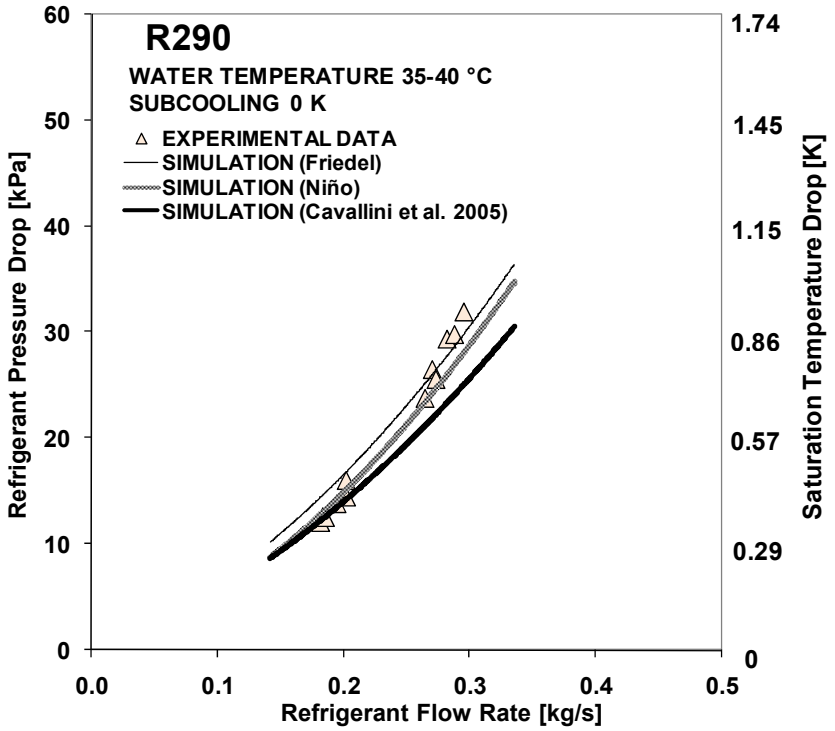

Fig. 2.36. Experimental and computed refrigerant pressure drop versus mass flow rate for R290, 35-40°C water temperature. Predictions by Cavallini *et al.* (2005), Friedel (1979, 1980) and Niño (2006). Saturation temperature drop is also depicted.

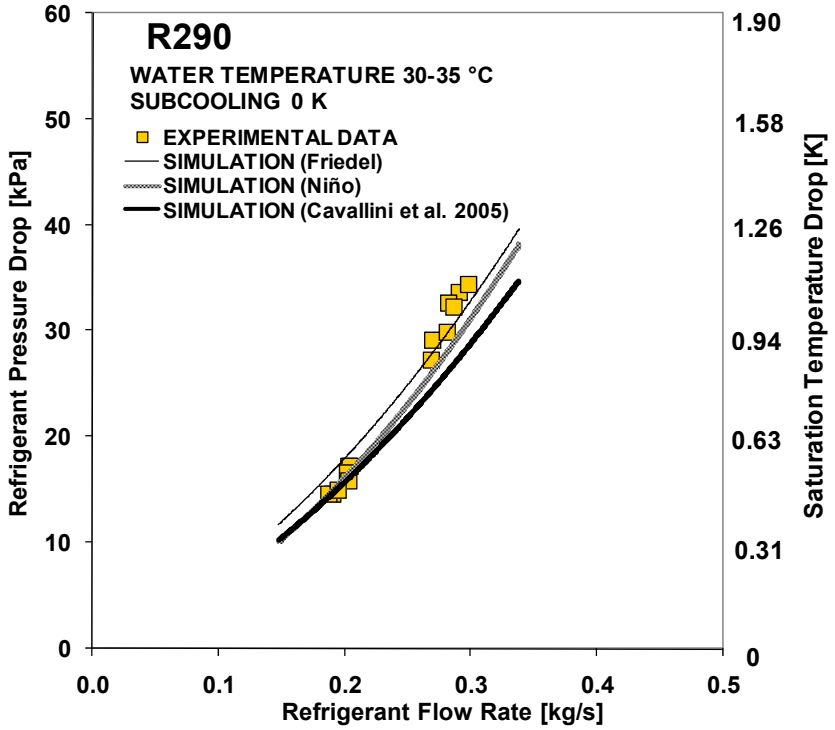

Fig. 2.37. Experimental and computed refrigerant pressure drop versus mass flow rate for R290, 30-35°C water temperature. Predictions by Cavallini *et al.* (2005), Friedel (1979, 1980) and Niño (2006). Saturation temperature drop is also depicted.

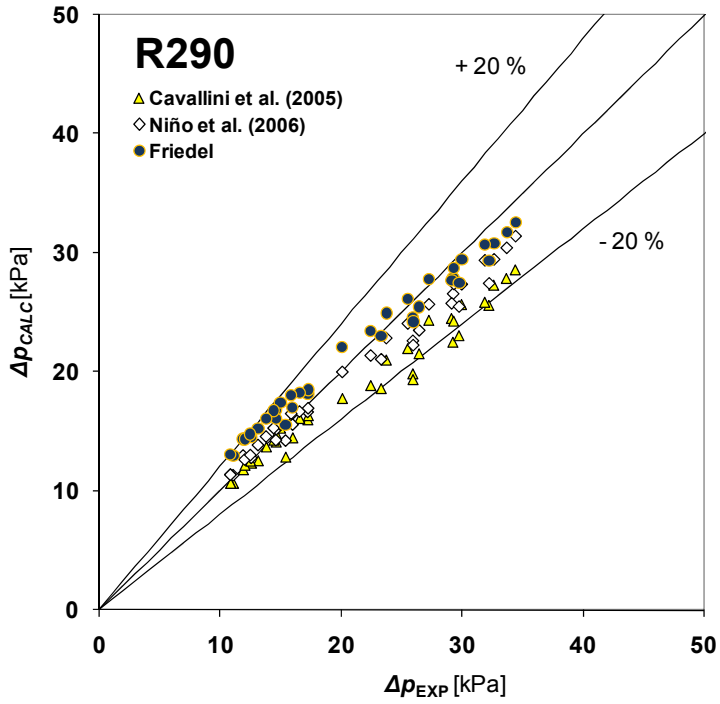

Fig. 2.38. Comparison between experimental and calculated refrigerant pressure drop with R290. Prediction by Cavallini *et al.* (2005), Friedel (1979, 1980) and Niño (2006).

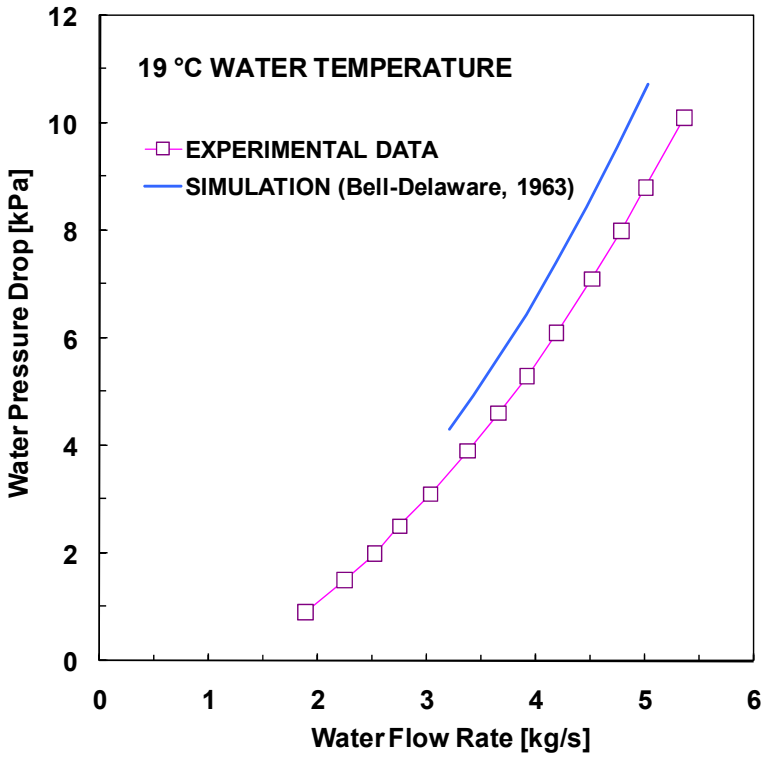

Fig. 2.39. Experimental and computed water pressure drop versus mass flow rate at 19°C. Predictions obtained from the Bell-Delaware method (Bell, 1963).

2.4.2 Computational procedure for the evaporator design

Flow boiling in minichannel cannot be considered a very well understood heat transfer phenomenon and a quite large degree of uncertainty is always present when trying to predict the evaporation heat transfer coefficient.

A review of the literature on flow boiling in channels with diameter 2 mm or less can be found in Bertsch *et al.* (2008), where predictions from 25 heat transfer correlations are compared to a large set of experimental data from different independent sources. According to their results, correlations that have been developed especially for minichannels show no improvements over those developed earlier for conventional-sized channels. Furthermore, the correlation that showed the best overall agreement with the experimental measurements database was the correlation of Cooper (1984), this showing that nucleate boiling appears to be the dominant heat transfer mechanism in microchannels. Among the flow boiling correlations that showed reasonable agreement with experimental data, the Liu and Winterton (1991) correlation is reported in Bertsch *et al.* (2008).

In the case of the present evaporator, the internal diameter of the minichannels is 2 mm, which corresponds to the largest channel size considered in the review by Bertsch *et al.* (2008). The evaporation heat transfer condition in the present heat exchanger is expected to be flow boiling. However, because of the small internal diameter, a low mass flux (i.e. around G = 150 kg $m^{-2}s^{-1}$ with propane) is needed in order to obtain an optimum saturation temperature drop, therefore the role of pool boiling is expected to be important.

Four different evaporation heat transfer correlations were considered in the computational procedure: the two flow boiling correlations by Liu and Winterton (1991) and Kandlikar and Balasubramanian (2004), and the two pool boiling correlations by Cooper (1984) and Stephan and Abdelsalam (1980).

The Liu and Winterton (1991) correlation was developed for conventional tubes with diameter varying from 3 mm up to 32 mm and is based on the superposition approach. The contributions of convective and nucleate boiling heat transfer mechanisms are combined as follows:

$$h_{TP}^2 = (Fh_L)^2 + (Sh_{pool})^2 \tag{2.1}$$

where h_{TP} is the evaporation heat transfer coefficient, h_L is a single-phase liquid-only heat transfer coefficient given by a forced convection correlation, h_{pool} is an heat transfer coefficient given by a pool boiling correlation, F is an adimensional forced convection heat transfer enhancement factor and S is an adimensional suppression factor.

In the Liu and Winterton (1991) correlation h_L is calculated from the Dittus-Boelter equation (McAdams, 1942) using the all-liquid Reynolds number $\mathrm{Re_{LO}} = GD/\mu_L$ and h_{pool} is calculated from Cooper (1984) pool boiling correlation. According to Bertsch *et al.* (2008), the fact that the Liu and Winterton (1991) correlation rely on the Cooper correlation may explain its success in predicting the heat transfer coefficient in tube with very small diameter.

The enhancement factor F and the suppression factor S are computed in the Liu and Winterton (1991) correlation as follows:

$$F = \left[1 + x \,\mathrm{Pr}_\mathrm{L} \left(\frac{\rho_L}{\rho_G} - 1 \right) \right]^{0.35} \tag{2.2}$$

$$S = (1 + 0.055 F^{0.1} \mathrm{Re}_{\mathrm{LO}}^{0.16})^{-1} \tag{2.3}$$

where x is the vapour quality and Pr_L is the liquid Prandtl number.

A correction term not reported here is also present in the equation if the tube is horizontal and the all-liquid Froude numbers is lower than 0.05.

Regarding to the Kandlikar and Balasubramanian (2004) correlation, this is an extension of the original Kandlikar (1990) equation to the transition and laminar flow typical of minichannel applications. According to the authors, this extension was needed since all the data used to develop the original Kandlikar (1990) equation for conventional diameter tubes was in the turbulent region, with all-liquid Reynolds number $\mathrm{Re}_{\mathrm{LO}}$>3000.

The evaporation heat transfer coefficient is computed by the Kandlikar correlation as the sum of the convective and the nucleate boiling terms, as follows:

$$\frac{h_{TP}}{h_L} = C_1 Co^{C_2} + C_3 Bo^{C_4} F_{fl} \tag{2.4}$$

where h_{TP} is the evaporation heat transfer coefficient, h_L is a single-phase liquid-only heat transfer coefficient given by a forced convection correlation, C_1, C_2 , C_3 , C_4 are constants, F_{fl} is a fluid–surface parameter, and Co and Bo are a convection number and a boiling number, defined as follows:

$$Co = \left(\frac{1-x}{x} \right)^{0.8} \left(\frac{\rho_G}{\rho_L} \right)^{0.5} \tag{2.5}$$

$$Bo = \frac{q}{G i_{LG}} \tag{2.6}$$

where q is the heat flux density and i_{LG} is the latent heat of vaporization.

Equation (2.4) is computed using two different sets of values for the constants C_1, C_2 , C_3 , C_4, representing the convective and the boiling region, and the greatest between the convective boiling dominant value and the nucleate boiling dominant value is taken as the heat transfer coefficient h_{TP}. Also in this correlation, a correction term here not reported is present in the equation for horizontal tubes if the all-liquid Froude number is lower than 0.04, in order to take into account the influence of stratification.

In the original Kandlikar (1990) equation the single-phase heat transfer coefficient h_L is calculated from the Dittus-Boelter equation (McAdams, 1942) using the all-liquid Reynolds number in the same way as the term h_L is treated in the Liu and Winterton (1991) correlation. The modification introduced by the Kandlikar and Balasubramanian (2004) correlation is given by the use of a different correlation to compute the term h_L in order to take into account the fact that the all-liquid flow can be not turbulent.

For $10^4 \leq \mathrm{Re_{LO}} \leq 10^6$ the Petukhov and Popov (1963) correlation should be used to compute h_T, while for $3000 \leq \mathrm{Re_{LO}} \leq 10^6$ the Gnielinski (1976) correlation is suggested. For $\mathrm{Re_{LO}} \leq 1600$ the all-liquid flow is considered laminar, and h_T should be computed according to the laminar flow theory. According to Kandlikar and Balasubramanian (2004), the transition between laminar and turbulent flow is not well defined and an appropriate interpolation scheme needs to be implemented in the transition region. A linear interpolation between $\mathrm{Re_{LO}} = 1600$ and $\mathrm{Re_{LO}} = 3000$ for the calculation of h_T is suggested in Kandlikar and Balasubramanian (2004).

Regarding the use of this correlation with propane, the fluid–surface parameter F_{fl}, which depends on the fluid and the heater surface characteristics, is given by the author for R22 in copper tubes (i.e. F_{fl} =2.20), but not for propane; however, Melin (1996) conducted experiments with a fluid heated copper test section for a number of fluids, including propane: the value recommended by Melin (1996) for propane is F_{fl} = 2.15, which is very close to the value for R22.

In most pool boiling correlations, the evaporation heat transfer coefficient is proportional to the het flux q raised to some exponent n (around 0.7), according to the following equation:

$$h_{pool} = Kq^n \tag{2.7}$$

where K is a constant depending on the fluid and surface properties.

The Cooper (1984) correlation for smooth cooper tubes is a quite simple correlation:

$$h_{pool} = 55q^{2/3} p_r^{\,0.12} (-\log_{10} p_r)^{-0.55} M^{-0.5} \tag{2.8}$$

where M is the molecular weight of the fluid and p_r is the reduced pressure (i.e. the rate of absolute pressure to critical pressure). As one can see, the exponent n in the Cooper correlation is 0.67.

The Stephan and Abdelsalam (1980) equation is more complex. It has been obtained by methods of regression analysis applied to experimental data measured using different fluids. It was found that data could be best represented by subdividing the fluids into four groups (i.e. water, hydrocarbons, cryogenic fluids and refrigerants). Eight different dimensionless numbers were found to be representative of the pool boil mechanism and one specific equation was developed for each of the four fluids groups considered. Each equation uses a different set of dimensionless numbers. Propane was considered by Stephan and Abdelsalam (1980) as part of the refrigerant fluids group and not in the hydrocarbons fluid group.

Discarding the analysis of these dimensionless numbers, which represent the influence of the physical properties of the fluid and the heater, the equation for refrigerants can be written in a simplified way as follows:

$$h_{pool} = Kq^{0.745} \tag{2.9}$$

As one can see, the exponent n in the Stephan and Abdelsalam (1980) correlation (i.e. $n = 0.745$) is higher than the one in the Cooper (1984) correlation (i.e. $n = 0.67$).

In Fig. 2.40 a comparison among the four correlations considered is given for the case of boiling R22, at 2°C saturation temperature, in 2 mm i.d. tubes. Data is computed at fixed vapour quality $x = 0.5$ and mass flux $G = 300$ kg $m^{-2}s^{-1}$, and different heat flux densities. The chosen value for the mass flux in Fig. 2.40, corresponds to around the mass flow rate needed in order to get the design 80 kW cooling capacity in the minichannel evaporator.

As one can see, the two flow boiling correlations and the two pool boiling correlations give similar results, and the evaporation heat transfer coefficient given by the flow boiling correlations is always higher than the one given by the pool boiling correlations.

The all-liquid Reynolds number is $Re_{LO} = 2839$ and lower than the threshold Re_{LO} =3000 given by Kandlikar and Balasubramanian (2004) for the use of the Gnielinski (1976) correlation; the reference single-phase heat transfer coefficient h_L in Eq. (2.4) is therefore in this case computed as a linear interpolation between the value given at Re_{LO} =3000 and the value given by the laminar flow theory (Nusselt number Nu=3.66 for constant temperature boundary condition). In Fig. 2.40 the heat transfer coefficient given by Eq. (2.4) using the laminar value for h_L is also reported. This is quite interesting in order to analyse the difference between the Liu and Winterton (1991) equation and the Kandlikar and Balasubramanian (2004) equation at low mass fluxes, which can be considered the typical situation for evaporation in minichannels. By reducing the mass flux G, the heat transfer coefficient given by Kandlikar and Balasubramanian (2004) tends to the value given by using the laminar heat transfer coefficient for h_L, while the Liu and Winterton (1991) equation tends to the value given by the Cooper (1984) correlation, since the h_L used in Eq. (2.1) tends to 0 and the suppression factor S tends to 1. As one can see in Fig. 2.40, the difference between these two equations at low mass fluxes value can be extremely high, since the heat transfer coefficient given by the Liu and Winterton (1991) would be much higher than the one given by the Kandlikar and Balasubramanian (2004).

The heat transfer coefficients given in the Fig. 2.40 are computed at fixed vapour quality $x = 0.5$, however, for the design of an evaporator, it is very important to compute the evolution of the heat transfer coefficient with the vapour quality. The evaporation correlations here considered are compared in Fig. 2.41 at fixed heat fluxed density q = 12000 W/m^2 and mass flux $G = 300$ kg $m^{-2}s^{-1}$, and different vapour qualities. The chosen values for q and G correspond to the design values in order to get 80 kW in the minichannel evaporator. The heat transfer coefficient clearly does not change with quality in the case of the pool boiling correlations. Regarding the flow boiling correlations, one can see that the trend predicted by the two equations here considered is different; however, the variation of the heat transfer coefficient with quality is not very high, and a similar average value is given by the Liu and Winterton (1991) correlation and the Kandlikar and Balasubramanian (2004).

The same comparison among correlations shown for R22 in Fig. 2.40 and Fig. 2.41, is given for R290 in Fig. 2.42 and Fig. 2.43. Also in this case, data has been computed at the mass flow rate needed in order to get the design 80 kW cooling capacity in the minichannel evaporator (i.e. $G = 150$ kg $m^{-2}s^{-1}$ with propane). The Stephan and Abdelsalam (1980) equation for hydrocarbons is also reported as a comparison.

While in the case of R22 similar values were predicted by the two flow boiling correlations and the two pool boiling correlations, with R290 the value given by the Liu

and Winterton (1991) equation is much higher than the value given by the Kandlikar and Balasubramanian (2004) equation, and the value given by the Cooper (1984) correlation is much higher than the value given by the Stephan and Abdelsalam (1980) correlation. It can also be seen in Fig. 2.43 that the heat transfer coefficient predicted by the Kandlikar and Balasubramanian (2004) equation at design conditions in the evaporator with R290 is very similar to the value predicted by the pool boiling Cooper (1984) correlation.

When comparing R22 with R290, according to the pool boiling correlations, it can be seen that very similar values of the heat transfer coefficient are given for the two fluids by the Stephan and Abdelsalam (1980) equation, while the Cooper (1984) correlation predicts a high improvement of the pool boiling performance with R290.

The molecular mass M and the reduced pressure p_r are the only fluid physical properties in the Cooper (1984) equation. While the reduced pressure p_r is very similar for the fluids, since they display very similar saturation temperature versus pressure curves, the molecular mass M is much lower for propane (i.e. $M_{R22} = 86$ and $M_{R290} = 44$) and this explain the much higher heat transfer coefficient predicted. It is interesting to notice that the molecular mass M has not been considered in the dimensionless numbers used for the Stephan and Abdelsalam (1980) correlation.

In a paper by Corberán *et al.* (2000), heat transfer coefficient values during evaporation of R22 and R290 are reduced from experimental data obtained with a PHE evaporator. In this kind of heat exchanger the predominant heat transfer mechanism is expected to be pool boiling. Experimental data with R22 was underpredicted by 10% by the Cooper (1984) correlation, while data with R290 was overpredicted by 60%. According to these results, a simple modification of the Cooper (1984) correlation was proposed in Corberán *et al.* (2000) for R290, writing the correlation as in Eq. (2.7) and changing the value of the constant K from the original value $K = 6.82$ to $K = 4.13$. This modified Cooper correlation has been plotted in Fig. 2.42 and Fig. 2.43. It is very interesting to notice that the heat transfer coefficients predicted are very similar to the ones given by the Stephan and Abdelsalam (1980) correlation.

When comparing R22 with R290, according to the flow boiling correlations, one can see that the Liu and Winterton (1991) correlation predicts a better performance for propane (it must be remembered that this correlation rely on the Cooper correlation), while the Kandlikar and Balasubramanian (2004) equation predicts a worse performance for propane. The fluid–surface parameter in the Kandlikar and Balasubramanian (2004) correlation is very similar for the two fluids (i.e. $F_{fl} = 2.20$ for R22 and $F_{fl} = 2.15$ for R22) and the difference among the predicted evaporation heat transfer coefficients for R22 and R290 is mainly due to the lower all-liquid Reynolds number at design conditions with R290 ($Re_{LO} = 2839$ for R22 and $Re_{LO} = 2439$ for R290).

Regarding the modelization of an evaporator, this is rather complex because at least three regions with different heat transfer features are present, i.e. the evaporating region, the post dryout region and the superheat region. The schematization of the simplified model adopted for the minichannel evaporator is depicted in Fig. 2.44: point 2 corresponds to the onset of dryout, while point 3 corresponds to the beginning of the superheated vapour region.

The most important point in the modelization of heat transfer in the evaporator can be considered the evaluation of the dry-out quality.

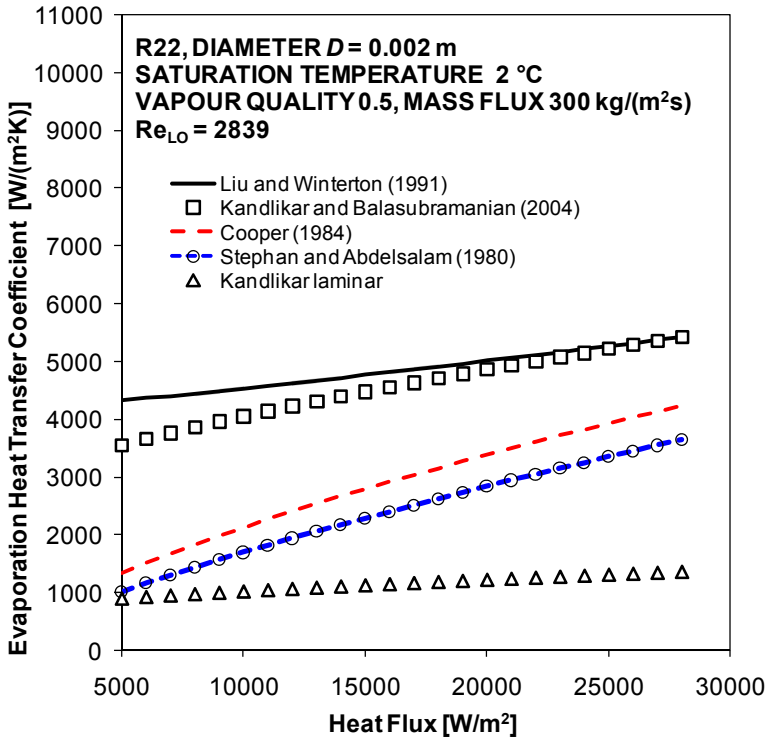

Fig. 2.40. Comparison among different evaporation heat transfer correlations with R22 at fixed mass flux $G = 300$ kg m^{-2}s^{-1} and different heat fluxes. Saturation temperature 2°C, $D = 2$mm, quality $x = 0.5$.

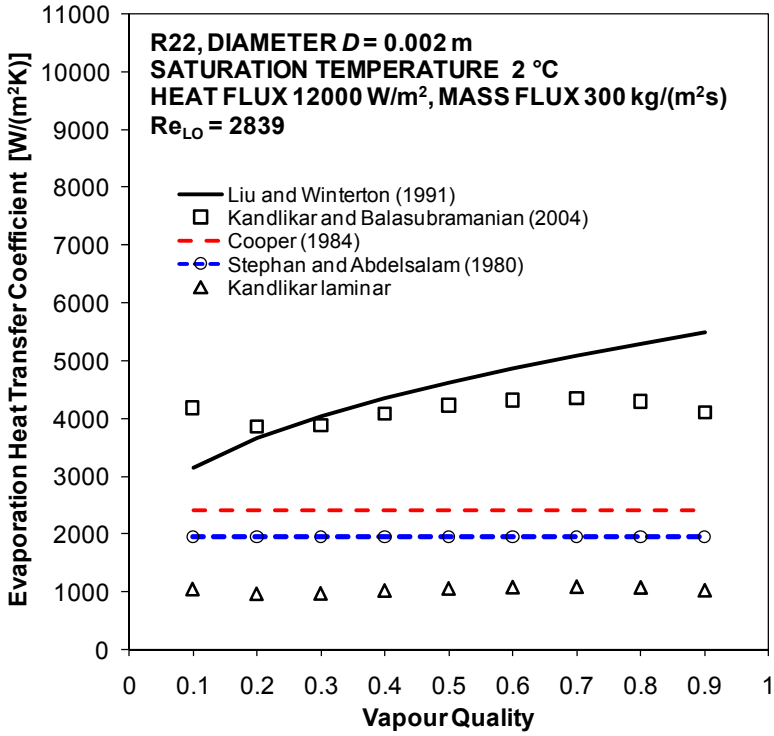

Fig. 2.41. Predicted evaporation heat transfer coefficient for R22 versus vapour quality at fixed mass flux $G = 300$ kg m^{-2}s^{-1} and heat flux $q = 12$ kW/m^2 and. Saturation temperature 2°C, $D = 2$mm.

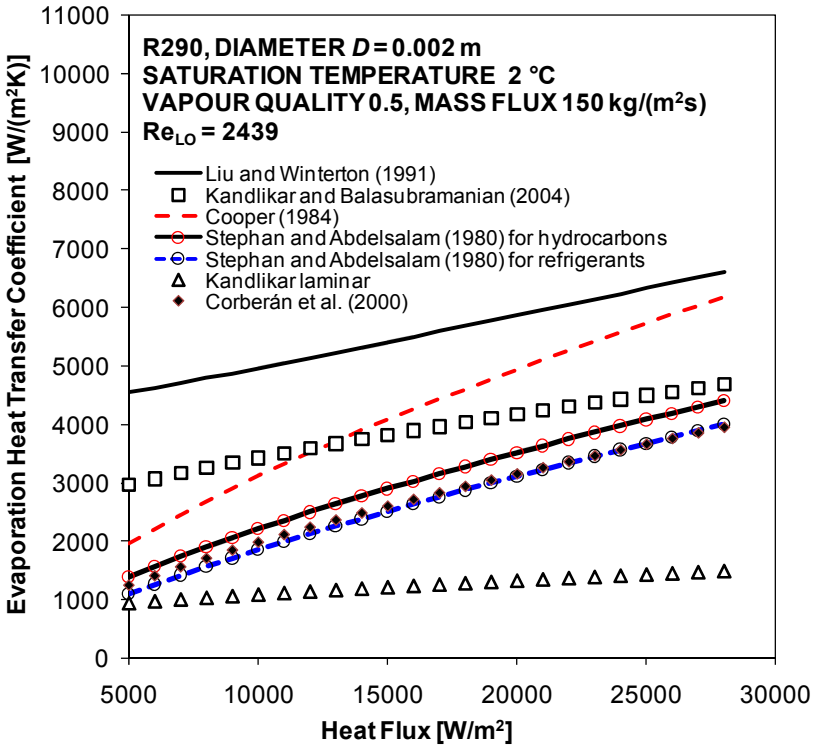

Fig. 2.42. Comparison among different evaporation heat transfer correlations with R290 at fixed mass flux G = 150 kg m^{-2}s^{-1} and different heat fluxes. Saturation temperature 2°C, D = 2mm, quality x = 0.5.

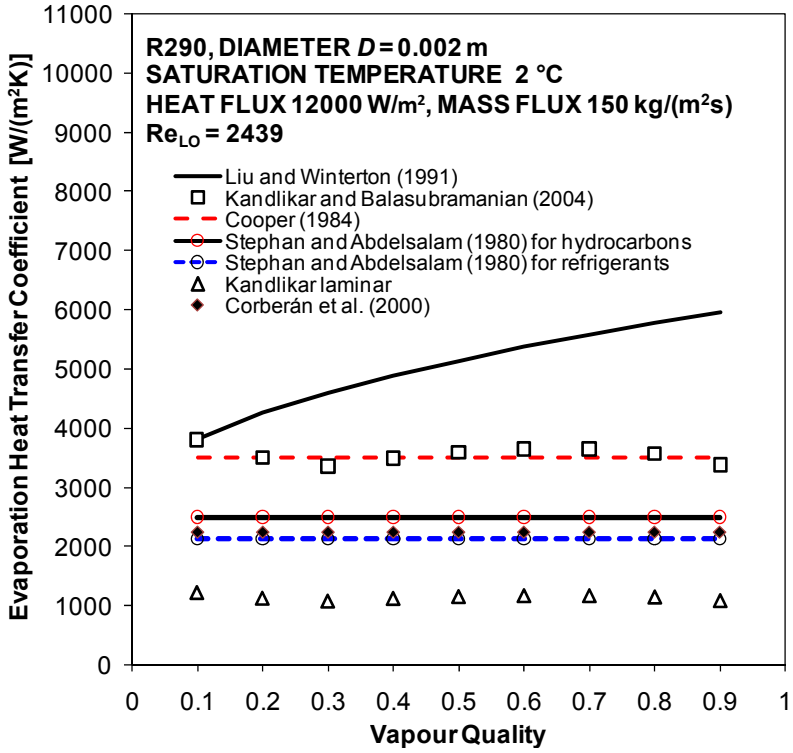

Fig. 2.43. Predicted evaporation heat transfer coefficient for R290 versus vapour quality at fixed mass flux G = 150 kg m^{-2}s^{-1} and heat flux q = 12 kW/m^2 and. Saturation temperature 2°C, D = 2mm.

In the computational procedure, given the values of pressure and quality at points 1, 2, 3 and 4, the heat transfer coefficient and the friction factor are computed considering a number of themodynamical points with pressure and quality evenly and linearly distributed between the values given at the extreme points. Then, the average heat transfer coefficient is computed by averaging the values obtained for these intermediate thermodynamical points. Refrigerant properties have been computed from the NIST database (2002).

The heat transfer rate, inlet and outlet water temperature, inlet vapour quality and superheating are given as inputs to the algorithm, whilst the program output is the outlet evaporating temperature required to fulfil the imposed conditions.

A number of different heat transfer and pressure drop correlations have been considered in the computational procedure. In the reference computation configuration, the evaporation heat transfer coefficient has been obtained from the Liu and Winterton (1991) correlation, while the refrigerant pressure drop in the evaporating and dryout regions has been computed by the Friedel (1979, 1980) correlation. The onset of dryout has been calculated by means of the Del Col *et al.* (2007) correlation for minichannels.

The Dittus-Boelter equation (McAdams, 1942) has been used to compute the heat transfer coefficient in both the post dryout and superheat regions; in the post dryout region, the heat transfer coefficient has been assumed equal to the single phase convective coefficient when the vapour fraction alone flows in the tubes. The pressure drop in the region of superheated vapour has been computed by the Blasius (1911) correlation.

The Kandlikar and Balasubramanian (2004) flow boiling correlation for minichannels and the Cavallini *et al.* (2005) correlation for two-phase pressure drop in minichannels have also been implemented in the program for comparison.

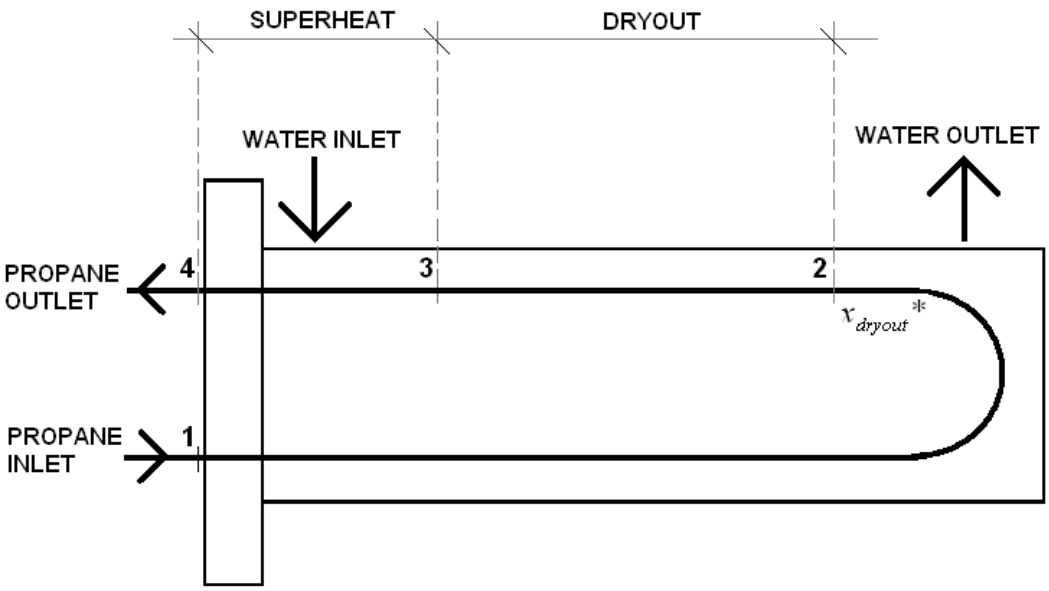

Fig. 2.44. Schematization of the evaporator.

The acceleration pressure drop has been evaluated using the Rouhani (1969) model for the void fraction, while the pressure drop due to the sudden flow expansion or contraction in the inlet and outlet headers has been computed according to Paliwoda (1992). The overall heat transfer coefficient and pressure drop on the shell side have been computed by the Bell-Delaware method (Bell, 1963) as published in the Heat Exchanger Design Handbook (Taborek, 1983).

Experimental data about evaporating heat transfer coefficient versus vapour quality shows that, when the initial dryout quality x_{dryout} is reached, this coefficient starts to decrease till reaching a much lower value at an intermediate quality between x_{dryout} and 1. However, in the schematization adopted, an average value of the heat transfer coefficient is calculated for each section of the evaporator: at point 2, in Fig. 2.44, the heat transfer coefficient suddenly decreases from the value predicted by a flow boiling correlation to that predicted for single phase forced convection of vapour. Since the difference between these two coefficients is extremely high, this way the average heat transfer coefficient in the dryout region would be underpredicted and the required heat transfer area would be overpredicted. Therefore, it was needed to modify the vapour quality corresponding to point 2, in Fig. 2.44, to compensate for the above schematization. Experimental data with R22 have been used to calibrate the computational procedure, in order to correctly estimate the performance with propane.

It was found that the computational procedure was able to predict well all experimental data when using the following equation to compute the quality x_{dryout}* corresponding to point 2 of Fig. 2.44:

$$x_{dryout}^{*} = x_{dryout} + \frac{1 - x_{dryout}}{3} \tag{2.10}$$

During the design of the evaporator a “design version” of the computational procedure was used, using as vapour quality at point 2, in Fig. 2.44, the x_{dryout} given by the Del Col *et al.* (2007) correlation. The “rating version” of the computational procedure, using the correction in Eq. (2.10), has then been used in this chapter to compare the computational results with experimental data.

In Table 2.3 some results obtained by the computational procedure have been reported. The performance with R22 and R290 are compared in Table 2.3 for a reference case of 80 kW cooling capacity with 5 K superheating at the evaporator outlet. The inlet and outlet water temperature are 12°C and 7°C, respectively. The Liu and Winterton (1991) correlation and the Friedel (1979, 1980) correlation have been used in the computation reported.

The inlet quality in Table 2.3 corresponds to the condition of 51°C and 3 K subcooling at the condenser outlet.

The expected length of each of the three regions considered in the schematization adopted and the corresponding average heat transfer coefficients are reported in Table 2.3. As one can see, the expected heat transfer coefficient is always higher for propane, in particular in the post dry-out and superheating region, this resulting in a higher outlet evaporating temperature.

Table 2.3. Performance of the evaporator with R22 and R290 according to the computational procedure.

	Refrigerant	R290	R22
	Heating Capacity	80 kW	
	Superheating	5 K	
Water side	T_{in}	12°C	
	T_{out}	7°C	
	Mass flow rate	3.8 kg/s	
	Pressure drop	27 kPa	
	Heat transfer coefficient	5566 $Wm^{-2}K^{-1}$	
Refrigerant side	Mass flow rate	0.311 kg/s	0.534 kg/s
	Mass flux	159 kg $m^{-2}s^{-1}$	273 kg $m^{-2}s^{-1}$
	Outlet evaporating temperature	4.54°C	3.53°C
	Total pressure drop	35.4 kPa	49.4 kPa
	Inlet/outlet pressure drop	4.3 kPa	4.7 kPa
	Acceleration pressure drop	1.7 kPa	2.7 kPa
	Saturation temperature drop	2.1 K	2.7 K
	Evaporating region HTC	5431 $Wm^{-2}K^{-1}$	4441 $Wm^{-2}K^{-1}$
	Evaporating region heat flux	11757 Wm^{-2}	12311 Wm^{-2}
	Dryout region HTC	866 $Wm^{-2}K^{-1}$	577 $Wm^{-2}K^{-1}$
	Superheating region HTC	893 $Wm^{-2}K^{-1}$	592 $Wm^{-2}K^{-1}$
	Inlet quality	0.31	0.27
	Dryout quality	0.92	0.91
	Evaporating region length	1.54 m	1.49 m
	Dryout region length	0.55 m	0.65 m
	Superheating region length	0.21 m	0.17 m
	Evaporating region pressure drop	23 kPa	31 kPa
	Dryout region pressure drop	7 kPa	13 kPa
	Dryout region Pressure drop	3 kPa	4 kPa

The computed dry-out quality is around 0.9 for both fluids and it is interesting to notice that the length of the region with low heat transfer coefficients (i.e. post dry-out region + superheating region) is expected to be around 30% of the total tube length.

While on the post dry-out and superheating regions the driving thermal resistance is on the tube side, in the evaporation region comparable heat transfer coefficients are computed on the water and refrigerant side.

By comparing the computed pressure drop, it can be seen in Table 2.3 how this is expected to be higher for R22 (i.e. 49 kPa) as compared to propane (i.e. 35 kPa). The corresponding saturation temperature drops are 2.7 K for R22 and 2.1 K for R290. Such values of saturation temperature drop are close to the optimal one, which can be considered to be around 1/3 of the mean temperature difference between the two fluids.

Comparisons between the experimental outlet evaporating temperature data and calculations are shown in Fig. 2.45 and Fig. 2.46. Predictions of the evaporation heat transfer coefficient are given by the Liu and Winterton (1991) correlation. “Simulation design” in these graphs refers to computation performed using as vapour quality at point 2, in Fig. 2.44, the x_{dryout} given by the Del Col *et al.* (2007) correlation, while

"simulation rating" refers to computation performed using the correction given by Eq. (2.10). As one can see, a very good agreement is obtained when using Eq. (2.10), and, in any case, also in the "simulation design" computation both the effect of inlet quality and superheat are well predicted.

The same comparisons are given in Fig. 2.47 and Fig. 2.48 when using the Kandlikar and Balasubramanian (2004) equation in the computational procedure. Also in this case, a very good agreement is obtained between experimental data and computations.

Fig. 2.49 reports a comparison between experimental and calculated total refrigerant pressure drop. It should be stressed that the computed values not only depend on the correlation used, but they also strongly depend on and the computation of the length of each of the three regions in the schematization adopted.

Both Friedel (1979, 1980) and Cavallini *et al.* (2005) correlations overpredict the measured values; however a satisfactory agreement has been achieved since the maximum deviation is below 20% for all the data points and both models.

The heat transfer calculations reported in Fig. 2.45, Fig. 2.46, Fig. 2.47 and Fig. 2.48 have been obtained using the Friedel (1979, 1980) correlation to determine the pressure drop. However, very little deviation in the evaluation of the evaporating temperature is obtained if the Cavallini *et al*. (2005) correlation is adopted instead.

With regard to the shell-side pressure drop, the graph in Fig. 2.50 reports the comparison between experimental data obtained at 17°C water temperature and the values predicted by the Bell-Delaware method (Bell, 1963). Shell side pressure drop is underpredicted by the computational procedure by about 20%. It should be reminded that, because of the small tube diameter, the application of the Bell-Delaware method (Bell, 1963) in the present case may provide not very accurate predictions.

The minichannel condenser has been tested with R22 also during evaporating conditions. This data was very useful in order to further validate the computational procedure used to design the evaporator. A comparison between the experimental outlet evaporating temperature and calculations is shown in Fig. 2.51, while experimental and computed refrigerant pressure drops are compared in Fig. 2.52.

The number of tubes in the condenser is around half the number of tubes in the evaporator, therefore the mass flux in the experimental measurements in Fig. 2.51 and Fig. 2.52 is almost double the mass flux in the experimental measurements for the evaporator and the consequent R22 pressure drop is very high. However, even if the evaporating conditions in the test performed using the minichannel condenser as an evaporator are very different from the design conditions for the evaporator, also in this case a very good agreement between the predictions of the computational procedure and experimental data is obtained for both for the evaporating temperature and pressure drop.

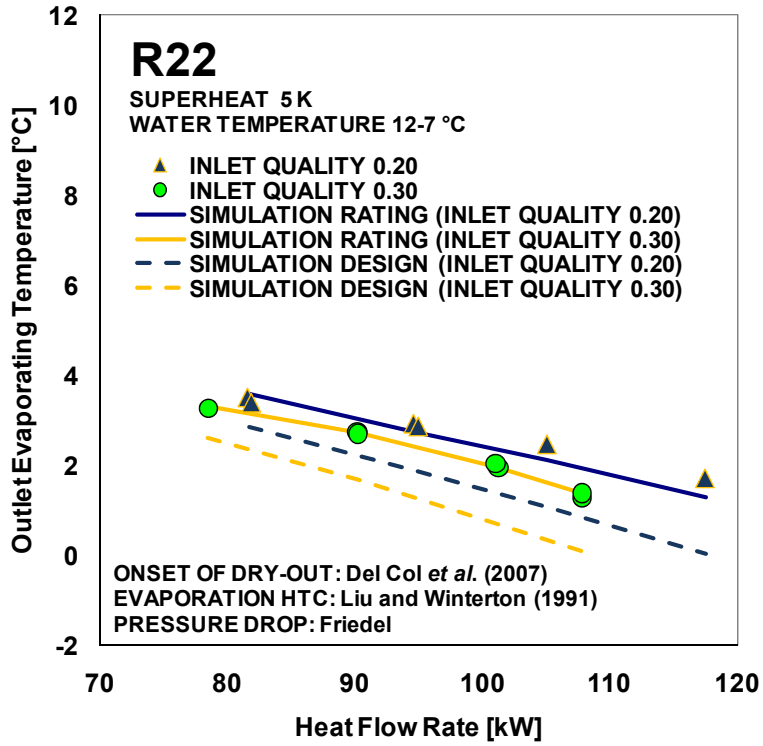

Fig. 2.45. Experimental and computed outlet evaporating temperature versus heat flow rate at fixed superheat. Predictions of evaporation heat transfer coefficient by Liu and Winterton (1991).

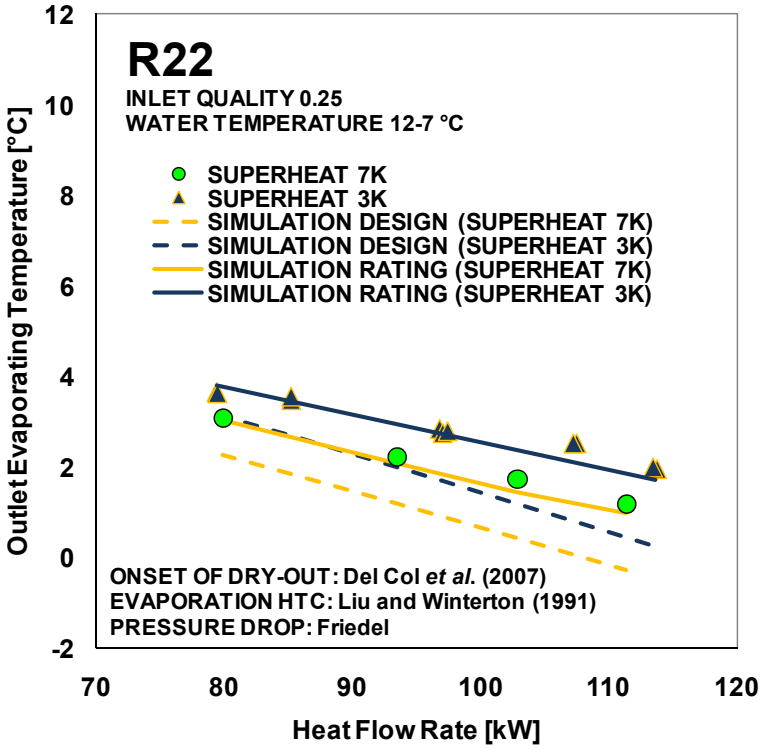

Fig. 2.46. Experimental and computed outlet evaporating temperature versus heat flow rate at fixed inlet vapour quality. Predictions of evaporation heat transfer coefficient by Liu and Winterton (1991).

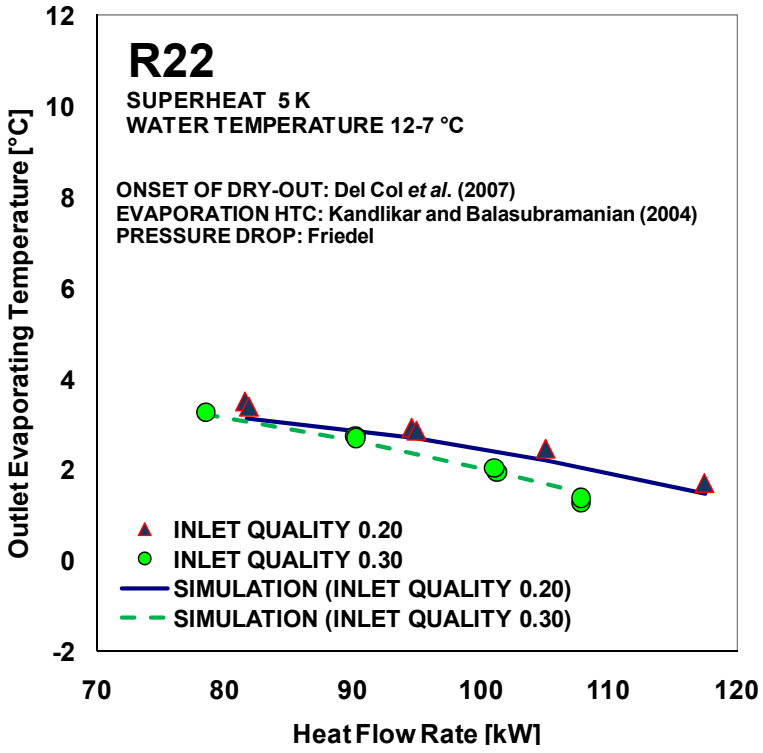

Fig. 2.47. Experimental and computed outlet evaporating temperature versus heat flow rate at fixed superheat. Predictions of evaporation heat transfer coefficient by Kandlikar and Balasubramanian (2004).

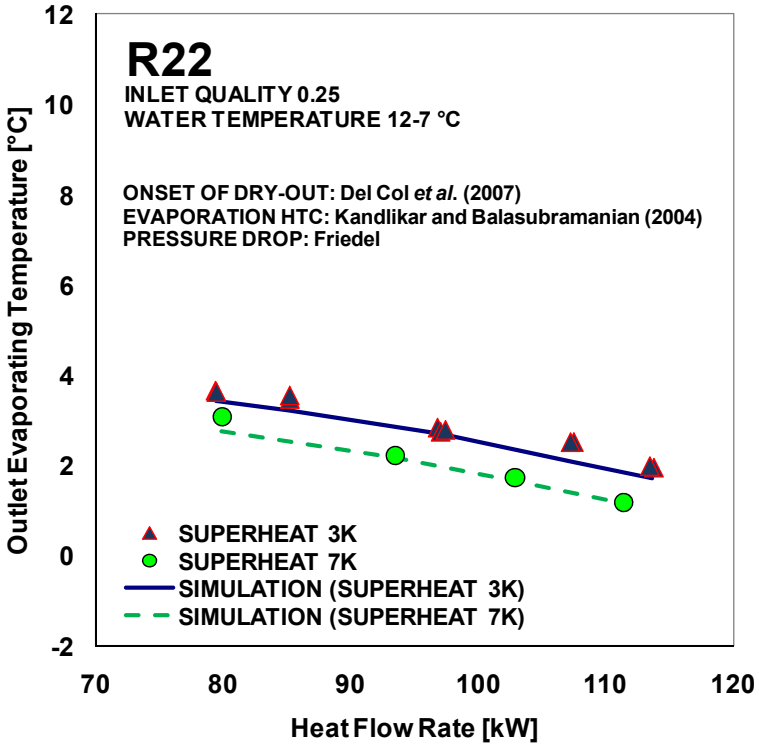

Fig. 2.48. Experimental and computed outlet evaporating temperature versus heat flow rate at fixed inlet quality. Predictions of evaporation heat transfer coefficient by Kandlikar and Balasubramanian (2004).

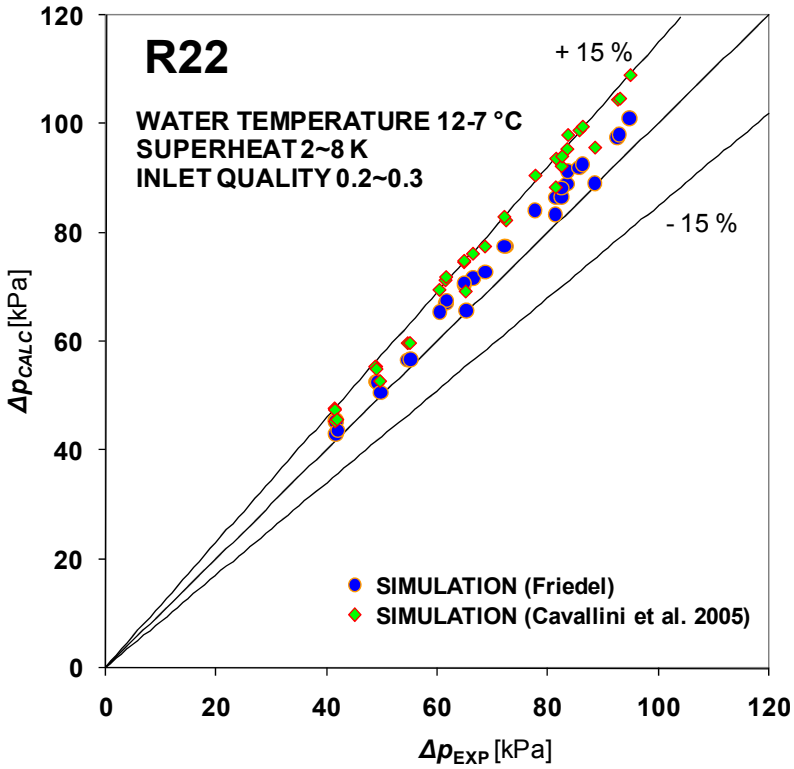

Fig. 2.49. Comparison between experimental and calculated refrigerant pressure drop. Predictions by Friedel (1979, 1980) and Cavallini *et al*. (2005).

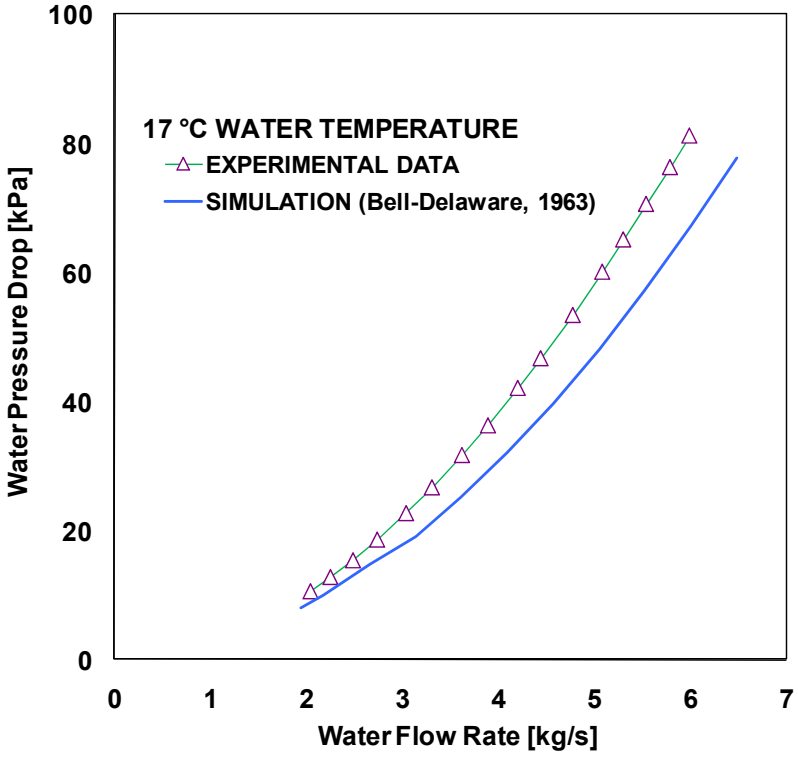

Fig. 2.50. Experimental and computed water pressure drop versus mass flow rate at 17°C. Predictions obtained from the Bell-Delaware method (Bell, 1963).

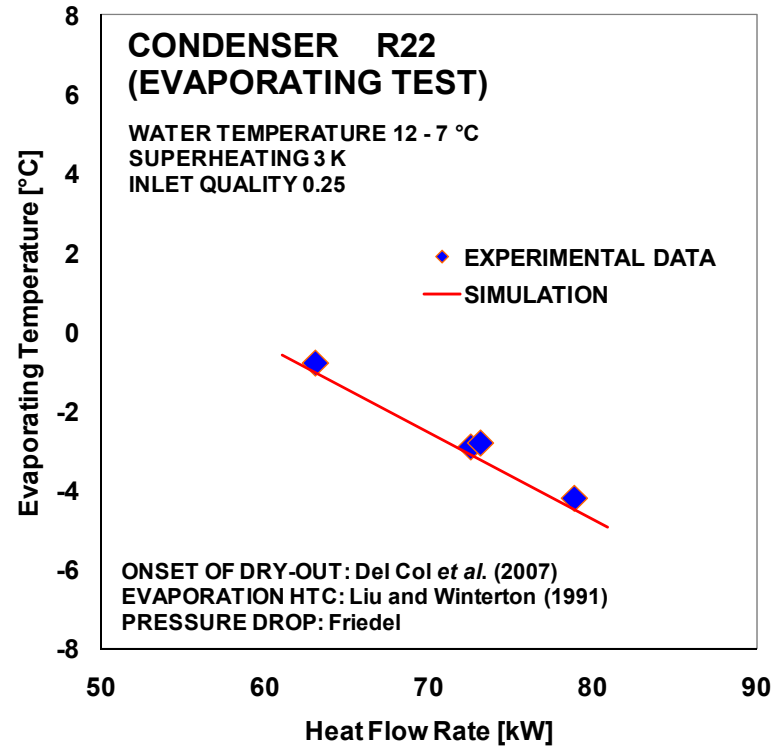

Fig. 2.51. Experimental and computed outlet evaporating temperature versus heat flow rate for the minichannel condenser during evaporation test.

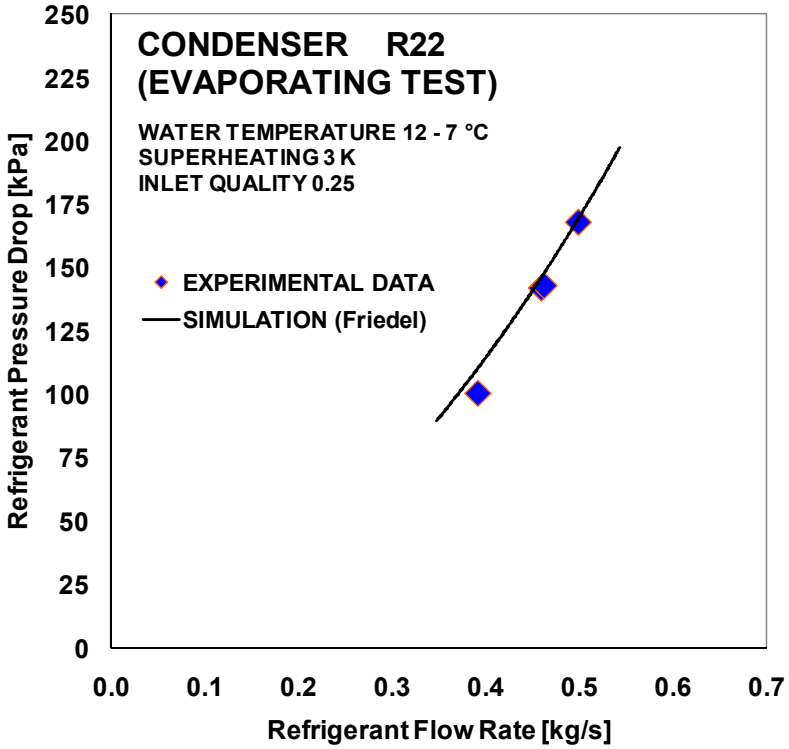

Fig. 2.52. Experimental and computed refrigerant pressure drop versus mass flow rate for the minichannel condenser during evaporation test.

2.4.3 Computational procedure for the IHX design

The modelization of the internal heat exchanger is much simpler than that of the condenser and the evaporator, because on both shell and tube sides single-phase flow is present. The heat transfer coefficient can be considered constant along the heat exchanger and the method of the mean logarithmic temperature difference, with a temperature correction factor to take into account the layout of the liquid and vapour streams, can be used.

In the computational procedure for the internal heat exchanger, the Dittus-Boelter equation (McAdams, 1942) has been used to compute the heat transfer coefficient in the tubes, and the Blasius (1911) correlation has been used for the pressure drop.

The estimation of the heat transfer coefficient on the vapour side is much more important than the one on liquid side, since the thermal resistance is on the shell side. The heat transfer coefficient and pressure drop on the shell side have been computed by the Bell-Delaware method (Bell, 1963) as published in the Heat Exchanger Design Handbook (Taborek, 1983). The temperature correction factor has been computed according to the Heat Exchanger Design Handbook (Taborek, 1983).

In the computational procedure, given the required inlet and outlet conditions of the liquid and vapour streams, the design overall heat transfer coefficient needed to get the required heat flow rate is computed and compared to the overall heat transfer coefficient given by the correlations.

A comparison between experimental data and computational procedure results when using propane is given in Table 2.4. In most of the test runs of the heat pump, the liquid at the outlet of the condenser was not completely condensated. For the comparison in Table 2.4, a couple of experimental data points with complete condensation, taken at full compressor capacity and 66 % compressor capacity, was chosen.

The “overall HTC margin” in Table 2.4 is computed as the percentage difference between the design heat transfer coefficient and the heat transfer coefficient given by the correlations. As one can see, a good agreement is obtained since the “overall HTC margin” is around 0.5% for the data point at low mass flow rate and around 4% for the data point at high mass flow rate. The tube side heat transfer coefficient is also reported, showing that the heat transfer resistance is fully on the shell side.

While the pressure drop on tube side has no influence of the performance of heating and refrigeration equipment, since in any case the condensated liquid pressure must be reduced down to the evaporation pressure in an expansion device, the pressure drop on the shell side does decrease the overall performance, because it increases the pressure rise required to the compressor, hence increasing the energy consumption of this device.

The pressure drop given by the Bell-Delaware method (Bell, 1963) has been computed by means of the computational procedure at different mass flow rates. These results are compared against experimental data in the graph in Fig. 2.53. In the facility used to get the present experimental data, no pressure transducers are present at the inlet and outlet of the internal heat exchanger, but the pressure is measured at the outlet of the evaporator and at the inlet of the compressor. Experimental data reported in Fig. 2.53 has been computed by comparing the pressure drop obtained for the configurations using the internal heat exchanger to the pressure drop for the configurations not using it, as described in Section 2.3.4.

Even if the Bell-Delaware method (Bell, 1963) was developed using water as fluid and tube bundles with conventional diameter size, it must be noticed that a good agreement with experimental data is observed both for the heat transfer coefficient and the vapour pressure drop.

Table 2.4. Comparison between experimental data and computational procedure results for the internal heat exchanger when using propane.

	Case number	1	2
Experimental data	T_{IN} liquid	50.63°C	45.00°C
	T_{OUT} liquid	39.03°C	32.40°C
	T_{IN} vapour	10.74°C	6.03°C
	T_{OUT} vapour	31.07°C	26.63°C
	Mass flow rate	0.257 kg/s	0.181 kg/s
	Liquid inlet saturation temperature	50.88°C	45.29°C
	Vapour inlet saturation temperature	0.19°C	-0.05°C
	Heat flow rate (vapour side)	9.4 kW	6.6 kW
Computation	Design overall HTC (tube ext. area)	379 $Wm^{-2}K^{-1}$	307 $Wm^{-2}K^{-1}$
	Overall HTC margin	+ 4.3 %	+ 0.4 %
	Vapour side HTC	509 $Wm^{-2}K^{-1}$	404 $Wm^{-2}K^{-1}$
	Liquid side HTC	3530 $Wm^{-2}K^{-1}$	2612 $Wm^{-2}K^{-1}$
	Shell side pressure drop	7.9 kPa	3.9 kPa
	Tube side pressure drop	10.3 kPa	5.3 kPa

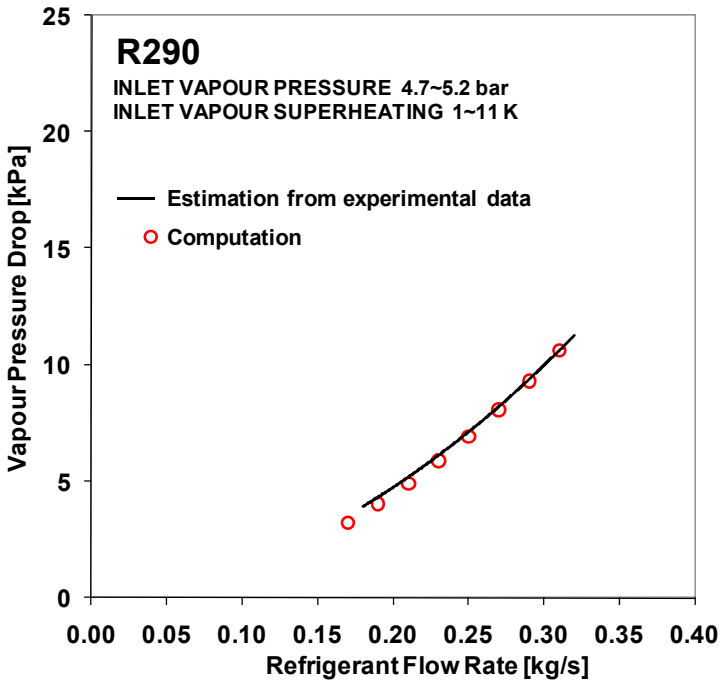

Fig. 2.53. Experimental and computed refrigerant pressure drop versus mass flow rate for the shell side of the minichannel internal heat exchanger when using R290.

2.5 Refrigerant charge estimation

An estimation of the charge required by the minichannel heat exchangers is useful to estimate the possible advantages of operating HVAC equipment with these prototypes.

The current industrial benchmark in charge minimization is given by plate heat exchangers; therefore, the minichannel condenser and evaporator have been compared to brazed plate heat exchangers (BPHE) available in the market providing about the same thermal performance when using propane. These BPHEs have been installed in the facility of the heat pump using propane as refrigerant along with the minichannel heat exchangers. The same BPHE has been chosen as the condenser and as the evaporator (i.e. AC120EQ with 80 plates by Alfa Laval).

Experimental data comparing the thermal performance of the two condensers with R290 have been reported in Section 2.3.1, while at the moment of writing the present thesis no experimental data are available for the performance of the minichannel evaporator with R290.

The total charge required by the heat pump has been measured. By comparing the charge required by the different configurations tested, some information can be obtained about the charge reduction given by the minichannel condenser. Experimental data about the heat pump facility propane charge is reported in Section 3.6.6. In this Chapter an attempt of theoretical estimation of the charge required by the prototypes is presented.

A first important comparison between the minichannels and the brazed plate heat exchangers is given by the volume of these devices.

The propane side internal volume is 2.9 L in the case of the minichannel condenser and 8.4 L in the case of the brazed plate heat exchanger; hence, 65% reduction in terms of internal volume has been obtained.

Regarding the evaporator, the refrigerant side internal volume is 5.8 L in the case of the prototype and 8.4 L in the case of the brazed plate heat exchanger; hence, 30% reduction has been obtained.

The computational procedures described in Section 2.4.1 and Section 2.4.2 have been used in order to theoretically estimate the charge in the minichannel condenser and evaporator. The actual amount of refrigerant trapped in a device is a function of the void fraction which depends on the flow conditions which are very different in the minichannels and in the brazed plate condenser. A number of void fraction models have been used in order to relate two-phase density to quality. Such values have been computed all along the prototype by means of the computational procedure simulating the heat transfer process. The amount of propane trapped in the inlet and outlet headers has also been included in the total estimation.

Estimation has been attempted also in the case of the BPHE condenser, where quality has been assumed to be linear between inlet and outlet.

Predictions have been obtained from the following models: Rouhani (1969) as published in the HEDH (Taborek, 1983), Niño *et al*. (2002) for annular flow, Lockhart and Martinelli (1949), CISE (Premoli *et al*., 1970), Zivi (1963) and Baroczy (1963). Among the correlations considered, the Niño model for annular flow (Niño *et al*., 2002) is the only one specifically developed for minichannels. Furthermore, the homogeneous model, which considers that the vapour and liquid phases flow at the same velocity, has

also been implemented; since, in general, the vapour phase has higher velocity than the liquid phase, the charge given by this model can be considered as the bottom limit.

In a paper by Harms *et al.* (2003), the measured total charge in three unitary air conditioners has been compared against a computational procedure using a number of void fraction correlations. According to their results, obtained at condenser subcooling values varying from 2 K to 20 K, the Baroczy (1963) void fraction correlation gave the best overall agreement with measured data; however, good agreement is reported also when using the Zivi (1963) and CISE (Premoli *et al*., 1970) models, particularly at low subcooling.

Fig. 2.54 reports the comparison between the condenser propane charge predicted in the case of the present prototype and in the case of the BPHE according to the different void fraction correlations considered. Simulations have been performed considering 110 kW heat flow rate, 40 – 45°C water temperature and 0 K subcooling.

In the case of the minichannel shell and tube condenser, the expected charge varies from about 0.25 kg (Niño *et al*., 2002 and homogenous model) to about 0.4 kg (Baroczy, 1963 and Zivi, 1963). In the case of the plate condenser much higher values have been obtained, varying from about 0.8 kg (Niño *et al*., 2002 and homogenous model) to 1.6 kg (Rouhani, 1969). Roughly speaking, the propane charge required by the prototype is expected to be less than half the quantity required by a traditional brazed plate condenser.

It is interesting to point out that the value computed in the case of the prototype by the Niño *et al*. (2002) correlation for annular flow, which is the only one specifically developed for minichannels, is the lowest. Hrnjak and Hoehne (2004) compared the void fraction to quality curve given by the Niño model to those given by traditional models, showing that higher void fraction is expected to be found in a minichannel as compared to a traditional round tube at the same quality. This aspect could represent another advantage of using minichannels in heat exchangers to minimize the charge.

By comparing the experimental measurements of the total charge in the heat pump facility for the test configuration with the minichannel condenser to the charge for the configuration with the BPHE condenser, 0.8 kg charge reduction is observed when the prototype condenser is used. As one can see in Fig. 2.54, this result is in good agreement with the predictions given by the Baroczy (1963), Zivi (1963) and CISE (Premoli *et al*., 1970) models.

It should be stressed that, according to experimental data, even if such great benefits are obtained in term equipment charge reduction, a very small reduction of the heat pump COP (i.e. around 2%) is measured when using the prototype condenser.

Regarding the minichannel evaporator, Fig. 2.55 reports the estimated propane charge according to the different void fraction correlations considered. Simulation has been performed at 80 kW heat flow rate, 12–7°C water temperature, 0.33 inlet vapour quality and 7 K superheat. The expected charge varies from about 0.18 kg (Zivi, 1963) to 0.23 kg (Niño *et al*., 2002 and Premoli *et al*., 1970).

Fig. 2.56 reports the calculated evaporating temperature versus heat flow rate when using propane in both the minichannel evaporator and in the BPHE at two operating conditions.

Calculations have been made using the computational procedure and a rating software provided by the BPHE manufacturer. Even if the internal volume of the prototype is 30% lower than that of the BPHE, a better thermal performance is

expected; therefore when using the prototype the equipment efficiency is expected to slightly increase.

Finally, given the internal volume, the charge in the internal heat exchanger can be computed without difficulties, since single-phase flow is present both at the shell and tube side.

The propane charge trapped in the internal heat exchanger is around 0.3 kg at design operating conditions. Even if the overall size of the internal heat exchanger is much smaller than the condenser and evaporator one, it must be noticed that the charge is comparable to the expected charge in the condenser and in the evaporator.

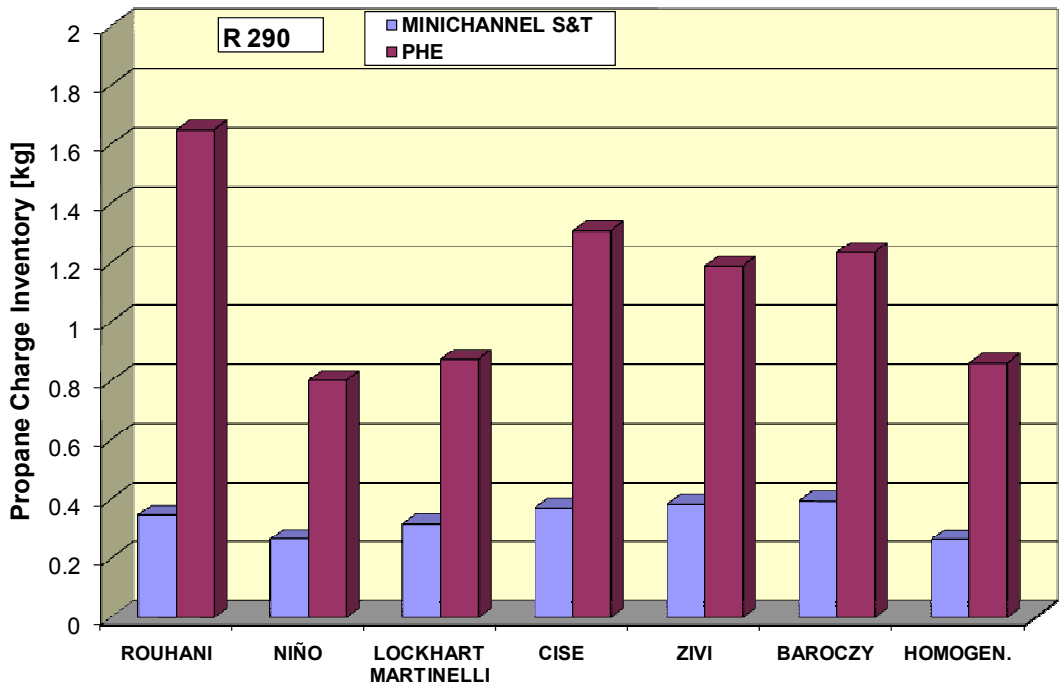

Fig. 2.54. Estimated total charge in the minichannel and the BPHE condenser when using propane (110kW, 40–45°C water temperature, 0 K subcooling).

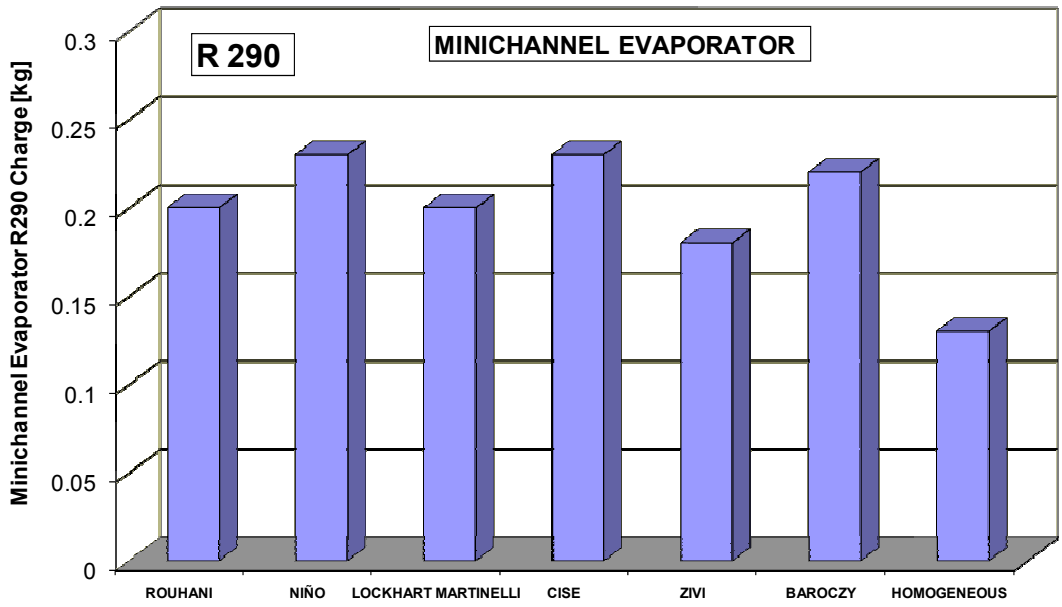

Fig. 2.55. Estimated total charge in the prototype evaporator when using propane (80 kW, 12–7°C water temperature, 0.33 inlet quality, 7 K superheat).

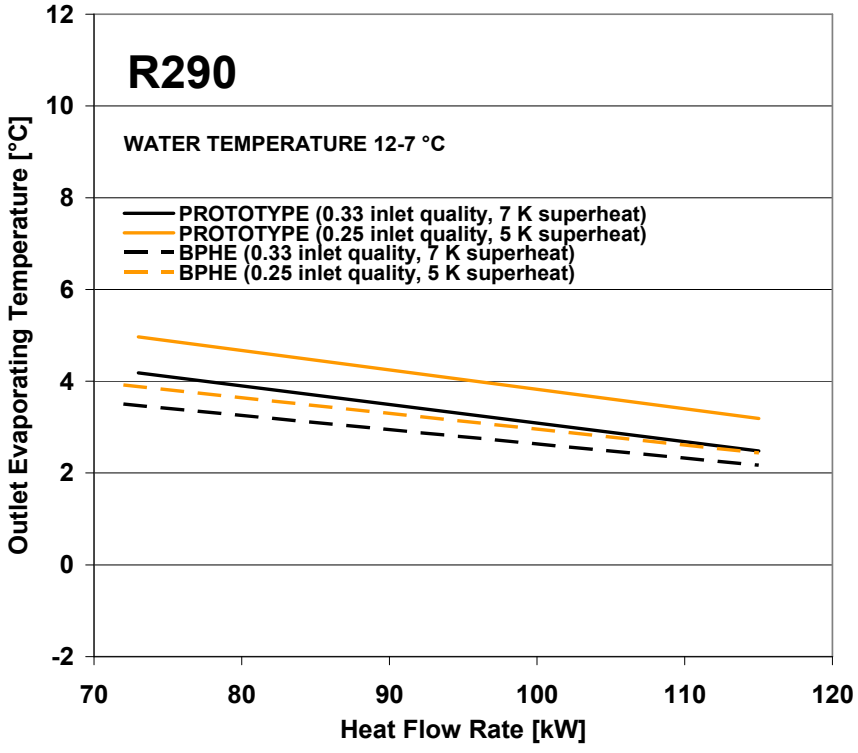

Fig. 2.56. Calculated outlet evaporating temperature versus heat flow rate when using propane in the minichannel evaporator and in a BPHE at two different operating conditions.

Chapter 3.

Propane heat pump

3.1 Introduction

As a consequence of the phase out of chlorinated refrigerants (i.e. CFCs and HCFCs) because of their negative influence on the ozone layer, hydrofluorocarbons (HFCs) containing no chlorine are nowadays being used by HVAC industry in newer equipment. These fluids display null ozone depletion potential, but in most cases are strong greenhouse gases (e.g. $GWP_{R134a} = 1300$, $GWP_{R407C} = 1520$, $GWP_{R410A} = 1720$).

The fluid leakages from equipment, as well as the possible atmospheric emissions during the whole lifetime, from manufacture to dismantling and through maintenance, cannot be considered negligible. As an example, typical leakage rates from supermarkets refrigeration systems are 15-20 % of the charge per year (A.D. Little Inc., 2002). Regarding automotive applications, the annual leakage rate per vehicle at normal operation in newer cars is expected to be around 50 g (i.e. 7% of the total charge), according to a study for the EC by Schwartz and Harnisch (2003).

Other applications may display lower leakage rates, however it's clear that leakages cannot be avoided, especially during equipment dismantling.

In Fig. 3.1 some data from Intergovernmental Panel on Climate Change (2007) about the emissions of anthropogenic greenhouse gases is reported.

As one can see in Fig. 3.1, in terms of CO_2 equivalent, the share of the fluorinated gases in the total emissions in 2004 is estimated to be 1.1%. Clearly, the contribution of fluorinated gases among the other anthropogenic greenhouse gases is not the biggest, however, it cannot be considered negligible.

Another important data in Fig. 3.1 is given by the share of different sectors in total emissions. The share of residential and commercial buildings is estimated to be 7.9 %. Most of these emissions is due to the heating demand. The use of HVAC technologies reducing the primary energy consumption such as heat pumps is important in order to reduce the emissions of greenhouse gases.

It must be stressed that, when developing new equipment using refrigerants with low or null GWP, this must be done without losses in terms of energy performance, since the indirect effect due to the energy consumption and the consequent carbon dioxide emissions caused by the electricity production process must be taken into account.

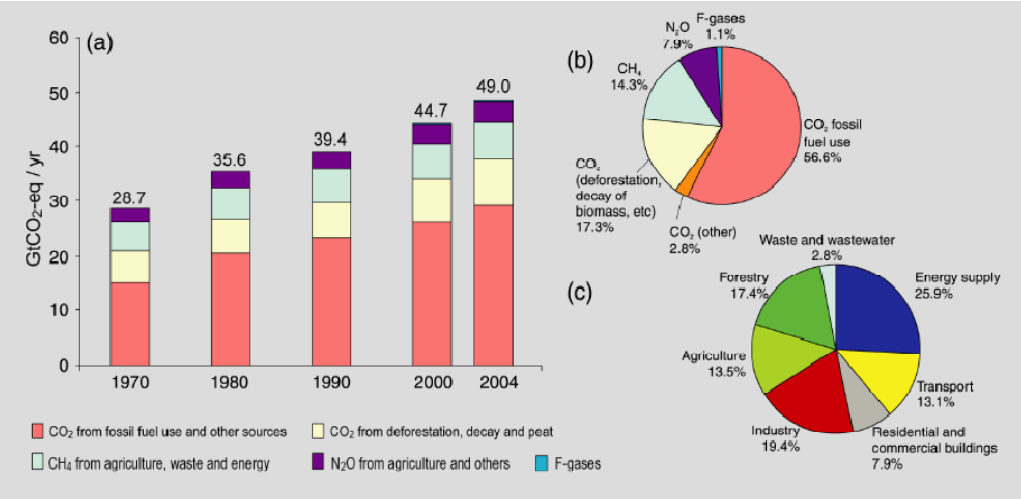

Fig. 3.1.a) Global annual emissions of anthropogenic greenhouse gases from 1970 to 2004. b) Share of different anthropogenic greenhouse gases in total emissions in 2004 in terms of CO_2 equivalent. c) Share of different sectors in total anthropogenic greenhouse gases emissions in 2004 in terms of CO_2 equivalent. From Intergovernmental Panel on Climate Change (2007).

Future environmental legislation concerning refrigerants in relation to the greenhouse effect is expected. In some countries (e.g. Austria, Switzerland, Denmark) new legislations have already been approved for a global phase out of HFCs and, even if no agreement has been achieved yet, regulations on greenhouse refrigerants are discussed within the Kyoto protocol and later amendments.

Regarding the heat pump applications, the ecological criteria for the award of the European Community eco-label ((EC) No 1980/2000) to heat pumps have been revised with the Decision 2007/742/EC. According to the new regulation, in case of a working refrigerant with GWP lower than 150, the minimum requirements for the coefficient of performance (COP) and primary energy ratio (PER) in heating mode and the energy efficiency ratio (EER) in cooling mode shall be reduced by 15 % in comparison to those applied to systems using a fluid with higher GWP.

Within the EC, since in mobile air conditioning the use of open compressors gives rise to a large amount of leakages, the gradual phase out in these kind of systems of fluids with GWP higher that 150 starting from 1st January 2011 has been regulated by the directive 2006/40/EC.

As a consequence of this directive, at least two major chemical manufacturers working jointly (i.e. DuPont Fluorochemicals and Honeywell) have redirected their focus to a new fluid called R-1234yf in order to find a substitute for R134a in automotive air conditioning applications. According to Minor and Spatz (2008) R-1234yf offers similar thermophysical properties to R-134a, thus minimizing equipment changes, while displaying a low greenhouse warming potential ($GWP_{R\text{-}1234yf} = 4$). The first results of toxicity tests are reported to be favourable, but an ames test (i.e. a biological assay to assess the mutagenic potential) showed slightly activity (Minor and Spatz, 2008).

The R-1234yf fluid is a fluoro-olefin. Fluoro-olefins generally are more reactive than compounds with only single carbon-carbon bonds, this leading to a shorter atmospheric lifetime, which is a very favourable property in order to reduce the ozone depletion potential ODP and the greenhouse warming potential GWP. However, the

higher reactivity is also generally leading to higher toxicity and lower stability; furthermore, because of the very short lifetime, these fluids tend to decompose in proximity to the location of release, giving birth to products which could be smog progenitors or contribute to the formation of other chemicals with higher GWP (Calm, 2008).

Part of the scientific community has suggested that "natural fluids" with no environmental impact on the ozone layer and very low impact on the greenhouse effect like hydrocarbons, ammonia and carbon dioxide should be used as substitutes for synthetic refrigerants. These fluids were among the very first fluids used in the history of refrigeration.

Even not considering the global warming issue, it must be noticed that the adoption of natural fluids, which are much better known than man-made ones, also provides some kind of intrinsic safety against potential unknown negative effects of man-made substances.

It should be here remembered that chlorofluorocarbons (CFCs) were invented in the '30s as completely inert and harmless fluids. Only 40 years later, in 1974, their effect on the ozone layer destruction was discovered. Since HFCs nowadays being used are quite new man-made fluids (like CFCs were when first introduced into the market) their potential negative effects cannot be completely known. These considerations are even stronger regarding the new generation of refrigerants chemical manufacturers are working on.

Among the natural fluids suggested as refrigerants, carbon dioxide presents a very low critical temperature (i.e. around 30°C). Therefore, at usual temperature levels for HVAC applications in buildings, a transcritical cycle is needed, this leading, in general, to lower energy efficiency as compared to ammonia and hydrocarbons. Furthermore, very high pressures are reached and the design of new devices is required.

In the field of automotive applications, however, carbon dioxide is a very promising candidate to replace R134a as refrigerant, and several manufactures are planning to introduce it in order to fulfil the european directive 2006/40/EC.

In an application like water heating, the use of a transcritical cycle in which the temperature of the fluid in the gas cooler can "follow" the temperature rise of the water (while in an usual cycle the condensation temperature is almost constant) is favourable. In Japan, where the energy demand for water heating is considerably higher as compared to other countries (i.e. approximately 30% of residential energy use) the number of heat pump water heaters using carbon dioxide as refrigerant is continuously increasing. Since commercialization in 2001, cumulative shipments of the "EcoCute" heat pump water heaters using CO_2 topped 1 million units in 2007, and the Japanese industry expects cumulative sales exceed 5.2 million units by 2010 (Hashimoto, 2006). It must be noticed that the initial success of the "EcoCute" heat pump water heaters was driven by Japanese government and utility subsidies.

Because of its very favourable heat transfer properties, carbon dioxide can be a very efficient secondary fluid in an indirect system. In particular, its use in commercial refrigeration applications such as supermarkets, coupled with refrigeration cycles using hydrocarbons or ammonia is very promising. Another possibility could be the use of a cascade cycle with carbon dioxide used at the lower temperature cycle and hydrocarbons or ammonia at the higher temperature cycle.

Regarding the use of ammonia as refrigerant, this can certainly be considered one of the refrigerants with the best heat transfer properties and very good energy performances can be obtained by using this fluid.

In the field of very big industrial systems it has been one of the first refrigerants adopted and is still the most largely used. However, in the case of smaller systems, and especially in the field of HVAC applications for buildings, the use of ammonia can be problematic. This refrigerant is toxic at high concentration and flammable, mainly together with traces of oil, but these issues could be solved by using indirect systems or reducing the charge. The main problems for its use in small and medium applications can be considered the fact that ammonia is not compatible with copper, and therefore cannot be used with traditional hermetic or semihermetic compressors, and the fact that its solubility with lubricant oils is very low. As a result, this fluid cannot be used in traditional equipment for HFCs, and a new design and devices development would be required.

Among the natural fluids suggested as substitutes of HFCs, hydrocarbons are the refrigerants most chemically related with the halogenated ones and their use would not involve major changes in the equipment design, since their thermodynamic properties and materials compatibility are similar to those of traditionally used synthetic fluids. Particularly, a system designed for R22 could be run with propane (R290) as the working fluid without any problem.

The main problem of hydrocarbons as refrigerant is their flammability which has prevented their use in large scale; additional safety restrictions are required and, since the possible hazards can be considered proportional to the total amount of refrigerant trapped in the system, charge minimization can be considered a major design constraint. Furthermore, charge reduction could be needed in order to fulfil safety legislation.

It should be remembered that isobutane (R600a) nowadays dominates the European market of domestic refrigerators, since the required charge in this application is very low (i.e. typically less than 150 g), therefore no safety concerns are present. However, it is interesting to notice how, mainly because of legislative considerations, hydrocarbons are not used in domestic refrigerators in the USA.

In general, it could be said that hydrocarbons can be considered a very good choice for HVAC applications, since any environmental direct effect can be avoided without energy efficiency loss and traditional equipment developed for HFCs can be used without further development.

Regarding this last aspect, it should be noticed that, until recently, no hermetic compressor manufacturers of commercial size allowed the use of HCs in their compressors. Even if compression efficiency was measured to be good when using hydrocarbons in hermetic compressor developed for halogenated fluid, the use of HCs was not allowed by the manufacturers because of safety reasons. However, recently some manufacturers (e.g. Danfoss) started to market hermetic compressors for R290.

The development of the future normative and legislation regarding the use of flammable refrigerant in HVAC applications is very important for the possible future massive use of hydrocarbons as refrigerants. A review of the existing standards and the available drafts of the forthcoming ones can be found in Corberán *et al.* (2008b).

Regarding the possibility of charge reduction in refrigeration equipment, at the system level, the use of secondary fluid loops both at the cold and hot side drastically reduces the charge when compared to direct systems. In the case of quite large systems, indirect systems are a good choice also because all the refrigerant containing parts can

be placed in a special machinery room or outdoors. Roof top chillers and heat pumps using a hydronic system to distribute chilled or hot water are an ideal solution to the safety problem, and they also fulfil most of the normative and legislation.

At the components level, most of the charge is found to be trapped in the heat exchangers, therefore the optimization of these devices, especially the condenser, is very important for equipment charge reduction, as already discussed in Section 2.1.

In a paper by Harms *et. al.* (2003), the charge inventory distribution among the components of three unitary air conditioners with capacity varying from 9 kW to 26 kW and using R22 and R407C as refrigerant has been estimated. Most of the heat exchangers used standard microfin tubes, with internal diameter varying from 6 mm to 9 mm. According to their results, most of the charge was expected to be trapped in the exchangers; in particular the computed charge in the condenser varied from 30% up to 70% of the total amount, while the charge in the evaporator was about 15%.

In a paper by Palm (2007), most of the charge in a 5 kW capacity water-to-water heat pump adopting brazed plate heat exchangers and using propane was experimentally measured to be trapped in the heat exchangers, and mainly in the condenser, where about 40% of the total charge was found. Similar results have been obtained in an estimation by Corberán and Martínez (2008a) of the charge inventory distribution among the components of a water-to-water propane heat pump using plate heat exchangers (PHEs): 50% of the total charge is expected to be found in the condenser, while about 15% should be trapped in the evaporator.

Prototype water-to-refrigerant heat exchangers using minichannels and providing a lower charge when compared to BPHE have been installed and studied at KTH, Stockholm, showing that a unit with 5 kW heating capacity can be designed with less than 0.2 kg charge of propane (Fernando *et al.*, 2004, Fernando *et al.*, 2008a, Fernando *et al.*, 2008b, Fernando *et al.*, 2008c).

Air-to-propane prototype heat exchangers employing minichannels have been developed and installed in a 2 kW cooling capacity refrigeration system at the University of Illinois, Urbana-Champaign, by Hrnjak and Hoehne (2004). The authors state that the use of microchannels tubes reduced the total system charge from approximately 0.2 kg in conventional systems to less than 0.13 kg.

An example of low propane charge equipment using brazed plate heat exchangers is a reversible water-to-water heat pump developed at the University of Valencia (UPV). A charge optimization study has been performed by Corberán and Martínez (2008a) showing that, depending on the unit design, the specific cooling capacities range from 25 to 33 W/g of propane.

In this Section of the thesis the design and the experimental performance of the heat pump realized installing the minichannel heat exchanger described in Chapter 2, together with conventional BPHEs, will be described. The heat pump is devoted to laboratory tests, and has been designed and realized in collaboration between the University of Padova and Hiref SpA in the framework of the European project SHERHPA (Sustainable Heat and Energy Research for Heat Pump Applications) dealing with the development of heat pumps in compliance with the future environmental regulations.

3.2 Propane as refrigerant

A short overview about the characteristics of propane as refrigerant is proposed in this Section. In particular, since propane is very favourable as a direct drop-in substitute to the HCFC R22, which has been widely used in the past by the HVAC industry, these two fluids are compared.

Propane with purity technical grade 99.5% (also called 2.5) is commonly suggested for refrigeration applications (Bitzer, 1997, Danfoss, 2000).

As one can see in the graph in Fig. 3.2, R22 and R290 display very similar pressure versus temperature saturation curves.

Some properties of the two fluids are given in Table 3.1. It is important to notice that the heat of vaporization of R290 is around double the heat of vaporization of R22; however, the density of propane at compressor suction is around half the density of R22. As a result, the two fluids display very similar volumetric capacities, therefore from a technical point of view, if neglecting safety issues, R290 could be used in a unit designed for R22 without changing the compressor.

The density of the liquid propane is around half the density of R22, while around the same flow cross sections are required by the two fluids in the pipes and heat exchangers and similar heat transfer coefficients are obtained, therefore the potential for minimum refrigerant charge is very good.

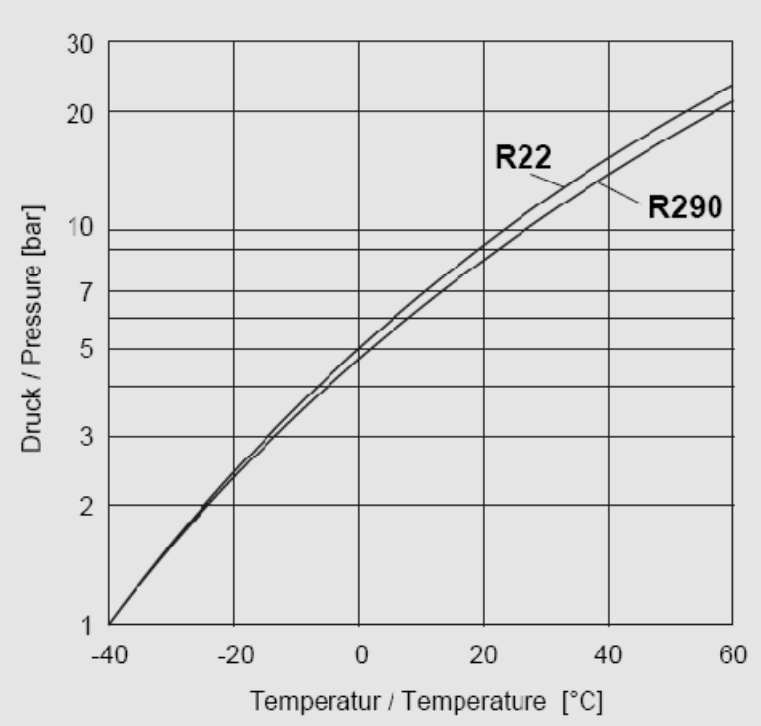

Fig. 3.2. Comparison of saturation pressure versus temperature curves of R22 and R290. From Bitzer Technical Documentation KT-660-2, 1997.

Table 3.1. Properties of propane in comparison to R22.

Refrigerant	Propane (R290)	R22
Formula	C_3H_8	CHF_2Cl
Ozone depletion potential ($ODP_{R11} = 1$)	0	0.05
Global warming potential ($GWP_{100yrs\text{-}CO2} = 1$)	3	1600
Toxicity AEL(TVL)	1000 ppm	1000 ppm
Flammability Vol. %	1.7 – 10.9	-
Critical temperature	96.7°C	96.1°C
Critical pressure	42.6 bar	49.9 bar
Molecular weight	44.1	86.5
Heat of vaporization (T= 40°C)	307.1 kJ/kg	166.6 kJ/kg
Heat of vaporization (T= 0°C)	374.9 kJ/kg	205.1 kJ/kg
Liquid density (T= 40°C)	467 kg/ m^3	1129 kg/ m^3
Vapour density (T= 0°C)	10.35 kg/ m^3	21.23 kg/ m^3
Isentropic compression index	1.14	1.18

Regarding material compatibility, propane is non critical when used with metals and elastomers normally used with R22. Zinc and alloys with magnesium over 2% should be avoided. Data about compatibility of R22 and R290 with plastic materials is given in Table 3.2.

In Fig. 3.3, thermodynamical parameters of R22 and R290 are compared at the same value of refrigeration capacity. The gas volumetric flow at the suction and discharge conditions is around 10% higher when using R290, while the liquid volumetric flow is around 30~40% higher. Both the liquid density and the vapour density are lower for propane. It can be said, as a general rough rule, that identical liquid lines can be used for the two fluids, while vapour suction and discharge lines can be reduced with propane (Bitzer, 1997).

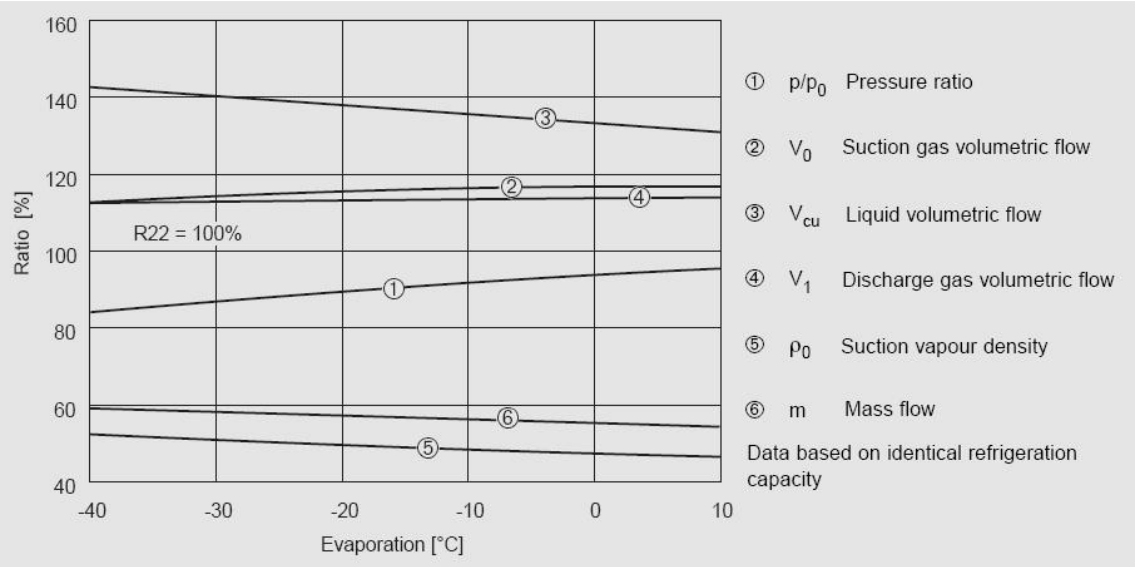

Fig. 3.3. Comparison of thermodynamical parameters between R22 and R290. From Bitzer Technical Documentation KT-660-2, 1997.

In Section 2.4.2 (Table 2.3) it has already been shown that the saturation temperature drop, at fixed heating and cooling capacity, is expected to be higher when using R22 in the minichannel evaporator.

An important property of propane is the very high solubility with conventional lubricant and ester oils. Even if this property is favourable for a good circulation of the oil in the system, it can lead to a considerable decrease of the oil viscosity in the compressor, especially at low oil temperature and high suction pressure. For this reason, the use of lubricant oil with a higher basic viscosity is suggested.

Since the solubility of propane in the oil decreases by increasing the temperature, high values of superheating for the suction vapour can provide some benefits. The manufacturer of the compressor used in the heat pump presented in this thesis suggests at least 20 K superheating when using mineral oil (Bitzer, 1997).

The compressor discharge temperature is extremely low for propane because of the low isentropic compression index (see Table 3.1). This could also be a problem for the high solubility of propane in the oil at low pressure ratios or low vapour superheating. The manufacturer of the compressor used in the heat pump suggests a discharge gas temperature at least 20 K above the condensation temperature (Bitzer, 1997).

The use of internal heat exchanger can be useful to help avoiding problems due to the solubility of R290 in the oil. Furthermore, by a theoretical point of view, it is generally found that for propane, as well as for most hydrocarbons, energy efficiency benefits can be achieved by using an internal heat exchanger. At 0°C evaporating temperature and 40°C condensing temperature, for example, the COP in cooling mode when using R290 as working fluid should increase by 0.09% per degree superheat assuming isentropic compression.

Finally, it must be noticed that, as compared to R22, a very big volume change is given by the evaporation of propane. Because of this, there is a strong degassing effect in the crankcase and lubricating spaces of the compressor, which leads to high foaming. Therefore, generously sized crankcase heaters are required.

A wider discussion about the benefits given by the internal heat exchanger and the solubility of propane in the oil is reported in Section 3.6.3 and Section 3.6.7.

Table 3.2. Compatibility of R22 and R290 with plastic materials. OK = good compatibility, N = normal compatibility, B = bad compatibility). From Zambolin (2007).

		R290	R22
Akrylnitrile butadiene styrene	ABS	OK	B
Cellulose acetato butyrate	CAB	N	
Epoxy	EP	OK	OK
Ethyltetrafluoethylene	ETFE	OK	N
Poiyamide	PA	OK	OK
Polycarbonate	PC	N	OK
Polyethylene	PE	OK	N
Polyethylene terefialate	PETP	OK	OK
Phenoi formaldehyde	PF	OK	OK
Polyethylene metacrylate	PMMA	N	B
Polyoxymethylene / Acetal	POM	OK	N
Polypropene (RC270)	PP	OK	N
Polyphenyloxide	PPO	B	
Polyphenylsulphide	PPS	OK	N
Polystyrene	PS	N	B
Polytetrafluoroethylene	PTFE	OK	N
Polyurethane	PUR	N	
Polyvinyl chioride	PVC	OK	N
Polyvinylfluoride	PVDF	OK	N
Polysulfone	SUF		B
Unsaturated Polyester	UP	OK	OK

3.3 Design of the heat pump

Since the safety restrictions due to the propane flammability have been considered a major design constraint, the heat pump has been planned to work situated outside in open air on the roof of the Fisica Tecnica department building. The main design goal is to achieve low propane charge and high energy efficiency at the same time.

It has been chosen to design a water-to-water heat pump, because an indirect system with a secondary fluid both at the cold and hot side is the best choice to achieve the reduction of the propane side volume.

Roof top chillers and heat pumps using a hydronic system to distribute chilled or hot water in the building are an ideal solution to the safety problem and they also allow to fulfil most of the normative and legislation.

Furthermore, by using an indirect system, equipment could be easily inserted in a geothermal system, using the ground as heat source both during the winter and the summer. The interest on reversible geothermal heat pumps, in fact, is nowadays increasing for the reason that, despite the high investment cost, they are the ideal solution to meet challenges such as environmental pollution minimization and economic and energy saving.

The set-up of the experimental facility is shown in Fig. 3.5: on the right side the propane heat pump with five heat exchangers is depicted, on the left side the hot and cold water loops are shown.

It could be possible to install a dry cooler at the cold water loop side, in such a way that an air-to-water heat pump can be obtained maintaining the benefits in terms of charge reduction given by the adoption of a water-to-water system. It should be considered, however, that the additional water loop between propane and air introduces an extra temperature difference, which reduces the global efficiency of the heat pump, when compared to direct air-to-water equipments.

Beside the possible refrigerant piping reduction, the adoption of an indirect system is useful to minimize the propane charge also because the evaporator and condenser size can be reduced when compared to air-R290 exchangers by exploiting the more favourable heat transfer properties of water as compared to air.

The present heat pump has been designed as reversible on the water side, instead that on the propane side, so that additional by-pass refrigerant piping and valves are not required and the minichannels S&T condenser and the evaporator could be optimized independently. It can be noticed that, in the case of the minichannel heat exchangers, the internal volume of the condenser is around half the internal volume of the evaporator, therefore if designing the heat pump as reversible on propane side, the condenser internal volume would be double the required volume.

The two hydraulic circuits shown in Fig. 3.5 for the hot and cold water allow to independently fix the mass flow rate and inlet water temperature both at the condenser and at the evaporator, in such a way that tests can be performed at the desired operating conditions. By switching the manual on/off valves water can flow through one of the two available condensers and evaporators, depending on which heat pump configuration is being tested. The water mass flow rate is measured by a Coriolis effect mass flow meter on the cold side and by a electromagnetic flow meter on the hot water side, while the inlet and outlet pressure and temperature at the evaporators and condensers, as well as the pressure drop, are measured by means of T-type thermocouples

(copper/constantan) using an ice-point and pressure transducers. Reservoirs are present at both hydraulic circuits in such a way to provide a sufficient thermal inertia for a stable adjustment of the cold and hot water temperature.

Since the heating and cooling capacities are very high (the heating capacity is about 100 kW), a heat exchanger is installed between the two hydraulic circuits and the cooling capacity is dissipated by the hot water exiting from the condenser; an automatic valve controlled by the cold water reservoir temperature adjusts the flow rate in the dissipator in such a way to get a stable secondary fluid inlet temperature at the evaporator.

The part of the heating capacity not dissipated by the cold water circuit can be computed by subtracting the cooling power from the heating one and is equal to the electrical power supplied to the compressor (i.e. about 30 kW at nominal operating conditions). A thermal power slightly higher than the required is dissipated by ground water whose flow rate through the heat exchanger shown in Fig. 3.5 is manually adjusted by a control valve; then the hot water temperature in the reservoir is adjusted by a couple of electric heaters with a PID controller in such a way that a more stable control can be achieved.

The heat pump facility is shown in Fig. 3.6. The present unit has been designed for testing applications, and five heat exchangers have been installed in it: two commercial brazed plate heat exchangers (BPHEs) are installed as the evaporator and the condenser, while low charge prototypes shell-and-tube (S&T) heat exchangers using minichannels are used as the condenser, the evaporator and the internal heat exchanger (IHX).

By switching the manual on/off valves 8 different testing configurations can be obtained. Since BPHEs are the current industrial benchmark to achieve internal volume minimization, the configuration with BPHEs both at the condenser and at the evaporator is the reference one to obtain experimental data to easily quantify the advantages of operating the heat pump using the S&T minichannel heat exchangers, with regard both to performance and refrigerant charge.

Furthermore, both configurations with and without internal heat exchanger can be tested at the same evaporation and condensation temperatures, in such a way that the influence on the system performance, as well as on the propane charge required by the heat pump, can be experimentally measured.

A semi-hermetic reciprocating compressor by Bitzer designed to operate with propane (model 6G-40.2-40P) is used in the present prototype; the compressor has 6 cylinders (with 75 mm bore and 55 mm stroke) with the possibility to switch off a pair of them to reduce the capacity to 66%.

As shown in Fig. 3.6, a 2 L liquid receiver has been installed at the propane liquid line downstream the compressor outlet. This device helps to reach faster the stable operation of the heat pump during the experimental tests. An indicator of the liquid level in the receiver has also been installed to get an immediate control of the active charge during the tests. Experimental tests of the different heat pump configurations have been performed keeping the same level inside the receiver, therefore maintaining analogous refrigerant charging conditions.

Since the two-phase refrigerant distribution can have a very strong influence on the evaporator performance, two mechanical thermostatic valves have been installed just in front of the two evaporators inlets, in order to avoid the presence of elbows in between the valves and the heat exchangers. In this way, homogenous testing conditions

and good propane distribution are ensured for both the BPHE and S&T minichannel evaporators.

As shown in Fig. 3.5, the pressure and temperature at inlet and outlet of all the heat exchangers, the compressor and the expansion valves are measured by means of pressure transducers and T-type thermocouples. In addition, the electric power supplied to the compressor is measured by an electrical power analyzer, while the propane mass flow rate is measured by a Coriolis effect mass flow meter.

Since high pressure drop occurs when propane flows through the Coriolis mass flow meter, this instrument, as well as the dehydrating filter, has been installed in the liquid line bypass downstream the internal heat exchanger, to avoid the formation of flash vapour before entering the expansion valve when the internal heat exchanger is not used and quasi saturated liquid propane is expected to exit from the condenser. When this flow meter is not used, the refrigerant mass flow rate is computed by the energy balance on the water side both at the condenser and the evaporator; then, the average value of mass flow rate is taken.

The Fig. 3.4 shows the actual layout of the heat pump.

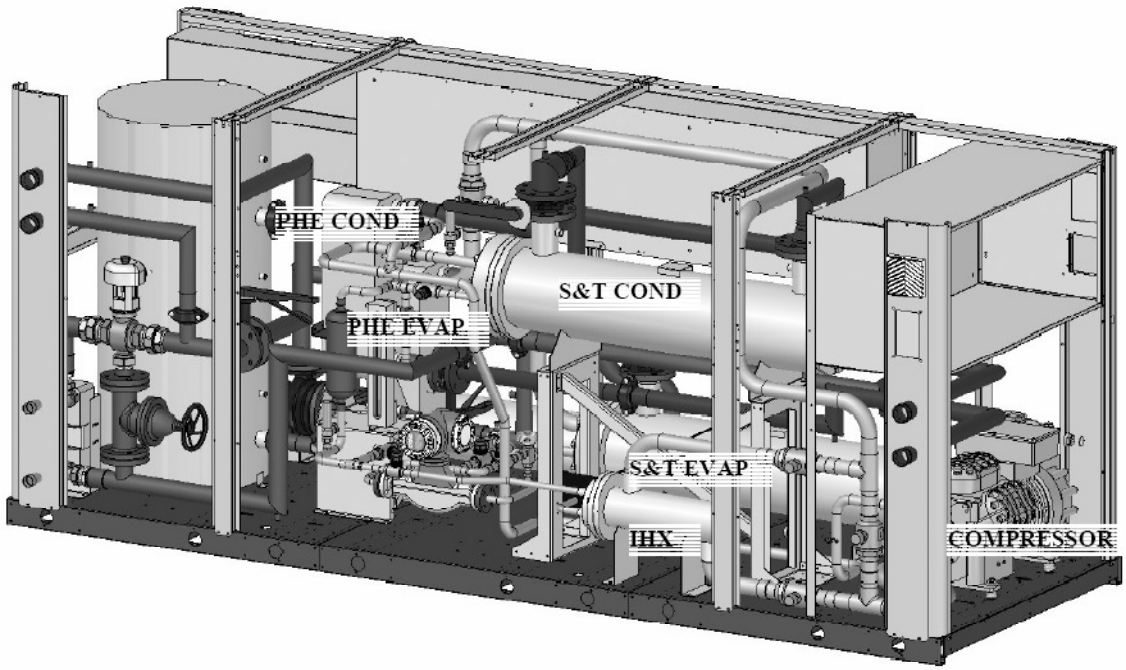

Fig. 3.4. Heat pump layout.

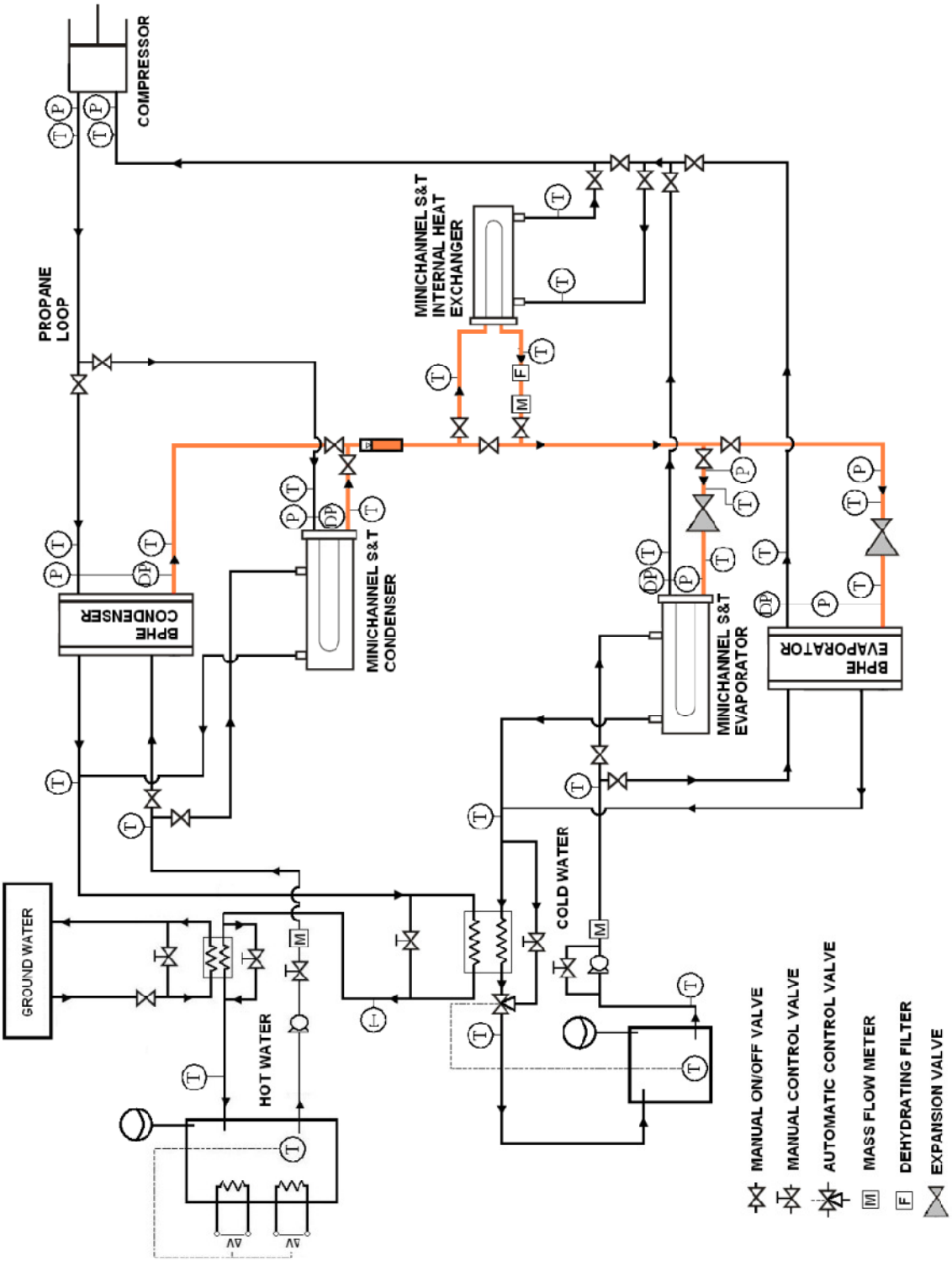

Fig. 3.5. Test rig.

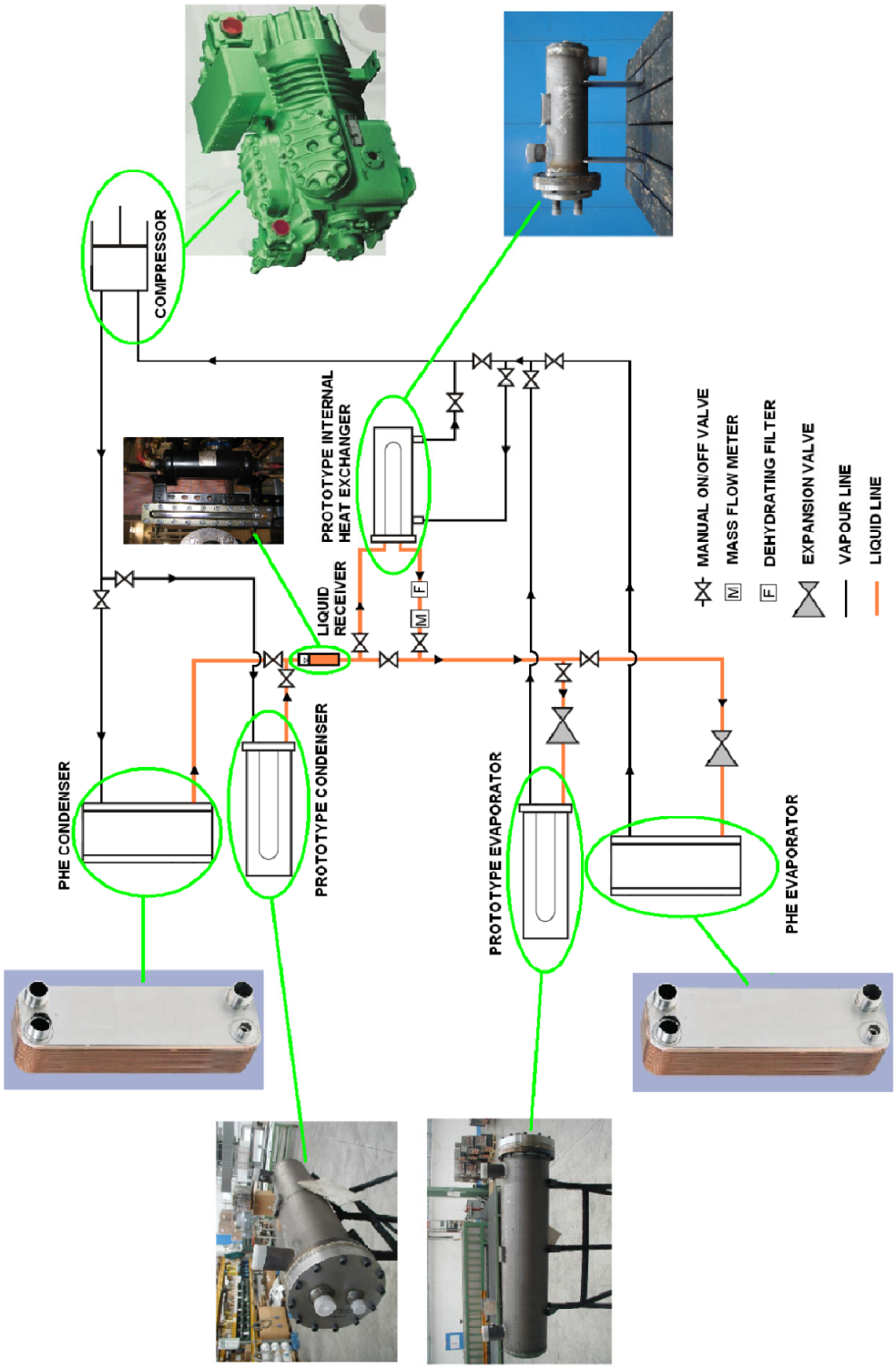

Fig. 3.6. Heat pump facility.

3.4 Safety considerations

Two environments with different levels of risk have been identified when analyzing the safety of the present system: the environment inside the piping and all the heat pump components and the external environment.

When considering a mixture of a flammable fluid and air, burning or explosion can occur upon contact with a source of ignition in the case that the mixture concentration is between the lower explosive limit (LEL) and the upper explosive limit (UEL). Furthermore, a self-sustained combustion in the absence of spark of flame can be obtained if the temperature exceeds the auto-ignition limit (AIL).

Experimental values of volumetric UEL and AIT by (Norman *et al.* 2006) obtained considering rich propane-air mixtures at different pressures and temperatures are reported in Fig. 3.7.

The maximum refrigerant temperature in the thermodynamic cycle is reached at the compressor outlet. At 50°C saturation temperature in the condenser, when using the internal heat exchanger, the compressor discharge temperature is about 90°C, while the auto-ignition limit (AIL) is far above 200°C, therefore the auto-ignition hazard can be considered extremely low. On the other hand, sparks could occur inside the compressor at the electric motor which is cooled by fresh refrigerant vapour at the suction pressure; therefore the possibility of the presence of air inside the piping leading to a propane-air mixture concentration lower than the UEL must be evaluated.

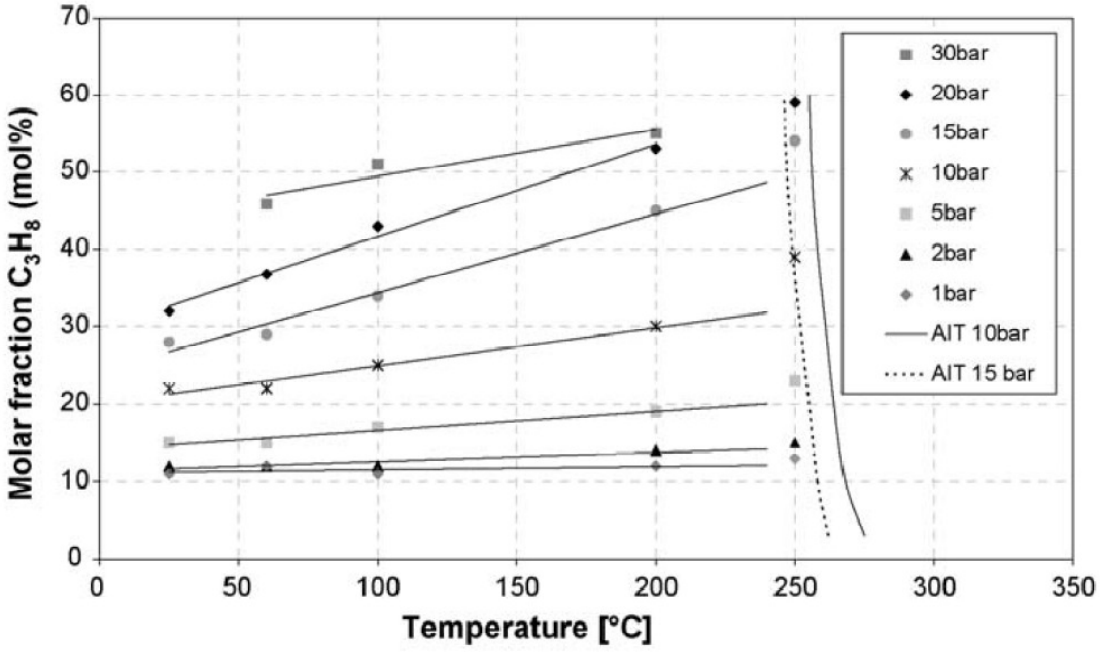

Fig. 3.7. Upper explosion limit (UEL) and auto-ignition temperature (AIT) of propane-air mixture (Norman *et al.* 2006).

The highest possible UEL (which corresponds to the worst possible condition) can be obtained considering 100°C system temperature and 24 bar system pressure, corresponding to the setting of the pressure relief valve; in this case the UEL is higher than 40% by volume.

Since the evaporation pressure, which is the lowest pressure in the system is always above the atmospheric pressure (i.e. around 5 bar), no atmospheric air can enter in the piping. However, some air could be present in the piping if the heat pump was not properly filled with the refrigerant. Nevertheless, even if the whole volume of the facility was filled with air at atmospheric pressure, it must be considered that, at 5 bar pressure, air density reduces to about a fifth when compared to atmospheric pressure, therefore it would be impossible to have volumetric propane-air concentrations below the UEL and the mixture will always be too rich to burn.

With regard to the external environment, the hazard of rare propane leakages from the compressor or the flanges connections exists. Referring to ATEX 94/9/CE directive, this environment has been classified in zone 2.

At atmospheric pressure, the LEL of a propane-air mixture is about 2.1% in volume, while the UEL is 9.5% by volume; therefore propane concentration above 2% must be avoided.

The Coriolis mass flow meter and some of the pressure transducers are EX-rated instruments. The pressure transducers which are not ex-rated have been installed outside the heat pump casing in an upper position.

Two IP44 electrical panels are present in the unit, one containing the heat pump microprocessor and the other containing some measurement instrumentation (i.e. data acquisition system, ice point for thermocouples and electrical power analyzer). These panels are kept in overpressure by two small fans that suck external air and are always kept on by a buffer 12 VDC battery in such a way that, even in case of propane leakage from the facility, the refrigerant cannot enter into the electrical panels. Fig. 3.8 shows a picture of the electrical panel for the instrumentation open.

Three propane sensors in compliance with EN 50194 and always kept on by the buffer battery have been installed nearby the compressor and inside both electrical panels. These sensors detect from 0 to 20% of the LEL and different safety levels have been considered depending on the concentration measured by the sensors.

When a level from 0 to 20% of the LEL is detected (i.e. safety level 1), the system switches off keeping the microprocessor operating and a signal of alarm is produced. Furthermore, the two fans shown in Fig. 3.8 are switched on in order to disperse the concentration to the environment external to the equipment case. The two fans elaborate double the required air flow computed according to CEI EN 60079-10.

When a propane concentration above 20% of LEL is detected (i.e. safety level 2) or sensor fault is detected by auto-diagnosis (i.e. safety level 3), the microprocessor is also switched off, while the fans are kept operating as well as the sensors and the electric panel small fans fed by the buffer battery.

Nevertheless, it must be remembered that the system has been planned to work situated outside in open air on the roof of the building and keeping the system casing partly open; this provides a reasonable level of intrinsic safety.

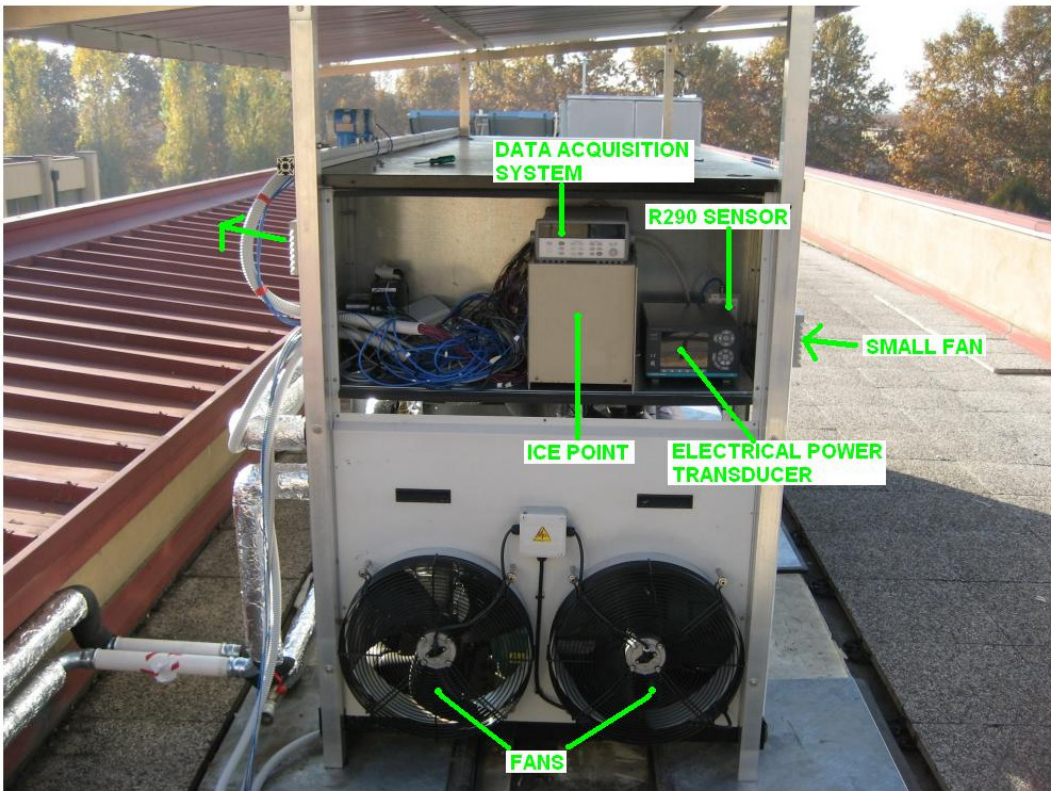

Fig. 3.8. View on the heat pump with the electrical panel for instrumentation and fans.

3.5 Instrumentation

The test facility wad supplied with an electronic data acquisition system connected to a computer. This system included 25 T-type thermocouples connected to an ice-point, 5 relative pressure transducers, 2 differential pressure transducers, 2 Coriolis mass flow meters, 1 magnetic flow meter and 1 electric power analyser. The position of the instrumentation in the test rig is shown in Fig. 3.5.

The electric power analyser was directly connected by RS232 to the computer, while the signals from the other measuring instruments were read by an Agilent 3490A data logger. Measurement data from the data logger was monitored and stored in the computer by means of the software National Instruments LabVIEW.

The uncertainty in the measurements reported in the present thesis has been computed according to the ISO "Guide to the Expression of Uncertainty in Measurements" (1995). The errors can occur when performing experiments can be categorised as systematic errors (i.e. "type B" errors according to ISO, 1995) and random errors (i.e. "type A" errors). In this Section, "type B" errors of the instrumentation used are discussed and reported.

The uncertainty in the measurements of the COP reported in this thesis in the Section 3.6 has been computed as a combination of uncertainty "type B" and uncertainty "type A".

3.5.1 Temperature measurements

Sixteen T-type thermocouples (copper-constantan) are present along the propane line and nine T-type thermocouples are present along the hot and cold waters lines. An ice point, model KAYE K17-50C, is used and the voltage signal is read by the Agilent 3490A data logger.

The equation given in Nicholas and White (1994) was used as reference for the voltage-temperature characteristic of T-type thermocouples. Thermocouples were then calibrated in-situ, by comparing the values given by the thermocouple to the values given by a high-precision PT-100 (measurement accuracy 0.002K). Calibration was performed at different temperatures, ranging from 0°C up to 80°C and a single corrected voltage-temperature equation was used for all thermocouples.

The standard deviation among the measurements given by the thermocouples and the average deviation from the temperature given by the PT-100 after calibration are reported in Table 3.3 at different temperatures.

The "type B" measurement uncertainty for the whole measurement chain for the temperature was considered ± 0.1K with 95% confidence level.

Table 3.3. Standard deviation among the thermocouples measurements and average error after calibration.

Temperature [°C]	Average error [K]	Standard deviation [K]
0.5	-0.01	0.04
12.2	0.02	0.02
18.0	0.02	0.02
42.9	0.00	0.03
57.6	0.03	0.04
71.8	0.08	0.06
80.7	0.06	0.06

3.5.2 Pressure measurements

A number of pressure transducers are used along the propane lines. Steel pressure lines with 1/8" diameter are used. A couple of relative pressure transducers by Endress-Hauser (model Cerabar S PMP 71) are used to read the pressure at the suction and discharge line of the compressor. Two differential pressure transducers by Endress-Hauser (model Deltabar S PMD 75) are used to measure the pressure drop at the condenser and at the evaporator. Finally, relative pressure transducers by Keller (model 33 X Ei) are used to measure the pressure at the condenser inlet, at the evaporator outlet and upflow the lamination valve. The transducers by Keller are ATEX approved for use in hazardous areas where there is a high risk of explosion, while the other transducers are not ATEX approved. The pressure transducers which are not EX-rated have been installed outside the heat pump casing in an upper position.

The voltage supply required by all the pressure transducers is 15 V. The analog signal output of 4..20 mA is directly read by the data logger in the case of the four Endress-Hauser transducers. In the case of the other transducers, the signal is first converted to a 4..20 mV signal by means of a 1 Ω calibrated electrical resistance.

The measurement range and the "type B" measurement uncertainty, with 68% confidence level, are reported in Table 3.4. Uncertainty has been computed according to data provided by the manufacturers, taking into account the long term stability of the instrumentation and the time passed since the manufacturer calibration. Since the confidence level was not given for the uncertainty data reported in the calibration certificates, a rectangular distribution was assumed and the standard deviation (i.e. the uncertainty with 68% confidence level) was obtained by dividing the values given by the manufacturers by $3^{1/2}$.

3.5.3 Flow rate measurements

A Coriolis mass flow meter by Endress-Hauser (model Promass F 80 DN 8) is used to measure the propane flow rate. This instrument has been installed in the liquid line bypass downstream the internal heat exchanger, in order to avoid the formation of flash vapour before entering the expansion valve when the internal heat exchanger is not

used. When this flow meter is not used, the refrigerant mass flow rate is computed by the energy balance on the water side.

Another Coriolis mass flow meter (Siemens Sitrans MASSFLO F C 2100 DI 25 with MASS 6000 transmitter) is used to measure the cold water flow rate, while a magnetic flow meter (Siemens Sitrans MAGFLO 1100 DI 40 with MAG 6000 transmitter) is used to measure the cold water flow rate.

The voltage supply required by the flow meters is 220 V. The analog signal output of 4..20 mA is converted to a 4..20 mV signal by means of a 1 Ω shunt and then read by the Agilent 3490A data logger.

The "type B" measurement uncertainty, with 68% confidence level, is reported in Table 3.4. Uncertainty has been computed according to data provided by the manufacturers. When the confidence level was not given for the uncertainty data reported in the calibration certificates, a rectangular distribution was assumed.

It must be noticed that, in the case of the Coriolis mass flow meter for the propane flow rate, a measurement "set span" of 10 kg/s was wrongly fixed for the set of data reported in this thesis, while the maximum propane flow rate is around 0.3 kg/s. As a result, the signal given by the instrument was always very close to the bottom limit 4 mA and the output resolution error was large. With a correct value of the "set span" the measurement error, with 68% confidence level, would be reduced from ± 0.0018 kg/s down to around ± 0.0003 kg/s.

3.5.4 Electric power measurement

The electrical power supplied to the compressor was measured by means of a LEM NORMA 4000 (with power phase PP30) power analyser. Since the upper measurement limit of the instrument for current is 10 A, while the current to be measured is around 80 A, three current transformer, model Zelisko KLW 3/3, with ratio 100:5 and accuracy class 0.2 were used. The voltage was directly measured by the power analyser.

The electric power analyser was directly connected by RS232 to the computer and a software provider by the seller of the instrument was used to monitor and store the measurement data.

The "type B" measurement uncertainty of the electrical power, with 68% confidence level, is reported in Table 3.4. Uncertainty has been computed according to data provided by the manufacturers, taking into account also the uncertainty given by the current transformers.

3.5.5 Data logger and shunts

When estimating the measurement uncertainty, the whole "measurement chain" must be considered. Uncertainties reported in Table 3.4 refer to the output signal from instrumentation.

Temperature, pressure and flow rate measurements, however, are measured by means of the Agilent 3490A data logger and, in most cases, the 4..20 mA signal is converted into a 4..20 mV signal by means of 1 Ω shunts. The uncertainty given by the data logger and the electrical resistance must be estimated and combined with the

uncertainty given in Table 3.4 in order to compute the total type B" measurement uncertainty.

The uncertainty of Agilent 3490A for current measurements, with range 100 mA, is ±0.050% v.m. ±0.005% range (where v.m is the value measured), while for voltage measurements, with range 100mV, it is ± 0.0050% v.m. ±0.0040% range. The uncertainty in the value of the resistance for the 1 Ω shunts (model Eurohm E-26-0-2-3 1 Ω) is ±0.05%.

These uncertainties have always been considered in the computation of the uncertainty for the COP measurements reported in the present thesis; however, it was found that the influence of the data logger and the shunts on the total uncertainty is negligible. It actually had an influence only on the measurement of the propane mass flow rate, but this was due only to the wrong setting of the set span of the instrument, as discussed in Section 3.5.3.

Table 3.4. Instrumentation "type B" measurement uncertainty (68% confidence level).

Instrument	Range	Uncertainty
Compressor suction pressure transducer (PMP71)	40 bar	± 0.035 bar
Compressor discharge pressure transducer (PMP71)	100 bar	± 0.173 bar
Condenser differential pressure transducer (PMD75)	0.5 bar	± 0.00043 bar
Evaporator differential pressure transducer (PMD75)	3 bar	± 0.0035 bar
Condenser inlet pressure transducer (33 X Ei)	30 bar	± 0.031 bar
Upflow of lamination valve pressure transducer (33 X Ei)	30 bar	± 0.031 bar
Evaporator outlet pressure transducer (33 X Ei)	10 bar	± 0.010 bar
Propane mass flow meter (Promass F 80)	0.556 kg/s	± 0.0018 kg/s
Hot water mass flow meter (MAGFLO 1100)	13.9 L/s	± 0.0173 L/s
Cold water mass flow meter (MASSFLO FC 2100)	6.95 kg/s	± 0.0049 kg/s
Electric power analyzer (LEM NORMA 4000)		±0.35% of reading
T-type thermocouples + ice point (KAYE K17-50C)		±0.05 K

3.6 Experimental results

All tests have been carried out using the brazed plate heat exchanger as the evaporator. Four different configurations have been tested:

I. plate evaporator + plate condenser (without IHX),
II. plate evaporator + minichannel condenser (without IHX),
III. plate evaporator + plate condenser + IHX,
IV. plate evaporator + minichannel condenser + IHX.

These four configurations are compared in order to quantify the influence of the low charge condenser and the internal heat exchanger on heating and cooling capacities, energy performance and total required propane charge.

Experimental tests have been carried out at different temperatures of the hot water provided by the condenser (i.e. 35°C, 40°C and 45°C) and different temperatures of the cold water at the evaporator inlet (i.e. 10°C and 12°C). The water temperature rise in the condenser, as well as the water temperature drop in the evaporator, was 5 K for all the tested conditions reported in this thesis.

The energy performance for the four configurations has been compared against the criteria for the European Community ecological award of the eco-label.

Experimental data about the compressor global, isentropic and volumetric efficiency are also reported.

For the configurations using the minichannel condenser (i.e. configuration II and configuration IV), tests have been carried out also at reduced compressor capacity (i.e. 66%).

The uncertainty in the measurement of the equipment COP values reported in this thesis has been computed according to the ISO “Guide to the Expression of Uncertainty in Measurements” (1995).

3.6.1 Data reduction and check of measurements

The experimental tests have been run according to the European Standard EN 14511 (2004). The desired water temperatures at the condenser and evaporator were set and then the behaviour of the heat pump was monitored. Once a stable operation of the unit was obtained, data was recorded every 5 seconds for at least 35 minutes time. According to the European Standard EN 14511 (2004), during this period, the maximum allowed deviation of the average temperature of the water from the set value is ± 0.2 K at the inlet and ± 0.3 K at the outlet; furthermore, the maximum deviation for every single measurement is ± 0.5 K at the inlet and ± 0.6 K at the outlet.

The average values of the measurements over the stable operation period were used for data reduction. The standard deviation of the measurements was used in order to compute the "type A" uncertainty measurement according to the ISO "Guide to the Expression of Uncertainty in Measurements" (1995); then "type A" and "type B" errors were combined. It was found, in general, that the influence of "type B" errors on the total errors was much bigger than the influence of "type A" ones.

The test rig with the position of all instrumentation is depicted in Fig. 3.5.

Water flow rate and water inlet and outlet temperatures were measured both at the condenser and at the evaporator. These measurements were used to compute the heating and cooling capacities of the heat pump.

The power consumption of the compressor is measured by an electric power analyser. These measurements, along with the computation of the heating and cooling capacities, were used to compute the COP. The power consumption of the circulating pumps has not been measured, therefore only the COP of the equipment is reported. However, an estimation of the power consumption of the circulating pumps is provided in Section 3.6.4.

A global energy balance has been performed in order to check the measurements for every test run. Results are reported in Fig. 3.9 along with the total uncertainty of the balance with 95% confidence level. As one can see, the global energy imbalance is very small if compared to the around 100 kW heating capacity, and it is always smaller than the measurement uncertainty.

Another check can be performed regarding the measurements at the evaporator inlet. At this point of the propane line, the temperature of the fluid is measured by a thermocouple. Besides, the evaporator outlet pressure and the pressure drop in this heat exchanger are measured by two transducers, therefore the value of the pressure at the inlet can be computed. The saturation temperature at the inlet corresponding to the computed value of pressure is compared against the thermocouple measurements in Fig. 3.10. The average error is 0.03 K and the standard deviation is 0.08 K.

The propane mass flow rate is directly measured by a Coriolis mass flow meter when the configurations with internal heat exchanger are tested, while it can be obtained from an energy balance at the condenser and at the evaporator in the other cases. Propane temperature at the inlet and outlet of the condenser, propane pressure at inlet and pressure drop are measured. Therefore, the inlet and outlet enthalpy can be computed, and the propane flow rate can be obtained from an energy balance, given the heating capacity measured on water side.

Regarding the evaporator, temperature and pressure are measured upflow the expansion valve in order to compute the propane enthalpy at the evaporator inlet; then,

outlet enthalpy is obtained from pressure and temperature measurements at the evaporator outlet, where superheated vapour is present. Propane flow rate can be finally obtained from an energy balance, given the cooling capacity measured on water side.

When the mass flow rate was not directly measurement, the average value of the mass flow rate given by these two energy balances was used.

The two values of propane mass flow rate, computed from the energy balance at the condenser and from the energy balance at the evaporator, are compared in Fig. 3.11 for all the test runs. The average difference is 0.4 %, with standard deviation 2 %.

For the cases referring to the testing configurations with internal heat exchangers, the values of mass flow rate computed from the two energy balances are compared against the Coriolis flow meter measurements in Fig. 3.12. As one can see, the mass flow rate computed from the energy balance is in general underestimated. The average deviation is 3% for the energy balance at the condenser and 1% for the energy balance at the evaporator.

The last measurement check reported is the energy balance for the internal heat exchanger. Temperature is measured at inlet and outlet of both tubes and shell sides, and the inlet and outlet enthalpies and the heat transfer rate at the two sides can be computed, assuming that subcooled liquid is present inside the tubes and superheated vapour is flowing on shell side. The difference between the two computed heat flow rates is plotted versus the measured subcooling at the condenser outlet in Fig. 3.13.

In all the test runs performed to compare the different configurations of the heat pump, the amount of refrigerant was charged in the facility in order to have around half of the receiver downstream the condenser outlet filled with liquid. This was checked by looking at the indicator of the liquid level. It was therefore assumed that saturated liquid was present at the outlet of the condenser. The temperature measured by the thermocouple was around 0.2 K lower than the saturation temperature corresponding to the pressure.

At these conditions, the computed heat flow rate on the liquid side of the internal heat exchanger was always lower than the heat flow rate on the vapour side. This imbalance was up to around 3~4 kW, corresponding to around 30 % of the heat flow rate. Some tests were run, only for the configuration with the minichannel condenser, by changing the setting of the expansion valve, in order to increase the superheating at the evaporator, this way causing a migration of the propane charge towards the condenser and therefore increasing the subcooling at the condenser outlet. Results of these tests are reported in Fig. 3.13. As one can see, by increasing the subcooling measured at the condenser outlet the energy balance improves, and when the measured subcooling is larger than around 1.4 K no imbalance is observed. These results are interesting, since they show that not complete condensation was obtained at the condenser outlet in most of the test runs, even if the temperature measured by the thermocouple was lower than the saturation temperature corresponding to the measured pressure, and a liquid level was observed in the indicator of the receiver. This means that at the outlet of some of the tubes of the minichannel condenser complete condensation with some degree of subcooling was obtained, while at the outlet of some other tubes the complete condensation was not obtained. The reason of this is probably due to an uneven distribution of the heat transfer coefficient of water side, more than to a problem of distribution of the superheated vapour at the inlet of the condenser.

A mixture of quasi saturated vapour and subcooled liquid not at thermodynamical equilibrium was present at the condenser outlet, and at the inlet of the internal heat

exchangers some bubbles of vapour were still present in the liquid line. The inlet enthalpy of the liquid computed from the temperature measurement assuming that the refrigerant was subcooled was therefore underpredicted, this explaining the imbalance in the calculations.

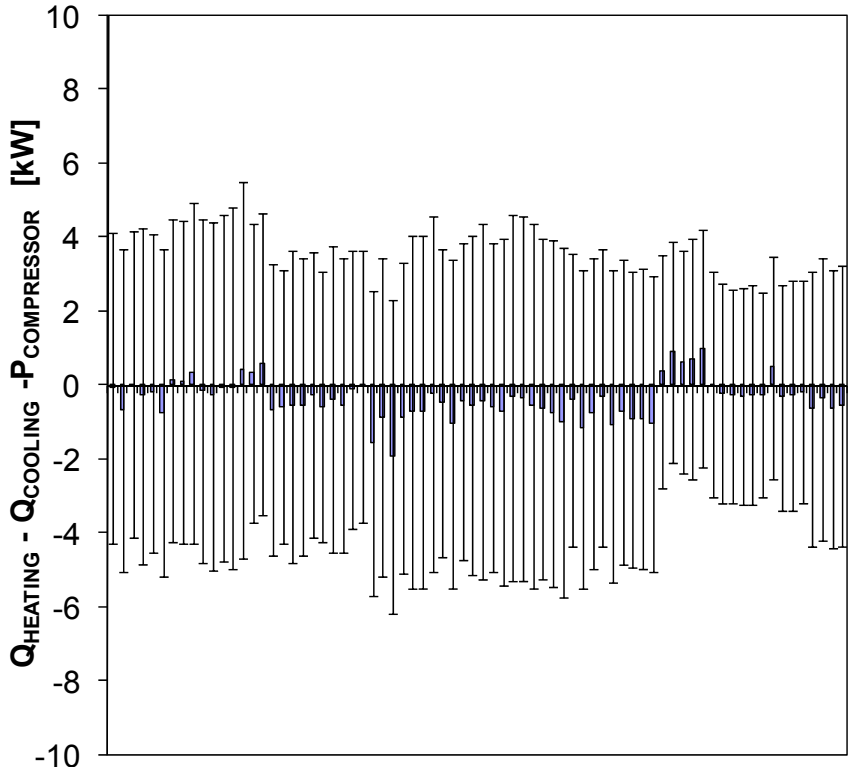

Fig. 3.9. Global energy balance check.

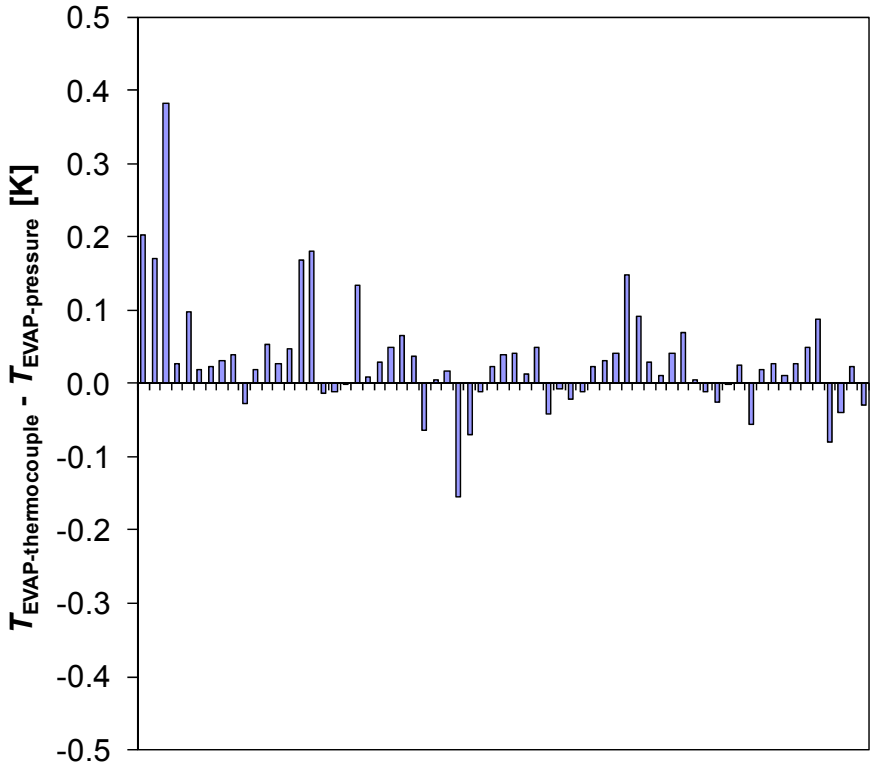

Fig. 3.10. Comparison between temperature measured at the evaporator inlet and saturation temperature corresponding to the pressure.

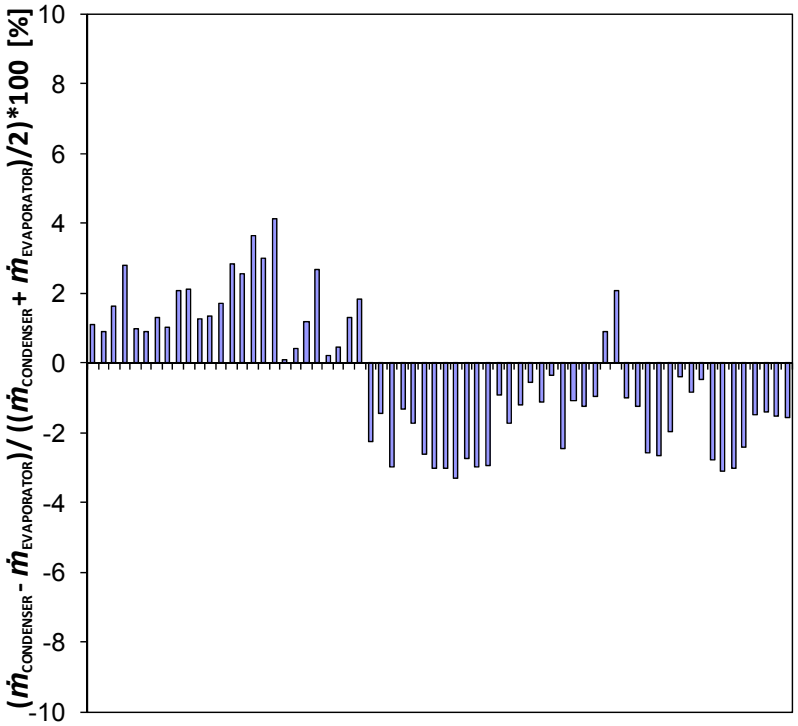

Fig. 3.11. Comparison between propane mass flow rate computed from energy balance at the condenser and mass flow rate computed from energy balance at the evaporator.

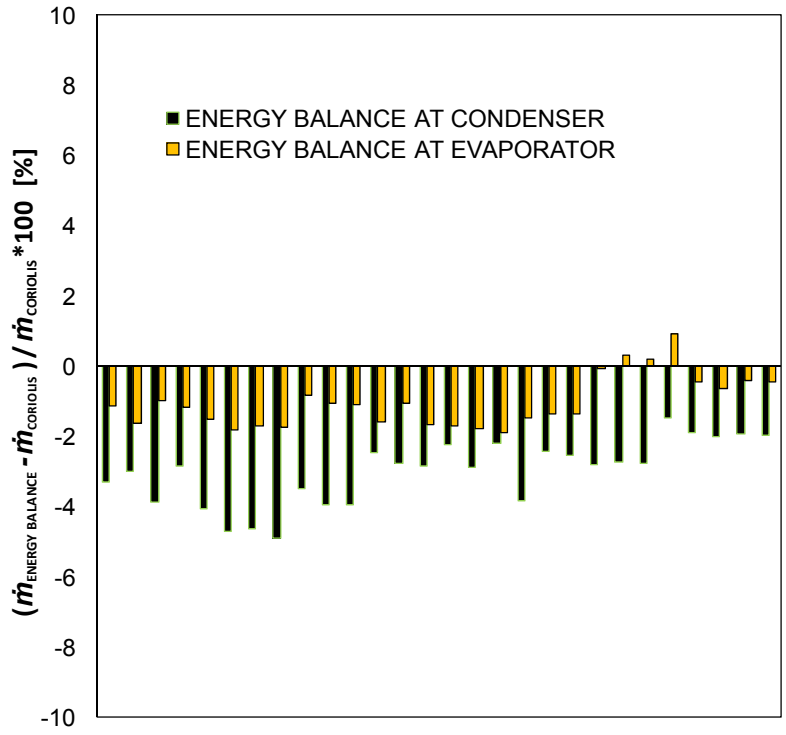

Fig. 3.12. Comparison between propane mass flow rate computed from energy balance (both at the condenser and at the evaporator) and measured mass flow rate. Data refers to test runs for the configurations with internal heat exchanger.

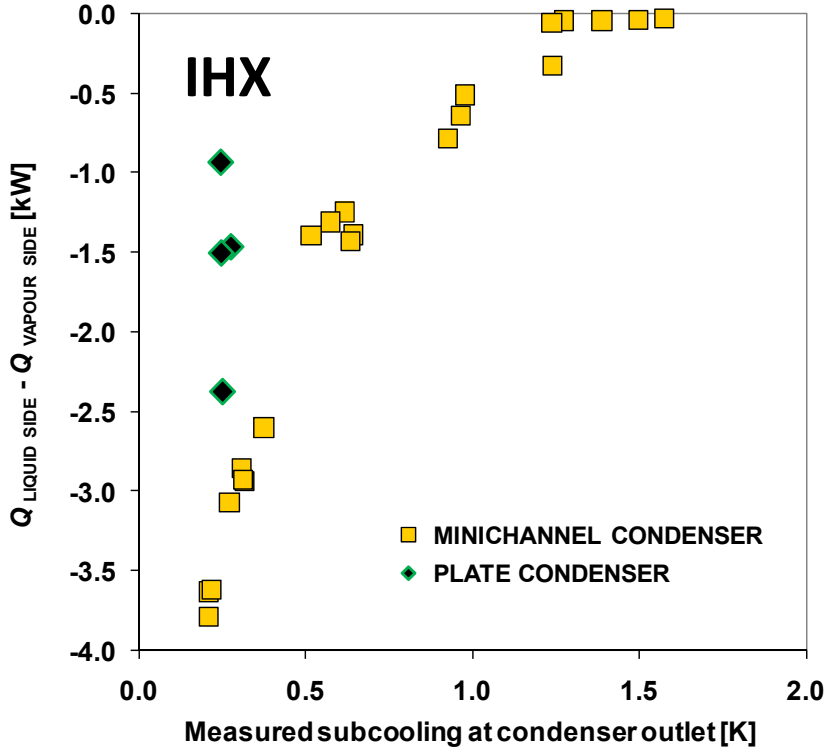

Fig. 3.13. Energy balance at the internal heat exchanger versus subcooling at the condenser outlet.

3.6.2 Minichannel vs plate condenser

The testing configurations using the minichannel condenser have been compared against the testing configurations using the plate condenser at the same levels of water temperature for the heat sink and the heat source.

In all the graphs regarding the heating and cooling capacities, as well as the coefficient of performance, reported in this and in the following Section, square dots refer to the configuration I (i.e. plate evaporator + plate condenser), triangles refer to the configuration II (i.e. plate evaporator + minichannel condenser), circles refer to the configuration III (i.e. plate evaporator + plate condenser + IHX), while diamonds refer to the configuration IV (i.e. plate evaporator + minichannel condenser + IHX). Furthermore, in all the four cases solid symbols refer to test runs at 12-7°C evaporator water temperature, while empty symbols refer to data obtained at 10-5°C evaporator water temperature.

Experimental data of heating capacity obtained using the plate condenser and the minichannel condenser is compared in Fig. 3.14 (for configurations without IHX) and Fig. 3.15 (for configurations with IHX). Data is plotted versus the temperature of the hot water at the outlet of the condenser. The uncertainty in the measurement of the heating capacity is reported, with 95% confidence level, in the graphs.

By increasing the water temperature, the condensing temperature increases and the heating capacity slightly reduces because of the reduction of the heat of vaporization. Besides, by reducing the cold water temperature, the vapour density at the compressor suction is reduced and a lower refrigerant mass flow rate is given by the compressor. This explains why data at 10-5°C evaporator water temperature is lower than data at 12-7°C evaporator water temperature.

The most relevant result shown in Fig. 3.14 and Fig. 3.15, however, is that the same heating capacity is measured when the low charge minichannel condenser is used instead of the plate condenser.

Experimental data of COP in heating mode using the plate condenser and the minichannel condenser is reported in Fig. 3.16 (for configurations without IHX) and Fig. 3.17 (for configurations with IHX). Data is plotted versus the temperature of the hot water at the outlet of the condenser. Solid lines in Fig. 3.16 and Fig. 3.17 are the linear interpolation for data referring to the plate condenser, while dotted lines refer to the minichannel condenser.

As one can see, at the same hot and cold water conditions, the measured COP in Fig. 3.16 and Fig. 3.17 is always slightly lower when using the low charge heat exchanger instead of the conventional one. However, the average COP reduction measured is equal to 1.5%, while the maximum reduction is 2.6%. It should also be noticed that such differences are within the uncertainty of the COP measurement (with 95% confidence level) given by the bars plotted in the graphs.

The thermal performances of the two condensers with R290 have already been compared in Section 2.3.1 (see Fig. 2.21), showing that a lower condensing temperature is obtained when using the plate condenser.

The saturation temperature measured at the inlet of the minichannel condenser is around 1.5 K higher than the saturation temperature at the PHE inlet, for all the tested conditions, hence a higher electric power is needed at the compressor, this reducing the COP of the equipment. The higher condensing temperature is due to the higher

refrigerant pressure drop in the minichannel condenser and, in general, to the slightly lower thermal performance.

In Fig. 3.18 and Fig. 3.19 the saturation temperature of propane at the condenser inlet and the condenser outlet, respectively, is reported for all the data shown in this Section. Solid squares refer to data obtained when using the PHE condenser (both with IHX and without IHX), while triangles refer to data obtained when using the minichannel condenser (both with IHX and without IHX).

It must be considered that the nominal heat transfer area of the plate condenser is around 7 m^2, while the propane side heat transfer area of the minichannel condenser is around 5 m^2, corresponding to 30% reduction. The internal volume, instead, is 2.9 L in the case of the prototype and 8.4 L in the case of the brazed plate heat exchanger; hence, 65% volume reduction has been obtained with a very low energy efficiency loss. Regarding the charge, around 0.8 kg propane reduction has been measured when using the minichannel condenser, corresponding to around 25% of the total charge required by the heat pump when using plate heat exchangers. These results will be further discussed in Section 3.6.6.

In Fig. 3.20 the experimental propane pressure drop for the two condensers is plotted versus the outlet water temperature. As one can see, the measured pressure drop when using the minichannel condenser is always higher. Reported data has been obtained for the configurations without internal heat exchanger at 12-7°C and 10-5°C evaporator water temperature, and for the configurations with IHX at 10-5°C evaporator water temperature.

The velocity of the refrigerant in a PHE condenser is usually very small as compared to the case of shear-dominated condensation inside tubes; as a consequence, the pressure drop is usually lower. The mass flux for the minichannel condenser is around G=300 kg/(m^2s), while it is around G=20 kg/(m^2s) in the PHE.

For each of these three conditions, when using the minichannel condenser, by increasing the temperature of the hot water the condensing temperature increases and the pressure drop decreases as a consequence of the propane properties change.

The mass flow rate given by a reciprocating compressor strongly depends on the density of the suction vapour; when the evaporation pressure is reduced, or the vapour temperature is increased by the use of an internal heat exchanger, the density decreases and a lower flow rate is given by the compressor. For the case reported in Fig. 3.20, with IHX, at 10-5°C evaporator water temperature, the measured flow rate is around 0.27 kg/s. At 10-5°C evaporator water temperature, the computed mass flow rate is around 0.28~0.29 kg/s, while it increases up to around 0.30 kg/s at 12-7°C evaporator water temperature. The influence of the mass flow rate on the pressure drop in the minichannel condenser is clearly shown by the three sets of data plotted in Fig. 3.20.

The PHE exchanger used in the test unit has a distributor; most of the pressure drop is supposed to be caused by the flow of the liquid through the distributor. The pressure drop at the PHE condenser is almost constant and it only shows a very small influence of the mass flow rate.

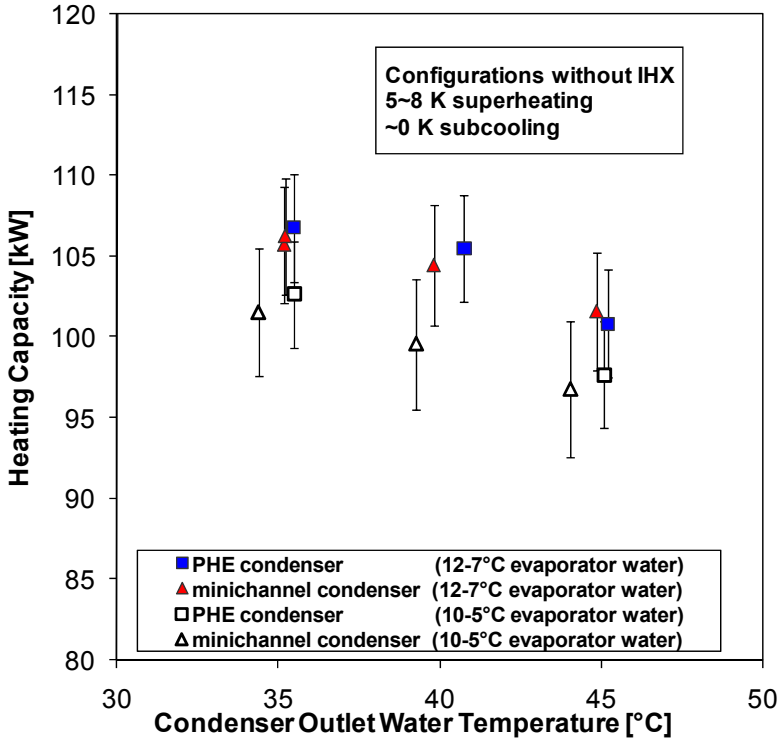

Fig. 3.14. Experimental heating capacity versus condenser outlet water temperature for the configurations with the plate condenser and the minichannel condenser (without IHX).

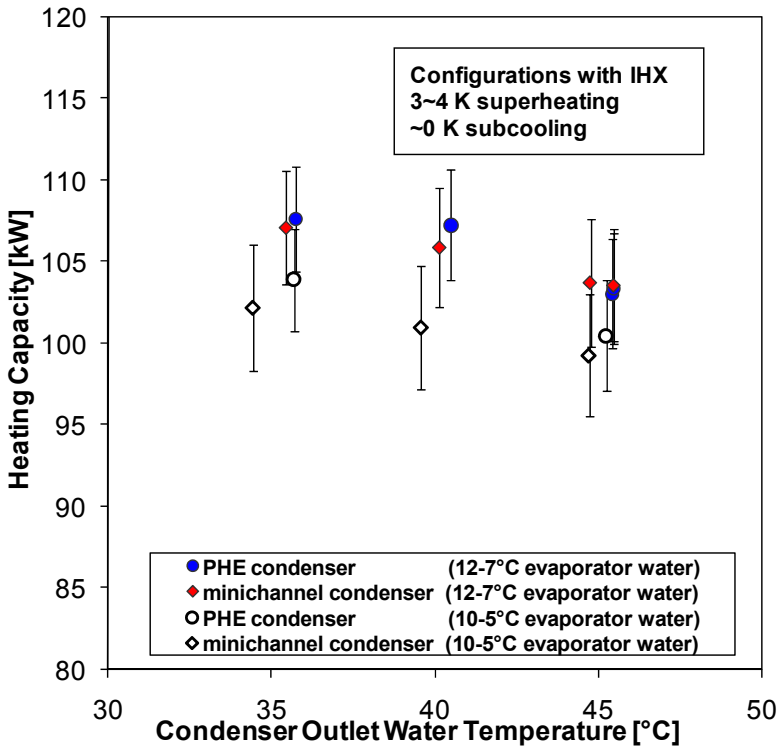

Fig. 3.15. Experimental heating capacity versus condenser outlet water temperature for the configurations with the plate condenser and the minichannel condenser (with IHX).

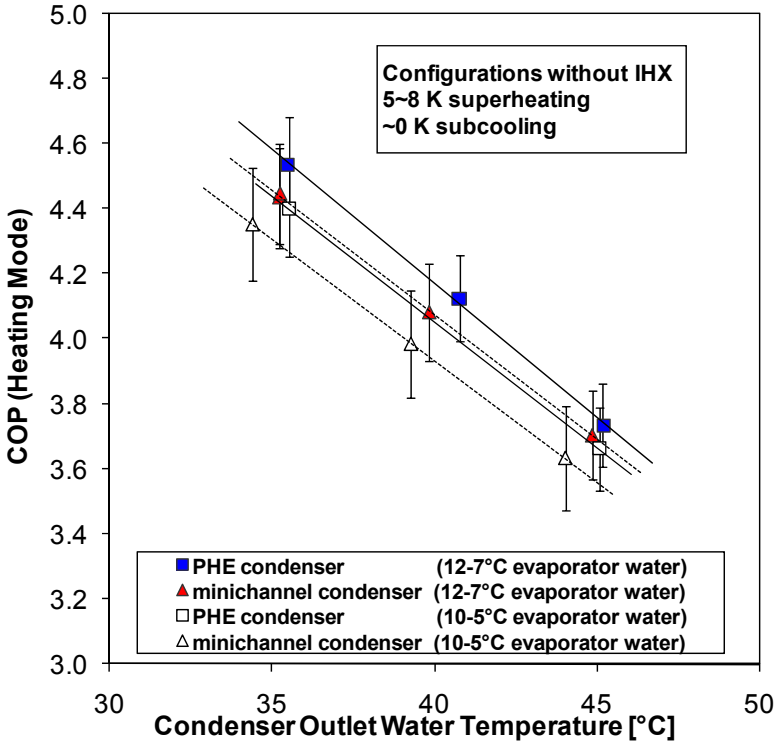

Fig. 3.16. Experimental COP versus condenser outlet water temperature for the configurations with the plate condenser and the minichannel condenser (without IHX).

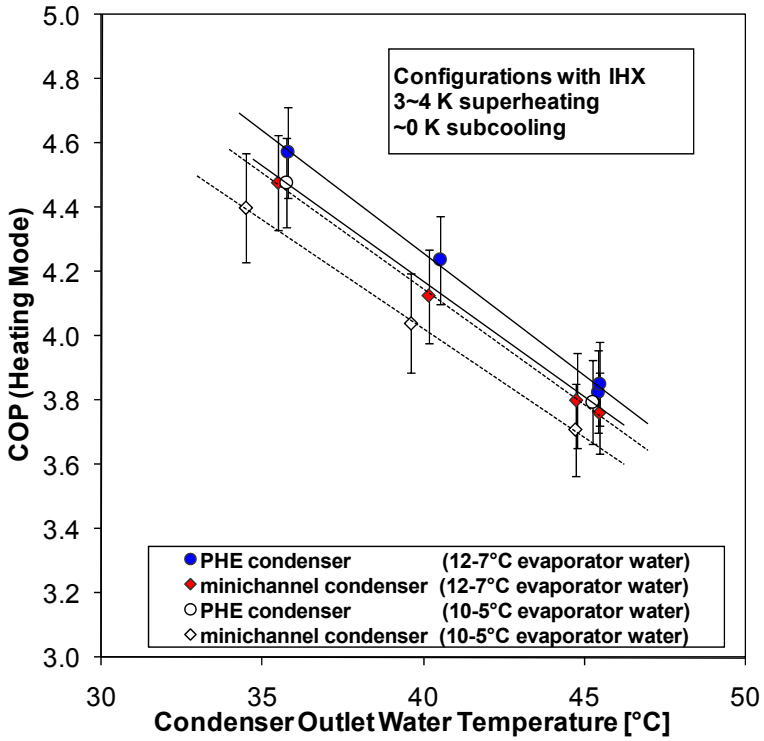

Fig. 3.17. Experimental COP versus condenser outlet water temperature for the configurations with the plate condenser and the minichannel condenser (with IHX).

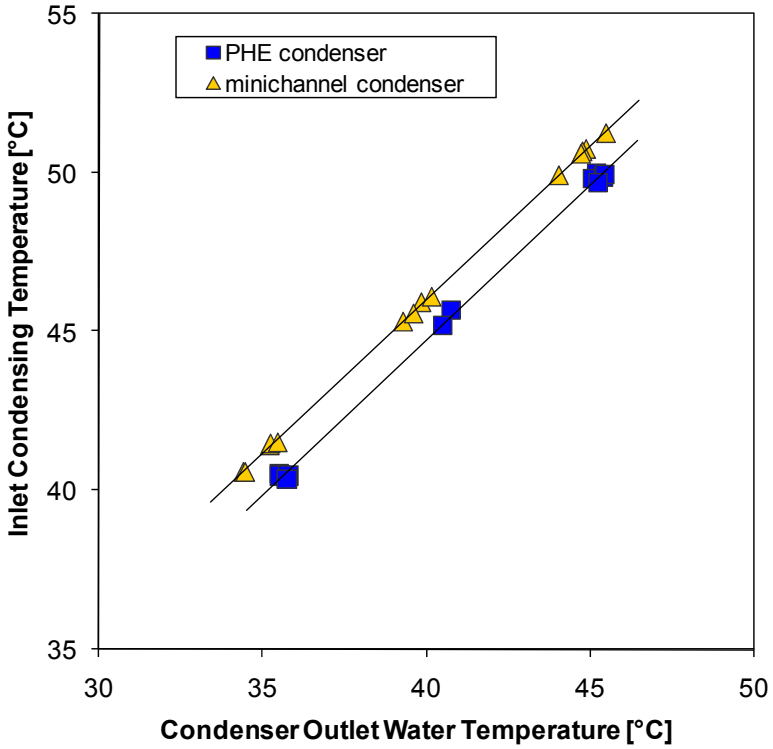

Fig. 3.18. Inlet condensing temperature versus condenser outlet water temperature for the configurations with the PHE condenser and the minichannel condenser.

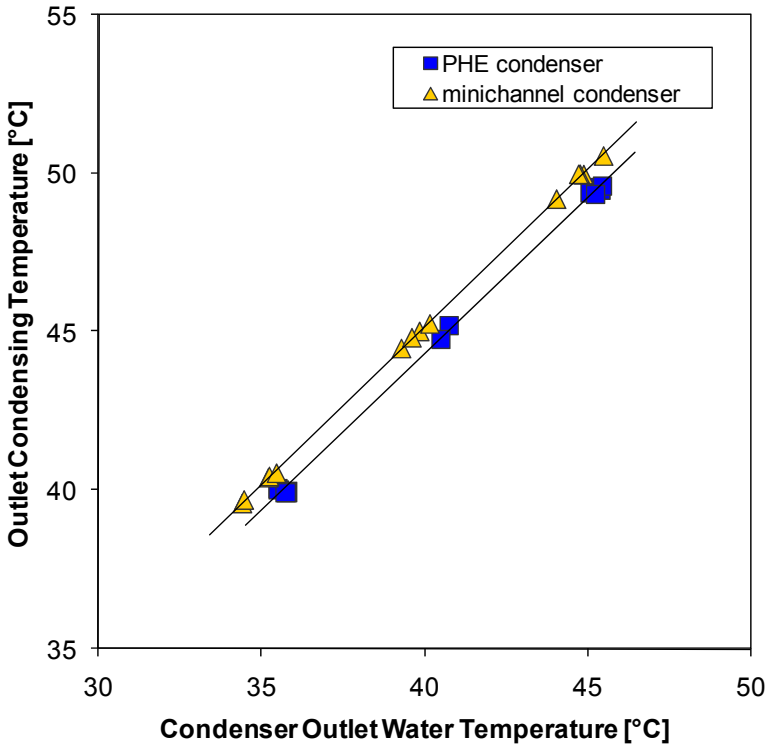

Fig. 3.19. Outlet condensing temperature versus condenser outlet water temperature for the configurations with the PHE condenser and the minichannel condenser.

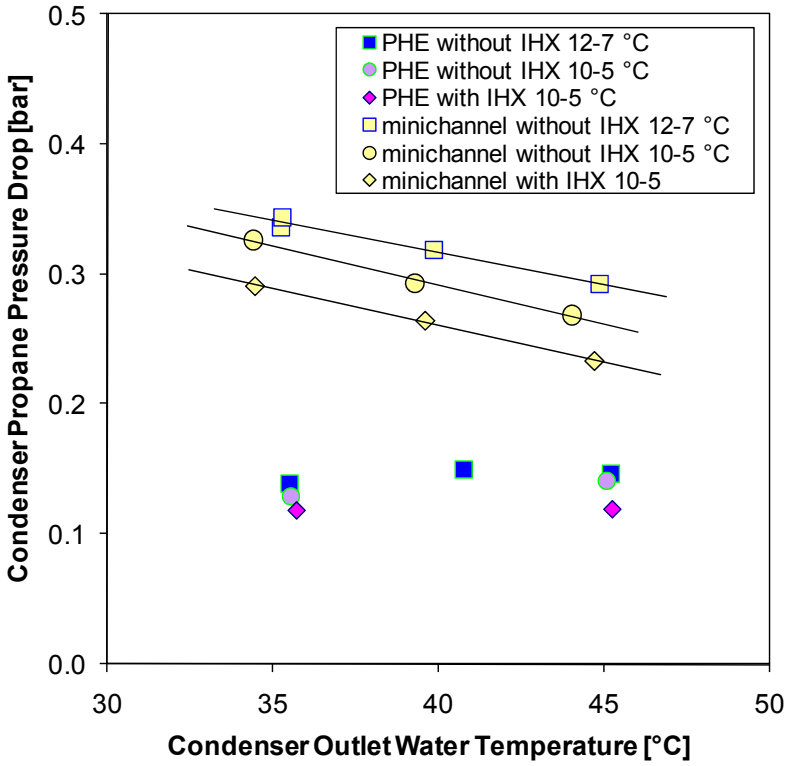

Fig. 3.20. Propane pressure drop versus condenser outlet water temperature for both condensers at different operating conditions.

3.6.3 Influence of the internal heat exchanger

At least 20 K superheat at compressor suction and a discharge temperature at least 20 K over the condensing temperature (preferably 30 K) are required by the manufacturer of the compressor in order to avoid problems due to excessive decrease of the oil viscosity because of the high solubility of propane in mineral oils. The use of an internal heat exchangers is suggested in order to fulfil these constraints (Bitzer, 1997).

By a theoretical point of view, the use of an internal heat exchanger has a direct positive effect on the ideal COP given by thermodynamic cycle. Then, the positive effect of the superheating on the compressor efficiency when using propane and the negative effect given by the increased suction line pressure drop must be taken into account.

Considering 0°C evaporating temperature, 50°C condensing temperature and 0.7 compression efficiency, when the suction vapour superheat is increased from 0 K up to 20 K, the theoretical COP in heating mode is increased by 2.4% from COP = 3.78 to COP = 3.87. The additional saturation temperature drop given by the internal heat exchanger is a around 0.6 K at full compressor capacity (see Section 2.3.4). If taking into account 0.6 K saturation suction temperature drop in the above theoretical estimation, the ideal COP in heating mode would be reduced from 3.87 down to 3.82.

Experimental data about the compressor efficiency are provided in Section 3.6.7 where the influence on the energy performance is also discussed.

Experimental tests have been carried out at different temperatures of the hot water provided by the condenser (i.e. 35°C, 40°C and 45°C) and different temperatures of the cold water at the evaporator inlet (i.e. 10°C and 12°C), with fixed 5 K temperature difference between inlet and outlet for both heat exchangers.

For the test runs using the configurations without the internal heat exchanger, around 7 K superheating was measured at the compressor suction, and the discharge temperature was around 22 K over the condensing temperature.

The heat transfer rate in the internal heat exchangers depends on the temperature difference between the subcooled liquid in the tubes and the superheated vapour on shell side. At the lowest level of the temperature of the condenser water (i.e. 30-35°C), around 23 K superheating was achieved at the compressor suction, and the discharge temperature was around 38 K over the condensing temperature. At the highest level of the temperature of the condenser water (i.e. 40-45°C), the superheating at the compressor suction increased up to around 28 K, while the superheating at the compressor discharge increased up to around 43 K. It is interesting to notice that, even at 40-45°C condenser water temperature and even when using the internal heat exchanger, the compressor discharge temperature when using propane as refrigerant is not excessively high (i.e. around 93°C).

The same heating capacity experimental points reported in Fig. 3.14 and Fig. 3.15 are plotted again in Fig. 3.21 and Fig. 3.22 to show the influence of the IHX on heating capacity. In Fig. 3.21, the configuration I (i.e. plate evaporator + plate condenser, square dots in the graph) is compared to the configuration III (i.e. plate evaporator + plate condenser + IHX, circles). In Fig. 3.22, the configuration II (i.e. plate evaporator + minichannel condenser, triangles in the graph) is compared to the configuration IV (i.e. plate evaporator + minichannel condenser + IHX, diamonds in the graph). Solid

symbols refer to data obtained at 12-7°C evaporator water temperature, while empty symbols refer to data obtained at 10-5°C evaporator water temperature.

When using the internal heat exchanger, the mass flow rate given by the reciprocating compressor is reduced by around 5 % because the density of the vapour at suction is reduced; however, a higher enthalpy is available at the inlet of the condenser. As one can see in Fig. 3.21 and Fig. 3.22, the heat capacity is in general increased by the use of the internal heat exchanger. This increase varies from around 1% (at 12-7°C, 30-35°C) up to around 3% (at 10-5°C, 40-45°C).

The same comparison given for the heating capacity in Fig. 3.21 and Fig. 3.22 is given in Fig. 3.23 and Fig. 3.24 for the cooling capacity. As one can see, the cooling capacity is in general increased by the use of the internal heat exchanger this has a higher influence on the cooling capacity than on the heating capacity.

If the internal heat exchanger is not used, when the hot water temperature at the condenser outlet is increased from 35°C up to 45°C, the corresponding inlet quality at the evaporator varies from around 0.23 up to top 0.30.

If the internal heat exchanger is used, the subcooling of the liquid feeding the expansion valve ranges from around 8 K up to around 12 K and a lower evaporator inlet quality is achieved, this increasing the heat of vaporization available. For the hot water temperature at the condenser outlet varying from 35°C up to 45°C, the corresponding inlet quality at the evaporator when using the internal heat exchanger varies from around 0.18 up to top around 0.23.

The cooling capacity increase achieved varies from around 2% (at 12-7°C, 30-35°C) up to around 5% (at 10-5°C, 40-45°C).

The COP in heating mode for the configurations with and without internal heat exchanger is compared in Fig. 3.25 and Fig. 3.26. Solid lines in these graphs are the linear interpolation for data obtained using the IHX, while dotted lines refer to the configurations without IHX. As one can see, at the same hot and cold water conditions, the measured COP in Fig. 3.25 and Fig. 3.26 is always slightly higher when using the IHX. The solid lines referring to configurations without IHX display a different slope as compared to those referring to configurations with IHX. By increasing the hot water temperature, indeed, the temperature difference between cold vapour and hot liquid in the IHX increases, since the cold water temperature is fixed for each data set; therefore, the vapour temperature rise in the IHX and the positive effect on the COP is higher.

The corresponding experimental improvement of COP in heating mode varies from around 1% (at 12-7°C, 30-35°C) up to around 3% (at 10-5°C, 40-45°C). It can be noticed, however that such differences are within the uncertainty of the COP measurement, with 95% confidence level.

The improvement of COP in cooling mode is higher, varying from around 2% (at 12-7°C, 30-35°C) up to around 5 % (at 10-5°C, 40-45°C).

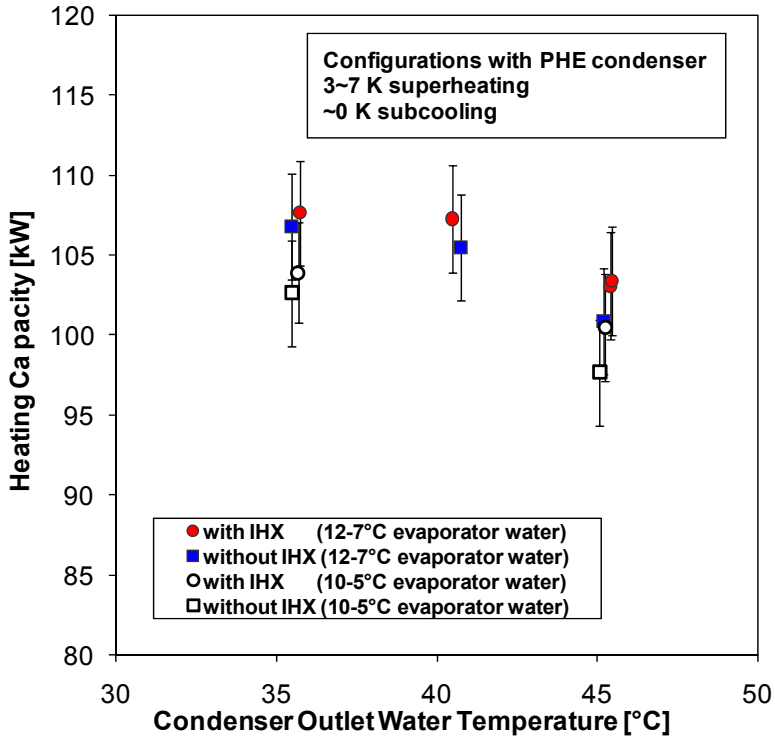

Fig. 3.21. Experimental heating capacity versus condenser outlet water temperature for the configurations with the IHX and without the IHX (with plate condenser).

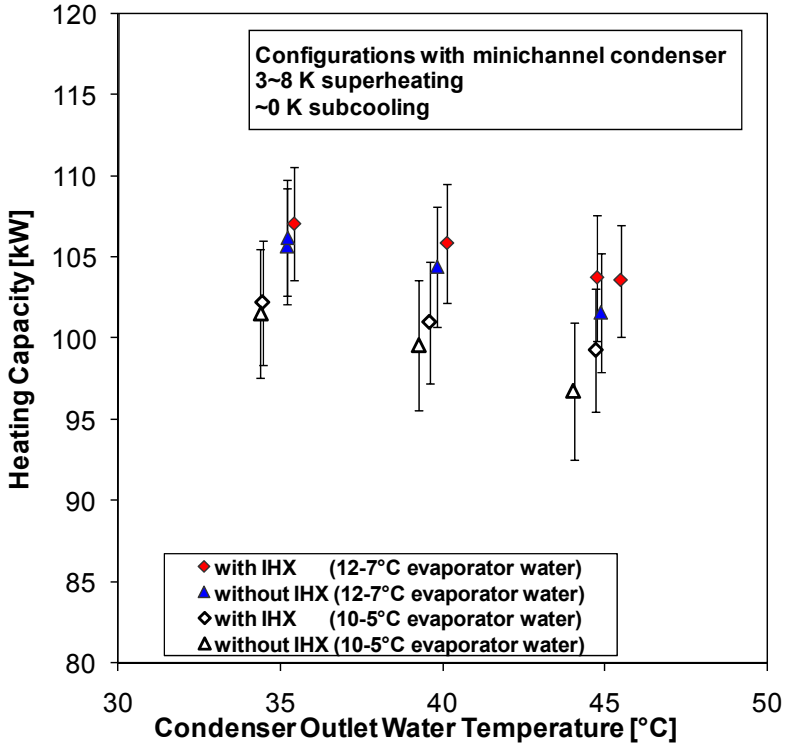

Fig. 3.22. Experimental heating capacity versus condenser outlet water temperature for the configurations with the IHX and without the IHX (with minichannel condenser).

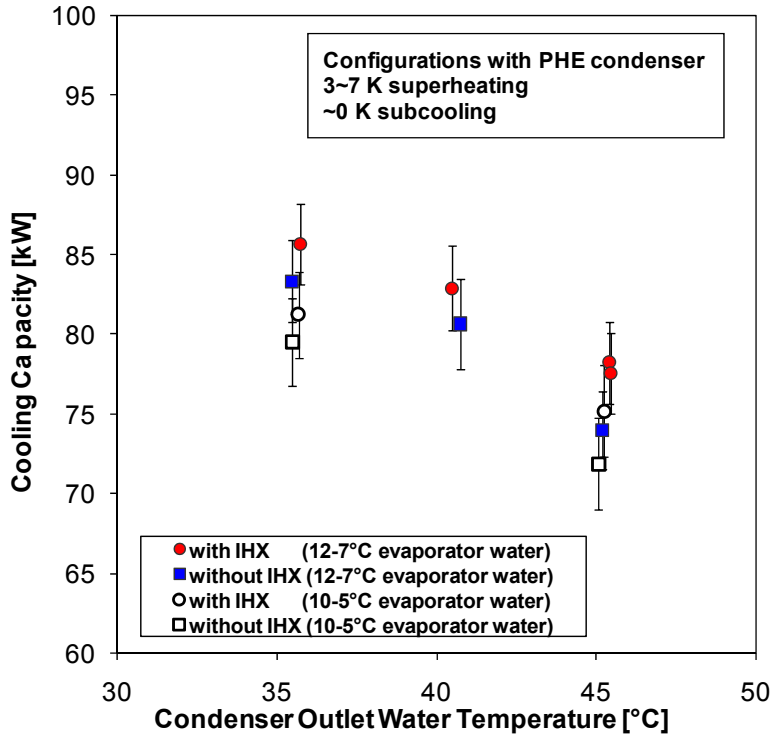

Fig. 3.23. Experimental cooling capacity versus condenser outlet water temperature for the configurations with the IHX and without the IHX (with plate condenser).

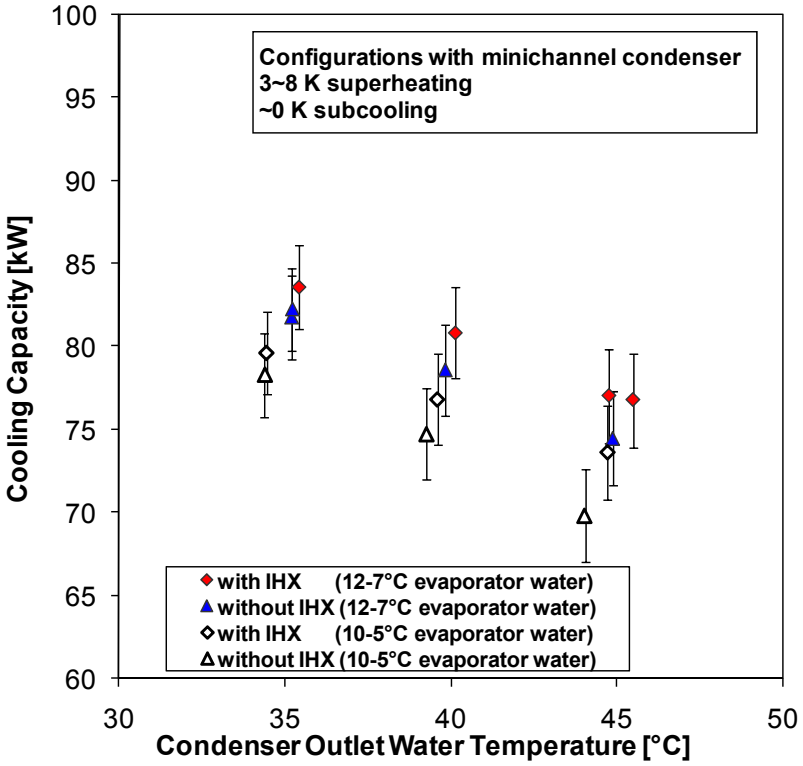

Fig. 3.24. Experimental cooling capacity versus condenser outlet water temperature for the configurations with the IHX and without the IHX (with minichannel condenser).

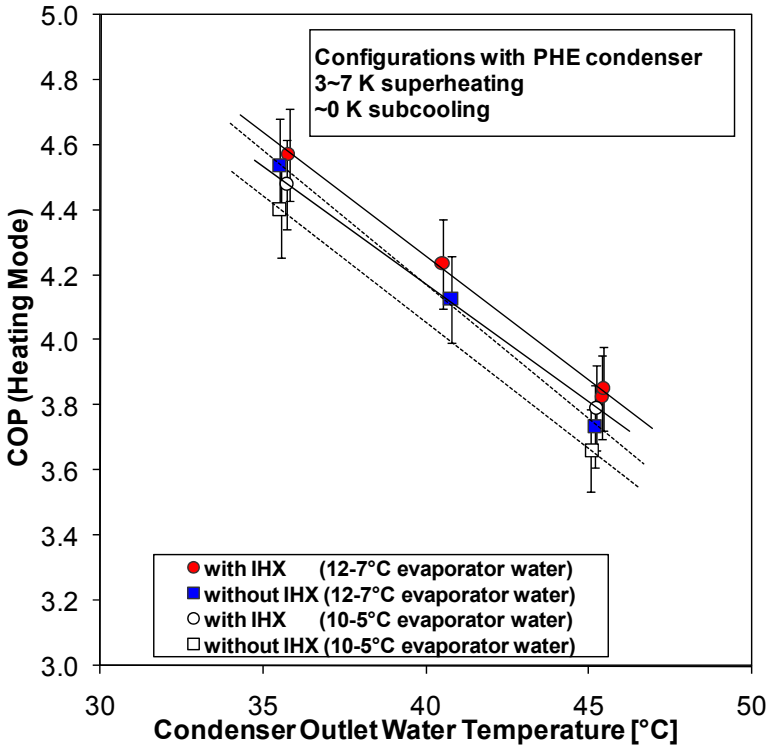

Fig. 3.25. Experimental COP versus condenser outlet water temperature for the configurations with the IHX and without the IHX (with plate condenser).

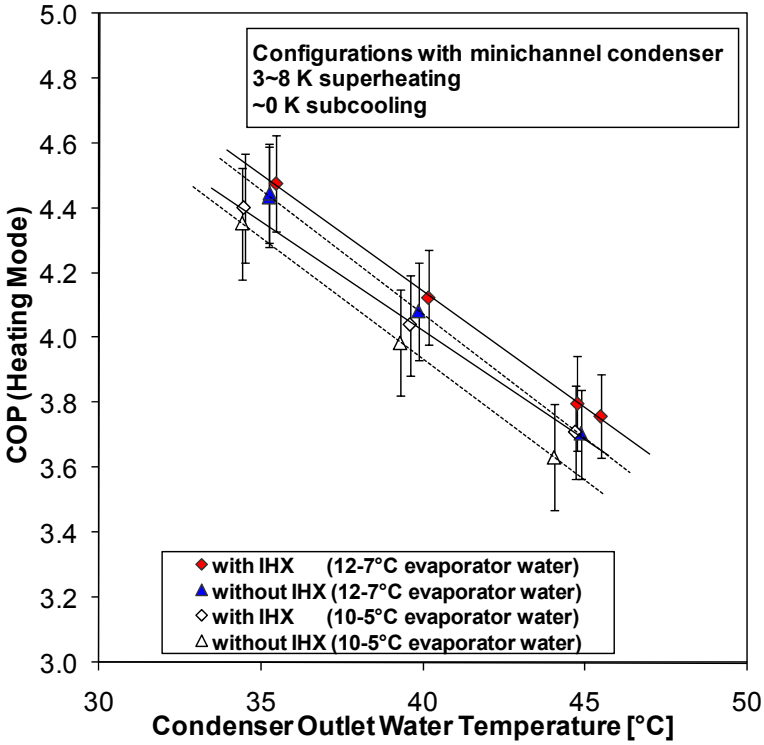

Fig. 3.26. Experimental COP versus condenser outlet water temperature for the configurations with the IHX and without the IHX (with minichannel condenser).

3.6.4 Estimation of water side pressure drop

In the experimental test rig, only the power consumption of the compressor is measured in order to compute the COP of the equipment. It is therefore interesting to provide some estimation of the power consumption of the circulating pumps, since this can have some influence on the actual system performance.

Experimental data about water pressure drop in the minichannel condenser obtained at 19°C is reported in Section 2.3.1 in Fig. 2.20. At nominal conditions (i.e. 100 kW heating capacity and 5 K water temperature rise), the shell side pressure drop is around 7 kPa.

No experimental data are available for the plate condenser. According to the rating software provided by manufacturer, the expected water pressure drop for the brazed plate condenser is around 34 kPa at the same flow rate and 40-45°C water temperature.

The corresponding values of pumping power are 35 W when using the minichannel condenser and 160 W when using the PHE.

Regarding the plate evaporator, according to the rating software, the expected water pressure drop is around 23 kPa at test conditions (i.e. water mass flow rate around 3.8 kg/s) and the corresponding value of pumping power is around 90 W.

At the testing condition with the lowest pressure ratio for the compressor (i.e. at water temperature levels 12-7°C, 30-35°C) the electric power required by the compressor is around 24 kW. It can be noticed that the additional power required to make the water flow through the plate evaporator and the plate condenser, is expected to be in this case around 1 % of the compression power (i.e. 250 W).

3.6.5 Comparison with ECOLABEL award criteria

The criteria for the European Community ecological award of the eco-label have been recently revised by the Decision 2007/742/EC. With the new regulation, the use of a fluid with GWP lower than 150 is prized with a 15% reduction of the minimum required COP in heating mode and EER in cooling mode. It is interesting to compare the energy performance of the present heat pump using propane as the working fluid with the eco-label criteria.

In Table 3.5 the minimum required system COP and EER are reported for three testing conditions. This value is compared to the experimental minimum equipment COP and EER obtained among the four tested configurations for the present heat pump.

For calculation of system COP, values of the power consumption of circulating pumps should be taken into account. In the present case, only the power consumption at the compressor has been measured.

As one can see in Table 3.5, with regard to the cooling mode the experimental EER of the present unit is far above the eco-label requirement. In heating mode, the experimental data reported have been obtained at 10-5°C evaporator water temperature, while the test condition for the eco-label is 10-7°C. However, even if the average cold water temperature was 1 K lower, the measured equipment COP is above the required system COP.

Table 3.5. Comparison of heat pump energy efficiency with eco-label award criteria.

	Heating		Cooling
Evaporator water temperature	10-7°C		12-7°C
Condenser water temperature	30-35°C	40-45°C	30-35°C
System COP/EER required when GWP<150	4.33	3.57	2.72
Minimum equipment COP/EER measured	4.36*	3.64*	3.45

* Data obtained at 10-5°C evaporator water temperature.

3.6.6 Propane charge

For each configuration, the heat pump facility has been filled with refrigerant till the receiver downstream the condenser was half full of liquid, in order to compare the propane charge required by each configuration at homogenous active charge conditions. Experimental data on the refrigerant charge required by the four configurations tested is reported in Table 3.6. The measured charge ranges from 3.1 kg for the configuration II (i.e. plate evaporator + minichannel condenser, without IHX) up to 5.1 kg for the configuration III (i.e. plate evaporator + plate condenser + IHX).

Since the present heat pump has been devoted only to test applications and the piping layout is quite complex because of the need to install five different heat exchangers in the same facility, the piping length could not be minimized (see Fig. 3.4 for a picture of the actual layout). In particular, the liquid line length varies from around 3 m up to 5 m, depending on the configuration, the vapour discharge line is around 5 m long and the suction line is around 8 m long.

A calculation of the amount of propane charge trapped in the piping is therefore needed in order to compare the different configurations and estimate the target minimum charge that could be achieved. Such calculation is provided in Table 3.7, assuming that in all the lines single-phase flow is present (with density ρ = 11 kg/m^3 in the suction line, ρ = 32 kg/m^3 in the discharge line and ρ = 450 kg/m^3 in the liquid line). As one can see, a large amount of propane, ranging from 0.9 kg up to 1.2 kg, is estimated to be present in the piping.

It must be notice that, as shown in Section 3.6.1, a mixture of quasi saturated vapour and subcooled liquid not at thermodynamical equilibrium was expected to be present at the condenser outlet during the test runs. Some bubbles of vapour were expected to be present inside the liquid line. Even if the vapour flow quality was very close to 0, it is well know that void fraction rapidly reach high values even at low vapour qualities.

Since when performing the energy balance at the internal heat exchanger assuming saturated liquid at the condenser outlet, the computed heat flow rate at the liquid side is underestimated by around 3 kW and the heating capacity at the condenser is around 100 kW (see Fig. 3.13), the thermodynamic vapour quality could be assumed to be around 0.03. Assuming that the flow quality is equal to the thermodynamic quality, according to the homogeneous model, the corresponding void fraction is around 0.3, while according to the Zivi (1963) and Rouhani (1969) the void fraction would be around 0.15. It can be noticed that, at such low values of quality, the void fraction is extremely dependent on the quality: as an example, at 0.02 quality the void fraction given by Rouhani (1969) is around 0.1, while at quality 0.06 it is 0.25. Therefore, the accurate estimation of the actual void fraction in the liquid line is almost impossible. As a very rough estimation, it could be said that the charge in the liquid line for the configurations without internal heat exchange could be up to around 0.2 kg lower than the value reported in Table 3.7 (i.e. 0.6 kg). When using the internal heat exchanger, half of the liquid line (i.e. the line downstream this device) is surely filled with subcooled liquid, therefore the charge value given in Table 3.7 should be closer to the actual one.

The most important result is the comparison between the charge required by each of the two configurations using the minichannel condenser to the corresponding

configuration using the plate heat exchanger. As one can see in Table 3.6, comparing configuration I to II and configuration III to IV, it is shown that 0.8 kg charge reduction is achieved when using the low charge heat exchanger.

A simple analysis of the charge distribution in the heat pump is provided in Table 3.8. Around 0.5 kg mass was contained in the receiver during the test run (it was half filled with liquid) and around 0.4 kg mass was expected to be trapped in the filter. The dehydrating filter is installed in the liquid line bypass downstream the internal heat exchanger, hence the amount of refrigerant trapped in the filter is not taken into account in the mass reported for the configurations without IHX.

A very interesting parameter shown in Table 3.8 is the estimation of the charge trapped in the heat exchangers (HXs) and compressor only. This varies from 1.7 kg for the configuration II (i.e. plate evaporator + minichannel condenser, without IHX) up to 3.0 kg for the configuration III (i.e. plate evaporator + plate condenser + IHX).

The main reason for installing the liquid receiver in the present heat pump is related to the need for controlling active mass during lab tests. However, such a heat pump can be run without the liquid receiver, thus decreasing total charge.

In Table 3.8 the value of the "minimum target charge" using heat exchangers and the compressor installed in the present heat pump facility is reported. This quantity has been computed discarding the dehydrating filter and the liquid receiver, and considering a liquid line 0.25 m long and a suction and discharge lines 1 m long. When using the minichannel condenser, this minimum target charge is 1.8 kg if not using the internal heat exchanger, and 2.3 kg if using the internal heat exchanger. The charge reduction provided by the use of the minichannel condenser, as compared to the "minimum target charge" for the configuration with plate exchanger and without IHX is 32%.

The "reference charge" reported in Table 3.7 has been computed discarding the liquid receiver but not the dehydrating filter and reducing the length of the piping to around 0.5 m liquid line and 4 m vapour line.

The additional charge trapped in the internal heat exchanger, computed from the value of the internal volume, is around 0.3 kg; it can be noticed that in the estimations of Table 3.7 the difference between the configurations with IHX and the ones without IHX is higher (i.e. 0.5 kg). This could be due to the error given by assuming single-phase liquid flow in the estimation of the charge trapped in the liquid line.

It should be pointed out that a large amount of refrigerant (i.e. around 1 kg) is expected to be trapped in the semi-hermetic reciprocating compressor, mainly solved in the 4.75 L of mineral oil. Therefore, once the charge in the condenser has been reduced, the compressor becomes the most relevant device for the charge minimization challenge. The use of lubricants not miscible with R290 could help to reduce this value.

Some interesting results by Corberán and Martínez (2008a) about the optimum charge in a propane heat pump using plate heat exchangers and a scroll compressor (without internal heat exchanger) are reported in Fig. 3.27. The heat pump has been tested with a polyolester (POE) oil and a mineral oil at different condenser water temperatures and different refrigerant charge. Experimental values of COP versus refrigerant charge and the corresponding values of condenser subcooling versus refrigerant charge are reported in the graphs in Fig. 3.27. When increasing the refrigerant charge, if a liquid receiver is not present (as in the case reported), the additional charge is trapped as liquid at the outlet region of the condenser, this increasing the subcooling. It is well know that the maximum energy efficiency is achieved in a vapour compression refrigeration cycle when some degree of subcooling

is achieved at the condenser. For the case shown in Fig. 3.27 this optimal value of condenser subcooling is around 10 K. It is very interesting to point that, because of the much higher solubility of propane in mineral oil than in POE oil, a much higher refrigerant charge was required in order to get the same value of subcooling. As a result, the optimal propane charge increases from around 450 g with POE up to 550 g with the mineral oil.

Furthermore, the COP is shown in Fig. 3.27 to be lower when using the mineral oil. According to the authors, this should arise from the better efficiency of the scroll compressor, probably because of the comparatively lower viscosity of the POE oil as compared to the mineral oil used (Corberán and Martínez, 2008a).

It can be noticed that the solubility of propane in PAG oil is even lower than in POE oils (Fernando *et al*., 2003). However, no data about the use of PAG oils with propane was found in the literature.

Table 3.6. Measured propane charge for the tested configurations.

Configuration	I	II	III	IV
Evaporator	PHE	PHE	PHE	PHE
Condenser	PHE	minichannel	PHE	minichannel
Internal heat exchanger	not used	not used	used	used
Measured charge	3.9 kg	3.1 kg	5.1 kg	4.3 kg

Table 3.7. Estimation of propane charge in the liquid and vapour lines assuming single-phase flow.

Configuration	I	II	III	IV
Evaporator	PHE	PHE	PHE	PHE
Condenser	PHE	minichannel	PHE	minichannel
Internal heat exchanger	not used	not used	used	used
Suction line	0.17 kg	0.17 kg	0.20 kg	0.20 kg
Discharge line	0.12 kg	0.12 kg	0.12 kg	0.12 kg
Liquid line	0.62 kg	0.61 kg	0.88 kg	0.86 kg
Total	0.92 kg	0.90 kg	1.20 kg	1.18 kg

Table 3.8. Target charge for the different heat pump configurations.

Configuration	I	II	III	IV
Evaporator	PHE	PHE	PHE	PHE
Condenser	PHE	minichannel	PHE	minichannel
Internal heat exchanger	not used	not used	used	used
Measured total charge	3.9 kg	3.1 kg	5.1 kg	4.3 kg
Charge in piping	0.9 kg	0.9 kg	1.2 kg	1.2 kg
Charge in liquid receiver	0.5 kg	0.5 kg	0.5 kg	0.5 kg
Charge in filter	-	-	0.4 kg	0.4 kg
Charge in HXs + compressor	2.5 kg	1.7 kg	3.0 kg	2.2 kg
Minimum target charge *	2.6 kg	1.8 kg	3.1 kg	2.3 kg
Reference charge **	3.1 kg	2.3 kg	3.6 kg	2.8 kg

* 0.25 m liquid line, without receiver and filter

** 0.5m liquid line, without receiver, with filter

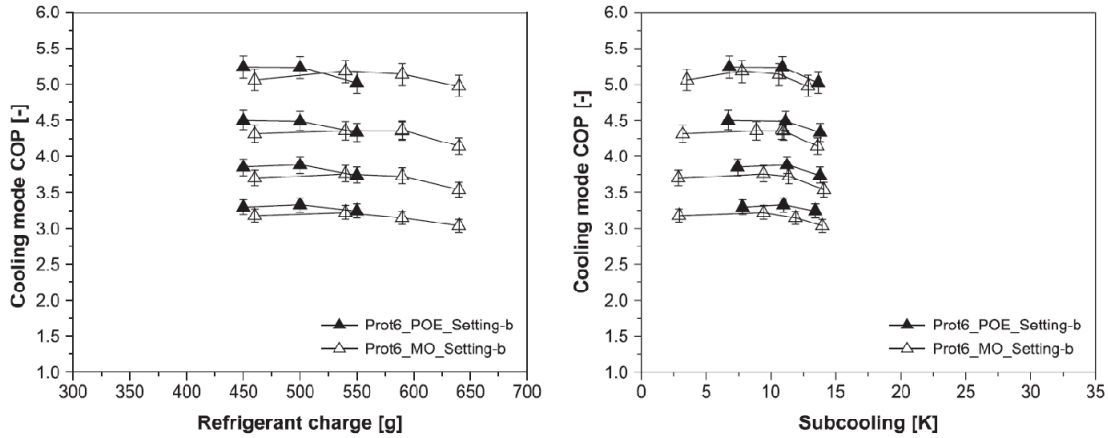

Fig. 3.27. COP versus charge (on the left) and versus condenser subcooling (on the right) for a propane heat pump at different operating conditions using mineral oil (MO) and polyolester oil (POE). From Corberán and Martínez (2008a).

3.6.7 Compressor efficiency

The viscosity of the oil is an important parameter for the efficiency of a refrigeration compressor. Excessive viscosity may result in poor mechanical efficiency, while if the viscosity is too low, this could results in lower volumetric efficiency and stronger wear on the moving parts.

R290 has a very high solubility with conventional lubricants and ester oils. Although this characteristic is advantageous for a good circulation of the oil in the system, it can lead to a substantial decrease of the viscosity, which may be harmful to the compressor, specially at low oil temperature and high suction pressure.

As reported in a recent review about the use of hydrocarbons in small refrigeration systems by Palm (2008), some system manufacturers have experienced intolerably high failure rates of compressors with hydrocarbon refrigerants, and this has been explained by the high solubility of refrigerant in the oil, while some other manufacturers have seen less failures with HCs than with H(C)FCs, providing that the proper oil was selected and crankcase heater and/or internal liquid line/suction line heat exchanger was used.

No data about long term durability of reciprocating compressors working with propane have been found in the literature. However, the performance of a single family propane heat pump using a hermetic scroll type compressor designed to operate with R407C has been experimentally investigated by Fernando *et al.* (2007). Ester oil was used as lubricant and the superheat at the evaporator was kept between 4 and 5 K, the compressor was operated more than 5,000 hours (from 2001 to 2005) without any kind of failure and the measured overall efficiency reported no reduction.

With regards to the compression efficiency when using propane, in an experimental investigation by Navarro *et al.* (2004, 2005), five R407C hermetic reciprocating compressors, covering different capacities and number of cylinders, have been characterized using propane as refrigerant and POE oil as lubricant. Tests have been performed at different operating conditions showing no significant difference between the oil behaviour with propane and R407C. Around 11 K superheat was used in the tests reported. Furthermore, Navarro *et al.* (2004, 2005) compared the performance of a piston compressor working with propane using two different oils, a mineral oil and a POE oil. They found that the volumetric efficiencies were identical. The isentropic compressor efficiencies were also similar, but the maximum in the efficiency versus pressure ratio plot was shifted slightly to lower pressure ratios with the POE oil.

An example of experimental data about volumetric and compressor efficiency for different compressors (i.e. scroll, hermetic and semihermetic) working with propane from Corberán *et al.* (2008c) is reported in Fig. 3.28.

The efficiency versus pressure ratio curves shown in these graphs display the typical behaviours given by the different compressor technologies, and no special difference given by the use of propane is reported. Another example about the total efficiency of the scroll compressor used by Fernando *et al.* (2007) is shown in Fig. 3.29.

In the heat pump presented in this thesis, a semi-hermetic reciprocating compressor by Bitzer designed to operate with propane (model 6G-40.2-40P) was installed; the compressor has 6 cylinders (with 75 mm bore and 55 mm stroke) with the possibility to shut-off the suction of a pair of them to reduce the capacity to 66%.

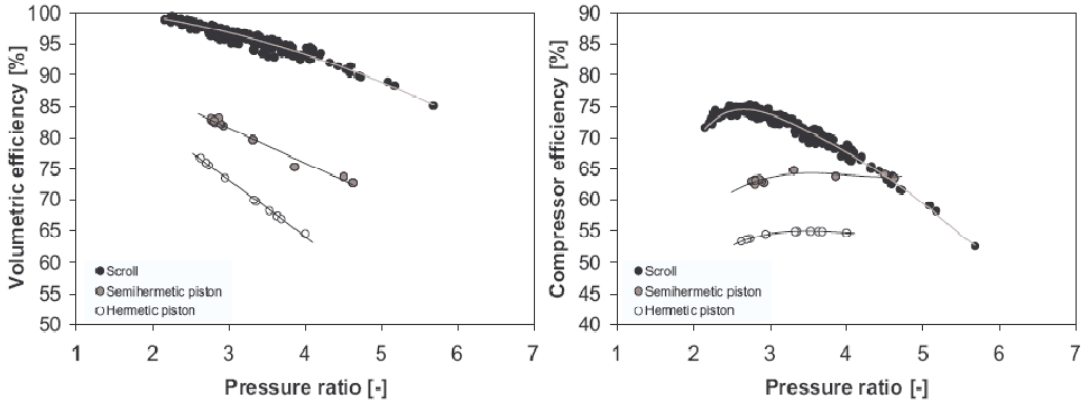

Fig. 3.28. Volumetric and compression efficiency for different compressors working with propane. From Corberán *et al.* (2008c).

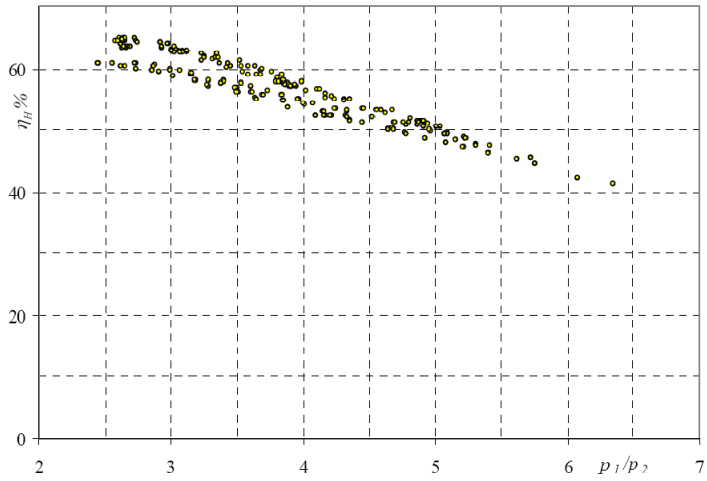

Fig. 3.29. Global efficiency of a scroll compressor with propane. From Fernando *et al.* (2007).

Because of the high solubility of propane with lubricants oils, the compressor is charged with 4.75 L of a higher basic viscosity mineral oil (cinematic viscosity 68 cSt at 40°C). Since, at fixed pressure, the solubility decreases by increasing the temperature, a sufficient suction superheat (i.e. at least 20 K), preferably with internal heat exchanger, and a minimum discharge gas temperature 20 K over the condensing one (preferably 30 K) are suggested by the manufacturer of the compressor (Bitzer, 1997).

In this Section experimental data about the global, isentropic and volumetric efficiency of the semi-hermetic compressor used are reported. Data refers to experimental runs at 12-7°C and 10-5°C evaporator water temperature with condenser water temperature ranging from 30-35°C up to 45-50°C, in order to cover the maximum possible range of pressure ratios. Data refers to both configurations with and without internal heat exchanger and different expansion valve setting have been used in order to change the superheating at the evaporator outlet. Some tests have also been run at reduced compressor capacity.

Compressor suction and discharge temperature and pressure are measured and the inlet enthalpy h_{in}, the actual discharge enthalpy h_{out}, and the discharge enthalpy for an isentropic process $h_{out\text{-}is}$ have been obtained by means of the NIST database (2002).

The global compressor efficiency η_{GLOBAL} has been computed according to the following equation:

$$\eta_{GLOBAL} = \frac{m(h_{out-is} - h_{in})}{W_{comp}} \tag{3.1}$$

where W_{comp} is the electric power supplied to the compressor and m is the propane mass flow rate. The electric power is directly measured, while the mass flow is directly measured by a Coriolis mass flow meter when the IHX is used, and it is obtained from the energy balances at condenser and at evaporator when the IHX is not used.

The volumetric efficiency η_{VOL} has been computed according to the following equation:

$$\eta_{VOL} = \frac{m / \rho_{in}}{V_S} \tag{3.2}$$

where ρ_{in} is density of the suction vapour, obtained by means of the NIST database (2002) from the measurements of pressure and temperature, while V_S is the theoretical swept-volume flow rate (i.e. 126.8 m3/h for Bitzer 6G-40.2-40P at 1450 rpm / 50 Hz).

The isentropic compressor efficiency η_{IS} has been computed according to the following equation:

$$\eta_{IS} = \frac{(h_{out-is} - h_{in})}{(h_{out} - h_{in})} \tag{3.3}$$

Experimental data about isentropic efficiency and global efficiency versus pressure ratio for all test runs performed are reported in Fig. 3.30, and Fig. 3.31, respectively.

It must be stressed that when using the internal heat exchanger the suction superheat ranges from around 23 K up to 35 K and the discharge superheat ranges from around 36 K up to 50 K, therefore the constraints given by the compressor manufacturer (i.e. 20 K suction superheat and 20 K, preferably 30K, discharge superheat) are fulfilled. When not using the internal heat exchanger, instead, the suction superheat in the test runs reported ranges from around 4 K up to 14 K and the discharge superheat ranges from around 19 K up to 30 K.

The isentropic efficiency of a reciprocating compressor usually displays a slight increase with pressure ratio, at small values of pressure ratios, and then decreases at higher pressure ratios. The achieved pressure ratio in the test runs varies from around 3 up to around 4.5. It must be noticed that this is the significant range of pressure for propane in typical heating and cooling applications, since the corresponding water temperatures ranges from 12-7°C/ 30-35°C (corresponding to the lowest pressure ratio) up to 10-5°C/ 45-50°C (corresponding to the highest pressure ratio).

As one can see in Fig. 3.30, the isentropic efficiency always increases with the pressure ratio for the range of pressure ratios considered. A lower isentropic efficiency was measured when the compressor was run at reduced capacity. The most interesting result is that lower compressor efficiency is measured when not using the internal heat exchanger.

Regarding the energy efficiency of equipment, however, the global efficiency of the compressor is a parameter much more significant that the isentropic efficiency. As one can see in Fig. 3.31, for the test runs using the internal heat exchanger the global efficiency versus pressure ratio display a similar curve as compared to the isentropic efficiency curve, but for the test runs without IHX data is much more scattered and a very important reduction (as compared to isentropic efficiency) is measured.

At full capacity with IHX the global efficiency varies from around 0.69 up to 0.71, but without IHX the maximum efficiency is around 0.67 and experimental values as low as 0.62 have been measured. Since, at fixed pressure ratio, the main difference between the test runs with IHX and the test runs without IHX is the temperature of the lubricant oil, it is clear from these results that the issue of the high solubility of propane in the oil is relevant, and that the fulfilment of the measures required by the manufacturer of the compressor is important in order to achieved the maximum efficiency.

Some of the data points of Fig. 3.31 for configurations without IHX are reported again in Fig. 3.32. In this new graph each data series has been obtained at fixed expansions valve setting (therefore at fixed superheating) and different pressure ratios. Triangles refer to test runs at full capacity, while circles refer to test runs at 66% capacity. As one can see, while in Fig. 3.31 data are scattered, quite clear trends can be seen in Fig. 3.32. In general, it can be said that data series at higher superheating (which means lower amount of propane solved in the oil) display higher efficiency. This rule is not always fulfilled: data points at full capacity with 7~10 K superheating in Fig. 3.32 display lower efficiency than data points at full capacity with 6~9 K superheating. In fact, this is the only case observed for which the above rule was not fulfilled. Some other parameters, like the environment temperature (the compressor is suited outside) or the charge of refrigerant and oil could have some influence.

Experimental data about volumetric efficiency versus pressure ratio for all test runs performed are reported in Fig. 3.33. As expected, the volumetric efficiency decreases with pressure ratios. It is very interesting to notice that data points about configurations with IHX a clear trend versus pressure ratio; on the contrary, data about configurations without IHX is much more scattered and displays considerably lower volumetric efficiency.

At full capacity with IHX the volumetric efficiency varies from around 0.82 up to 0.89, but without IHX experimental values as low as 0.73 have been measured.

Some of the data points of Fig. 3.33 for configurations without IHX are reported again in Fig. 3.34, using the same series as in Fig. 3.32. Quite clear trends can now be seen and the same relationship between the different series found in the graph for the global efficiency is seen in the graph for the volumetric efficiency.

The main conclusion regarding all the experimental data reported is that the use of an internal heat exchanger does have an influence on the efficiency of the compressor, since it increases both the volumetric and the global efficiency.

The volumetric efficiency seems to be the parameter most influenced by the superheating at suction and discharge of the compressor. In the opinion of the writer,

when these two values are too low, the viscosity of the oil is too low, and the sealing effect of the lubricant in the cylinder is reduced; internal leakages increases and this have a remarkable influence on the global efficiency since a part of the volumetric flow rate is compressed (spending electric power) but not actually used.

It could be interesting to try to estimate the actual viscosity of the oil at different operating conditions. Data from Bitzer about the solubility of propane on the mineral oil used in the heat pump (i.e. Shell Clavus G68) and about viscosity of propane-mineral oil mixtures are reported in Fig. 3.35 and Fig. 3.36.

The temperature of the cylinder varies on space and time, therefore it could be difficult to estimate a meaningful average value for the oil temperature. Furthermore, different parts of the compressor would be at different temperatures and higher temperatures are expected at partial load, because of the lower refrigerant mass flow rate and lower cooling of the electric motor.

In Fig. 3.35 and Fig. 3.36 the typical stable operation for the compressor, the starting from standstill condition with crankcase heater and the starting from standstill condition without crankcase heater are compared. The ambient temperature is assumed to be 20°C in this estimation.

At stable operation with 5°C evaporating temperature and 50°C condensing temperature, the estimated discharge temperature is 79°C and the estimated oil temperature is 49°C; at these conditions the percentage of oil in the oil-refrigerant mixture is around 7% and the viscosity is around 9 cSt.

When starting from standstill the pressure in the compressor is assumed to be 8.5 bar. When using the crankcase heater, the temperature of the oil is expected to be 40°C, at these conditions the percentage of oil in the oil-refrigerant mixture is 17% and the viscosity is around 4 cSt. If not using the crankcase heater, the percentage of oil in the oil-refrigerant mixture would be 60% and the viscosity would be around 1 cSt.

Furthermore, with 4.5 L of oil, when starting from standstill when using the crankcase heater, 26 L of propane vapour are produced because of the degassing effect of the oil-refrigerant mixture. Without crankcase heater, the huge volume of 286 L of propane vapour would be produced, this causing the danger of heavy liquid slugging.

It is clear from this estimation that the use of a crankcase heater is needed, since starting the compressor at such low oil viscosity would be harmful.

The graphs in Fig. 3.35 and Fig. 3.36 can be used to try to estimate the influence of the use of the internal heat exchanger on the solubility of the oil. At 12-7°C, 40-45°C water temperature conditions the evaporating pressure is around 5 bar and the measured suction and discharge temperatures were around 9°C and 73°C. To a first approximation, the oil temperature is computed here as the average of suction and discharge temperature, i.e. around 40°C. At these conditions, the percentage of oil in the oil-refrigerant mixture is expected to be around 8%.

If using the internal heat exchanger, both the suction and discharge compressor temperatures are increased by around the 20 K, therefore the oil temperature is estimated to be around 60°C. At these conditions, the percentage of oil in the oil-refrigerant mixture is expected to decrease from around 8% down to 5%.

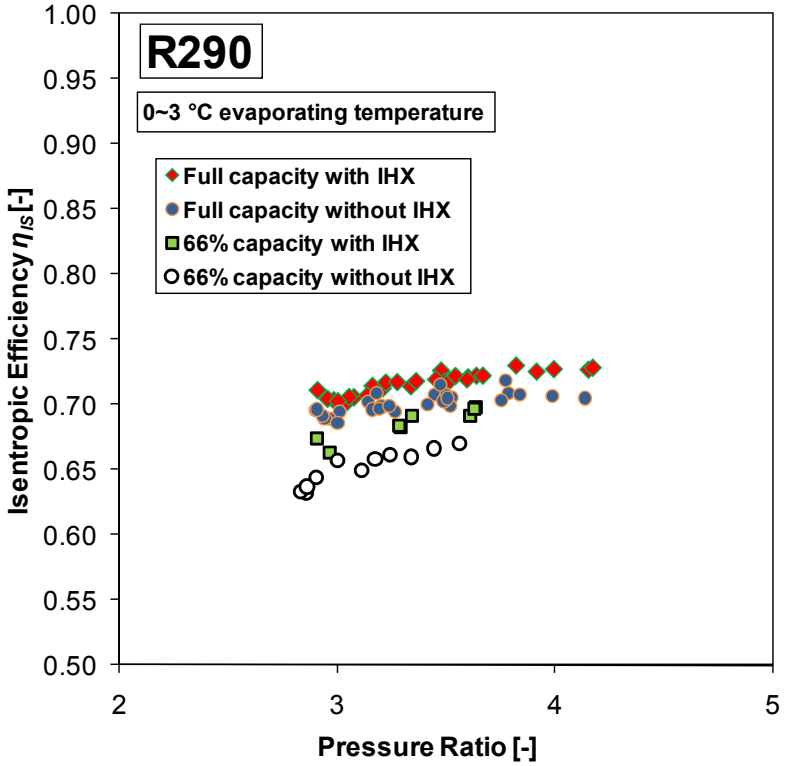

Fig. 3.30. Isentropic efficiency versus pressure ratio for all the test runs.

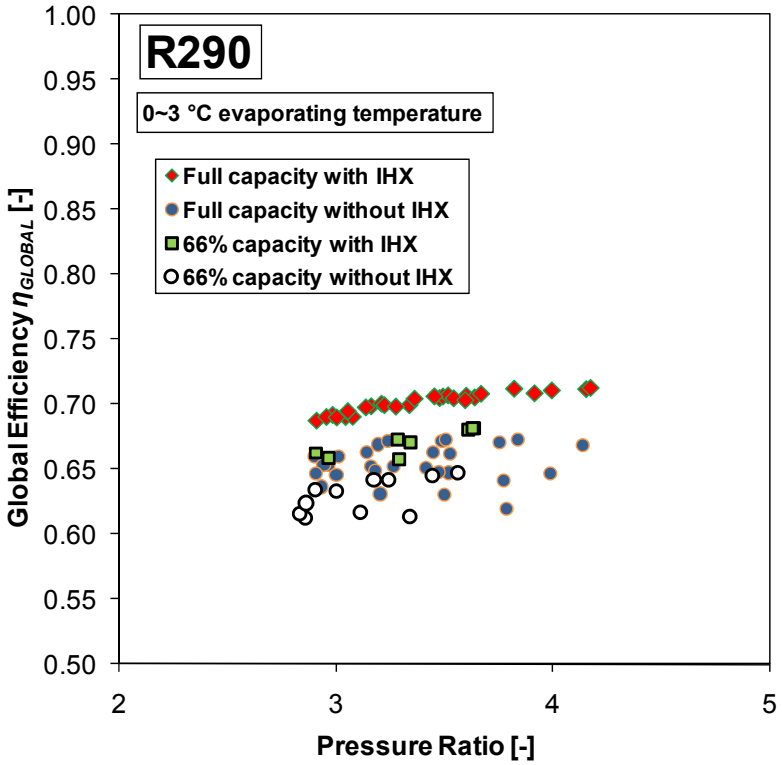

Fig. 3.31. Global efficiency versus pressure ratio for all the test runs.

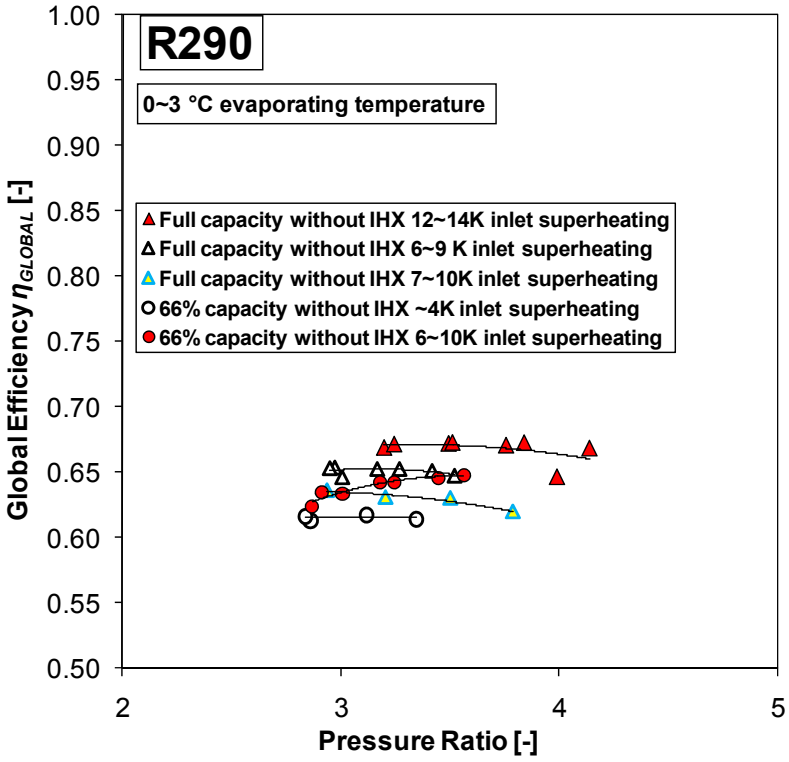

Fig. 3.32. Global efficiency versus pressure ratio for some test runs without IHX at fixed expansion valve setting.

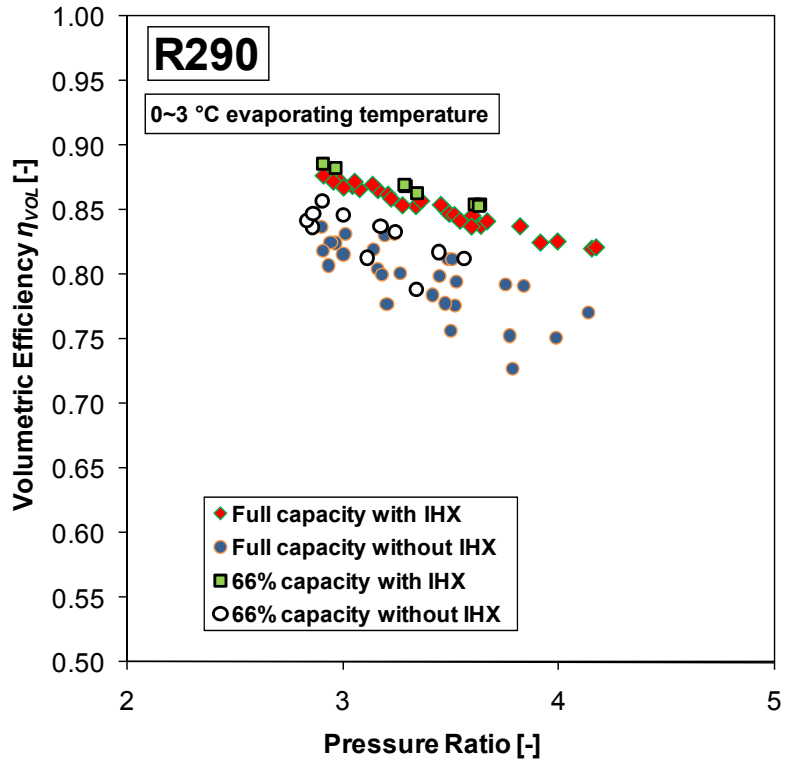

Fig. 3.33. Volumetric efficiency versus pressure ratio for all the test runs.

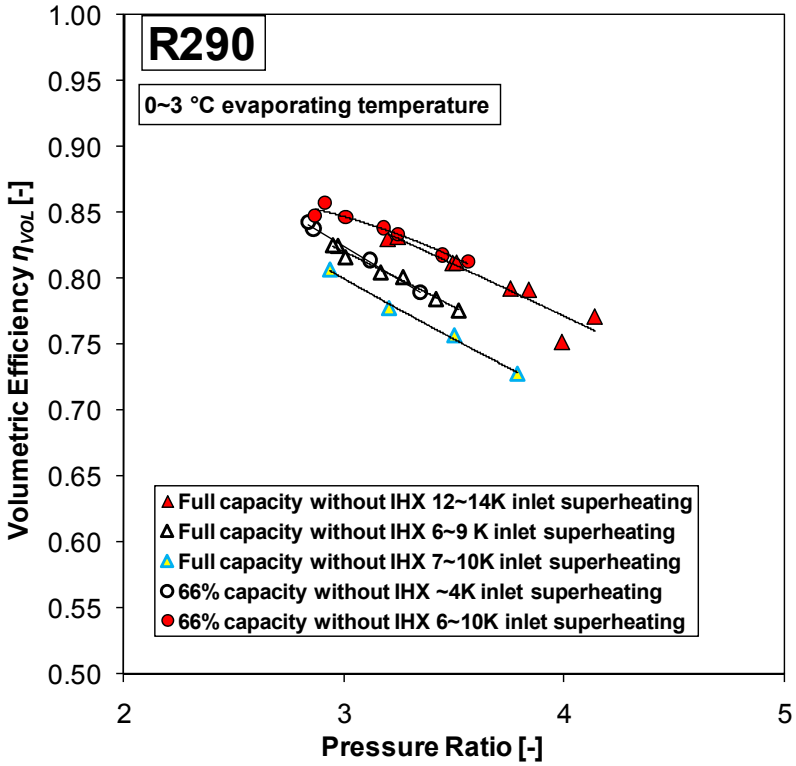

Fig. 3.34. Volumetric efficiency versus pressure ratio for some test runs without IHX at fixed expansion valve setting.

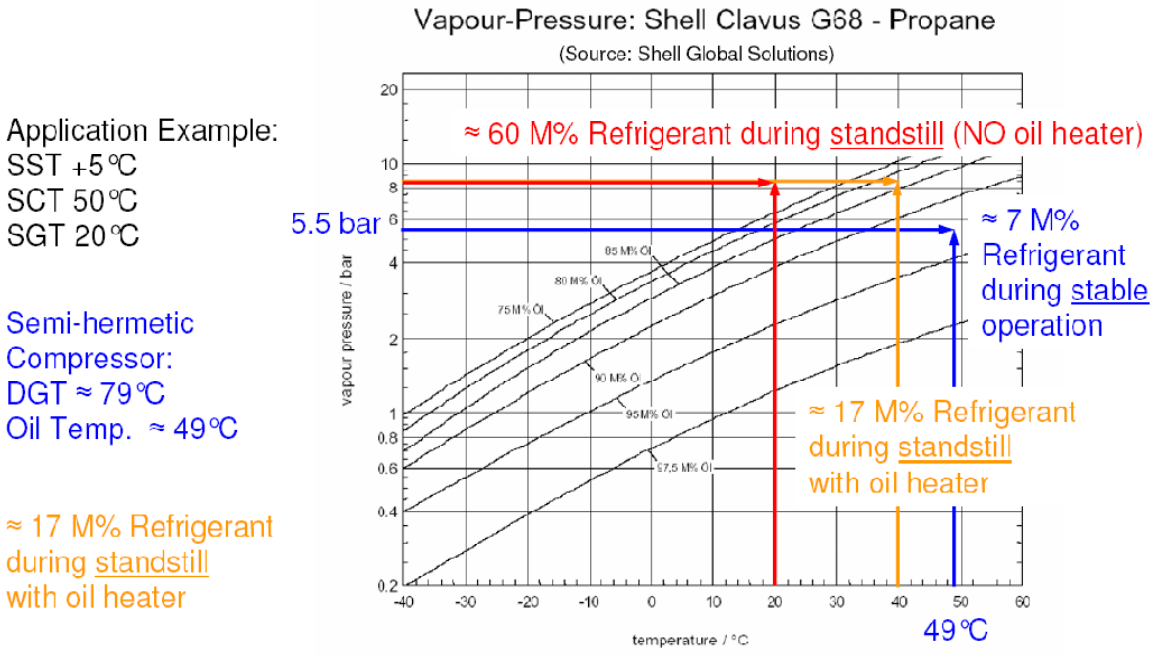

Fig. 3.35. Solubility of propane on mineral oil Shell Clavus G68. From Bitzer, private communication.

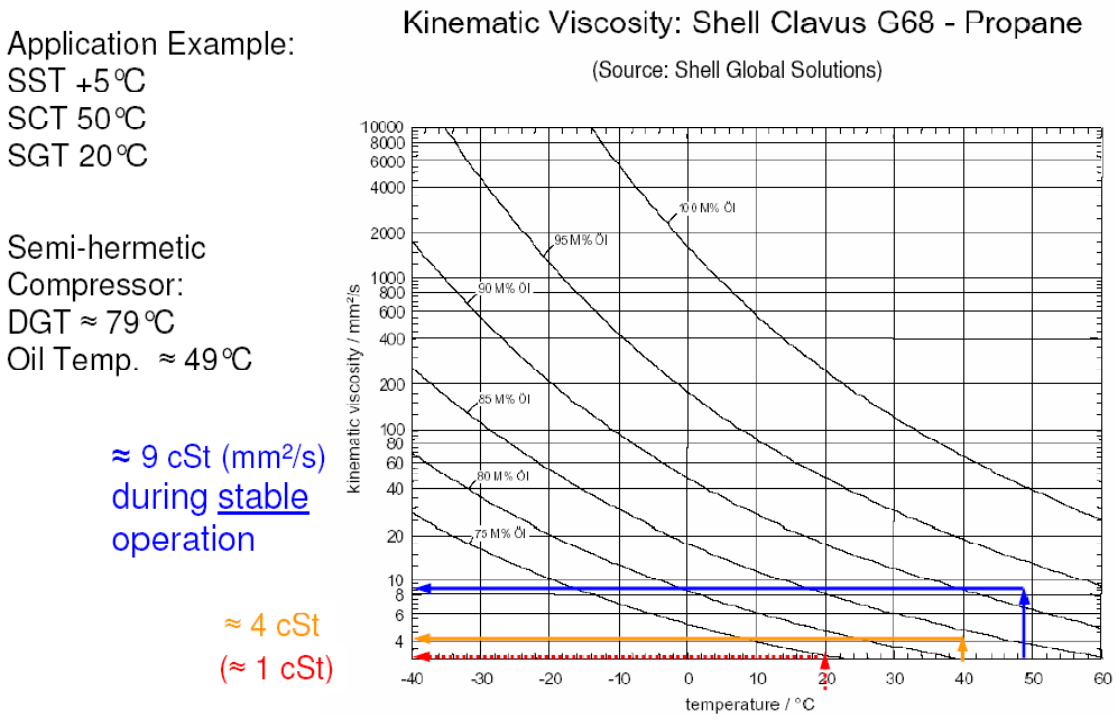

Fig. 3.36. Viscosity of propane-mineral oil mixtures. From Bitzer, private communication.

3.6.8 Capacity control

Since during the actual operation of heating and refrigeration equipment the heating and cooling capacities provided must be controlled according to the actual demands, the energy efficiency at partial load operation is a key factor for the energy seasonal performance.

The use of an inverter is well known to be a very good solution to control the mass flow rate provided by the compressor (and so the heating or cooling capacities) in order to match exactly the energy demand with very low energy loss.

In the propane heat pump, no inverter is used, but a two step capacity control (100%-66%) is allowed by the reciprocating semihermetic compressor installed. The capacity control is based on the principle of suction shut-off. When the capacity is switched to 66% the suction-side gas flow to two cylinders (over six total cylinders) is shut off by means of a control piston. In part-load operation the pistons of the switched off cylinders run idle without gas pressure.

At such operating conditions the mechanical and electrical losses are expected to increase, and the temperature of the compressor is expected to be higher because of the lower mass flow rate and the reduced motor cooling.

Experimental data of coefficient of performance in heating mode obtained at full and 66% capacity is compared in Fig. 3.37 (for the configuration with minichannel condenser and IHX) and Fig. 3.38 (for the configurations with minichannel condenser and without IHX). Data is plotted versus the temperature of the hot water at the outlet of the condenser. The uncertainty in the measurement of the heating capacity is reported, with 95% confidence level, in the graphs.

As one can see, very similar values are measured for operation at 66% capacity as compared to full capacity, and the difference between the two cases is within the uncertainty of the COP measurement.

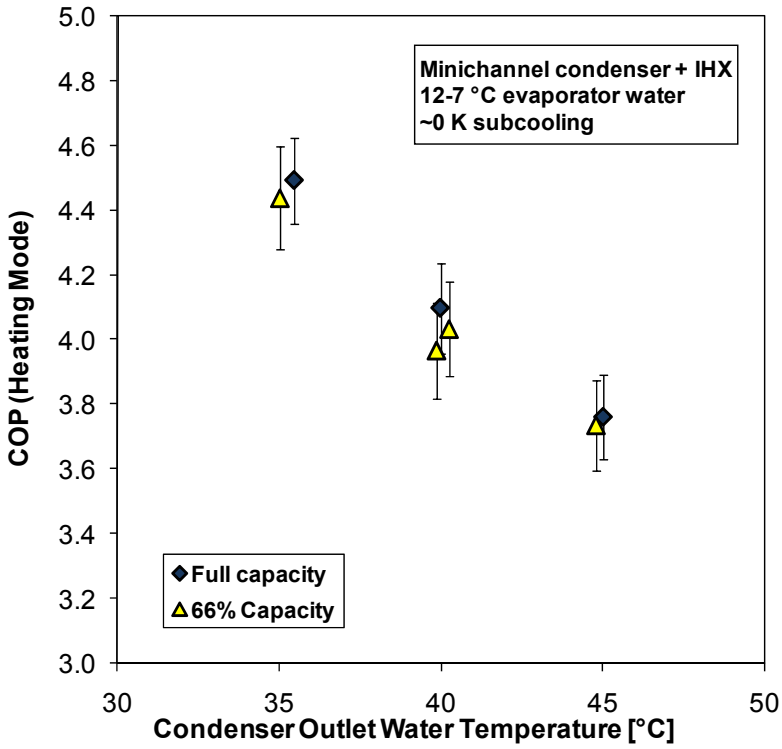

Fig. 3.37. COP versus condenser outlet water temperature for the configuration minichannel condenser + IHX at full and 66% capacity.

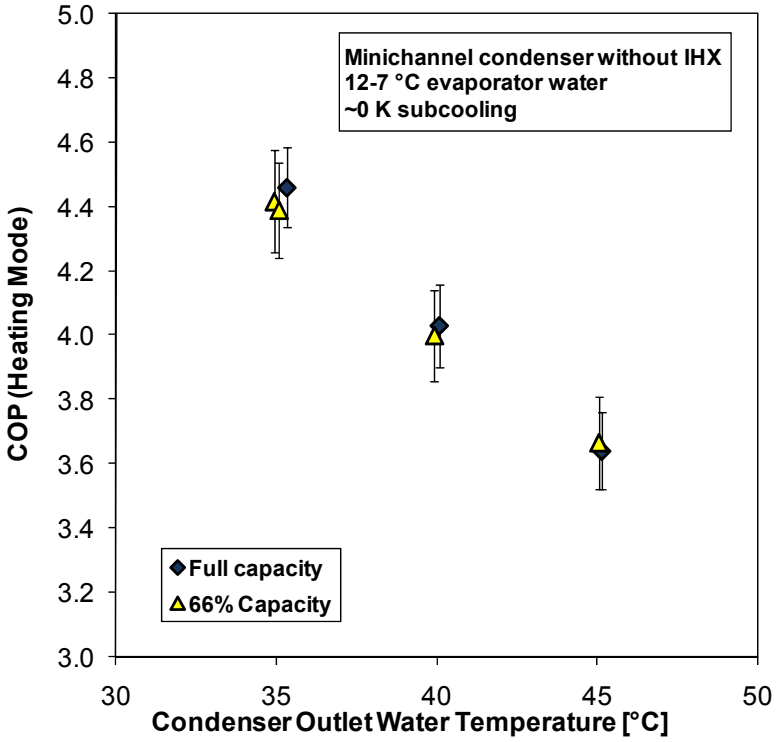

Fig. 3.38. COP (heating mode) versus condenser outlet water temperature for the configuration with minichannel condenser and without IHX at full and 66% capacity

Chapter 4.

VOF simulation of condensation in minichannel

4.1 The Volume Of Fluid (VOF) method

A number of different methods (i.e. VOF, Direct Interface Tracking, Level Set, Phase Field, etc.) are nowadays available for the direct simulation of multiphase flows. While in the traditional methods all the phases are considered to be present in the elementary volume cell, and the interaction between phases is computed by means of semi-empirical closure laws, in the direct simulations all scales of motions and all interfacial configurations are directly solved: volume cells with much smaller dimensions are therefore required in order to track the interface and the computational demand is high.

In this work, the method of multiphase flow direct simulation called Volume Of Fluid (VOF) has been used. This method is able to compute multiphase flows of immiscible fluids tracking the motion of the interface between them. Even if the first VOF-methods date back to the end of the 70's and the code SOLA-VOF developed at the Los Alamos National Laboratory was already available in 1980 (Nichols *et al.*, 1980), it's only nowadays that, thanks to the increased computational capabilities, this technique can actually be used to simulate quite complex flows. The simulations presented in this work and in the following chapter have been obtained by means of the VOF method implemented in the finite volume method code FLUENT.

In the VOF method a scalar field called "volume fraction" and representing the portion of the volume of the cell (or the area for 2D problems) filled with one phase is used. Considering a two-phase vapour-liquid flow, when the liquid volume fraction α_L in a cell is equal to 1 this means that the cell is inside the liquid phase and when $\alpha_L = 0$ this means that it is inside the vapour phase, while the condition $0 < \alpha_L < 1$ represents a cell including a portion of the gas-liquid interface. In an incompressible flow, mass conservation is equivalent to conservation of volume and hence of the volume fraction α. An example of volume fraction field corresponding to a circle arc interface is shown in Fig. 4.1.

In general, the VOF method will be accurate whenever the radius of curvature of the interface is large with respect to the mesh size.

Volume fractions of all phases sum to unity; in the considered case of a vapour-liquid flow this leads to the following constraint:

$$\alpha_L + \alpha_G = 1 \tag{4.1}$$

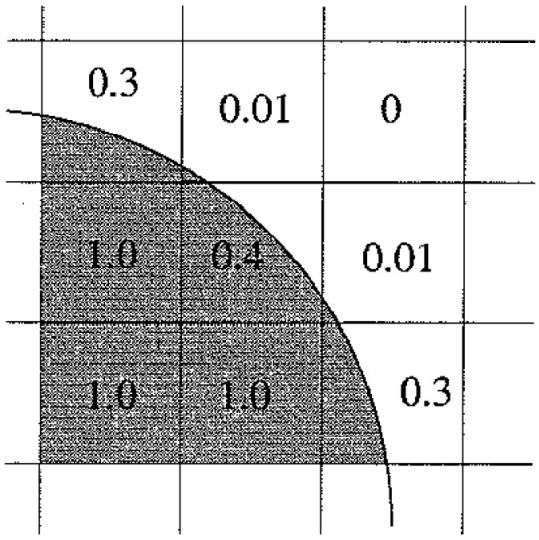

Fig. 4.1. Volume fraction for a smooth circular arc over a square grid.

In general, a VOF algorithm solves the problem of updating the field of the volume fraction α given the fixed mesh, the velocity field and the field of the volume fraction α at the previous step. The algorithm is divided into two parts: a reconstruction step and a propagation step. The problem of interface reconstruction is that of finding an approximation to the section of the interface in each cut cell, by knowing only the volume fraction in that cell and in the neighbouring ones. Once the interface has been reconstructed, its motion by the underlying flow field is modelled by a suitable advection algorithm.

The simplest types of VOF methods are first order in the accuracy of the reconstruction of the interface, which typically is made up of a sequence of segments aligned with the grid. More accurate VOF techniques are now known as Piecewise Linear Interface Construction (PLIC) methods and they attempt to fit the interface through piecewise linear segments.

In the commercial code FLUENT, when the explicit scheme is used for time discretization, a PLIC scheme (i.e. the "geometric reconstruction" scheme) based on the work of Youngs (1982) is available. When the implicit scheme is used, the "geometric reconstruction" scheme is not available, and the most accurate scheme available is the modified High Resolution Interface Capturing (HRIC) scheme, which consists of a non linear blend of upwind and downwind differencing. The modified HRIC scheme is not as accurate as the "geometric reconstruction" one, but provides improved accuracy for the VOF calculations when compared to second order-schemes, and is less computationally expensive than the "geometric reconstruction" scheme (Fluent Inc., 2006).

The two-phase mixture is considered in the VOF method as a single fluid with properties changing depending on the value of the volume fraction α. As an example, the density ρ and the viscosity μ for a vapour-liquid mixture are locally computed for each cell as follows:

$$\rho = \rho_L \alpha_L + \rho_G (1 - \alpha_L) \tag{4.2}$$

$$\mu = \mu_L \alpha_L + \mu_G (1 - \alpha_L) \tag{4.3}$$

All other properties (i.e. thermal conductivity, heat capacity, etc.) are computed by means of an arithmetic mean as shown in Eq. (4.2) and Eq. (4.3). In some cases, however, it has been found to be preferable to use a harmonic means for the viscosity (this in fact is the exact value when the flow velocity is parallel to the interface).

The following continuity equation for the liquid volume fraction α_L is solved:

$$\frac{\partial \alpha_L}{\partial t} + \nabla \cdot (\vec{u} \alpha_L) = \frac{S}{\rho_L} \tag{4.4}$$

where u is the velocity and S is a mass source term due to phase change.

Regarding to the momentum equation, the usual Navier-Stokes equations are used in the cells where only one of the two phases are present (i.e. $\alpha_L = 0$ or $\alpha_L = 1$). At the interface, instead, singularities appear, and the force due to the surface tension, shown by the last term in the following equation, must be taken into account:

$$\frac{\partial}{\partial t}(\rho \vec{u}) + \nabla \cdot (\rho \vec{u} \vec{u}) = -\nabla p + \nabla \cdot [\mu (\nabla \vec{u} + \nabla \vec{u}^T)] + \rho \vec{g} + \vec{F} \tag{4.5}$$

The effect of surface tension is written in terms of a pressure jump across the interface. The volume force due to the effect of the surface tension is computed in FLUENT by means of the CSF (Continuum Surface Force) model proposed by Brackbill *et al.* (1992). In this model, the surface tension σ is considered constant.

The vapour-liquid surface normal n is computed as the gradient of the volume fraction scalar:

$$n = \nabla \alpha_L \tag{4.6}$$

The required value of surface curvature κ is then numerically obtained as the divergence of the normalized surface normal:

$$\kappa = \nabla \cdot \frac{n}{|n|} \tag{4.7}$$

The volumetric force in Eq. (4.5) due to the surface tension is finally computed by the VOF method implemented in FLUENT as follows:

$$\vec{F} = \sigma_{LG} \frac{\rho \kappa_L \nabla \alpha_L}{0.5(\rho_L + \rho_G)} \tag{4.8}$$

where ρ is the volume-averaged density computed using Eq. (4.2).

The calculation of surface tension effects on triangular and tetrahedral meshes is not as accurate as on quadrilateral and hexahedral meshes, therefore in FLUENT the

region where surface tension effects are most important should be meshed with quadrilaterals or hexahedra (Fluent Inc., 2006).

All scalar values are shared by the phase throughout the domain, therefore no particular issues for the treatment of energy or turbulence equations arise when using the VOF method. These equations are solved in the same way as for the case of single-phase flow, providing that the physical properties for each cell are averaged as in Eq. (4.2) and Eq. (4.3).

4.2 Turbulence modelling

In this Section a VOF simulation of condensation of R134a inside a minichannel with internal diameter D = 0.001 m is proposed. In the simulation, vapour quality at the inlet is around 1 and the fluid is condensated till reaching around 0.5 quality. The simulation has been performed at mass flux G = 200 kg $m^{-2}s^{-1}$, which is a quite low value for the case of condensation inside channels.

The gas only Reynolds number Re_{GO} at this condition is around 15500, therefore, at least inside the vapour phase, the flow cannot be treated as laminar, and some turbulence modelling is needed.

Regarding the liquid phase, the value of the liquid only Reynolds number Re_{LO} at this condition is around 1400. If trying to estimate the Reynolds number for the two phases based on the actual cross sectional areas occupied by the two phases, it must be considered that the typical flow regime is annular flow with very high values of the void fraction even at low vapour quality. The cross sectional area occupied by the vapour phase is close to the total cross sectional area of the tube and the actual Re for the gas phase at 0.5 vapour quality (which is the lowest in the range of conditions considered in the simulation) is around 7000. The liquid phase, instead, flows inside an annular section with small thickness, therefore the actual Reynolds number for the liquid phase is much smaller than the Re_{LO}.

For these reasons, it has been assumed in the simulation that the flow is laminar inside the liquid phase and turbulent inside the vapour phase.

Available turbulence models for CFD computations are semi-empirical models which have been developed for single-phase flows and a lack of accurate knowledge about their applicability for the simulation of two-phase flow with the presence of a gas-liquid interface exists.

Among the turbulence models based on the Reynolds Averaged Navier Stokes equations (RANS) approach, the two most widely used models for CFD computations are the k-ε model and the k-ω model. Some examples can be found in the literature about the simulation of stratified gas-liquid flows using both these turbulence models (e.g. Lorencez *et al.* 1997, de Sampaio, *et al.* 2008, Berthelsen and Ytrehus, 2005).

The k-ε is the most widely used and the best tested model of all the two-equation models for turbulence; however, a modified k-ω model has been used in the simulation since k-ω model is considered substantially more accurate than k-ε model in the near wall layers and a good calculation of the near wall region is crucial for the simulation of condensation inside tubes.

The standard k-ω model implemented in FLUENT is based on the Wilcox (1998) model. The following transport equations are used for the turbulent kinetic energy k and the specific dissipation rate ω, which can also be thought as the ratio of ε to k:

$$\frac{\partial}{\partial t}(\rho k) + \frac{\partial}{\partial x_i}(\rho k u_i) = \frac{\partial}{\partial x_j}\left(\Gamma_k \frac{\partial k}{\partial x_j}\right) + G_k - Y_k \tag{4.9}$$

$$\frac{\partial}{\partial t}(\rho \omega) + \frac{\partial}{\partial x_i}(\rho \omega u_i) = \frac{\partial}{\partial x_j}\left(\Gamma_\omega \frac{\partial \omega}{\partial x_j}\right) + G_\omega - Y_\omega \tag{4.10}$$

where the G and Y terms in both equations represents the production and dissipation of k and ω. The effective diffusivities Γ_k and Γ_ω in Eq. (4.9) and Eq. (4.10) are computed for the standard k-ω model as follows:

$$\Gamma_k = \Gamma_\omega = \mu + 0.5\mu_t \tag{4.11}$$

where μ is the molecular viscosity and μ_t is the turbulent viscosity.

The scalar fields of k and ω are solved in order to compute the local values of turbulent viscosity μ_t which is added to the molecular viscosity to compute the effective viscosity to use in the Reynolds Averaged Navier Stokes (RANS) equation. The turbulence viscosity is computed for the standard k-ω model as follows:

$$\mu_t = \alpha^* \frac{\rho k}{\omega} \tag{4.12}$$

In the case of the standard k-ε model, the turbulent viscosity μ_t is computed as follows:

$$\mu_t = C_\mu \frac{\rho k^2}{\varepsilon} \tag{4.13}$$

where C_μ is a constant.

As one can see, since the specific dissipation rate ω can be thought as the ratio of ε to k, the same approach is used by the two models for the calculation of the turbulent viscosity.

The coefficient α^* in Eq. (4.12) is equal to 1 in the high-Reynolds-number form of the k-ω model. In the simulation reported in the present chapter, the low-Reynolds-number form (called "Transitional Flows" option in FLUENT) was used. In this approach, the coefficient α^* damps the turbulent viscosity causing a Low-Reynolds-number correction. The coefficient α^* is given by:

$$\alpha^* = \frac{0.024 + \mathrm{Re}_t / 6}{1 + \mathrm{Re}_t / 6} \tag{4.14}$$

where:

$$\mathrm{Re}_t = \frac{\rho k}{\mu \omega} \tag{4.15}$$

The near wall modelling is very important because solid walls are the main source of vorticity and turbulence. The use of a dumping function allows the use of the same turbulent model also for the cells of the domain close to the wall. If a dumping function is not used, other approaches must be followed, because the equations used for k, ω and ε in the core flow cannot be used in the near wall region. One possible, and computationally inexpensive, solution is not solving the laminar sublayer, imposing

some wall function for the solution of the velocity profile in the near wall region. Another commonly implemented solution is the "two-layer approach": the computational domain is divided into a viscosity affected region and a fully turbulent region and a simplified model (typically a one-equation k model) is used for the near-wall zone.

Regarding to the options available in FLUENT, both the "wall function" approach and the "two-layer" approach (which is called Enhanced Wall Treatment (EWT) in the software) are available for the k-ε model. In both cases the distance from the wall is used as coefficient in the equations for the solution of the low-Re regions.

In the case of the present simulation, the liquid-vapour interface, even if the velocity is not equal to zero for this surface, could be considered as a sort of wall, at least because the flow is believed to be laminar in the liquid film. It is clear that wall function traditionally used for single-phase flows cannot be used in this case. The "two-layer" approach implemented in FLUENT, furthermore, is also not suitable for the present simulation, since it is based on the distance from the wall and in this way the presence of the liquid-vapour interface, which is close to but not coincident with the wall of the tube, is not taken into account.

In the Eq. (4.14) and Eq. (4.15) no such parameters as the distance of the cell from the solid wall are used, but only the physical properties of the fluid and the values of the turbulent quantities. According to the writer, the use of a dumping function for the computation of the turbulent viscosity in the viscosity affected region should therefore be the best option for the computation of the turbulence in the case of the present simulation, where a vapour-liquid annular flow is present, at least among the options available in FLUENT.

Even if some low-Re k-ε models are available in FLUENT, the low-Re k-ω model (called standard k-ω model with "Transitional Flows" option in the software) was chosen for the present simulation, since it is more suitable for this kind of approach. The model, however, was modified in order to impose the condition of laminar flow inside the liquid phase and turbulent flow inside the vapour phase.

Transport equations for k and ω are used in the RANS approach only to compute the local values of effective viscosity (i.e. the sum of molecular viscosity and turbulent viscosity) in the computational domain. In the cells where the turbulent viscosity is equal to zero, the RANS equations correspond to the Navier Stokes equations for the laminar case.

A User Defined Function (UDF) is available in FLUENT to specify a custom turbulent viscosity, and it has been used to modify Eq. (4.12) as follows:

$$\mu_t = \alpha^* \frac{\rho_G k}{\omega} \alpha_G \tag{4.16}$$

where α_G is the vapour phase volume fraction.

The user defined function hooked to the FLUENT code is reported in Table 4.1. Here the numerical value of α_G (i.e. the "*vof*" variable in the UDF) is computed from the value of the local density of the cell (i.e. "*rho*" in the UDF) which is computed by the VOF method as shown by Eq. (4.2). The numerical values of ρ_L, ρ_G and μ_G are used in the UDF, therefore these should be changed in order to use this UDF at different saturation temperature or for a different fluid.

As one can see in Table 4.1, when the vapour phase volume fraction α_G is lower than 0.01 the value of the turbulent viscosity returned by the UDF is zero.

In the cells where only the vapour phase is present, the turbulent viscosity given by Eq. (4.16) is equal to the value given by the low-Re k-ω model. In the cells where only the liquid phase is present, instead, the computed turbulent viscosity is null, therefore the laminar flow is here imposed. At the interface, the turbulent viscosity given by Eq. (4.16) is blended between zero and the value given inside the vapour phase.

The modified function for the turbulent viscosity computation has also a big influence on the fields of the turbulent kinetic energy k and the specific dissipation rate ω, since the turbulent viscosity μ_t is present in the transport equations for k and ω. The turbulent viscosity increases the diffusivities Γ_k and Γ_ω in Eq. (4.9) and Eq. (4.10), but its most important role is played in the production terms G_k and G_ω.

The production of turbulent kinetic energy G_k is modelled in the same way for the k-ε model and the k-ω model as follows:

$$G_k = \mu_t S^2 \tag{4.17}$$

where S is the modulus of the mean rate-of-strain tensor.

As one can see, by fixing to zero the turbulent viscosity in the liquid film in the simulation, also the turbulence production term is suppressed.

Table 4.1. User defined function to specify custom turbulent viscosity function for R134a vapour-liquid mixture at 50°C saturation temperature (ρ_L=1102.3 kg/m^3, ρ_G=66.272 kg/m^3, μ_G=1.2917 e^{-5}).

```
#include "udf.h"

DEFINE_TURBULENT_VISCOSITY(mu_t,c,t)
{
  double k,mut,ret,rho,vof,w;

  k = C_K(c,t);
  w = C_O(c,t);
  rho = C_R(c,t);

  vof = (1102.3-rho)/(1102.3-66.272);
  ret = 66.272*k/w/1.2917e-5;
  mut = ((0.024+ret/6.0)/(1.0+ret/6.0))*66.272*k/w*vof;

 if (vof<0.01)
       {
       return 0.000;
       }
    else
       {
       return mut;
       }
}
```

The production of the specific dissipation rate ω, is modelled as follows:

$$G_\omega = G_k \alpha \frac{\omega}{k} \tag{4.18}$$

where α is a damping factor for Low-Re correction.

The production of the specific dissipation rate is therefore also suppressed inside the film of liquid.

Some examples of profiles of axial velocity, turbulent kinetic energy and turbulent and effective viscosity are here proposed. Results obtained from simulations of adiabatic annular flow of R134a using the high-Reynolds-number forms of the standard k-ε model and the standard k-ω model are compared against the results obtained in the simulation of condensation using the modified low-Re k-ω model here proposed. The aim of this comparison is just to show, from a qualitative point of view, the influence of the model of turbulence used on the computed two-phase flow.

All data reported have been obtained at mass flux G = 200 kg m^{-2}s^{-1}. The vapour quality is 0.5 in the simulations of adiabatic flow obtained with the standard k-ε and k-ω model and 0.6 in the simulation of condensation obtained using the modified low-Re k-ω model. For all cases the void fraction is around 0.85 and the flow regime is annular, with a thicker liquid film on the bottom of the tube as compared to the top.

The Cartesian axis convention used in this chapter is shown in Fig. 4.2 together with the gravitational acceleration vector. All graphs shown in this chapter display the profiles of axial velocity and turbulent parameters along the y-axis.

Examples of profiles of turbulent kinetic energy k obtained with the standard turbulence models and the modified low-Re k-ω model are shown in Fig. 4.3 and Fig. 4.4, respectively. In these and in the following graphs of this section, diamonds represent the position of the vapour-liquid interface. It can be seen that the thickness of the liquid film at the bottom of the tube (i.e. at negative values of y coordinate) is much larger than the thickness at the top of the tube.

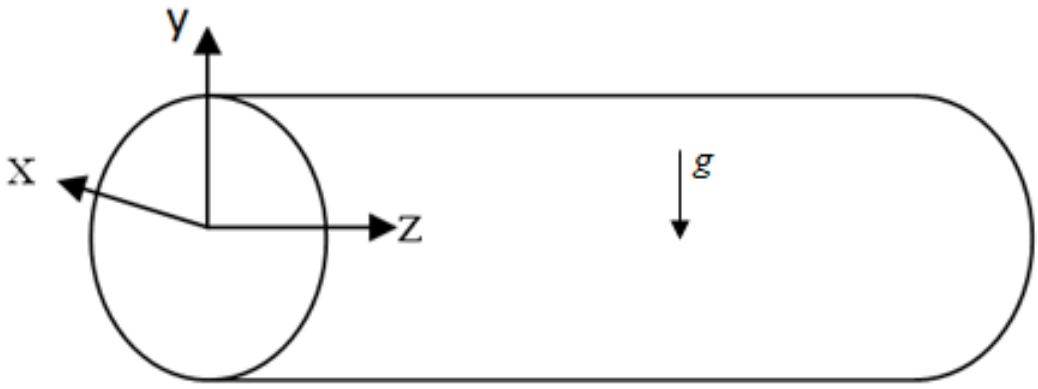

Fig. 4.2. Cartesian axis convention for the minichannel.

High values of turbulence are produced in the region of vapour phase close to the interface, because of the high gradients of velocity in this region.

The turbulent kinetic energy k is set equal to zero at the tube wall as boundary condition. As one can see, while some level of turbulence is shown in Fig. 4.3 inside the liquid region at the bottom of the tube, when using the modified low-Re k-ω model this is very low inside all the liquid phase, since the production of turbulent kinetic energy is suppressed as described above.

The corresponding profiles of turbulent viscosity are compared in Fig. 4.5 and Fig. 4.6. When the standard turbulence models are used, the turbulent viscosity is computed according to Eq. (4.12) and Eq. (4.13). Across the vapour-liquid interface there is a discontinuity in the value of the density of the fluid, which gives rise to the high peaks for the computed values of the turbulent viscosity shown in Fig. 4.5. Such a solution has been considered not physically sound, and the observation of such kind of results has been the main reason for the modification of the turbulence model.

When using Eq. (4.16), as shown in the graph in Fig. 4.6, the turbulent viscosity is suppressed in the liquid phase, this ensuring that the computed flow is laminar in this region. Furthermore, it must be noticed that also the solution in the vapour core is modified, since much lower values of turbulent viscosity are obtained as compared to Fig. 4.5.

The profiles of the effective turbulent viscosity (i.e. the sum of turbulent and molecular viscosity) are shown in Fig. 4.7 and Fig. 4.8.

Finally, the profiles of the axial velocity are reported in Fig. 4.9 and Fig. 4.10. As one can see, the computed velocity profile is absolutely dependent on the modelling of turbulence. When the standard models are used, the profile of the velocity versus y-coordinate in the region of bottom liquid film next to the interface is almost horizontal because of the peak of the effective viscosity. When the modified low-Re k-ω model is used, instead, the flow is laminar and the velocity profile is linear.

The computed velocity inside the vapour core is also very different when the modified low-Re k-ω model is used as compared to the standard k-ε and k-ω models.

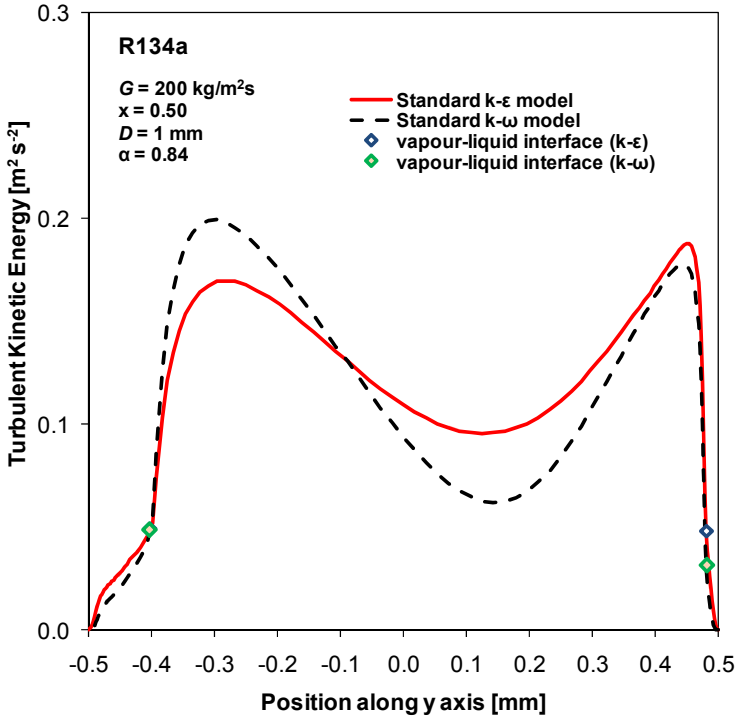

Fig. 4.3. Example of turbulent kinetic energy distribution along y-axis for annular flow of R134a when using standard k-ε and standard k-ω models.

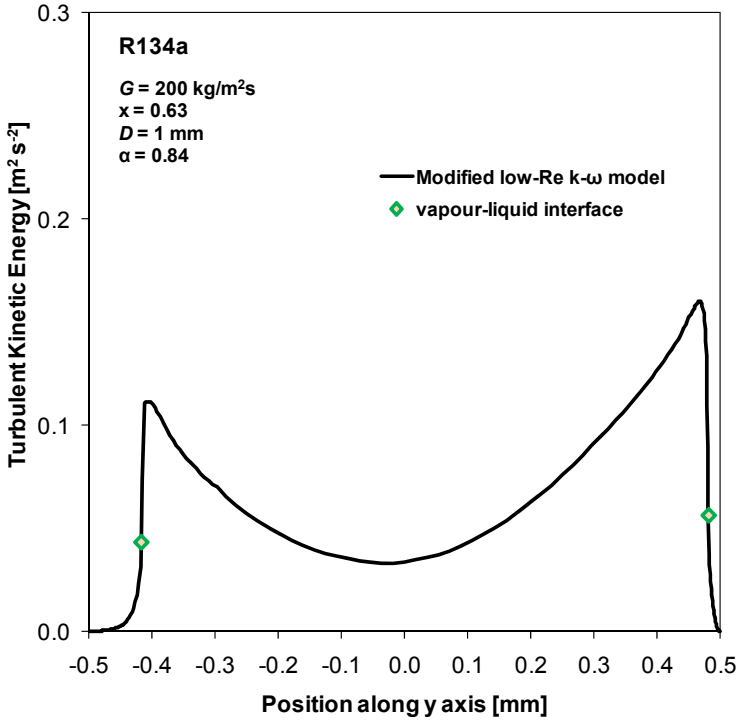

Fig. 4.4. Example of turbulent kinetic energy distribution along y-axis for annular flow of R134a when using the proposed modified low-Re k-ω model.

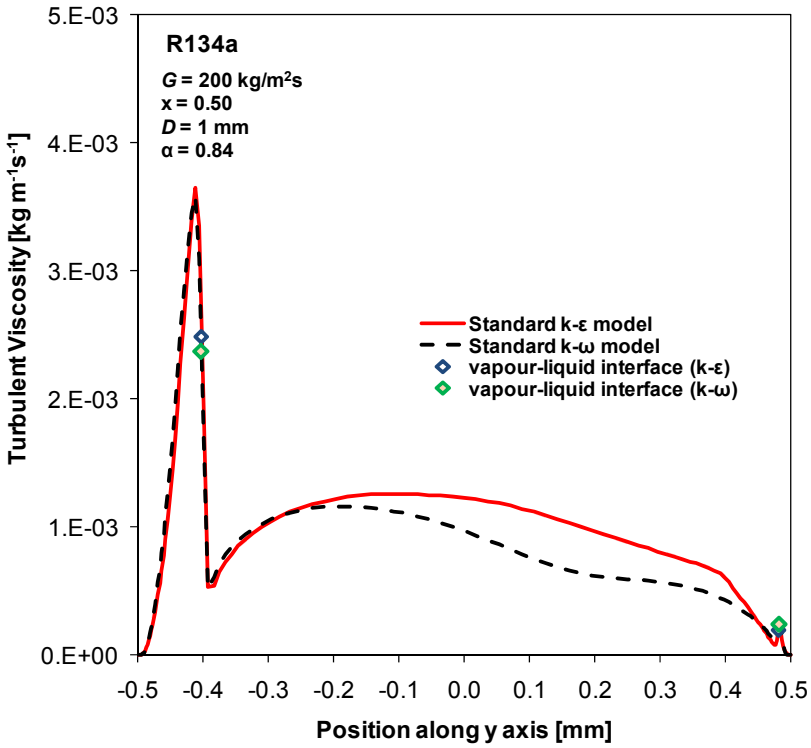

Fig. 4.5. Example of turbulent viscosity distribution along y-axis for annular flow of R134a when using standard k-ε and standard k-ω models.

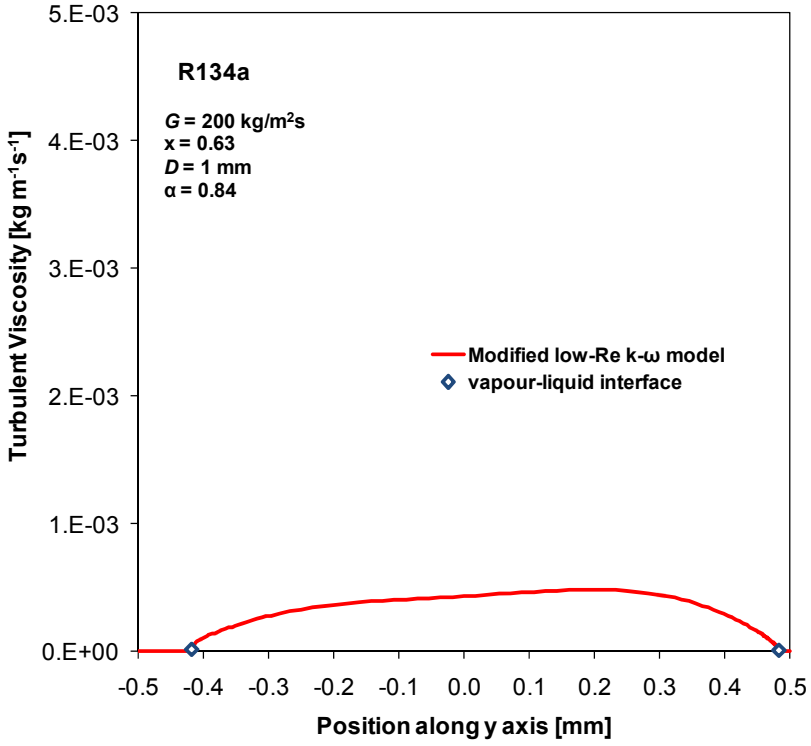

Fig. 4.6. Example of turbulent viscosity distribution along y-axis for annular flow of R134a when using the proposed modified low-Re k-ω model.

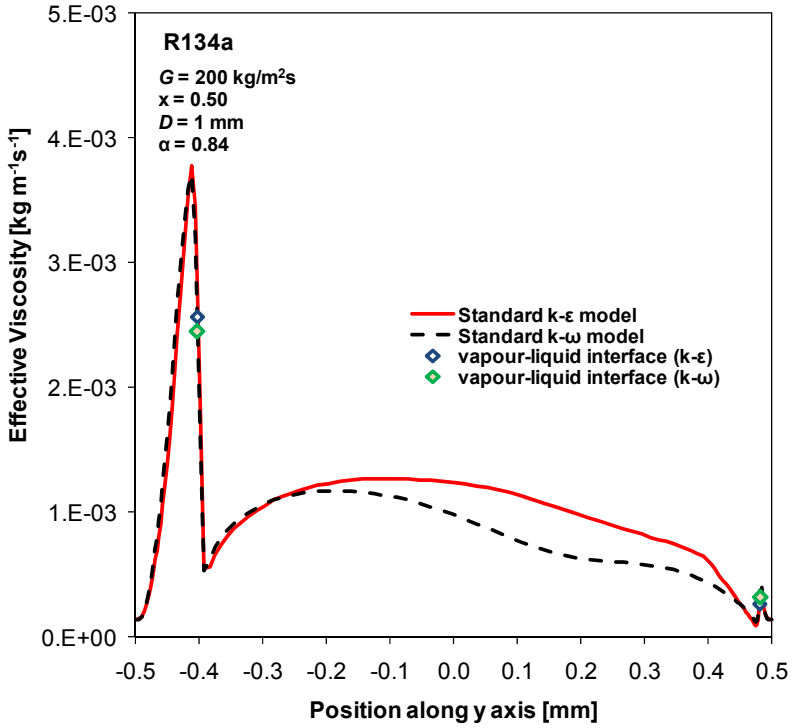

Fig. 4.7. Example of effective viscosity distribution along y-axis for annular flow of R134a when using standard k-ε and standard k-ω models.

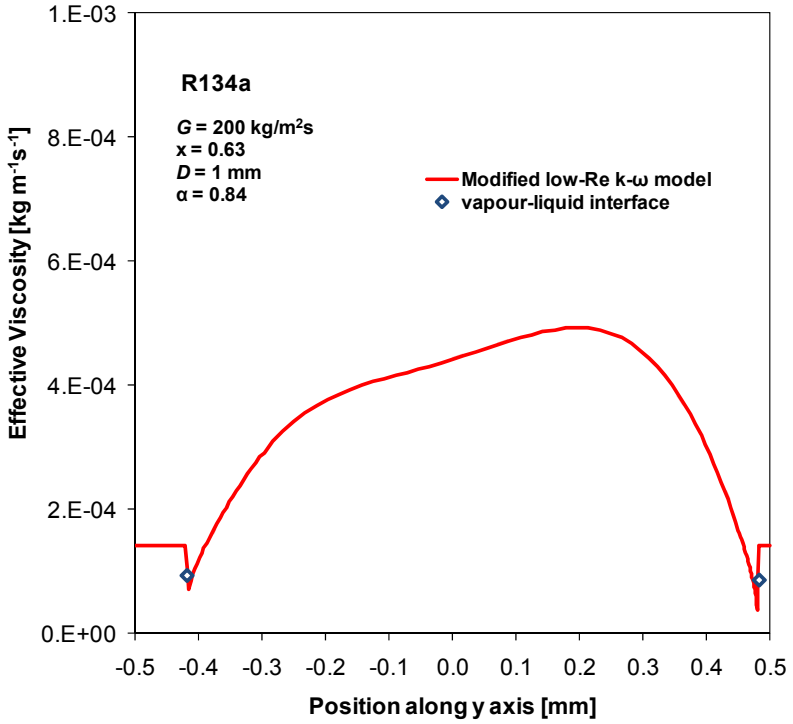

Fig. 4.8. Example of effective viscosity distribution along y-axis for annular flow of R134a when using the proposed modified low-Re k-ω model.

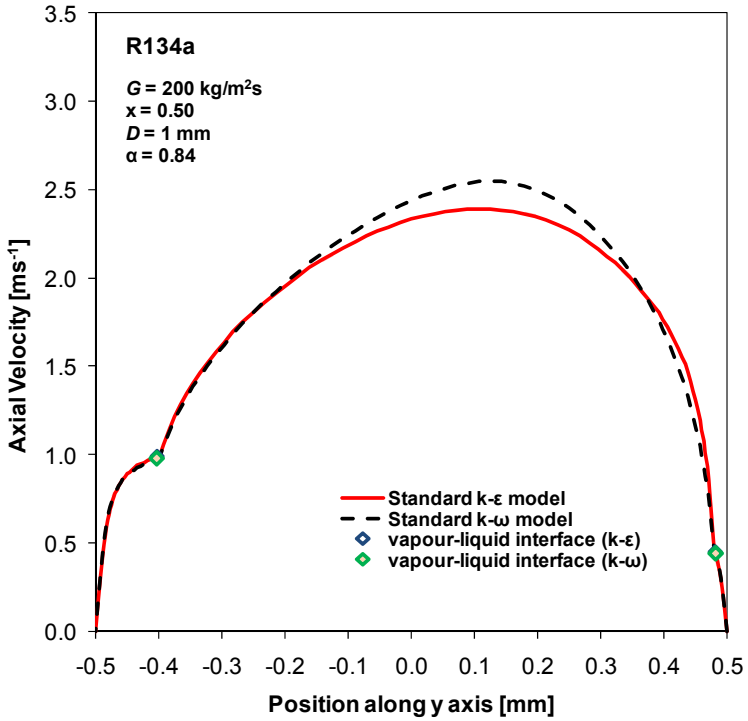

Fig. 4.9. Example of axial velocity distribution along y-axis for annular flow of R134a when using standard *k-ε* and standard *k-ω* models.

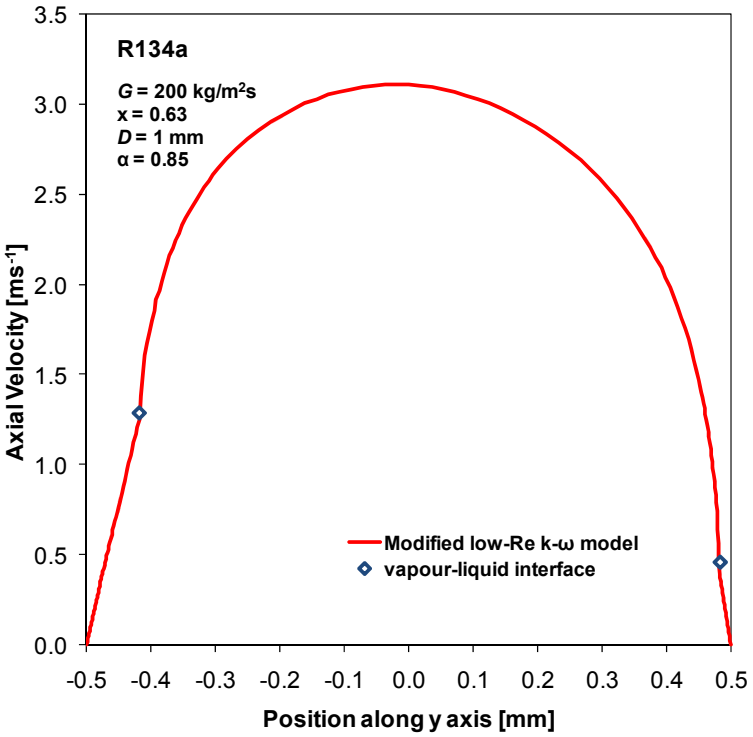

Fig. 4.10. Example of axial velocity distribution along y-axis for annular flow of R134a when using the proposed modified low-Re *k-ω* model.

4.3 Phase change modelling

In the case of condensation of a pure fluid, the vapour-liquid interfacial temperature can be assumed to be the saturation temperature. This assumption has been imposed as boundary conditions in the simulations.

The numerical technique used to fix the interfacial temperature is described by the following equation:

$$\begin{aligned} S &= -r_L \alpha_L \rho_L \frac{T - T_{SAT}}{T_{SAT}} \qquad T \geq T_{SAT} \\ S &= r_G \alpha_G \rho_G \frac{T_{SAT} - T}{T_{SAT}} \qquad T \leq T_{SAT} \end{aligned} \tag{4.19}$$

where S is the source term due to phase change in the continuity equation for the liquid volume fraction, α is the volume fraction, ρ is the density, T is the temperature of the cell and r is a positive numerical coefficient.

The continuity equations for the two phases are here reported:

$$\frac{\partial \alpha_L}{\partial t} + \nabla \cdot (\vec{u} \alpha_L) = \frac{S}{\rho_L} \tag{4.20}$$

$$\frac{\partial \alpha_G}{\partial t} + \nabla \cdot (\vec{u} \alpha_G) = -\frac{S}{\rho_G} \tag{4.21}$$

Eq. (4.19) describes a numerical method to fix the temperature of the cells belonging to the vapour-liquid interface at the saturation temperature without imposing any kind of physical model about the heat and mass transfer process. If at some step of the numerical simulation the temperature of a cell in the domain is higher than the saturation temperature, the first of the two equations (4.19) is used: as one can see, if this cell belongs to the gas phase (i.e. $\alpha_L = 0$) no mass transfer is computed (i.e. $S = 0$); if this cell belongs to the liquid phase (i.e. $\alpha_L > 0$), however, a negative value of the source term S, which means mass transfer from the liquid to the vapour phase, is computed. The corresponding source term due to the latent heat of condensation is used in the energy equation and the temperature of that cell is decreased by the evaporation.

If at some point the temperature of a cell in the domain is lower than the saturation temperature, the second equation is used: if this cell belongs to the liquid phase (i.e. $\alpha_G = 0$) no mass transfer is computed, while if this cell belongs to the vapour phase (i.e. $\alpha_G > 0$) a positive value of the source term S, which means mass transfer from the vapour to the liquid, is computed and the temperature of the cell is increased by the corresponding latent heat of condensation.

The presence of cells in the vapour phase with temperature lower than the saturation temperature, as well as the presence of cells in the liquid phase with temperature higher than the saturation temperature is in this way avoided. It must be noticed that the amount of mass transferring from one phase to the other at each computational step, as described by Eq. (4.19) is arbitrary fixed. However, mass,

momentum and energy are conserved at every step and at convergence the vapour-liquid interface should reach the saturation temperature, while all cells belonging to the liquid phase should reach a lower temperature and all cells belonging to the vapour a higher temperature.

In order to avoid numerical problems of convergence, the amount of mass transferred from one phase to the other at each computational step should never be higher than the total mass of the first phase initially present in the cell. For this reason, the source term S in Eq. (4.19) is proportional to the terms $\alpha_G\rho_G$ or $\alpha_L\rho_L$ which describe the amount of vapour and liquid, respectively, present in the cell.

In practice, the temperature of the interface obtained by the use of this numerical technique will not be exactly the saturation temperature. Excessively small values of the coefficients r_L and r_G lead to a significant deviation between the interfacial temperature and the saturation temperature, while when using higher values the interfacial temperature will be closer to the desired saturation temperature; however, too large values of r_L and r_G cause numerical convergence problems.

Furthermore, when higher values of the coefficient r are used, the interface (i.e. the region of cells with $0 < \alpha < 1$) is sharper and thinner.

In Fig. 4.11 an example about the temperature profile computed for the liquid film in the simulation about condensation is reported. The two profiles reported have been computed using two different quite small values of the coefficient r. When using the highest value of the coefficient, the curve with highest values of temperature in Fig. 4.11 is obtained. As one can see, by increasing the coefficient the solution is closer to the ideal one, since the interfacial temperature is closer to the saturation one (i.e. T_{SAT} = 323 K).

It must be noticed that the value of the coefficient r has an influence on the computed heat transfer rate, since by increasing the interfacial temperature the temperature drop across the liquid film is increased (the wall temperature is fixed as boundary condition in the simulations). However, when an enough high value is used for r the computed interfacial temperature is very close to the saturation temperature.

In the simulation performed, the maximum deviation observed was around 0.3 K, while the difference between the temperature of the tube wall and the saturation temperature was 10 K.

A user defined function (UDF) to specify phase-change mass transfer available in FLUENT has been used to implement the numerical technique described in the simulations. The source code of the UDF used is reported in Table 4.2.

The value of the numerical coefficient r of Eq. (4.19) used in the UDF reported in Table 4.2 is $r_L = r_G = 10^7$ s^{-1}, but higher values, up to $r = 4\ 10^7$ s^{-1}, where used in the simulations when convergence problems were not observed. In the simulations of condensation reported in this thesis, the temperature of the interface (computed as the temperature of the surface with $\alpha_G = 0.5$) was always lower than the saturation temperature.

It must be stressed that the optimal values for the coefficients r_L and r_G strongly depend on the particular problem solved; therefore, because of the inherently numerical nature of this technique, suitable values of r must be found for each case. It is interesting to notice, as an example, that the default value given in the FLUENT User Guide is $r = 0.1$ s^{-1}, while Yang *et al.* (2008) performed a VOF simulation of boiling in a coiled tube using the value $r = 100$ s^{-1} and maintaining the deviation between saturation and interfacial temperature below 1 K.

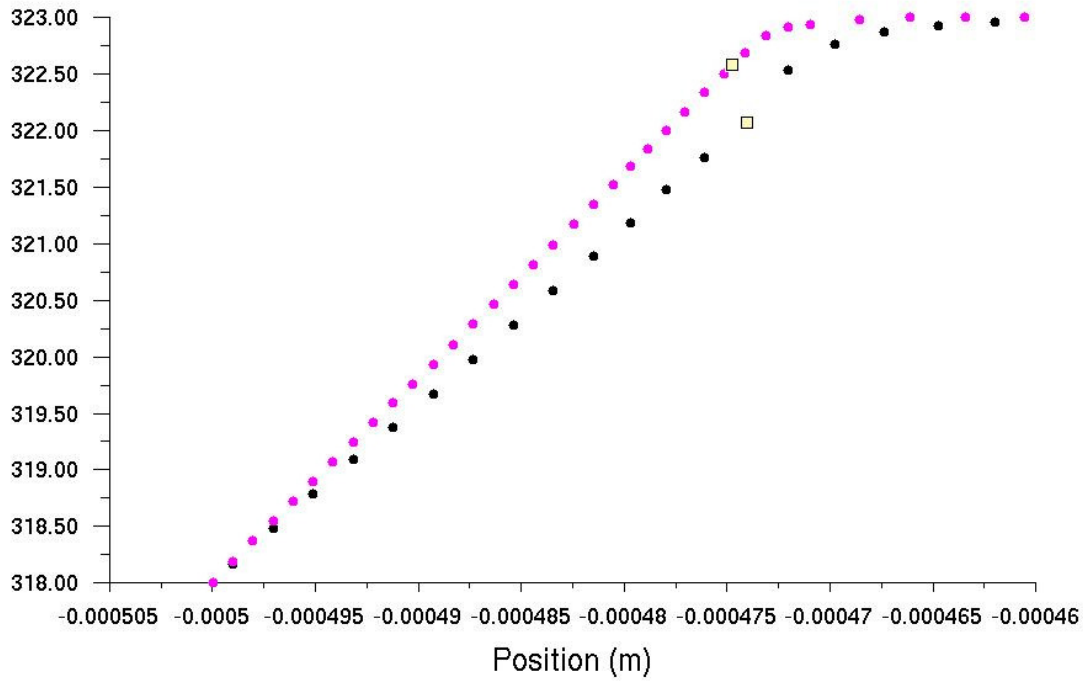

Fig. 4.11. Example of temperature profile in the liquid film of the condensation simulations computed by two different values of the coefficient *r* in Eq. (4.19)

Table 4.2. User defined function to specify phase-change mass transfer at 50°C saturation temperature (constant in Eq. (4.19) $r=10^7$).

```
#include "udf.h"

DEFINE_MASS_TRANSFER(liq_gas_source1e7,cell,thread,from_index,from_spe
cies_index,to_index,to_species_index)
{
   double m_lg;
   double T_SAT = 323.0;
   Thread *gas = THREAD_SUB_THREAD(thread, from_index);
   Thread *liq = THREAD_SUB_THREAD(thread, to_index);

   m_lg = 0.;
   if (C_T(cell, liq) >= T_SAT)
     {
       m_lg = -10000000.*C_VOF(cell,liq)*C_R(cell,liq)*
              fabs(C_T(cell,liq)-T_SAT)/T_SAT;
     }
   if ((m_lg == 0. ) && (C_T(cell, gas) <= T_SAT))
     {
       m_lg = 10000000.*C_VOF(cell,gas)*C_R(cell,gas)*
         fabs(T_SAT-C_T(cell,gas))/T_SAT;
     }
   return (m_lg);
}
```

4.4 Numerical simulation and results

A numerical steady-state simulation of condensation of R134a in a minichannel with 1 mm internal diameter has been performed by means of the VOF method implemented in FLUENT. The numerical technique described in the previous section of this chapter was used to handle the phase change process by fixing the temperature of the vapour-liquid interface.

The simulation has been performed at mass flux G = 200 kg $m^{-2}s^{-1}$, which is a quite low value for condensation inside channels. It has been assumed that the flow was laminar inside the liquid phase and turbulent inside the vapour phase. Turbulence was handled by the modified low-Re k-ω model described in the Section 4.2.

It must be noticed that, since a steady-state simulation has been performed, it's avoided the presence of waves at the vapour-liquid interface, which could have some influence on the two-phase flow and heat transfer process.

The Cartesian axis convention used is shown in Fig. 4.2. The minichannel is horizontally oriented and the effect of gravity has been taken into account in the simulations. This force, indeed, is expected to have a big influence on the condensation process at such low values of mass flux.

The implicit interpolation scheme was used for time discretization and the modified High Resolution Interface Capturing (HRIC) scheme was used for the volume fraction discretization. The volume force due to the effect of the surface tension was computed by means of the CSF (Continuum Surface Force) model. It should be stressed that the effect of the surface tension is expected to be important in minichannels.

The PRESTO! (PREssure STaggering Option) scheme was used for the pressure interpolation, while the pressure-velocity coupling was handled by means of the SIMPLE algorithm. The third order MUSCL scheme was used for the momentum equation, the two turbulence equations and the energy equation. This third-order convection scheme was conceived from the original MUSCL (Monotone Upstream-Center Schemes for Conservation Laws) by blending a central differencing scheme and second-order upwind scheme. Compared to the second order upwind scheme, it has a potential to improve spatial accuracy for all type of meshes by reducing numerical diffusion, most significantly for complex three-dimensional flows (Fluent Inc., 2006).

A uniform wall temperature (i.e. T_W = 40°C) was fixed as boundary condition, while the saturation temperature of the fluid was T_{SAT} = 50°C.

Pressure was fixed as boundary condition at outlet. At the inlet of the computational domain the velocity and spatial distribution of phases was fixed as boundary condition, as well as a uniform temperature $T_{INLET} = T_{SAT}$ = 50°C. The first two layers of mesh cells close to the wall were filled with liquid phase, while the remaining cells were filled with the vapour phase, in order to assure the presence of a vapour-liquid interface at the inlet. It must be noticed that such a boundary condition at the inlet is close to the expected flow at the beginning of the condensation region, but it is, in any case, arbitrary. The two-phase flow, however, is believed to fast develop downstream the inlet and reach a solution which is expected to be independent from the boundary condition at inlet.

The computational domain used was 25 mm long. Since the thickness of the liquid film is very small, a large number of cells is needed in order to capture the thermal and velocity profiles next to the wall of the tube. For this reason, in the mesh

generated for the computation, cells with smaller size were used next to the wall of the computational domain.

Simulations were first run using a mesh with around 800,000 cells. Once convergence was achieved, the region of the mesh corresponding to the whole liquid film and the portion of the vapour core next to the interface, where the gradients of velocity and turbulent properties are higher, was adapted. The number of cells in the final mesh was in this way increased up to around 4,000,000.

A portion of the cross section of the computational mesh used, after adaptation, is shown in Fig. 4.12.

It must be noticed that the length of tube needed to reach some degree of fluid condensation is very large as compared to the tube diameter. At the conditions considered for this simulation, the drop of vapour quality from inlet to outlet of the whole 25 mm long computational domain was less than 0.1. The ratio of the tube length to the tube diameter is very high, so a mesh with a very large number of cells would be needed in order to simulate the whole condensation process. For this reason, the solution obtained at the outlet of the computational domain was used as boundary condition at the inlet of the same mesh in order to run another simulation and compute the condensation process downstream the first 25 mm length of the minichannel.

This process was repeated a number of times and the results reported in this thesis totally correspond to a minichannel around 125 mm long. The inlet vapour quality was around 0.94, and the refrigerant was in this way condensated in the simulation down to vapour quality 0.54.

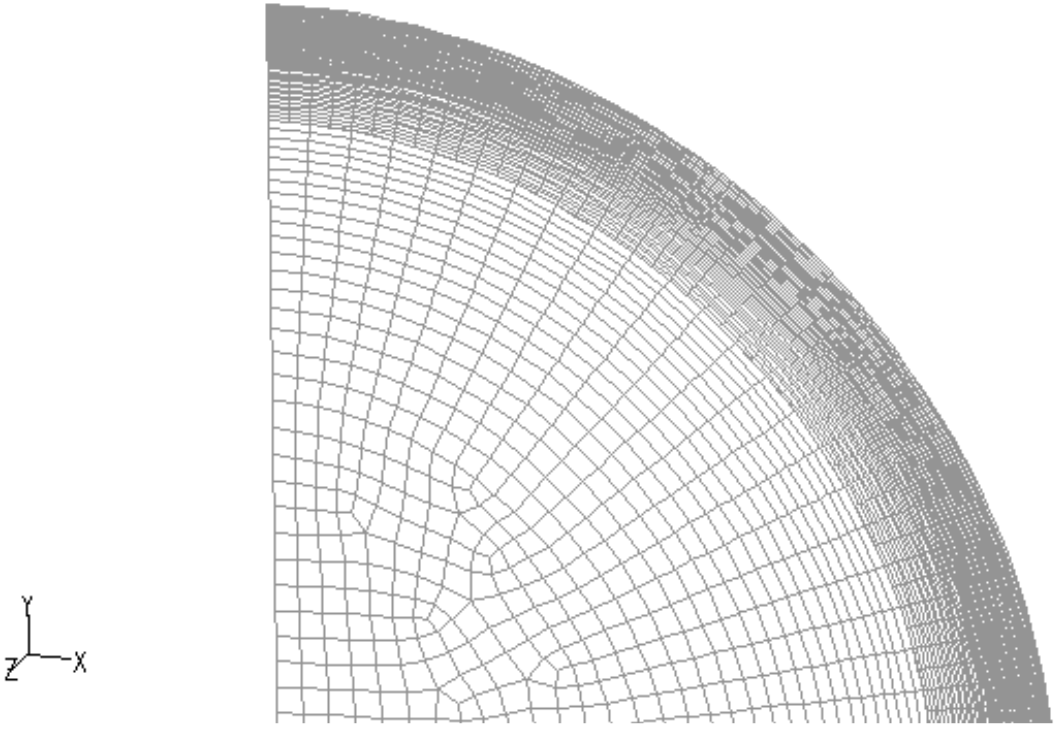

Fig. 4.12. Example of cross section of the computational mesh after adaptation.

The evolution of the vapour-liquid interface along the channel is very important since the heat transfer process strongly depends on the local thickness of the liquid film. In Fig. 4.13 the cross sectional shape of the interface is reported at different vapour qualities. At vapour quality 0.9, the thickness of the liquid film is evenly distributed all along the tube circumference. It is very interesting to notice how the condensate liquid is drained towards the bottom of the channel: by decreasing the vapour quality from 0.9 down to 0.6, the thickness of the liquid in the entire upper half of the tube keeps almost constant, while the liquid film at the bottom becomes thicker. This means that all the liquid condensated in the upper part of the tube (which is more than the liquid condensated in the lower part because the film is thinner and the heat transfer coefficient is higher) is drained towards the bottom because of the gravity force instead of being immediately carried in the tube axial direction by means of the shear stress due to the vapour flow.

Computational results about the evolution of vapour quality and void fraction along the channel are reported in the graphs in Fig. 4.14 and Fig. 4.15. As one can see, the two-phase flow rapidly evolve from the inlet boundary condition, then vapour quality and void fraction vary almost linearly with the axial coordinate.

The computed void fraction is plotted versus vapour quality in Fig. 4.16 together with the classical void fraction correlation by Rouhani (1969) as published in the Heat Exchanger Design Handbook (HEDH) (Taborek, 1983). As one can see, the VOF simulation and the empirical correlation displays the same slope of void fraction versus vapour quality, but the void fraction predicted by the correlation is about 0.05 higher than computational results.

The cross-sectional average heat transfer coefficient is plotted versus axial coordinate and vapour quality in Fig. 4.17 and Fig. 4.18, respectively. At the very first cells of the computational domain very high values of the heat transfer coefficient are computed because of the boundary condition imposed and the fact that the liquid film is very thin.

The heat transfer process is essentially driven by the difference of temperature between the vapour-liquid interface, which is at the saturation temperature, and the tube wall, where the temperature is 10 K lower. The condensation heat transfer coefficient, therefore, depends on the thickness of the liquid film.

As shown in Fig. 4.13, once the liquid starts to condensate, this is drained towards the bottom of the tube, where the thickness of the liquid is increased, this reducing the local heat transfer coefficient in this region. When the vapour quality is decreased from 0.9 to 0.8, as an example, the thickness of the liquid film at the bottom is doubled, and a very strong reduction of the cross sectional average heat transfer coefficient is caused, as shown in Fig. 4.18. Going on with the condensation process, the same decrease of the vapour quality has a smaller effect on the cross sectional average heat transfer coefficient. As an example, when the vapour quality is decreased from 0.7 to 0.6, the relative influence of the same increase of the thickness, as compared to the film thickness itself, is smaller.

This explains the computational results shown in Fig. 4.17 and Fig. 4.18. The slope of heat transfer coefficient versus vapour quality is large at high qualities and then gradually decreases at lower qualities. At the beginning of the condensation process, high heat transfer coefficients are achieved because the liquid film is very thin all around the tube wall; then condensate liquid drains and the local coefficient at the bottom of the tube decreases. At some point, the coefficient at the bottom is very low as

compared to the one on the upper part, and most of the condensation takes place in this latter region: the effect of the increase of the liquid film at the bottom is therefore almost negligible and the trend of the average heat transfer coefficient versus the axial coordinate or the vapour quality is almost flat.

The results reported in this thesis are preliminary results. It is clear that extending the simulation performed till reaching the complete condensation would be very interesting. At some point, indeed, the surface tension should starts to play an important role on the shape of the vapour-liquid interface and the study of such kind of phenomenon is very important for the understanding of condensation inside minichannels.

Experimental data was available for the condensation of R134a inside a minichannel with the same diameter and at the some mass flux as the simulation performed. The saturation temperature of the fluid in the experimental test was 40°C, while in the simulation this is 50°C, therefore data cannot be directly compared, since the heat transfer coefficient strongly depends on the saturation temperature. In both experimental test and simulation the difference between the saturation and wall temperature was 10K.

Experimental data and computational results about heat transfer coefficient versus vapour quality are plotted in Fig. 4.19 along with predictions by the Cavallini *et al.* (2006) correlation at both T_{SAT} =40°C and T_{SAT} =50°C. As one can see, at least at vapour quality below 0.75, this correlation predict very well experimental data at 40°C saturation temperature, therefore it is expected to work well also at 50°C saturation temperature.

Heat transfer coefficients predicted by the simulation are in general lower than the values predicted by the empirical correlation; furthermore, it must be noticed that the slope of HTC versus vapour quality is slightly lower in the case of the simulation. At 0.55 vapour quality, the deviation between numerical results and the empirical correlation predictions is 16%, while at 0.75 vapour quality the deviation is 22%.

The analysis of the velocity field is very interesting. Numerical results about the velocity profile along the y-axis at 0.9, 0.8, 0.7 and 0.6 vapour quality are reported in the graphs in Fig. 4.20, Fig. 4.21, Fig. 4.22 and Fig. 4.23, respectively. Diamonds dots in the graphs represent the position of the vapour-liquid interface.

As one can see, since laminar flow is imposed for the liquid phase, the computed velocity profile is linear inside the liquid film.

At vapour quality 0.9, the velocity profile is symmetrical and no effect of the stratification of liquid at the bottom of the tube is shown, but moving downstream the minichannel, the velocity profile becomes more and more asymmetrical.

By reducing the vapour quality because of the condensation process, the velocity of the vapour phase decreases. The thickness of the liquid film at the top of the channel keeps almost constant, while the velocity at the vapour-liquid interface decreases from 0.63 m/s at 0.9 quality down to 0.42 m/s at 0.6 quality. The corresponding thickness of the liquid film varies from 0.015 mm up to 0.018 mm.

A different behaviour is observed at the bottom of the pipe (corresponding to the negative values of the y-coordinate in the graphs). The thickness of the liquid film increases from 0.018 mm at 0.9 quality up to 0.093 mm at 0.6 quality and a very relevant change is observed for the corresponding interfacial velocity, which increases from 0.67 m/s up to 1.3 m/s.

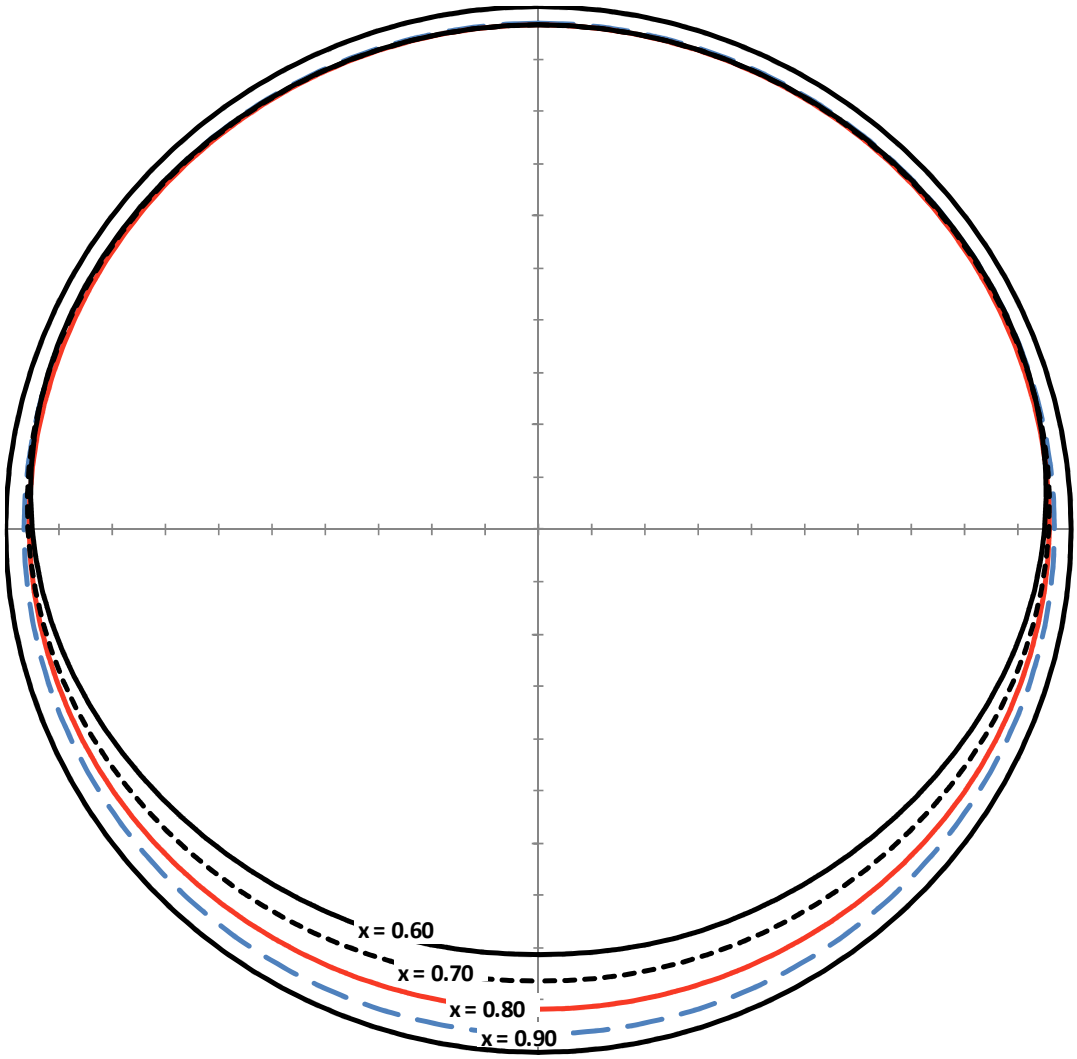

Fig. 4.13. VOF simulation: vapour-liquid interface at tube cross section at different vapour qualities. R134a, Saturation temperature = 50°C, T_{SAT} - T_{WALL} = 10K.

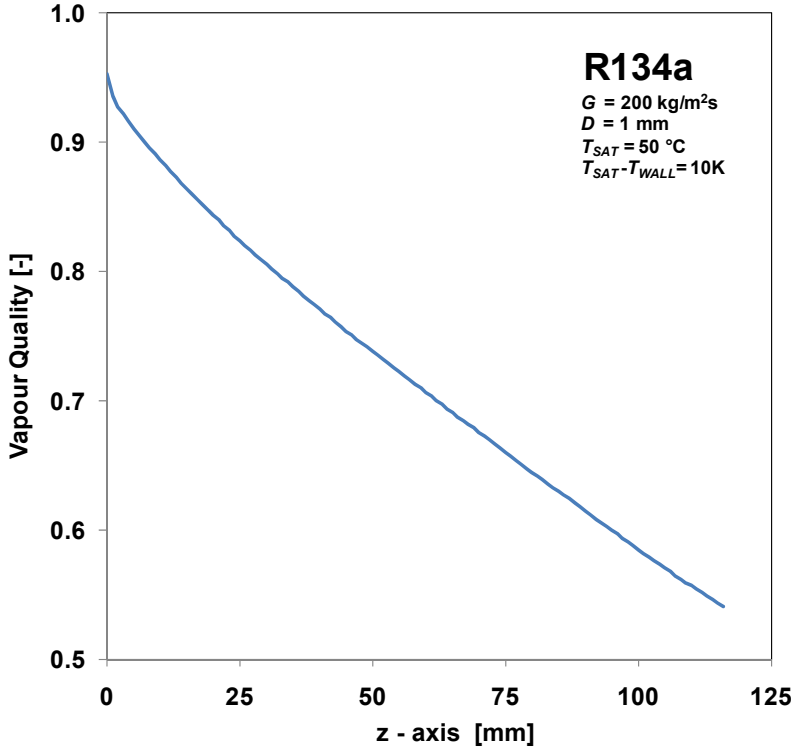

Fig. 4.14. VOF simulation: vapour quality versus axial position. R134a, Saturation temperature = 50°C, T_{SAT} - T_{WALL} = 10K.

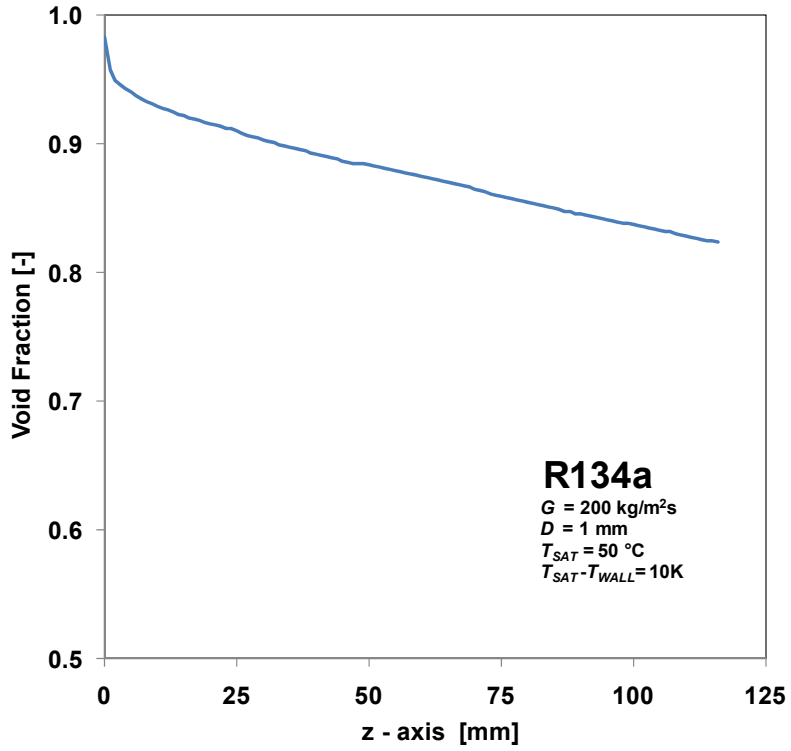

Fig. 4.15. VOF simulation: cross-sectional void fraction versus axial position. R134a, Saturation temperature = 50°C, T_{SAT} - T_{WALL} = 10K.

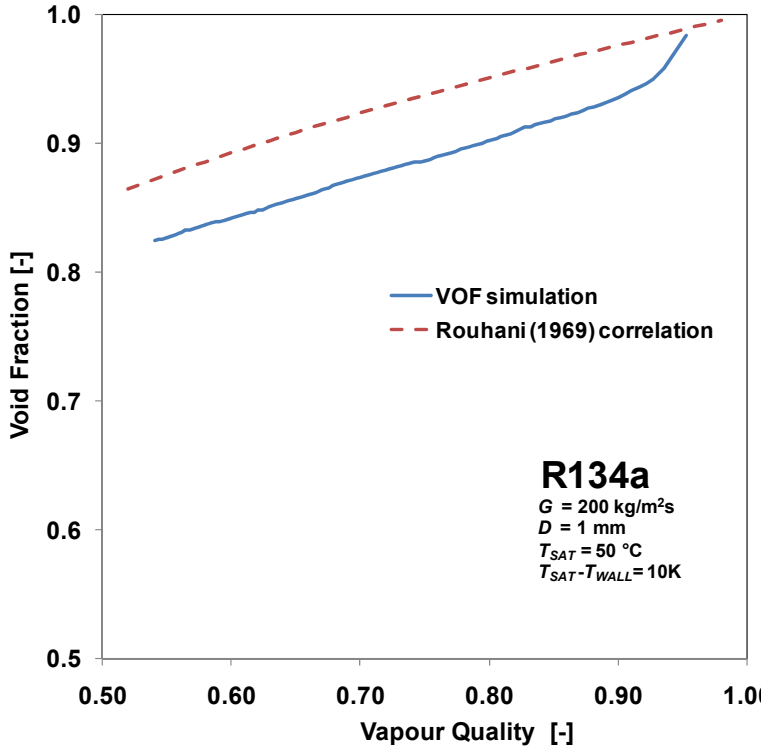

Fig. 4.16. Void fraction versus vapour quality: comparison between VOF simulation and Rouhani (1969) correlation.

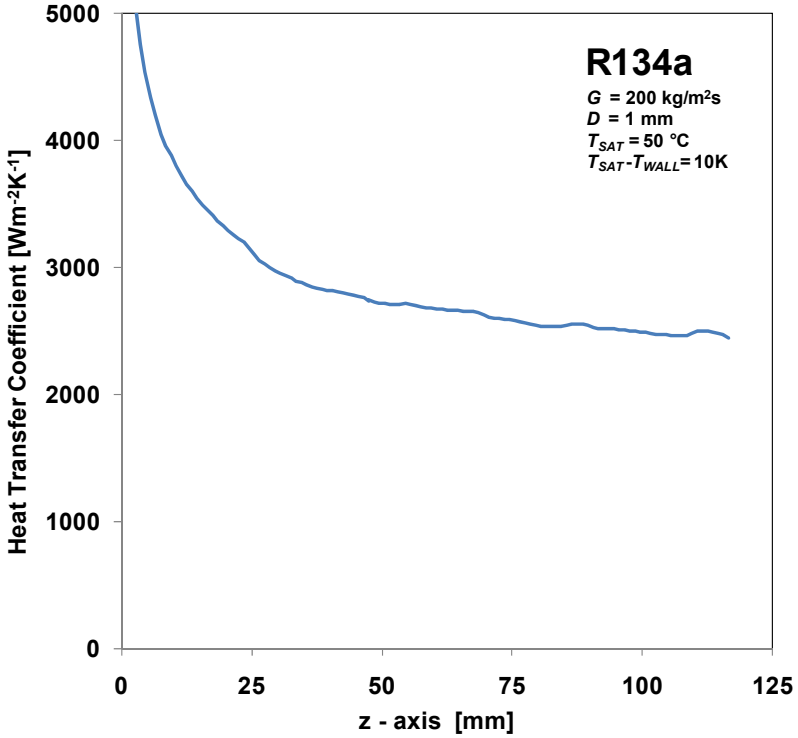

Fig. 4.17. VOF simulation: average cross sectional heat transfer coefficient versus axial position. R134a, Saturation temperature = 50°C, T_{SAT} - T_{WALL} = 10K.

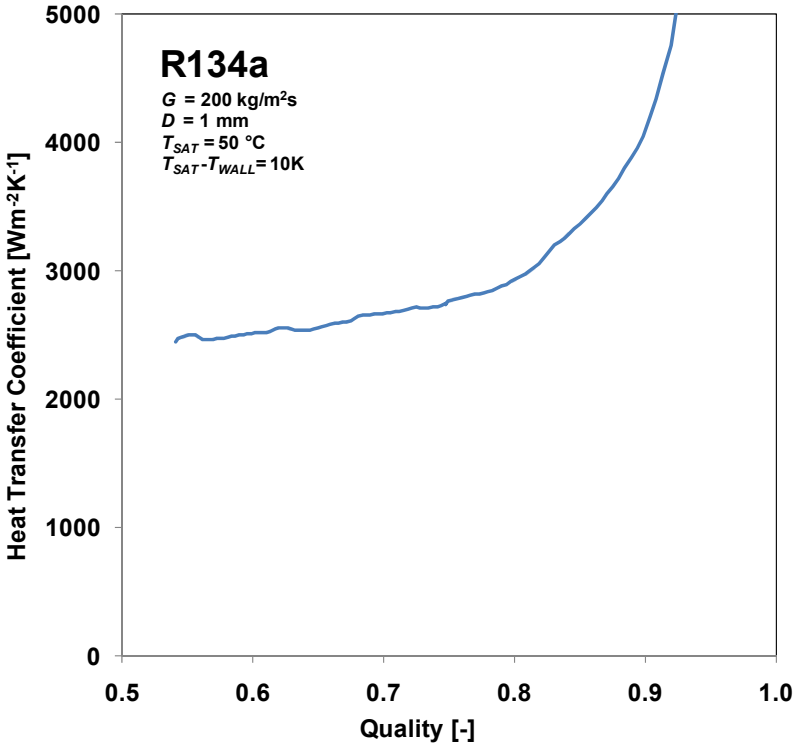

Fig. 4.18. VOF simulation: average cross sectional heat transfer coefficient versus vapour quality. R134a, Saturation temperature = 50°C, T_{SAT} - T_{WALL} = 10K.

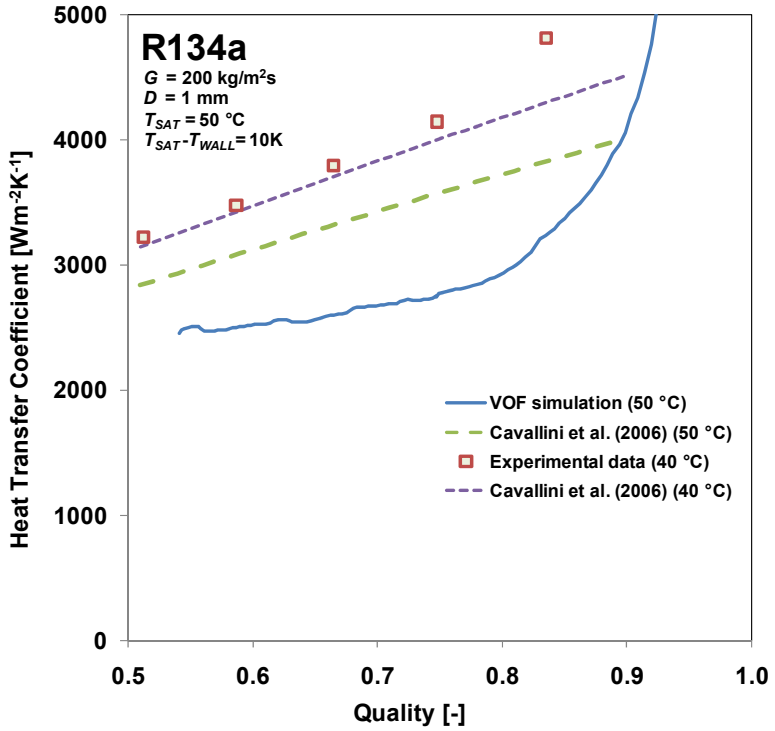

Fig. 4.19. Heat transfer coefficient for condensation of R134a inside 1 mm i.d. minichannel: VOF simulation at T_{SAT} =50°C, experimental data at T_{SAT} =40°C, predictions by Cavallini *et al.* (2006) at T_{SAT} =40°C and T_{SAT} =50°C.

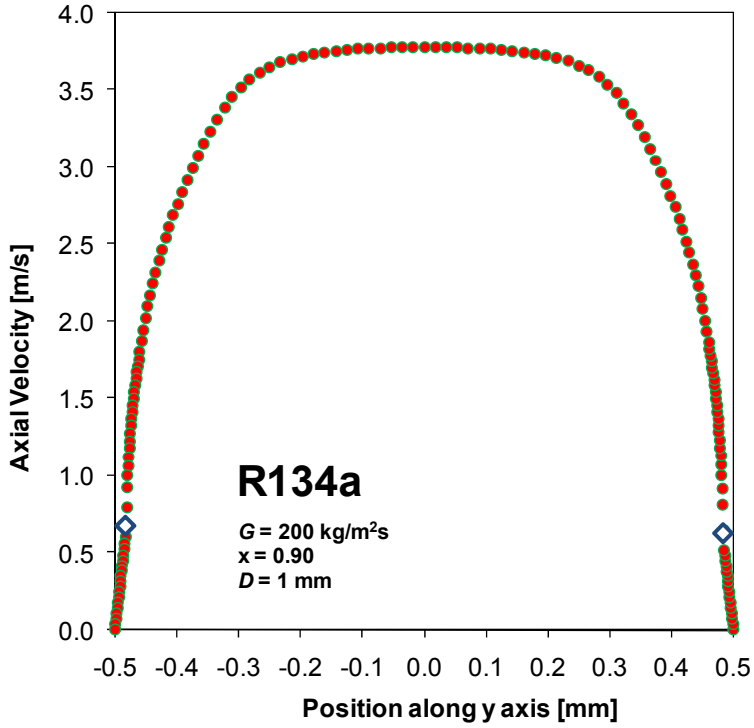

Fig. 4.20. VOF simulation: axial velocity distribution along y-axis at 0.90 vapour quality. R134a, Saturation temperature = 50°C, T_{SAT} - T_{WALL} = 10K.

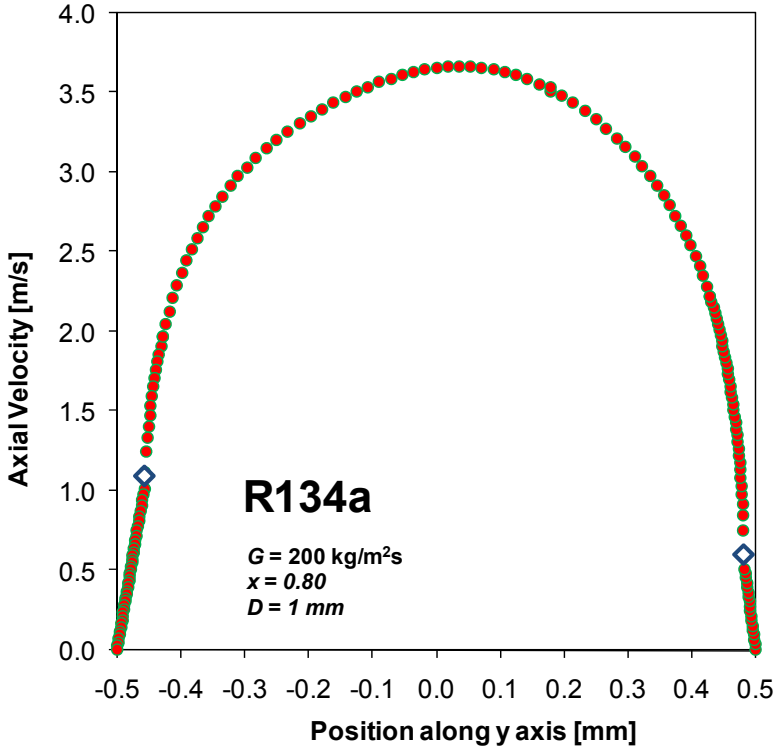

Fig. 4.21. VOF simulation: axial velocity distribution along y-axis at 0.80 vapour quality. R134a, Saturation temperature = 50°C, T_{SAT} - T_{WALL} = 10K.

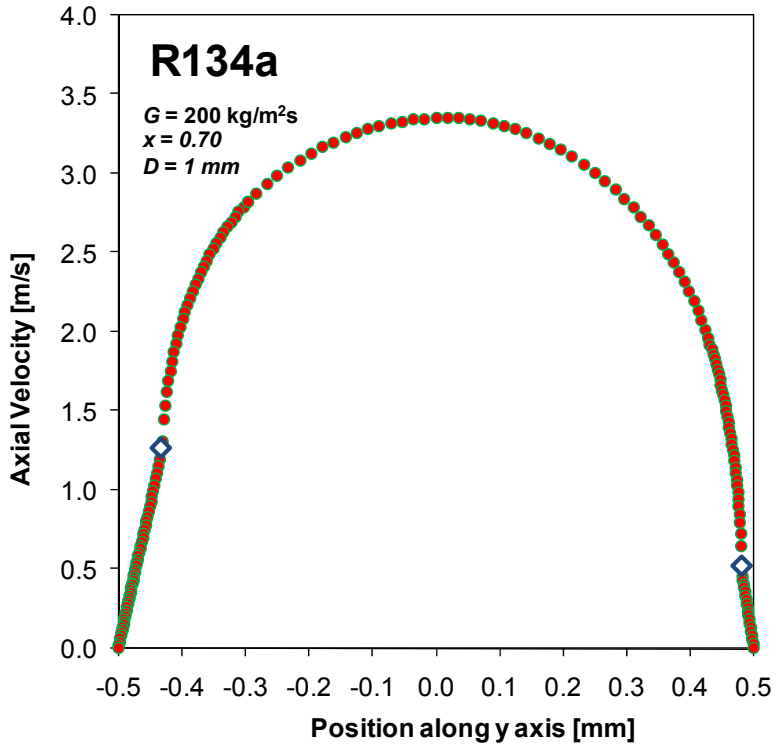

Fig. 4.22. VOF simulation: axial velocity distribution along y-axis at 0.70 vapour quality. R134a, Saturation temperature = 50°C, T_{SAT} - T_{WALL} = 10K.

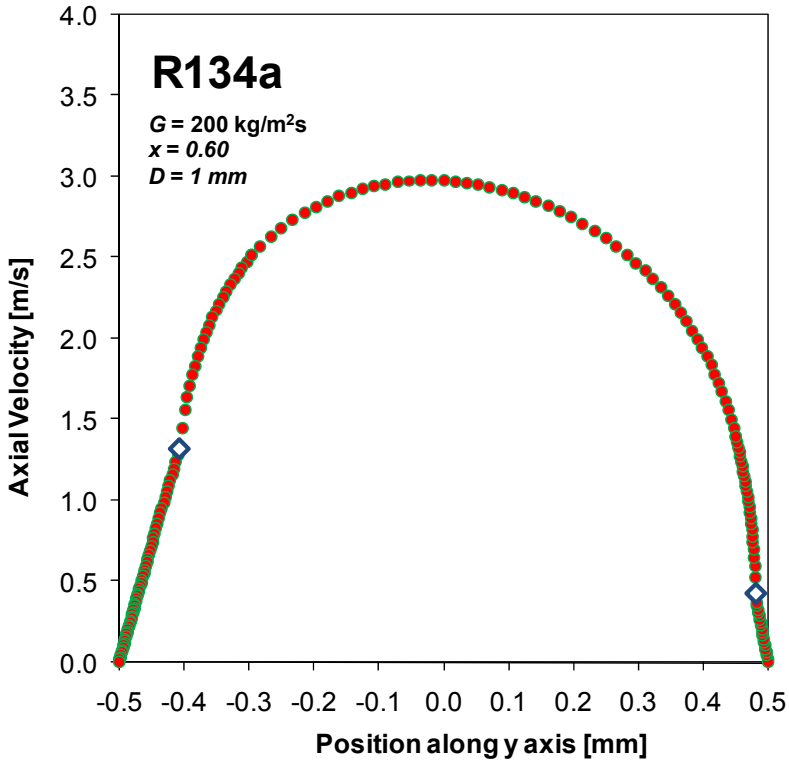

Fig. 4.23. VOF simulation: axial velocity distribution along y-axis at 0.60 vapour quality. R134a, Saturation temperature = 50°C, T_{SAT} - T_{WALL} = 10K.

Chapter 5.

VOF simulation of churn flow

Beside the experimental and modelling work on the minichannel heat exchangers and their applications to heat pumps, some work has been performed also in the field of CFD simulations. The aim of this work was the study of two-phase flow and heat transfer in heat exchangers.

Two-phase heat transfer is a very complex phenomenon, mainly because of the presence of a vapour-liquid interface and different flow regimes and spatial distributions of the phases which have a very strong influence on the heat transfer. The VOF method implemented in FLUENT was used because it allows to track the motion of vapour-liquid interfaces, actually performing a direct simulation of multiphase flows.

In this Section a numerical simulation by means of the VOF method of the churn flow regime of air-water and R134a vapour-liquid mixtures is presented. This study is not directly linked to the study concerning heat exchangers, however it was important in order to assess the capability of the method to compute the motion of the interface in gas-liquid flows, which is crucial to characterize the two-phase heat transfer in heat exchangers.

The study was conducted using an axisymmetrical domain reproducing the region next to the porous wall liquid injector of a typical test section for the investigation of vertical gas-liquid flows.

A simplified model of the levitation process of the ring-type waves typical of churn flow is proposed. The influence of the gas Froude number on the flooding waves amplitude is shown by the simplified model and used to explain the numerical results.

A comparison of the numerical results with experimental visualizations available in the literature is performed. The velocity field in the forming wave region and the pressure and shear stress variations along the interface are shown. Simulations have been performed at different liquid and gas superficial velocities and pipe diameters and the influence of these parameters on the gas-liquid interface is discussed.

The results of this work were published in Da Riva *et al.* (2007) and Da Riva and Del Col (2007).

The model was then extended to the study of condensation of R134a inside a minichannel with 1 mm internal diameter at low mass flux. Result about this study are reported in this thesis in Chapter 4.

5.1 The churn flow regime

The flow features and spatial distribution of phases in the upflow of a gas-liquid mixture are nowadays described and grouped by means of a set of quite well established flow patterns (i.e. “bubbly flow”, “slug flow”, “churn flow”, “annular flow” and “wispy annular flow”). The word “churn flow” has been employed in the past years by a number of research groups to describe different flows. In the present work it has been adopted the definition of Hewitt and Hall-Taylor (1970) which considers it as the regime which occurs after the breakdown of slug flow as velocity and/or quality increase.

The most relevant features of churn flow are the presence of a central gas core and the oscillatory nature of the motion of the liquid phase, which leads to violent fluctuations of the pressure drop and the liquid holdup. Experimental visualization studies by means of photochromic dye tracing by Hewitt *et al.* (1985) showed that liquid is transported upwards in large waves which pick up liquid from a film falling by gravity above them and shed it to a falling film behind them.

Jayanti and Hewitt (1992) reported the presence in literature of four major interpretations about the slug/churn transition criterion: Taitel *et al.* (1980) and Dukler and Taitel (1986) considered churn flow as a developing slug flow due to an entrance effect; Nicklin and Davidson (1962), Wallis (1962), McQuillan and Whalley (1985) and Govan *et al.* (1991) attributed the transition to local flooding of the liquid film falling by gravity around the Taylor bubble and flowing in counter-current to the gas; Mishima and Ishii (1984) attributed the transition to the reduction of the liquid slug length which would lead to a strong wake effect of the Taylor bubble and the destabilization and destruction of the slug itself; finally, Brauner and Barnea (1986) attributed the transition to the excessive entrainment of bubbles in the liquid slug and their subsequent coalescence.

An extended data set about fully developed upwards air-water flows in a 23 m long and 32 mm i.d. vertical pipe has been obtained and interpreted by Owen (1986). This data covers gas mass fluxes up to 300 kg/(m^{2}s) and liquid mass fluxes up to 1 000 kg/(m^{2}s), covering also the case of churn flow. The sudden increase in pressure gradient, reported by Owen, when the breakdown of slug flow and formation of churn flow are reached by increasing the mixture quality, from a physical point of view is qualitatively consistent with the hypothesis proposed for the first time by Nicklin and Davidson (1962) (i.e. transition due to flooding of the liquid film around the Taylor bubble), since an analogous behaviour is observed when the flooding condition is achieved in counter-current gas-liquid flows.

Jayanti and Hewitt (1992) developed a model for the slug/churn transition based on the proposal of local flooding inside the Taylor bubble which gives good prediction of experimental data, including the effect of the system pressure (Watson and Hewitt, 1999).

Recently, Carvalho (2006) has reported visual observations of individual gas slugs in the case of argon-water flow in a 20 mm i.d. vertical tube showing slug/churn transition due to flooding inside the Taylor bubble, as proposed by Nicklin and Davidson (1962).

Some evidence of the intimate connection between churn flow and the flooding phenomenon can also be found in the experimental study by Govan *et al.* (1991). In the

test section used, the gas was forced to flow upwards, while the liquid was let to drain downwards for some length by injecting and removing it through two sections of porous wall tubing. The gas flow rate was increased till reaching flooding conditions: a single coherent wave was created at the liquid outlet and started to travel upwards till passing beyond the liquid inlet; after this point, part of the liquid injected started to flow upwards and churn flow was observed in this portion of the test section.

It should be stressed that, as reported by Jayanti *et al.* (1996), there are two different widely accepted mechanisms of flooding, i.e. the formation and upward transportation of large waves and the entrainment and carryover of droplets. Jayanti *et al.* (1996) claim that the two mechanisms have different nature and that the wave mechanism should prevail in relatively small diameter pipes (i.e. $D < 50$ mm), where the presence of a coherent ring-type wave causes a relatively large reduction in the flow area available for the gas at the wave crest, thus giving rise to a high form drag and the wave levitation. In big pipes, instead, the gas velocity required to entrain and carry droplets upward should be lower than that required to transport waves, so that the droplets mechanism should prevail. The churn flow should be related to the wave mechanism, and the nature of the huge waves typical of churn flow could be considered the same as that of the flooding waves.

The force exerted by the gas flowing over a standing wave has been studied by means of a CFD simulation by Jayanti *et al.* (1996) concluding that in typical churn flow conditions this force should be mainly due to the drag force caused by pressure variation around the wave, rather than to the frictional force due to shear stress.

The pressure and velocity fields, as well as the shear stress variation along the interface, have also been analysed in the case of the present simulation. It should be stressed that, differently from the study by Jayanti *et al.* (1996), where the shape of the wave had to be assumed a priori, no such assumptions have been made in the present numerical simulation performed by means of the VOF method, since with this method the gas-liquid interface motion and deformation is directly tracked.

Sawai and Kaji (2001) and Sawai et al. (2004) have reported a study about the pressure drop and the gas-liquid interfacial structure for churn flow in a 26 mm i.d. pipe obtained by means of electrical conductance probes measuring the local instantaneous liquid holdup.

Furthermore, Barbosa *et al.* (2001) have reported a study about the process of the flooding-type wave formation and motion in air-water churn flow in a 32 mm i.d. tube by means of a transparent liquid injector and high-speed video recordings. The results of the present simulation have been compared to the visualizations reported by Barbosa *et al.* (2001).

5.2 Numerical simulation

The commercial CFD code FLUENT has been used for the unsteady simulation of adiabatic gas-liquid churn flow by means of the Volume Of Fluid (VOF) method.

Since a validation was necessary, an air-water two-phase flow has been considered, because most of the experimental data and visualizations available in the literature are given for this mixture. However, a pair of simulations has been performed considering the flow of a liquid-vapour equilibrium mixture of the refrigerant R134a.

The advection of the gas-liquid interface has been computed by means of a PLIC (Piecewise Linear Interface Calculation) scheme implemented in the FLUENT code and based on the work by Youngs (1982), while the effect of surface tension on the momentum equation has been computed by the CSF (Continuum Surface Force) model proposed by Brackbill *et al.* (1992). The average value of time step for the simulations reported was about 10^{-5} s.

Gravity has been taken into account. The two phases have been assumed as incompressible and not miscible, with no mass transfer between them and turbulence has been taken into account by the use of the RNG k-ε model combined with the standard wall functions approach. The scalar values of the turbulent kinetic energy k and its dissipation rate ε have been shared by the two phases throughout the domain, as well as all the other scalars have been treated.

Since using a high-order discretization scheme for the convective terms in the momentum equation may reduce the stability of the solution in VOF modelling, the first order upwind scheme was used. The second order upwind scheme was used for the two turbulence equations, and PRESTO! scheme was used for the pressure interpolation, while the pressure-velocity coupling was handled by means of the PISO algorithm.

In the apparatuses for the experimental study of air-water churn flow, air is usually forced to flow upwards, while the liquid is usually injected and removed through two sections of porous wall, in such a way that the liquid enters at very low velocity and a film adherent to the wall is developed.

In the visualisation study by Barbosa *et al.* (2001), flooding-type waves are formed at the liquid inlet and transported upwards giving rise to churn flow in the region above the water injector. The computational domain of the present simulation, shown in Fig. 5.1, reproduces the zone next to the liquid inlet of such a kind of typical experimental arrangement. A constant velocity is imposed as boundary condition at the liquid and gas inlet, while pressure is fixed at the outlet.

The diameter of the reference configuration is D = 32 mm to make possible a comparison, as a validation, with the experimental visualizations by Barbosa *et al.* (2001), which were obtained for an equal tube diameter. Other simulations have been performed considering a 10 mm i.d., a 20 mm i.d. and a 30 mm i.d. tube using the same computational domain and adopting the appropriate scaling factors.

Since the inner nature of churn flow is believed to be the presence of coherent ring-type waves, the problem has been handled as 2D axisymmetrical. A cartesian mesh with 80 000 cells (100 x 800) with size of 15 10^{-5} m for the reference configuration, down to about 5 10^{-5} m for the simulation of the 10 mm i.d. pipe, has been used.

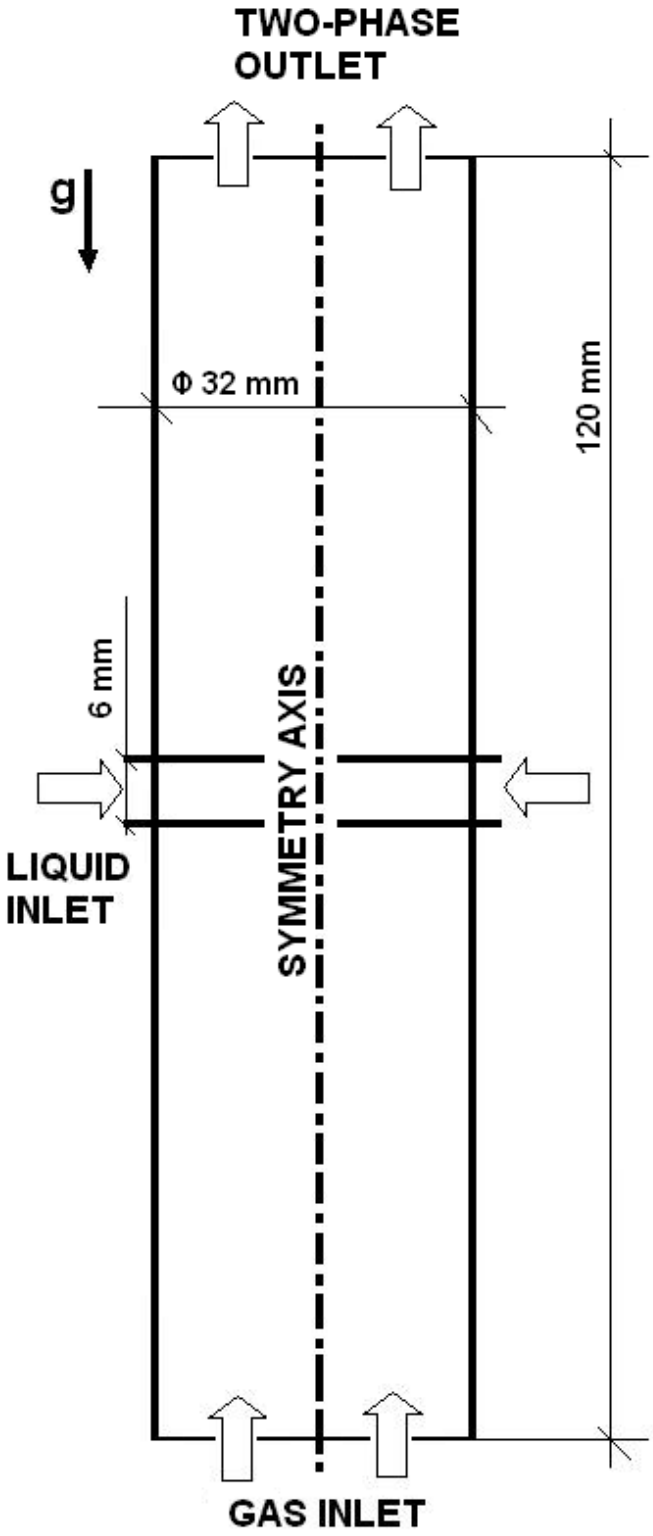

Fig. 5.1. Reference Computational domain.

By considering the problem as axisymmetrical, the presence of quasi spherical droplets in the gas core cannot be rightly handled. Furthermore, the computational cell size could be not small enough to get a good resolution of the interface of small droplets.

It should be considered that experimental data published in the past years (e.g. Wallis, 1962), reported in Fig. 5.8, Azzopardi and Zaidi, 2000) suggest that the measured liquid entrained fraction in the gas core of churn flow, is considerably high. However, a paper by Azzopardi and Wren (2004) questions whether this fraction is carried as drops or as flooding-type waves. As reported by Azzopardi and Wren (2004), the data present in the literature have usually been obtained by means of a concentric pipe arrangement to separate the core and wall zone (e.g. Wallis, 1962), or by measurements of film flow rates obtained by sucking off the liquid film through a porous wall device (e.g. Azzopardi and Zaidi, 2000): the entrainment measured in such a way does not give any helpful information about the structure of the liquid travelling in the core.

In an initial simulation case, the air flow rate has been set to zero and the water has been let to drain downwards forming a falling film adherent to the pipe wall; then a high gas flow rate has been set till obtaining the onset of flooding and the complete flow reversal with the development of churn flow in the upper half of the computational domain. All the simulations have been obtained starting from this case and by changing the gas and liquid flow rates. Table 5.1 shows the operating conditions for each simulation; j_G and j_L are the superficial velocities for the gas and the liquid, respectively, while U_G^* is the dimensionless gas velocity, which corresponds to the root mean square of the gas Froude number $\mathrm{Fr_G}$, defined as follows:

$$\mathrm{Fr_G} = \frac{\rho_G j_G^{\,2}}{(\rho_L - \rho_G) g D} = U_G^{*2} \tag{5.1}$$

where D is the tube diameter, ρ_G and ρ_L are the gas and liquid densities and g is the gravity acceleration.

When dealing with vertical two-phase flow, the flow pattern map of Hewitt and Roberts (1969) is usually considered; in this map, the operating conditions are plotted in terms of the superficial momentum flux for each phase. The position of the simulations performed in the Hewitt and Roberts (1969) map is shown in Fig. 5.2.

In some cases (i.e. at low gas velocity), part of the injected liquid could drain toward the gas inlet of the computational domain, where a constant velocity is imposed and the liquid volume fraction is set to zero as the boundary condition. Since this situation would led to computational problems, the wall surface below the liquid inlet is set in the simulations as non-wettable to avoid the presence of a liquid film below the injector.

Govan *et al.* (1991) have experimentally compared the flow features of the churn flow region above the injector both in the cases with and without the falling film below it, finding no significant differences. Therefore, the condition here imposed here should not affect the results of the simulations about the churn flow in the upper half of the computational domain.

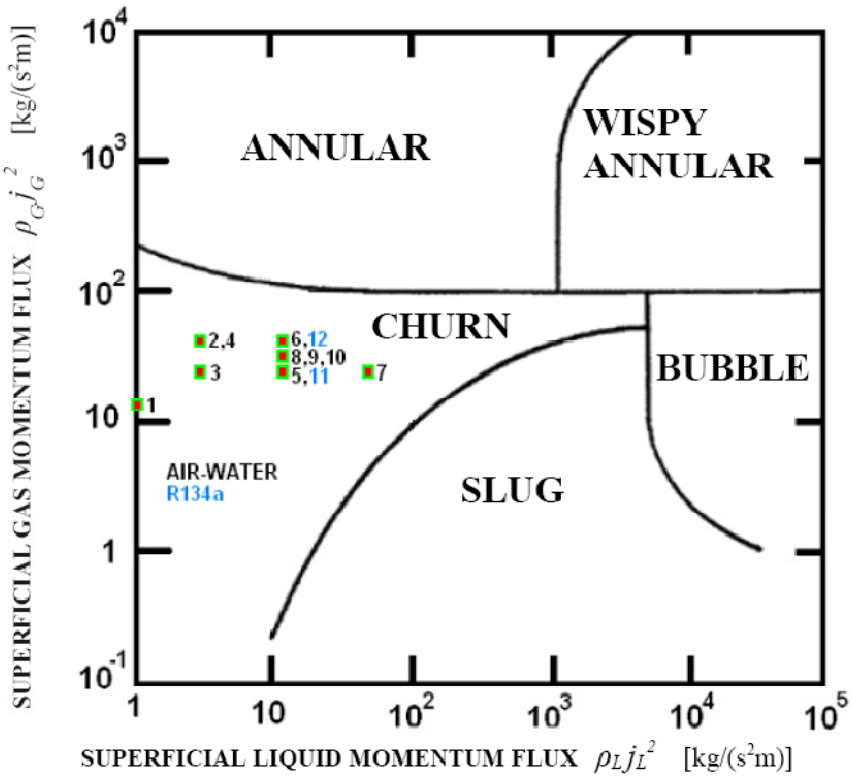

Fig. 5.2. Simulation cases plotted in the flow pattern map of Hewitt and Roberts (1969).

Table 5.1. Simulations of churn flow performed.

	Mixture	Diameter [mm]	Pressure [bar]	Gas Flow Rate [kg/s]	Liquid Flow Rate [kg/s]	j_G [m/s]	j_L [m/s]	U_G^* [adimensional]
1	air-water	32	1.33	3.6 10-3	27 10-3	2.8	0.03	0.20
2	air-water	32	1.33	6.9 10-3	51 10-3	5.3	0.06	0.38
3	air-water	30	1	3.9 10-3	42 10-3	4.5	0.06	0.29
4	air-water	30	1	5.2 10-3	42 10-3	6	0.06	0.39
5	air-water	30	1	3.9 10-3	85 10-3	4.5	0.11	0.29
6	air-water	30	1	5.2 10-3	85 10-3	6	0.11	0.39
7	air-water	30	1	3.9 10-3	169 10-3	4.5	0.22	0.29
8	air-water	30	1	4.3 10-3	85 10-3	5	0.11	0.32
9	air-water	20	1	1.9 10-3	38 10-3	5	0.11	0.40
10	air-water	10	1	0.48 10-3	9.4 10-3	5	0.11	0.56
11	R134a	32	7.7	24.4 10-3	104 10-3	0.8	0.1	0.26
12	R134a	32	7.7	32.7 10-3	104 10-3	1.1	0.1	0.35

5.3 Results and Discussion

5.3.1 *Comparison with experimental visualizations*

Fig. 5.3 shows a qualitative comparison with high-speed video recordings by Barbosa *et al.* (2001) of the wave formation process for air-water churn flow in a 32 mm i.d. pipe. The visualizations reported have been obtained at the pressure of 1.33 bar (with gas density $\rho_G \sim 1.6$ kg/m^3); the air flow rate was 6.8 10^{-3} kg/s (corresponding to superficial gas velocity $j_G = 2.8$ m/s) and the total water flow rate was 108 10^{-3} kg/s. The liquid flow rate actually flowing upwards was 27 10^{-3} kg/s (corresponding to superficial liquid velocity in the churn flow region $j_L = 0.03$ m/s). Since in the numerical simulation the presence of a falling film below the injector was avoided, the water flow rate was fixed equal to the experimental rate actually contributing to the churn flow (i.e. 27 10^{-3} kg/s).

A quite good agreement between the numerical and experimental results, with regard to the shape of the interface, can be observed.

At the time $t = 0$, s a coherent ring wave starts to grow at the inlet porous section; then the wave grows till reaching its maximum amplitude at about $t = 12\ 10^{-3}$ s in the visualization and $t = 18\ 10^{-3}$ s in the simulation. At this time, the shape of the wave is quasi triangular and its windward interface is almost perpendicular to the pipe wall because of the effect of gravity attracting the water downwards.

At the wave crest, the gas velocity increases because of the occlusion of the channel, giving rise to a drag force on the wave. By increasing the wave amplitude, the drag force increases too. When the maximum amplitude is reached, the drag force has become higher than gravity, and the wave starts to rotate: at the time $t = 20\ 10^{-3}$ s in the visualization and $t = 29\ 10^{-3}$ s in the simulation, the leeward interface has become almost perpendicular to the pipe wall; afterwards, the whole wave starts to be carried upwards.

The dark area above the water injector in the visualization shows a high entrainment, while in the simulation this entrainment is not obtained. This could be due to the fact that the cell size (15 10^{-5} m) is not small enough to capture small droplets and also to the 2D axisymmetrical assumption.

The experimental wave frequency reported by Barbosa *et al.* (2001) in the case corresponding to the visualizations reported in Fig. 5.3 is 9.8 Hz; the wave frequency obtained from the numerical procedure is 10 Hz. A second comparison has been performed considering experimental data by Barbosa *et al.* (2001) obtained at higher gas and liquid superficial velocities (i.e. $j_G = 5.3$ m/s and $j_L = 0.06$ m/s); in this case the experimental frequency is over predicted by 50%.

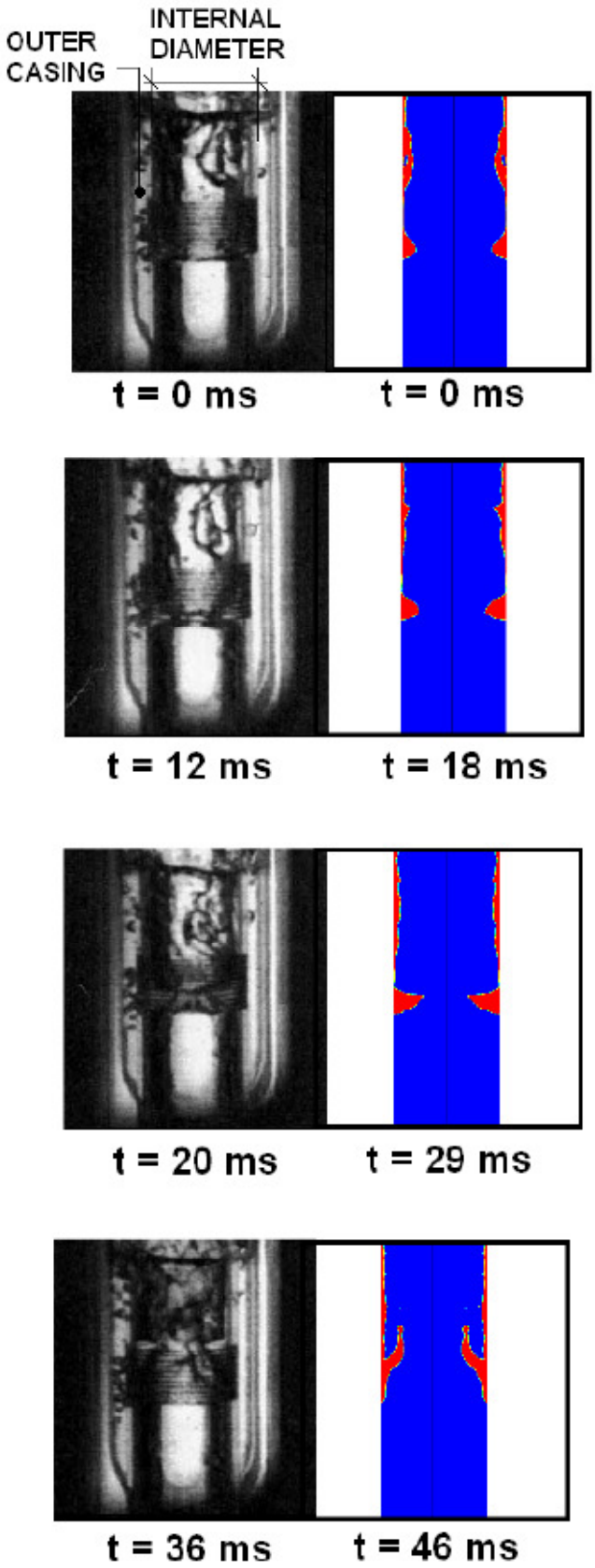

Fig. 5.3. Comparison between experimental visualizations by Barbosa *et al.* (2001) on the left and simulation on the right (case 1 in Table 1), D=32 mm, air-water, j_L = 0.03 m/s, j_G = 2.8 m/s, U_G^* = 0.20.

5.3.2 Simplified model of the wave levitation process

Here, an approximate model of the wave levitation process is proposed; it is based on the balance of forces acting on the forming wave. A similar treatment of the problem has been reported by Whalley (1987) to predict the gas velocity required for flooding. The present analysis is not aimed to provide a detailed or quantitatively consistent description of the problem, but its purpose is to give a qualitative explanation of the dependence on the governing parameters.

It has been assumed that during the whole growing process the wave has a semicircular shape, as shown in the Fig. 5.4, and amplitude equal to $\alpha D/2$, where D is the diameter of the pipe and α is a dimensionless diametral occlusion (i.e. the ratio of the total diametral occlusion to the diameter). No considerations have been made about the stability of the wave.

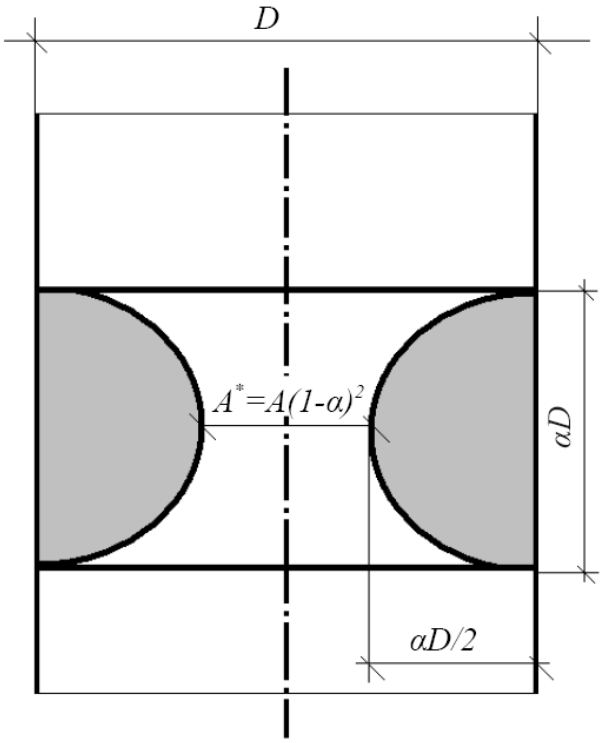

Fig. 5.4. Wave shape assumption.

The presence of the liquid film has not been taken into account and only the effects of the weight and the pressure variations in the gas core due to the air acceleration at the wave crest have been considered, while the shear stress on the gas-liquid interface has been neglected. With regard to this last assumption, it should be stressed that in a theoretical study by Jayanti *et al.* (1996) the force exerted on a standing wave by the gas flowing over it has been computed by means of a CFD code in typical flooding conditions, showing that the form drag is much more relevant that the

frictional force due to the shear stress. The same conclusions have been obtained in the present study by analysing the numerical simulations results.

Assuming that the air flow separates immediately after the crest of the wave, a rough estimation of the pressure drop between the windward and leeward sides of the wave could be given as follows:

$$\Delta p = \frac{\rho_G {j_G}^2}{2}\left[\left(\frac{A}{A^*}\right)^2 - 1\right] = \frac{\rho_G {j_G}^2}{2}\left[(1-\alpha)^{-4} - 1\right] \tag{5.2}$$

where A^* is the cross sectional area for the gas flow at the wave crest, j_G is the gas superficial velocity, and ρ_G is the gas density.

Assuming that constant pressures act on the windward and leeward sides, the force $F_{\Delta P}$ exerted on the wave in the upward direction can be roughly estimated by multiplying the pressure drop Δp by the projection of the wave surface on a plane perpendicular to the pipe axis (i.e. A-A^*):

$$F_{\Delta p} = \frac{\rho_G {j_G}^2}{2}\frac{\pi D^2}{4}\left[(1-\alpha)^{-4} - 1\right]\left[1-(1-\alpha)^2\right] \tag{5.3}$$

The total volume of the wave is:

$$V = \frac{\pi^2 D^3}{4}\alpha^2\left(\frac{1}{2} - \frac{2\alpha}{3\pi}\right) \tag{5.4}$$

Thus, the wave weight F_W is:

$$F_W = (\rho_L - \rho_G)g\frac{\pi^2 D^3}{4}\alpha^2\left(\frac{1}{2} - \frac{2\alpha}{3\pi}\right) \tag{5.5}$$

where ρ_G and ρ_L are the gas and liquid densities, while g is the gravity acceleration.

Now, the ratio of the upwards force to the downwards force $F_{\Delta P}/F_W$ can be expressed as:

$$\frac{F_{\Delta p}}{F_W} = \frac{\rho_G {j_G}^2}{(\rho_L - \rho_G)gD}\frac{3\left[(1-\alpha)^{-4} - 1\right]\left[1-(1-\alpha)^2\right]}{\alpha^2(3\pi - 4\alpha)} \tag{5.6}$$

The first term is a dimensionless gas Froude number $\mathrm{Fr_G}$, while the second one is a function of the dimensionless diametral occlusion α, thus the equation could be rewritten in the following form:

$$\frac{F_{\Delta p}}{F_W} = \mathrm{Fr_G}\, f(\alpha) = {U_G}^{*2} f(\alpha) \tag{5.7}$$

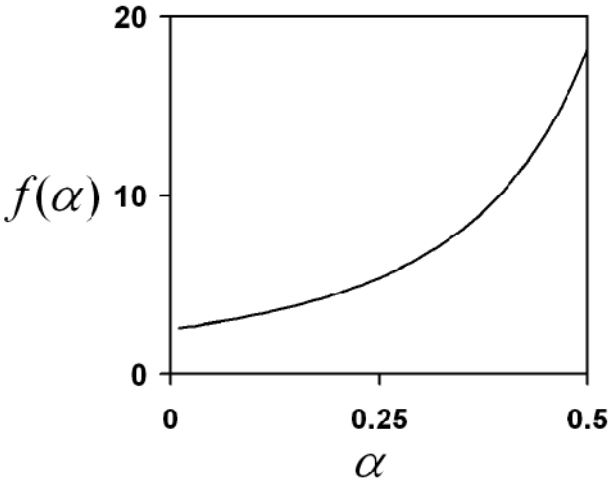

Fig. 5.5. *f(α)* versus α as defined in Eq. (5.7).

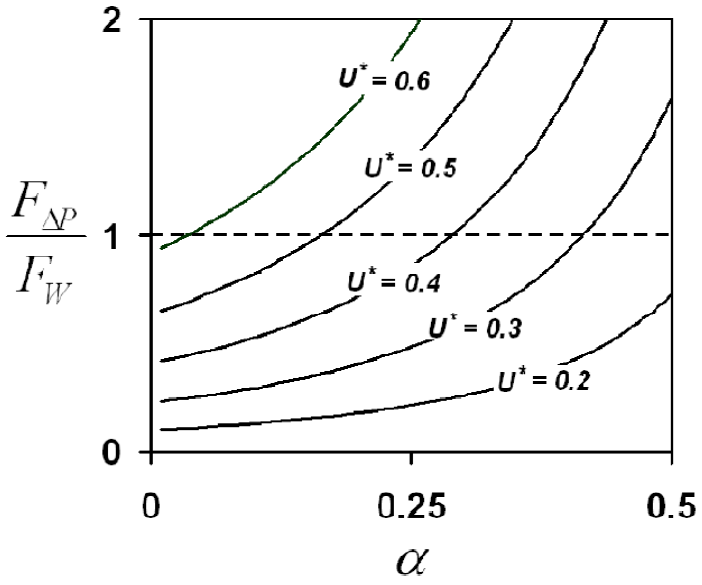

Fig. 5.6. Ratio of the upwards to the downwards forces at different gas dimensionless velocities (5.6).

The values assumed by *f(α)* are reported in Fig. 5.5: by increasing the wave amplitude (i.e. by increasing α), the ratio of the upwards force to the downwards force increases.

The wave forming at the liquid inlet continues growing until it reaches an amplitude big enough that it can be carried upwards; this condition is reached when the ratio of the upwards to the downwards force becomes bigger than unity. In Fig. 5.6 the ratio of the two opposing forces is computed by means of Eq. (6) for different values of the dimensionless gas velocity U_G^*. By increasing U_G^*, the critical value of α needed to achieve the wave levitation and corresponding to the unitary value of the ratio in the y-axis decreases: for this reason, the gas-liquid interface is expected to get flatter when

increasing the gas superficial velocity j_G or reducing the pipe diameter D, because the flooding-type waves are expected to have smaller amplitude.

When the dimensionless gas velocity is big enough (i.e. $U_G^* > 0.6$), the critical condition is always complied, hence it could be concluded that the flooding waves, if present, should have in this case a small amplitude. It is interesting to notice that in the experimental work by Owen (1986), at values of the dimensionless gas velocity U_G^* between 0.5 and 0.6, a transition is reported between what the author calls "churn flow" and what the author calls "churn/annular flow", as shown in Fig. 5.7.

The illustration by Owen shown in Fig. 5.7 also reports the characteristic experimental distribution of the dimensionless pressure gradient Δp^* against dimensionless gas velocity U_G^*, where Δp^* is defined as follows:

$$\Delta p^* = \frac{dp/dz - \rho_G g}{(\rho_L - \rho_G) g} \tag{5.8}$$

The breakdown of slug flow is accompanied by a sudden increase in the pressure drop, then, in the case of fully developed churn flow at medium and low water flow rates, the pressure drop decreases when increasing the air flow rate, eventually increasing again when entering the annular flow region. This fact could be explained by considering that when increasing U_G^*, as predicted by the simplified model developed, the gas-liquid interface should become flatter and this could have a stronger effect on the pressure gradient than the opposite effect due to the increase of the air superficial velocity j_G.

Furthermore, the flooding wave amplitude reduction when increasing the gas Froude number Fr_G could also explain typical experimental entrainment data as that shown in Fig. 5.8 by Wallis (1962), which shows that the entrained fraction decreases with increasing gas velocity in the churn flow region. In fact, the measured entrained fraction when churn flow occurs could be mainly carried in flooding-type waves, rather than as droplets.

It must be notice that in the simplified model proposed in this work the influence of the liquid film has been neglected. However, as reported in sections 5.3.4 and 0, in the numerical results a strong effect of the superficial liquid velocity j_L is observed.

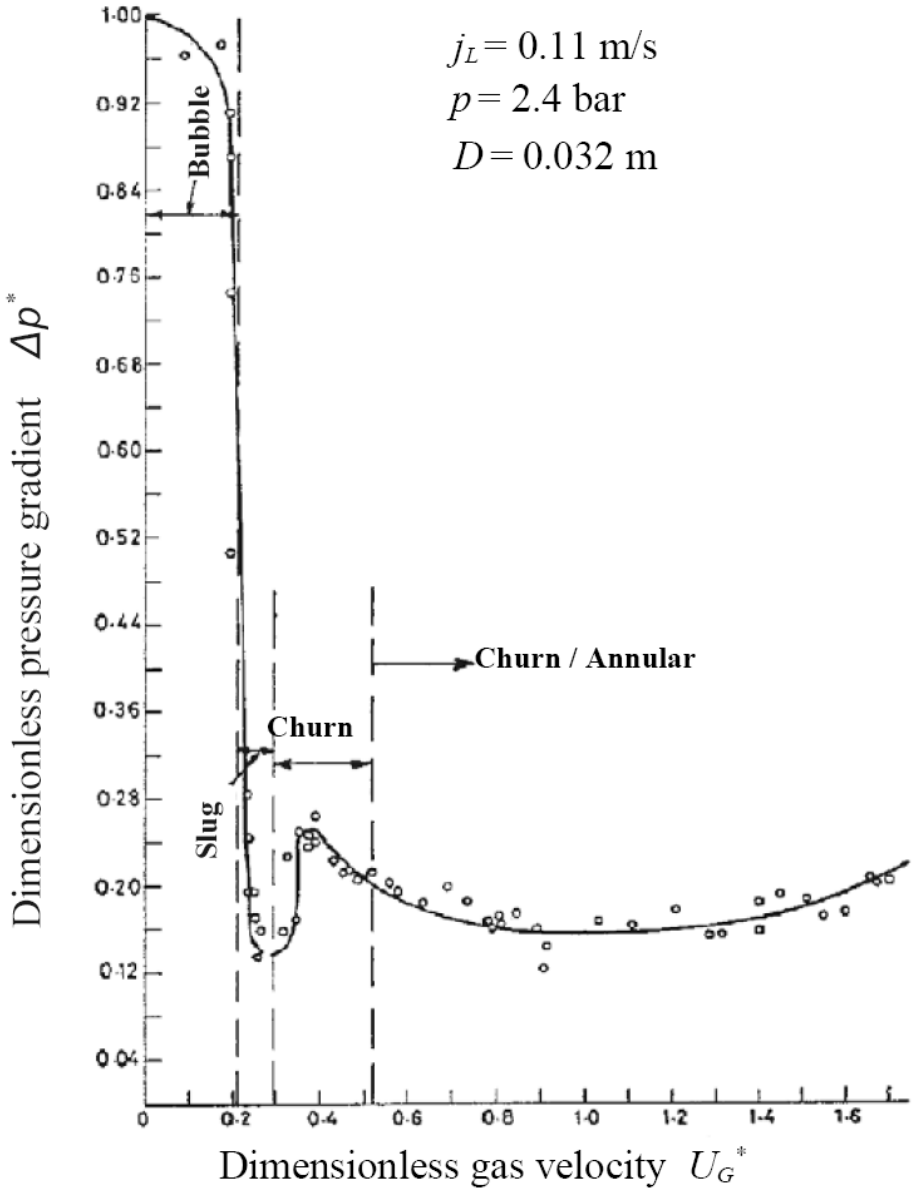

Fig. 5.7. Illustration of the dimensionless pressure gradient versus dimensionless gas velocity in Owen (1986).

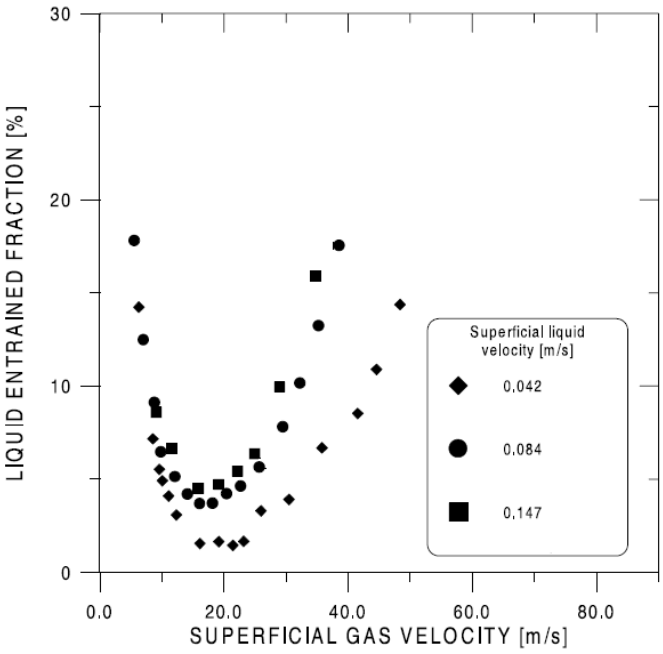

Fig. 5.8. Experimental entrained fraction in upwards co-current annular flow in Wallis (1962).

5.3.3 Typical flow field

Fig. 5.9 and Fig. 5.10 show the water and air velocity fields, respectively, obtained in the case of the simulation number 1 at the time when the forming wave at the liquid inlet has reached its maximum amplitude and is starting to travel upwards.

Above the wave, a thin water film falling by gravity can be seen. In the simulations performed at higher liquid flow rates such a flat water film is not obtained since the flooding wave formation has a higher frequency and water is continuously thrown in the region above the injector. However, in all the cases part of the film periodically flows downwards.

As shown in Fig. 5.10, the air flow accelerates on the windward side of the wave and the velocity profile becomes flatter at the crest; flow separation with a considerably big wake is present just after the crest of the wave. Even considering that in the case reported the gas superficial velocity is low (i.e. j_G = 2.8 m/s), the present result confirms the assumption made in section 5.3.2 about the flow separation.

Fig. 5.11 shows the variation of the air pressure on the wave interface and at the pipe axis, as a function of the axial distance; in the same picture, the shape of the interface is also plotted. As it can be seen, the phenomenon is similar to that of a vena contracta occurring when a fluid is forced to flow through an orifice. The pressure along the axis reaches the minimum at a point further downstream the crest of the wave, then it increases again, but a net pressure drop is obtained. The air pressure next to the gas liquid interface, instead, decreases violently at the wave crest, then it suddenly increases and reaches a constant value. This plateau corresponds to the wake region where flow separation occurs; moving further downstream, the flow reattaches and the pressure at the interface recovers reaching the same value as in the centreline. The variation of the shear stress in the gas phase next to the wave interface is shown in Fig. 5.12. Due to the acceleration on the wave windward side, the absolute value of the shear stress increases reaching its maximum at the crest; then the absolute value decreases till crossing zero just downstream the crest where flow separation is obtained.

By integrating the pressure and shear stress fields over the wave, the form drag due to the pressure variations around the wave and the frictional force have been calculated for the present case, concluding that the latter force is about 5% of the former one. This result confirms the hypothesis that, in typical churn flow regime, the effect of the interfacial shear stress is negligible. Similar results concerning the pressure and shear stress variations along the wave have been obtained by Jayanti *et al.* (1996) by simulating with a CFD code the air flow in a rectangular channel whose wall had the same shape as the standing wave obtained experimentally by Shearer and Davidson (1965) for air-water countercurrent flow.

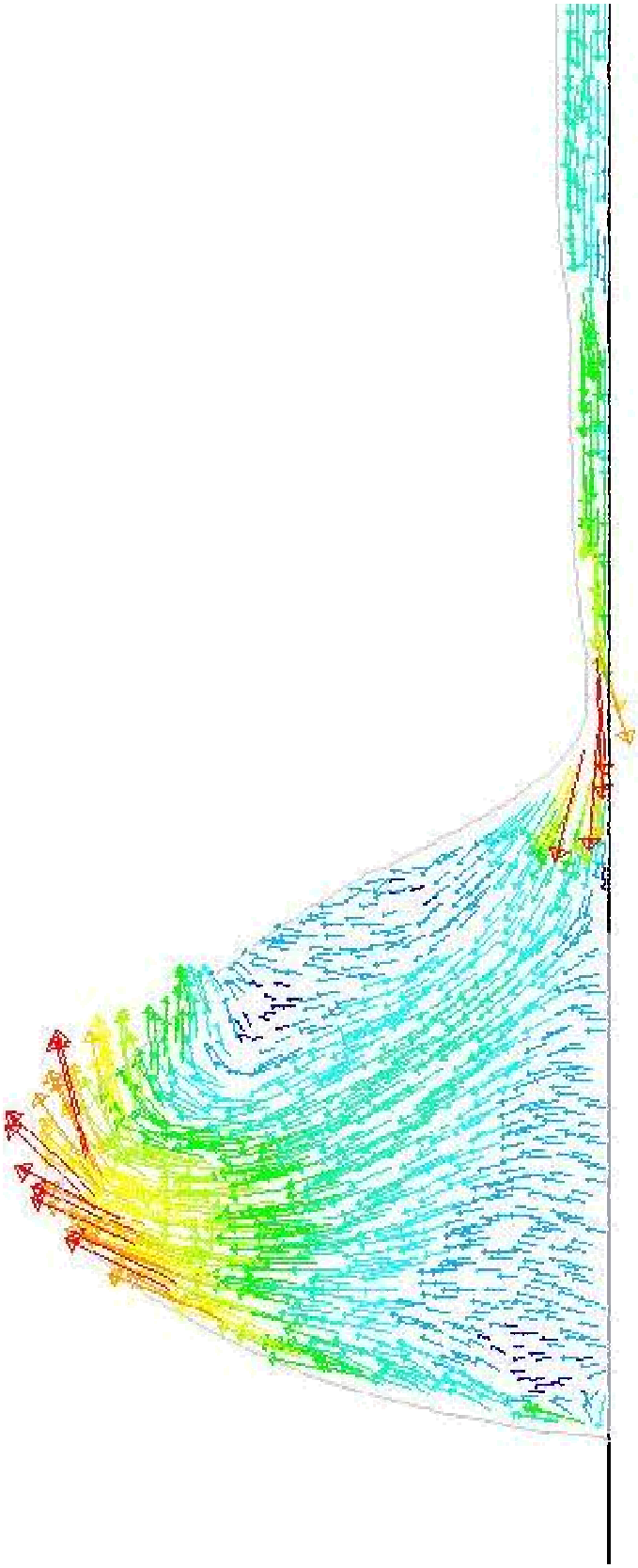

Fig. 5.9. Water velocity field when the forming wave has reached the maximum amplitude (case 1 in Table 5.1).

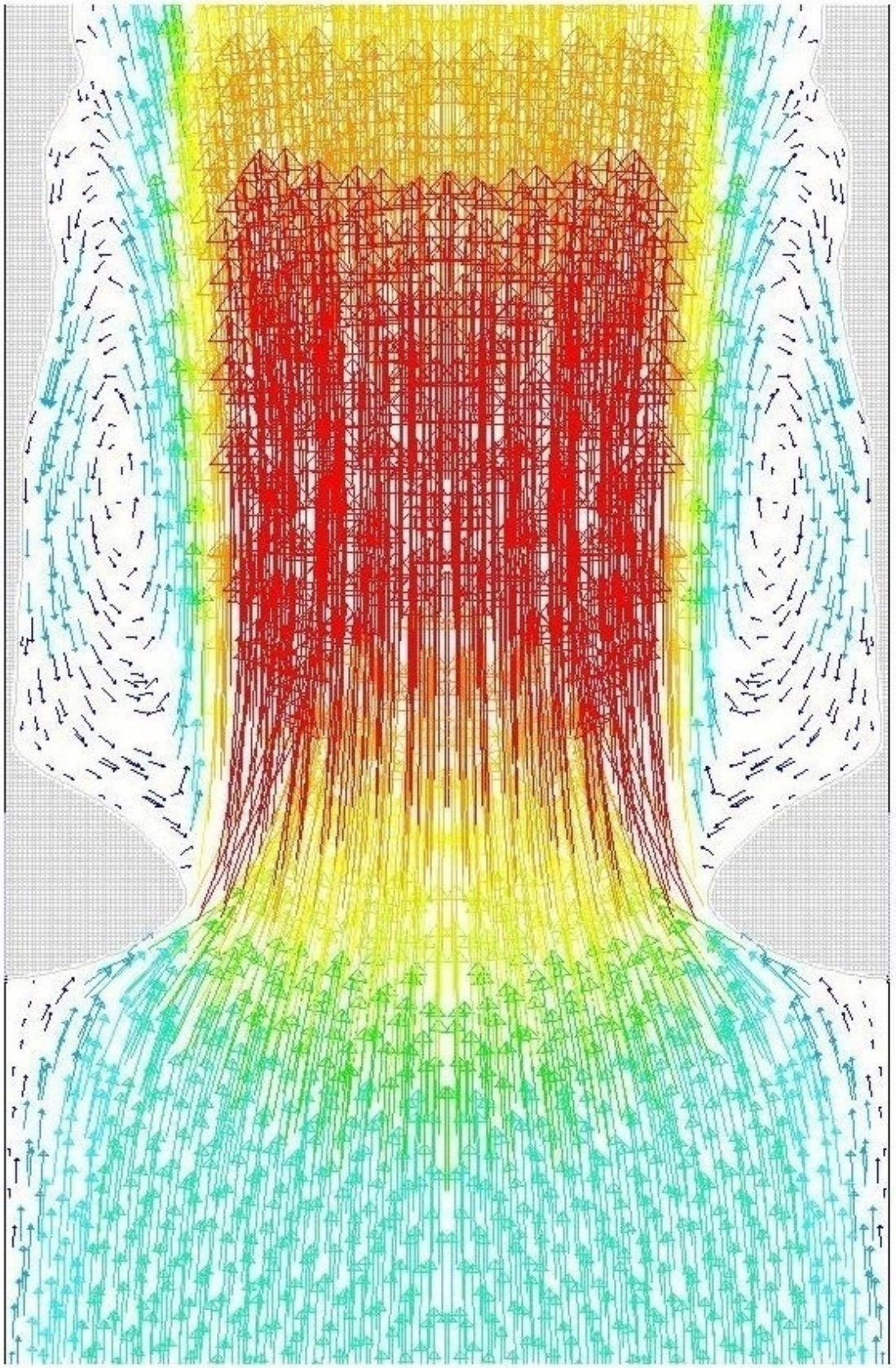

Fig. 5.10. Air velocity field when the forming wave has reached the maximum amplitude (case 1 in Table 5.1).

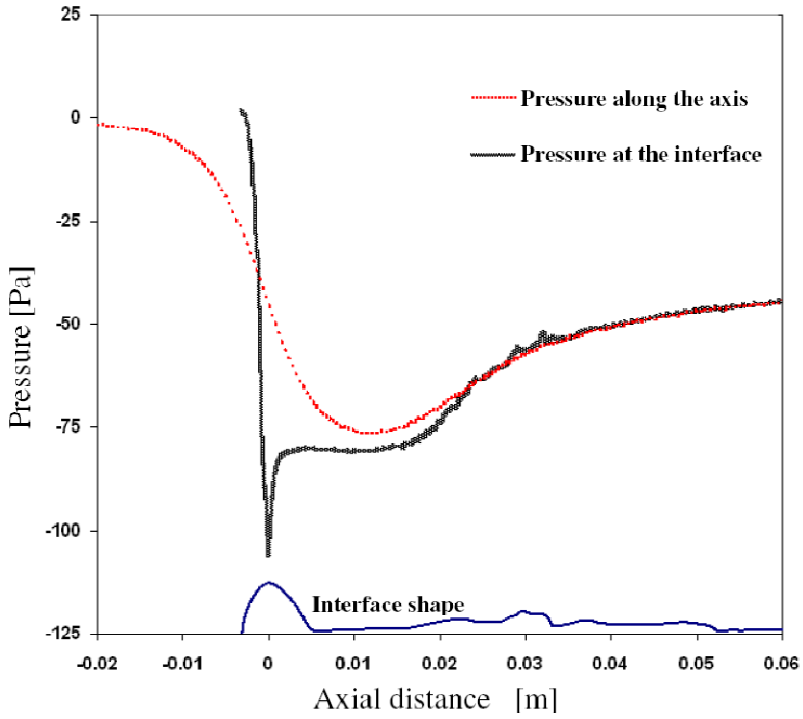

Fig. 5.11. Variation of pressure when the forming wave has reached the maximum amplitude (case 1 in Table 5.1).

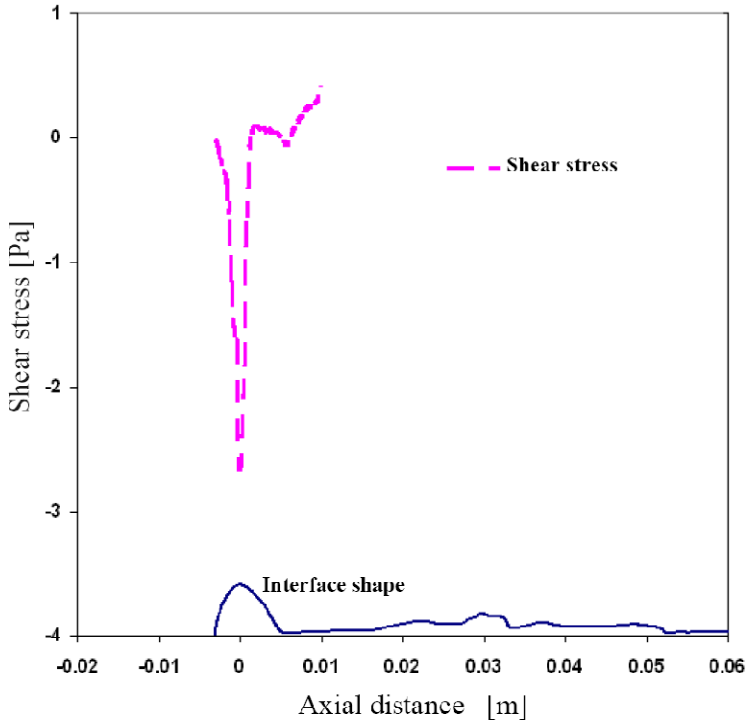

Fig. 5.12. Variation of shear stress on the forming wave when it has reached the maximum amplitude (case 1 in Table 5.1).

5.3.4 Effect of gas and liquid superficial velocity

Fig. 5.13 to Fig. 5.18 show pictures of the phases distribution for simulations performed considering an air-water mixture, with tube diameter D=32 mm or D=30 mm, taken at regular temporal steps of 10^{-2} s. The operating conditions for each case considered are reported in Table 1.

The two-phase flow computed in this simulations exhibits the distinctive characteristics of churn flow as they have been reported in the experimental works available in the literature: a central gas core is present and, since the gas velocity is not high enough to carry upwards the liquid by interfacial shear stress (as it happens in the annular flow regime), the net upward flow is due to flooding-type waves of big amplitude caused by the partial occlusion of the air flow and carried upwards by means of the drag force.

The characteristic water flow reversal is also predicted in the simulations. The presence of a water falling film has already been shown in Fig. 5.9, but it can also be seen in the pictures from Fig. 5.13 to Fig. 5.18: by watching, for example, the pictures from 5) to 8) in Fig. 5.15, it can be seen that part of the liquid film is falling by gravity and part of the wall is not wetted because no water entrance from the upper edge of the domain is taken into account in the mathematical model. However, when this film becomes thick enough, another flooding-type wave is formed and the water is thrown upwards again.

At the water inlet, flooding waves are continuously formed: because of the liquid entering the domain, the wave amplitude increases till the drag force becomes big enough to win the gravity force. The wave starts to travel upwards when a sufficient channel occlusion is reached; then, the crest breaks out, some water can be peeled and subsequently the finger-like shape is developed.

The effect of the superficial gas velocity j_G can be examined by comparing, for example, Fig. 5.16 with Fig. 5.17, since they refer to simulations obtained at the same superficial liquid velocity (j_L = 0.11 m/s) and different superficial gas velocities (j_G = 4.5 m/s and j_G = 6 m/s, respectively). By looking at the wave forming at the liquid injector, it can be seen that by increasing the superficial gas velocity, the critical wave amplitude required to achieve the levitation gets smaller, hence the gas-liquid interface becomes flatter. It can also be noticed that the wave breakdown process and the formation of finger-type waves seem to be in some way suppressed or delayed. These results are in agreement with the qualitative dependence of the wave amplitude on the dimensionless gas velocity U_G^* predicted by the simplified model reported in section 5.3.2.

The effect of the superficial liquid velocity j_L, which has not been considered in the theoretical model, is also very strong. The simulation shown in Fig. 5.13 has been performed at the lowest liquid velocity considered (j_L = 0.03 m/s); in this case a very thin and flat liquid film adherent to the pipe wall is shown and only a single flooding wave travelling upwards is present inside the computational domain. The following figures refer to simulations performed at increasing liquid velocities (j_L = 0.06 m/s for Fig. 5.14 and Fig. 5.15, j_L = 0.11 m/s for Fig. 5.16 and Fig. 5.17, and j_L = 0.22 m/s for Fig. 5.18). By increasing the liquid flow rate, the flooding-type waves at the injector grow faster, hence the formation frequency increases and, since water is continuously thrown upwards, the liquid has not enough time to develop a flat film. For this reason,

the gas-liquid interface becomes much more disturbed and the simultaneous presence of more than one flooding wave is computed.

It could be reminded here that the domain adopted for the simulations is quite short just to reduce the required computational effort, and this could have an influence on the results obtained. In fact, due to the oscillatory nature of the liquid motion in churn flow, the water falling by gravity downstream affects the flow upstream, but in the mathematical model considered no water entrance from the upper edge of the domain is taken into account.

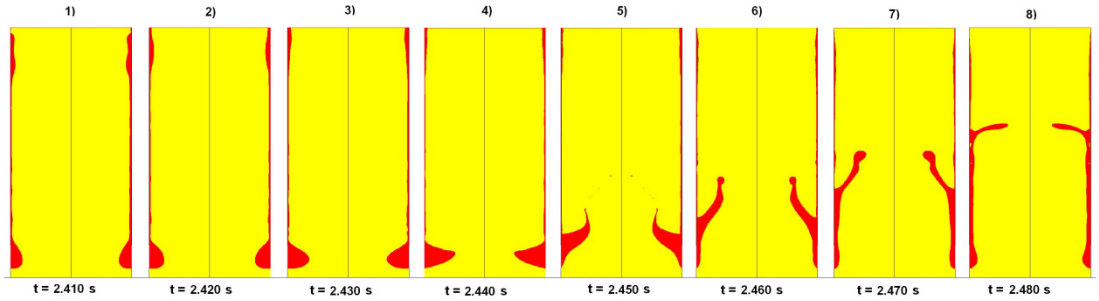

Fig. 5.13. Simulation 1, air-water, D = 32 mm, j_L = 0.03 m/s, j_G = 2.8 m/s, U_G^* = 0.20.

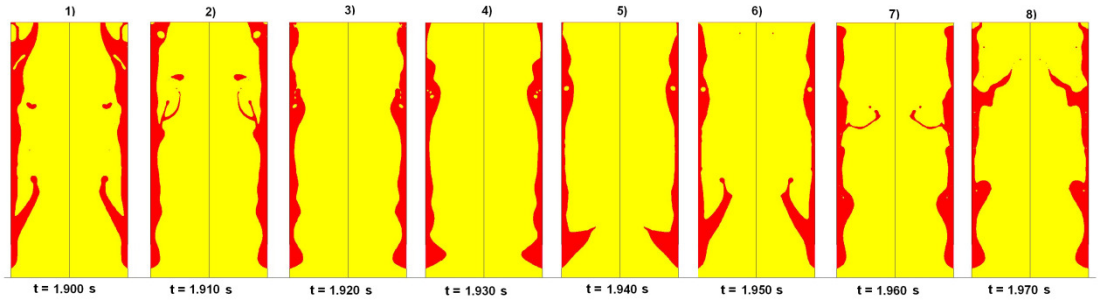

Fig. 5.14. Simulation 3, air-water, D = 30 mm, j_L = 0.06 m/s, j_G = 4.5 m/s, U_G^* = 0.29.

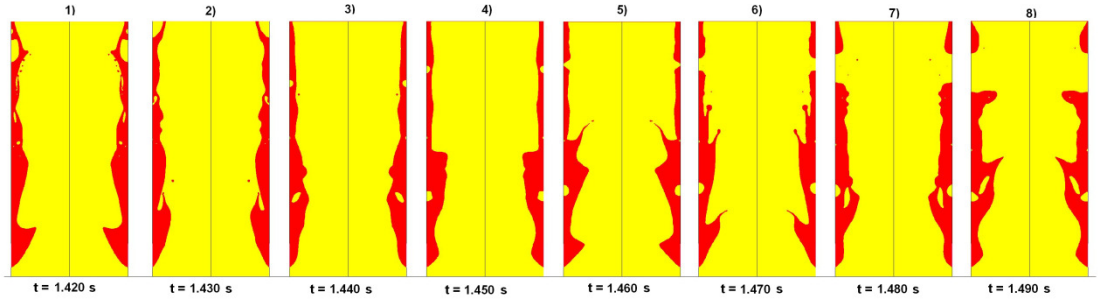

Fig. 5.15. Simulation 4, air-water, D = 30 mm, j_L = 0.06 m/s, j_G = 6 m/s, U_G^* = 0.39.

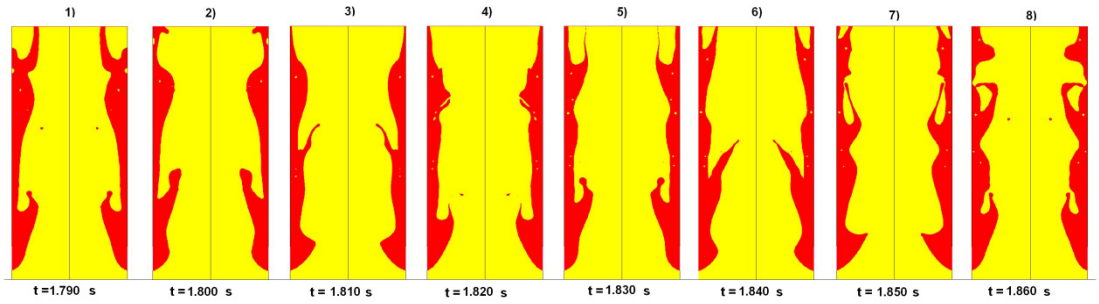

Fig. 5.16. Simulation 5, air-water, D = 30 mm, j_L = 0.11 m/s, j_G = 4.5 m/s, U_G^* = 0.29.

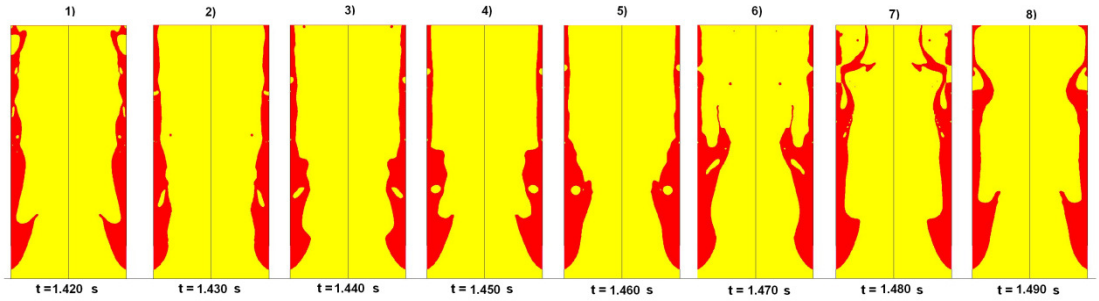

Fig. 5.17. Simulation 6, air-water, D = 30 mm, j_L = 0.11 m/s, j_G = 6 m/s, U_G^* = 0.39.

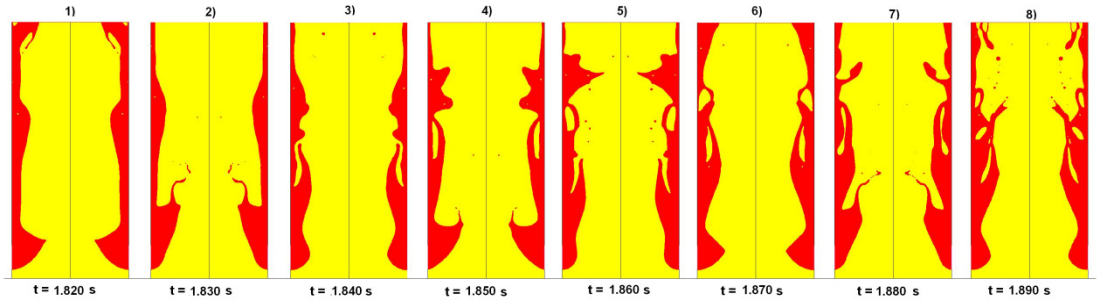

Fig. 5.18. Simulation 7, air-water, D = 30 mm, j_L = 0.22 m/s, j_G = 4.5 m/s, U_G^* = 0.29.

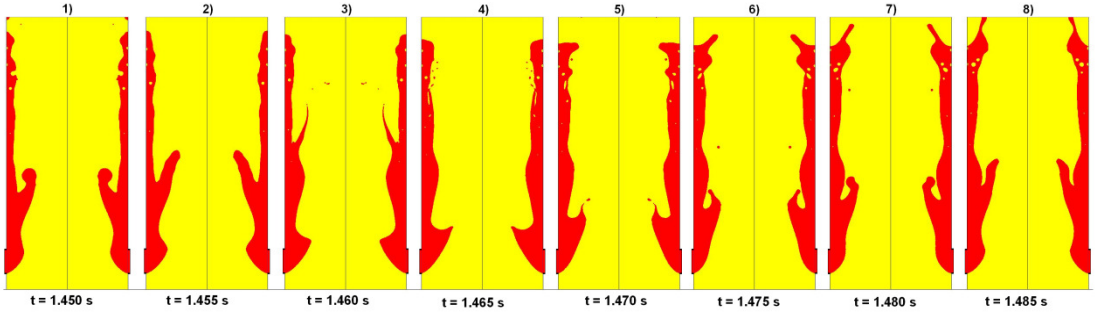

Fig. 5.19. Simulation 8, air-water, D = 30 mm, j_L = 0.11 m/s, j_G = 5 m/s, U_G^* = 0.32.

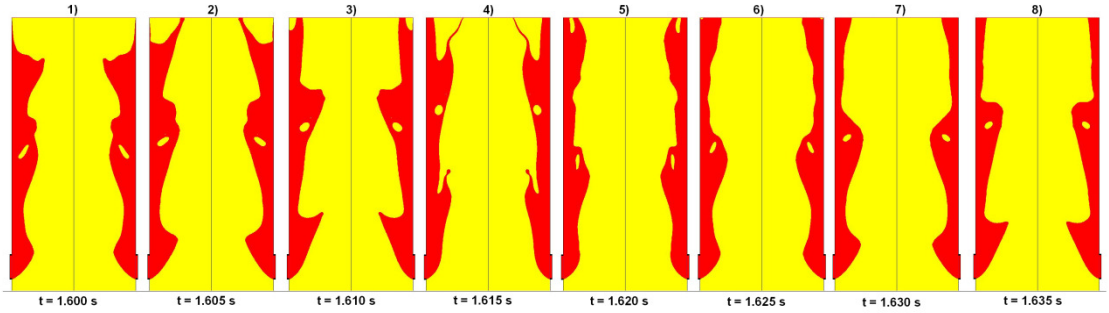

Fig. 5.20. Simulation 9, air-water, D = 20 mm, j_L = 0.11 m/s, j_G = 5 m/s, U_G^* = 0.40.

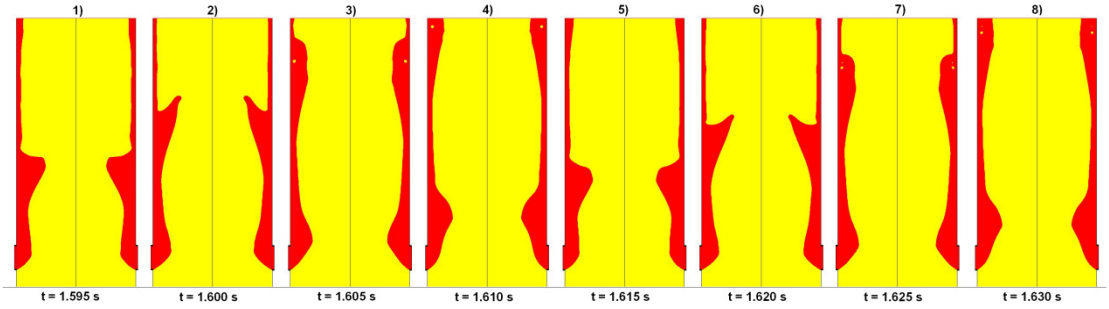

Fig. 5.21. Simulation 10, air-water, D = 10 mm, j_L = 0.11 m/s, j_G = 5 m/s, U_G^* = 0.56.

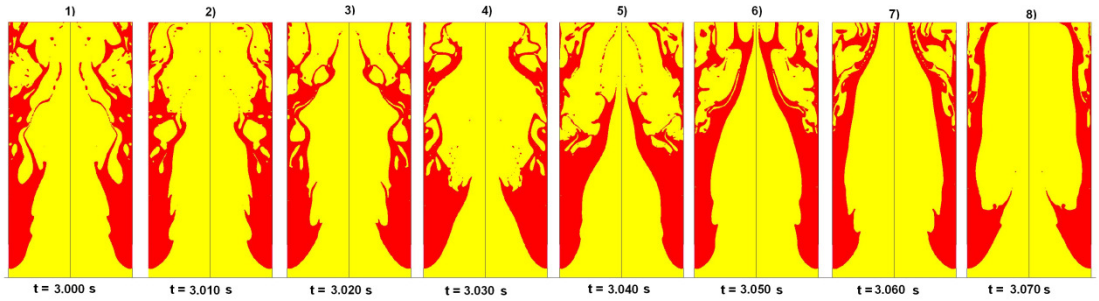

Fig. 5.22. Simulation 11, R134a vapour-liquid, D = 32 mm, j_L = 0.1 m/s, j_G = 0.8 m/s, U_G^* = 0.26.

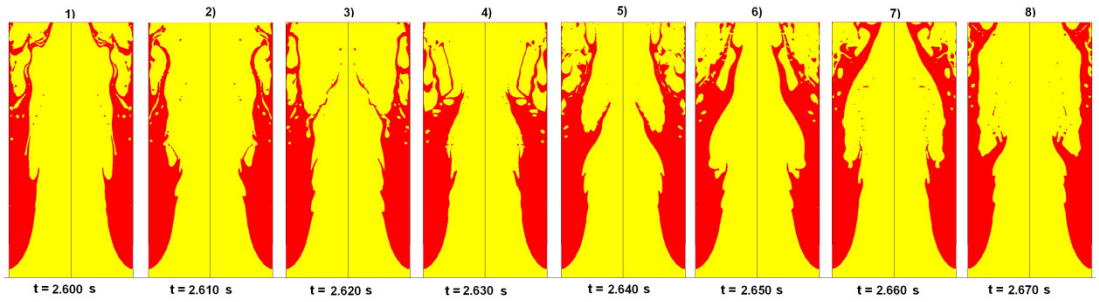

Fig. 5.23. Simulation 12, R134a vapour-liquid, D = 32 mm, j_L = 0.1 m/s, j_G = 1.1 m/s, U_G^* = 0.35.

5.3.5 Effect of diameter

Fig. 5.19, Fig. 5.20 and Fig. 5.21 show some pictures taken at regular temporal intervals of 5 10^{-3} s of simulations obtained by considering the same superficial velocities (i.e. j_L = 0.11 m/s and j_G = 5 m/s), but decreasing pipe diameters (i.e. D = 30 mm, D = 20 mm and D = 10 mm); the corresponding values of the dimensionless gas velocity U_G^* vary from 0.32 up to 0.56. It should be stressed that these three simulations refer to the same point in the Hewitt and Roberts (1969) flow patter map (i.e. points 8, 9 and 10 in Fig. 5.2).

By observing the pictures reported in Fig. 5.19 to Fig. 5.21, it can be seen that the computed flooding waves are quite different in the three cases: by reducing the pipe diameter, the ratio of the maximum wave amplitude to diameter required to achieve the levitation gets smaller, hence the gas-liquid interface becomes flatter.

Since the dimensionless gas velocity increases by decreasing the tube diameter, also these results are in agreement with the qualitative dependence of the wave amplitude on the dimensionless gas velocity U_G^* predicted by the simplified model reported in section 5.3.2.

5.3.6 Simulations of R134a vapour-liquid churn flow

Fig. 5.22 and Fig. 5.23 report pictures of the phases distribution taken at regular temporal intervals of 10^{-2} s for the two simulations performed considering R134a liquid-vapour mixture. The two phases have been considered to be in equilibrium at 30°C saturation temperature; the simulations operating conditions are shown in Table 1.

The two simulation have been performed at the same liquid superficial velocity (j_L = 0.1 m/s) and different gas superficial velocities (j_G = 0.8 m/s and j_G = 1.1 m/s). The gas flow rates for the R134a simulations have been chosen in such a way that the dimensionless gas velocities U_G^* were comparable to those obtained in the air-water mixture simulations (i.e. U_G^* = 0.26 in the case of simulation 11 and U_G^* = 0.35 in the case of simulation 12). Since the R134a vapour density is much higher than the air density, the superficial vapour velocities in the two R134a simulations are considerably lower.

As it can be immediately seen, the vapour-liquid interface is much more indented than in the case of air-water and a high amount of small size structures are formed and peeled by stretching of thin liquid filaments. Furthermore, a lot of small amplitude waves are present at the vapour-liquid interface, whereas this phenomenon was not present at all in the air-water simulations. Since the surface tension has a stabilizing effect on the interface distortions, the results obtained could be qualitatively explained by noticing that this property is ten times lower for R134a as compared to air-water mixture. The phenomenon of liquid peeling from the interface can be considered to be ruled by the following gas Kutateladze number Ku_G:

$$Ku_G = \frac{j_G \rho_G^{1/2}}{\left[g\sigma(\rho_L - \rho_G)\right]^{1/4}} \tag{5.9}$$

where σ is the surface tension. In the case of air-water, the values of Ku_G obtained for the simulations performed vary from 0.7 to 1.3, while in the case of the refrigerant they vary from 1.6 to 2.2.

Even if small amplitude waves are present at the R134a vapour-liquid interface it should be stressed that the upward flow of the liquid phase is not due to this phenomenon, but it is due once again to the formation of large amplitude flooding-type waves. In picture 4) of Fig. 5.22 the formation of one of these waves can be seen, while in the following images it can be seen how the wave is able to throw the liquid upwards. As well as in the case of air-water mixture, the liquid motion has a pulsating nature, since most of the liquid structure peeled from the surface starts to fall some distance downstream the point where they have been torn off and the net liquid upward flow is due to flooding-type waves.

By comparing Fig. 5.22 with Fig. 5.23 it can been seen that also in the case of R134a simulations, by increasing the adimensional gas velocity U_G^*, the critical channel occlusion required to achieve the levitation of the flooding waves gets smaller, hence the gas-liquid interface becomes flatter.

5.4 Conclusions

Numerical simulations of air-water and R134a vapour-liquid churn flow performed by means of the VOF method implemented in the commercial code FLUENT have been reported. The study was conducted using an axisymmetrical domain reproducing the region next to the porous wall liquid injector of a typical test section for the investigation of vertical gas-liquid flows.

This work is not directly linked to the study concerning minichannel heat exchangers, however it has been important in order to assess the capability of the method used to compute the motion of the gas-liquid interface, which is crucial to characterize two-phase flow and heat transfer.

The simulations have shown to be able to qualitatively capture the distinctive characteristics of churn flow as they have been reported in the experimental works available in the literature, yielding a satisfactory agreement with experimental visualizations and data about the formation and levitation of the ring-type waves typical of churn flow. The liquid motion in the simulations has shown to have a pulsating nature since flow reversals are present and the net upward flow is due to flooding-type waves of big amplitude caused by the partial occlusion of the air flow and carried upwards by means of the drag force.

Simulations have been performed at different liquid and gas superficial velocities and pipe diameters.

According to a simplified model of the wave levitation process proposed in this work, at increasing dimensionless gas velocities U_G^* (i.e. at increasing gas superficial velocity or decreasing pipe diameter) the channel occlusion by the liquid required to achieve the levitation of the flooding waves is expected to get smaller, hence the gas-liquid interface is expected to become flatter. The same trend is shown in the simulations performed both in the case of air-water and R134a vapour-liquid mixtures.

An analysis of the gas and liquid velocity fields at the time when a forming wave at the liquid inlet has reached its maximum amplitude and is starting to travel upwards has been reported, and the effects of the pressure and shear stress variations at the interface have been computed concluding that the drag force is much higher than the frictional one at churn flow conditions.

In the simulations performed, a strong effect of the superficial liquid velocity on the distribution of the two phases in the pipe is shown: by increasing the liquid flow rate the flooding waves formation frequency increases and the liquid film adherent to the pipe wall becomes thicker and much more disturbed.

In the simulations concerning the R134a vapour-liquid mixture, besides the big amplitude flooding waves typical of churn flow, small amplitude waves are present at the vapour-liquid interface and a high amount of small size structures are formed and peeled by stretching of thin filaments of liquid; this phenomenon can be attributed to the low value of the surface tension.

Chapter 6.
Conclusions

Design of minichannel shell-and-tube heat exchangers

Refrigerant charge minimization is a major design objective for equipment using hydrocarbons or ammonia because the possible hazard when dealing with toxic or flammable fluids is proportional to the total amount of refrigerant trapped in the system. The same restriction should be adopted, in any case, in systems operating with halogenated fluids when trying to reduce emissions for environmental reasons. Since most of the charge in HVAC equipment is trapped in the heat exchangers, and especially in the condenser, the first step in order to minimize the refrigerant charge is the optimization of these devices, and minichannels technology is a very good opportunity to obtain this target.

The design of an innovative condenser, an evaporator and an internal heat exchanger (IHX) for the use with propane is presented. These devices are shell-and-tube heat exchangers designed to minimize the refrigerant side internal volume and employing 2 mm i.d. copper minichannels instead of conventional tubes. In the case of the condenser and the evaporator, propane flows inside the tubes and water flows on the shell side, while in the case of the IHX the liquid flows inside the tubes and the vapour flows on the shell side.

Experimental data of heat transfer performance and pressure drop is reported. The measurements have been obtained using R22 for the minichannel evaporator and propane for the IHX, while experimental data using both propane and R22 is available for the minichannel condenser.

Data has also been compared against simplified computational procedures based on correlations available in the literature and used for the design of the heat exchangers.

The overall heat transfer coefficient and pressure drop on shell side of the heat exchangers have been computed by the Bell-Delaware method (Bell, 1963). The heat transfer coefficient in the condenser has been computed by means of the Cavallini *et al.* (2006) correlation, while the Cavallini *et al.* (2005), Friedel (1979, 1980) and Niño (2006) correlations have been implemented for pressure drop. In the computational procedure for the minichannel evaporator, the Liu and Winterton (1991) correlation and the Friedel (1979, 1980) correlation were used for the evaluation of the evaporation heat transfer coefficient and pressure drop, while the onset of the dryout was predicted by means of the Del Col *et al.* (2007) correlation for minichannels. The Kandlikar and Balasubramanian (2004) correlation for evaporation heat transfer coefficient was also implemented as a comparison. Finally, the classical Dittus-Boelter equation (McAdams,

1942) was used for the superheating and post-dryout regions of the evaporator and the tube side of the IHX.

The computed thermal performance of the condenser is slightly higher than the experimental one when using both propane and R22 (i.e. maximum deviation around 15% in terms of average temperature difference between water and refrigerant). Regarding the evaporator, both the effect of inlet quality and superheat are well predicted by the computational procedure.

Applications of minichannel heat exchangers in a heat pump

A heat pump using propane as the refrigerant and having a heating capacity of about 100 kW has been designed and realized. The heat pump has been designed for laboratory tests and the minichannel shell-and-tube heat exchangers have been installed in the facility together with a conventional brazed plate condenser and an evaporator, in order to test and compare different configurations. Since brazed plate heat exchangers are the current industrial benchmark to achieve internal volume minimization, they have been used as reference to experimentally quantify the advantages of operating the heat pump using the shell-and-tube minichannel heat exchangers, in terms of both energy efficiency and refrigerant charge.

The propane side internal volume is 2.9 L in the case of the minichannel condenser and 8.4 L in the case of the brazed plate heat exchanger; hence, 65% reduction in terms of internal volume has been obtained. Regarding the evaporator, the refrigerant side internal volume is 5.8 L in the case of the minichannel heat exchanger and 8.4 L in the case of the brazed plate evaporator; hence, 30% reduction has been obtained.

It has been chosen to design a water-to-water heat pump, since roof top chillers and heat pumps using a hydronic system to distribute chilled or hot water are an ideal solution to the safety problem.

The energy performance of the heat pump has been tested at different water temperatures at the condenser outlet (i.e. 35°C, 40°C and 45°C) and at the evaporator inlet (i.e. 10°C and 12°C). All tests have been carried out using the brazed plate evaporator and four different configurations have been tested (i.e. minichannel condenser without IHX, plate condenser without IHX, minichannel condenser with IHX and plate condenser with IHX).

The minimum equipment COP in heating mode measured among all the configurations tested is 4.36 at water temperatures 10-5°C/30-35°C, while the minimum COP in cooling mode is 3.45 at water temperatures 12-7°C/30-35°C.

The performance when using the minichannel condenser has been compared to the one obtained when using the brazed plate condenser, showing that a very small COP reduction (i.e. average reduction 1.5% and maximum reduction 2.6%) is obtained when using the condenser designed for low charge. It must be considered that the nominal heat transfer area of the plate condenser is around 7 m^2, while the propane side heat transfer area of the minichannel condenser is around 5 m^2.

Propane has a very high solubility with conventional lubricants and ester oils. Although this characteristic is advantageous for a good circulation of the oil, it can lead to a substantial decrease of the viscosity, which may be harmful to the compressor, especially at low oil temperature and high suction pressure. In order to decrease the

solubility of the refrigerant in the oil, at least 20 K vapour superheat at the compressor suction and discharge are suggested by the manufacturer of the compressor used in the heat pump (Bitzer, 1997). The minichannel IHX has been designed in order to provide around 20 K additional vapour superheat at design operating conditions. When the IHX is used, the experimental COP in heating mode is increased from around 1% at 12-7°C/30-35°C up to around 3% at 10-5°C/40-45°C.

Experimental data of isentropic efficiency, global efficiency and volumetric efficiency of the semihermetic reciprocating compressor used in the heat pump are reported. At full compressor capacity when using the IHX the global efficiency varies from around 0.69 up to 0.71, while without IHX the maximum efficiency is around 0.67 and experimental values as low as 0.62 have been measured. Regarding the volumetric efficiency, this varies from around 0.82 up to 0.89 with IHX, while without IHX experimental values as low as 0.73 have been measured. Since, at fixed pressure ratio, the main difference between the test runs with IHX and the test runs without IHX was the temperature of the lubricant oil, it is clear from the results obtained that the issue of the high solubility of propane in the oil is relevant, and that the fulfilment of the measures required by the manufacturer of the compressor is important.

Experimental measurements of the propane charge required by the different configurations tested are reported. The measured charge ranges from 3.1 kg for the configuration using the minichannel condenser without IHX up to 5.1 kg for the configuration using the plate condenser with IHX. By using the minichannel condenser instead of the brazed plate condenser 0.8 kg refrigerant charge reduction has been experimentally measured, while the additional internal volume due to the use of the IHX gives rise to around 0.3 kg propane charge increase.

Since the heat pump has been devoted only to test applications and the piping layout is quite complex because of the need to install five different heat exchangers in the same facility, the piping length could not be minimized and around 1 kg of propane is estimated to be trapped in the piping. Furthermore, a liquid receiver and a dehydrating filter are installed in the facility. By discarding the dehydrating filter and the liquid receiver, and considering a liquid line 0.25 m long and suction and discharge lines 1 m long, the present heat pump could be run with less than 2 kg of propane in the configuration with minichannel condenser without IHX. It should be pointed out that a large amount of refrigerant (i.e. around 1 kg) is expected to be trapped in the semi-hermetic reciprocating compressor, mainly solved in the mineral oil.

Use of VOF method for modelling of two-phase flow

Besides the development and validation of empirical correlations able to predict the global thermal performances, a more complete understanding of the two-phase flow and heat transfer processes in minichannels is needed for the design and optimization of heat exchangers. The study of two-phase heat transfer in minichannels, however, is very complex, mainly because of the presence of a vapour-liquid interface and different flow regimes and spatial distributions of the phases which have a very strong influence on the heat transfer.

While in the past CFD simulations were not suitable for the study of such kind of complex phenomena, a number of different methods are nowadays available for the direct simulation of multiphase flows because of the increased computational

capabilities. These new techniques can be very useful, in particular when trying to extend the investigation to new minichannel geometries for which a lack of experimental data or correlations exists. Some simulations are presented in this thesis using the Volume Of Fluid (VOF) method implemented in FLUENT, which is able to compute multiphase flows of immiscible fluids, tracking the motion of the interface between them without using any empirical closure law to model the interaction between the phases.

Numerical simulations of air-water and R134a adiabatic churn flow have been performed. The study was conducted using an axisymmetrical domain reproducing the region next to the porous wall liquid injector of a typical test section for the investigation of vertical gas-liquid flows.

This work is not directly linked to the study concerning minichannel heat exchangers, however it has been important in order to assess the capability of the method used to compute the motion of the gas-liquid interfaces, which is crucial to characterize two-phase flow and heat transfer.

The simulations have shown to be able to qualitatively capture the distinctive characteristics of churn flow as they have been reported in the experimental works available in the literature, yielding a satisfactory agreement with experimental visualizations and data about the formation and levitation of the ring-type waves typical of churn flow. The liquid motion in the simulations has shown to have a pulsating nature since flow reversals are present and the net upward flow is due to flooding-type waves of big amplitude caused by the partial occlusion of the air flow and carried upwards by means of the drag force.

Simulations have been performed at different liquid and gas superficial velocities and pipe diameters and a simplified model of the wave levitation process showing the influence of the gas Froude number on the flooding waves amplitude is proposed and used to explain the numerical results. At increasing gas Froude numbers (i.e. at decreasing pipe diameter or increasing gas superficial velocity), the channel occlusion by the liquid required to achieve the levitation of the flooding waves is expected to get smaller, hence the gas-liquid interface is expected to become flatter.

VOF method applied to the study of condensation in minichannels

The study in the field of VOF modelling has then been extended to the 3D steady-state simulation of condensation of R134a inside a 1 mm internal diameter minichannel horizontally oriented. This work was performed at the Cooling Technologies Research Center (CTRC) of the Purdue University, West Lafayette, Indiana, USA under the supervision of Prof. Suresh Garimella and Prof. Jayathi Murthy.

The wall temperature (i.e. T_W = 40°C) and the fluid saturation temperature (i.e. T_{SAT} = 50°C) were imposed as boundary conditions. The simulation has been performed at mass flux G = 200 kg m^{-2} s^{-1}, and both the effects of gravity and surface tension have been taken into account. The inlet and outlet vapour qualities were 0.94 and 0.54, respectively.

In the case of condensation of a pure fluid, the vapour-liquid interfacial temperature can be assumed to be at the saturation temperature. This assumption has been imposed as boundary condition in the simulations by means of a user defined function to specify phase-change mass transfer.

It has been assumed that the flow was laminar inside the liquid phase and turbulent inside the vapour phase. Turbulence has been handled by the low Reynolds form of the standard k-ω model, which has been modified in order to take into account this assumption.

Computational results about the shape of the vapour-liquid interface at different vapour qualities are reported. The computed flow regime is annular. At the inlet of the computational domain the liquid film is evenly distributed all along the tube circumference, but moving downstream the minichannel the liquid film at the bottom of the pipe becomes thicker because of the stratification of the condensate liquid draining from the top, while the thickness of the liquid in the entire upper half of the tube keeps almost constant.

Computational results about the cross sectional average heat transfer coefficient are reported and compared to predictions by the Cavallini *et al.* (2006) correlation. Heat transfer coefficients predicted by the simulation are in general lower than the values predicted by the empirical correlation and the maximum deviation is around 20%.

The simulations of condensation reported in this thesis are just preliminary results. A better understanding of two-phase flow and heat transfer during condensation in minichannels would be very important for the optimization of minichannel heat exchangers. Future work should extend the VOF study to the complete condensation process, and the simulation of different minichannel geometries and dimensions. In particular, the capability of the VOF method to take into account the surface tension force is very promising, since the effect of surface tension is expected to be important at small diameter sizes and when using non circular minichannels.

References

A.D. Little Inc., 2002. Global Comparative Analysis of HFC and Alternative Technologies for Refrigeration, Air Conditioning, Foam, Solvent, Aerosol Propellant, and Fire Protection Applications, Report for The Alliance for Responsible Atmospheric Policy, A.D. Little Inc., Acorn Park, Cambridge, MA, Reference 75966.

Azzopardi, B.J. and Zaidi, S.H., 2000. Determination of entrained fraction in vertical annular gas/liquid flow. J. Fluids Eng. 122, 146–150.

Azzopardi, B.J. and Wren, E., 2004. What is entrainment in vertical two-phase churn flow? Int. J. Multiphase Flow 30, 89-103.

Barbosa, J., Govan, A.H., Hewitt, G.F., 2001. Visualisation and modelling studies of churn flow in a vertical pipe. Int.J. Multiphase Flow 27, 2105–2127.

Baroczy, C. J., 1963, Correlation of liquid fraction in two-phase flow with application to liquid metals, NAA-SR-8171.

Bell, K.J., 1963. Final report of the cooperative research program on shell-and-tube heat exchangers, University of Delaware Eng. Exp. Stat. Bull. 5.

Berthelsen, P.A., Ytrehus, T., 2005, Calculations of stratified wavy two-phase flow in pipes, International Journal of Multiphase Flow 31, 571-592.

Bertsch, S.S., Groll, E.A., Garimella, S.V., 2008. Review and comparative analysis of studies on saturated flow boiling in small channels. Nanoscale and Microscale Thermophysical Engineering, 12, 187-227.

Bitzer Technical Documentation KT-660-2, 1997, Application of propane (R290) with semi-hermetic reciprocating compressors", Available from <www.bitzer.de>.

Blasius, H., 1911. Das Ahnlichkeitsgesetz bei reibungsvorgangen, Physik. Zeitschr., XII, 1175-1177.

Brackbill, J.U., Kothe D. B., Zemach, C., 1992. A Continuum Method for Modeling Surface Tension. J. Comput. Phys. 100,335-354.

Brauner, N. and Barnea, D., 1986. Slug/churn transition in upward gas–liquid flow. Chem. Eng. Sci. 41, 159–163.

Calm, J.M., 2008. The next generation of refrigerants – historical review, considerations, and outlook, International Journal of Refrigeration, 31, 1123-1133.

Carvalho, J.R.F.G., 2006. Experimental study of the slug/churn flow transition in a single Taylor bubble. Chemical Engineering Science 61, 3632-3642.

Cavallini, A., Rossetto, L., Matkovic, M. and Del Col, D., 2005. A model for frictional pressure drop during vapour-liquid flow in minichannels, IIR International Conference Thermophysical Properties and Transfer Processes of Refrigerants, Vicenza, Italy, pp. 71-78.

Cavallini, A., Del Col, D., Doretti, L., Matkovic, M., Rossetto, L. and Zillio, C., 2006. Condensation in horizontal smooth tubes: a new heat transfer model for heat exchanger design, Heat Transfer Engineering 27, 31-38.

Cavallini, A., Del Col, D., Matkovic, M., and Rossetto, L., 2008a. Frictional pressure drop during vapour-liquid flow in minichannels: experimental data and modelling. MNHT2008. Micro/Nanoscale Heat Transfer International Conference, January 6-9, 2008, Tainan, Taiwan.

Cavallini A., Censi G., Da Riva E., Del Col D., Mancin S., 2008b, Shell-and-Tube Minichannel Condenser for Low Refrigerant Charge, Proc. 19th National & 8th ISHMT-ASME Heat and Mass Transfer Conference, January 3 - 5 2008, JNTU Hyderabad, India.

Cooper, M. G., 1984. Saturation nucleate boiling. A simple correlation, 1st U.K. National Conference on Heat Transfer, Vol. 2, 785-793 (J. Chem. E. Symp. Series No. 86.

Corberán, J.M., Urchueguía, J., Gonzálvez, J., Setaro, T., Boccardi G. and Palm, B. 2000. Two phase heat transfer in brazed plate heat exchangers, evaporators and condensers for R22 and propane, 3rd European Thermal Sciences Conference.

Corberán J. M., Martínez I. O., 2008a, Charge optimisation study of a reversible water-to-water propane heat pump, International Journal of Refrigeration 31, 716-726.

Corberán J. M., Segurado, J., Colbourne, D., Gonzálvez, J., 2008b. Review of standards for the use of hydrocarbon refrigerants in A/C, heat pump and refrigeration equipment. International Journal of Refrigeration 31, 748-756.

Corberán J. M., Gonzálvez, J., Martínez, I. O., Radulescu, C., 2008c. Development and performance characterisation of a water to water reversible heat pump working with propane.8th IIR Gustav Lorentzen Conference on Natural Working Fluids, Copenhagen.

Da Riva, E., Cavallini, A., Del Col, D., 2007. Numerical simulation of two-phase churn flow in a vertical pipe by VOF method. In: Proceedings of the 6th International Conference on Multiphase Flow, Leipzig, Germany, July 9-13, 2007.

Da Riva, E., Del Col, D., 2007. Interfacial waves in churn flow of air-water mixture: simulation by VOF method, XXV UIT National Heat Transfer Conference, June 18-20, 2007, Trieste, Italy.

Danfoss, 2000. Technical Information CN.60.F1.02, Practical application of refrigerant R290 propane in small hermetic systems, Available on line.

de Sampaio, P.A.B., Faccini, J.L.H, Su, J., 2008, Modelling of stratified gas-liquid two-phase flow in horizontal circular pipes, International Journal of Heat and Mass Transfer 51, 2752-2761.

Decision 2007/742/EC, 2007. "Ecological criteria for the award of the Community eco-label to electrically driven, gas driven or gas absorption heat pumps", Official Journal L 301 of 20.11.2007.

Del Col, D., Fantini, F., and Rossetto, L., 2007. Dryout quality in minichannel flow boiling, XXV UIT National Heat Transfer Conference, Trieste, June 18-20, 2007.

Del Col, 2008. Minichannel heat exchangers for natural refrigerants, Proc. XXVI UIT National Heat Transfer Conference, June 23-25, 2008, Palermo, Italy.

Del Col, D., Cavallini, A., Censi, G., Da Riva, E., 2008, Design and performance of a shell-and-tube evaporator using minichannels, Proc. Eurotherm 2008, 5th European Thermal-Sciences Conference, May 18-22, Eindhoven, the Netherlands.

Directive 2006/40/EC relating to emissions from air conditioning systems in motor vehicles and amending Council Directive 70/156/EEC, Official Journal L 161 Vol. 49 of 14.06.2006.

Dukler, A.E. and Taitel, Y., 1986. Flow pattern transitions in gas-liquid systems: measurement and modelling. In: Hewitt, G.F., Delahaye, J.M., Zuber, N., (Eds.), Multiphase Science and Technology, Vol. 2, Hemisphere, Washington, DC, pp. 1-94.

European Standard EN 14511 2004, Air conditioners, liquid chilling packages and heat pumps with electrically driven compressors for space heating and cooling.

Fernando, P., Han, H., Palm, B., Granryd, E., Lundqvist, P., 2003.The solubility of propane (R290) with commonly used compressor lubrication oils, Proceedings of the International Conference on Compressors and their Systems. IMechE Conference Transactions 2003–4. ISSN: 1356-1448.

Fernando, P., Palm, B., Lundqvist P., and Granryd, E., 2004. Propane heat pump with low refrigerant charge: design and laboratory tests, International Journal of Refrigeration, Vol. 27, No. 7 (Nov.), pp. 761-773.

Fernando, P., Palm, B., Lundqvist, P., Granryd, E. 2007. Performance of a single-family heat pump at different working conditions using small quantity of propane as refrigerant, Experimental Heat Transfer, Vol. 20, No. 1 (Jan.), 57-71.

Fernando, P., Palm, B., Ameel, T., Lundqvist P., and Granryd, E., 2008a. A minichannel aluminium tube heat exchanger - Part I: Evaluation of single-phase heat

transfer coefficients by the Wilson plot method, International Journal of Refrigeration, Vol. 31, 669-680.

Fernando, P., Palm, B., Ameel, T., Lundqvist P., and Granryd, E., 2008b. A minichannel aluminium tube heat exchanger - Part II: Evaporator performance with propane, International Journal of Refrigeration, Vol. 31, 681-695.

Fernando, P., Palm, B., Ameel, T., Lundqvist P., and Granryd, E., 2008c. A minichannel aluminium tube heat exchanger - Part III: Condenser performance with propane, International Journal of Refrigeration, Vol. 31, 696-708.

Fluent Inc., 2006. Fluent 6.3 User's Guide.

Friedel, L., 1979. Improved friction pressure drop correlations for horizontal and vertical two-phase pipe flow, Proc. Europ. Two-phase Flow Group Meet., Ispra, Paper E2.

Friedel, L., 1980. Pressure drop during gas/vapour-liquid flow in pipes, Int. Chem. Engineering 20, 352-367.

Gnielinski, V., 1976, New equations for heat and mass transfer in turbulent pipe and channel flow, International Chemical Engineer, 16, 359–368.

Govan, A. H., Hewitt, G. F., Richter, H. J. and Scott, A., 1991. Flooding and churn flow in vertical pipes. Int. J. Multiphase Flow 17, 27-44.

"Guide to the Expression of Uncertainty in Measurements", 1995, International Organization for Standardization.

Harms, T. M., Groll, E. A. and Braun, J. E., 2003. Accurate charge inventory modeling for unitary air conditioners, HVAC&R Res. 9 (1), 55-78.

Hashimoto, K., 2006. Technology and market development of CO_2 heat pump water heaters (EcoCute) in Japan. IEA Heat Pump Centre Newsletter 24 (3), 12–16. Borås, Sweden.

Hewitt, G.F., Roberts, D.N., 1969. Studies of two-phase flow patterns by simultaneous X-ray and flash photography. UKAEA Report No. AERE-M2159.

Hewitt, G.F. and Hall-Taylor, N.S., 1970. Annular Gas–Liquid Flow. Pergamon Press, Oxford.

Hewitt, G.F., Martin, C.J., Wilkes, N.S., 1985. Experimental and modelling studies of annular flow in the region between flow reversal and the pressure drop minimum. Physiochem. Hydrodyn. 6, 69–86.

Hrnjak, P. S. and Hoehne, M. R., 2004. Charge minimization in systems and components using hydrocarbons as a refrigerant, ACRC TR-224, University of Illinois at Urbana-Champaign.

Hrnjak, P., 2005. Charge minimization in ammonia refrigeration system, IIR Conf.: Ammonia refrigerant System, Ohrid, 2005.

Intergovernmental Panel on Climate Change, 2007. Fourth Assessment Report, Climate Change 2007: Synthesis Report – Summary for Policymakers.

Jayanti, S. and Hewitt, G.F., 1992. Prediction of slug-to-churn transition in vertical two-phase flow. Int. J. Multiphase Flow 18, 847–860.

Jayanti, S., Tokarz, A., Hewitt, G.F., 1996. Theoretical investigation of the diameter effect on flooding in countercurrent flow, International Journal of Multiphase Flow 22, 307-324.

Kandlikar, S. G., 1990. A general correlation for saturated two-phase flow boiling heat transfer inside horizontal and vertical tubes, ASME Journal of Heat Transfer 112: 219-228.

Kandlikar, S. G. and Balasubramanian P., 2004. An extension of the flow boiling correlation to transition, laminar, and deep laminar flows in minichannels and microchannels, Heat Transfer Engineering 25(3), 86–93.

Liu, Z. and Winterton R. H. S., 1991. A general correlation for saturated and subcooled flow boiling in tubes and annuli, based on a nucleate pool boiling equation, International Journal of Heat and Mass Transfer 34 (11), 2759-2766.

Lockhart, R. W. and Martinelli, R. C., 1949, Proposed correlation of data for isothermal two-phase, two-component flow in pipes, Chem. Engng. Progr. 45, 39-48.

Lorencez, C., Nasr-Esfahany, M., Kawaji, M., Ojha, M., 1997, Int. J. Multiphase Flow 23, 205-226.

McAdams, W.H., 1942. Heat transmission, 2nd edn., McGraw-Hill, New York, 1942.

McQuillan, K. W. and Whalley, P. B., 1985. Flow patterns in vertical two-phase flow. Int. J. Multiphase Flow 11, 161–175.

Melin, P., 1996. Measurements and modelling of convective vaporization for refrigerants in a horizontal tube, PhD Thesis, Department of Heat and Power Technology, Chalmers University of Technology, Göteborg, Sweden.

Minor, B., Spatz, M., 2008. HFO-1234yf low GWP refrigerant updates, International Refrigeration and Air Conditioning Conference at Purdue, July 14-17, West Lafayette, IN, USA.

Mishima, K. and Ishii, I., 1984. Flow regime transition criteria for two-phase flow in vertical tubes. Int. J. Heat and Mass Transfer 27, 723-734.

Navarro, E., Urchueguía, J.F., Gonzálvez, J., Corberán, J.M., 2004. Comparative experimental investigation of oil behaviour in a hermetic piston compressor using propane (R290) as refrigerant. In: Proceedings of the Sixth IIR-Gustav Lorentzen Conference on Natural Working Fluids, Glasgow, pp. 45–49.

Navarro, E., Urchueguía, J.F., Gonzálvez, J., Corberán, J.M., 2005. Test results of performance and oil circulation rate of commercial reciprocating compressors of different capacities working with propane (R290) as refrigerant. International Journal of Refrigeration, Vol. 28, No. 6 (Sept.), 881-888.

Nicholas, J.V., White, D. R., 1994. Traceable temperatures, Wiley series in measurement science and technology, Wiley.

Nichols, B. D., Hirt, C. W., Hotchkiss, R. S., 1980. SOLA-VOF: A solution algorithm for transient fluid flow with multiple free boundaries, Technical Report LA-8355, Los Alamos National Laboratory.

Nicklin, D.J. and Davidson, J.F., 1962. The onset of instability in two-phase slug flow. In: Institution Mechanical Engineers Symposium on Two-Phase Flow, London.

Niño, V.G., Hrnjak P.S. and Newell, T.A., 2002. Characteristics of Two-Phase Flow in Microchannels, Ph.D. Thesis, ACRC TR-202, University of Illinois at Urbana-Champaign.

Niño, V. G., Jassim, E.W., Hrnjak, P.S., Newell, T.A., 2006. Flow-regime based model for pressure drop predictions in microchannels, HVAC&R Res. 12 (1), 17-34.

NIST, National Institute of Standard and Technology, 2002. Refprop Versione 7.0, Boulder Colorado.

Norman, F., Van den Schoor, F., Verplaetsen, F., 2006. Auto-ignition and upper explosion limit of rich propane-air mixtures at elevated pressures. Journal of Hazardous Materials, Vol. 137, pp. 666-671.

Owen, D.G., 1986. An experimental and theoretical analysis of equilibrium annular flows. Ph.D. thesis, University of Birmingham, UK.

Paliwoda, A., 1992, Generalized method of pressure drop calculation across pipe components containing two-phase flow of refrigerants, Int. J. Refrigeration Vol. 15 No. 2, 119-125.

Palm, P., 2007. Refrigeration systems with minimum charge of refrigerant, Applied Thermal Engineering, Vol. 27, No. 10 (July), pp. 1693-1701.

Palm, P., 2008. Hydrocarbons as refrigerant in small heat pump and refrigeration systems – A review. International Journal of Refrigeration 31, 552-563.

Pelletier, O., Palm, B., 1996. Performance of plate heat exchangers and compressor in a domestic heat pump using propane. Proc. of IIF/IIR Conf. Applications for Natural Refrigerants, Aarhus, Denmark, pp. 497-505, 1996.

Petukhov, B.S., and Popov, V.N., 1963. Theoretical calculation of heat exchange in turbulent flow in tubes of an incompressible fluid with variable physical properties, Teplofiz. Vysok. Temperature (High Temperature Heat Pysics), vol. 1, no. 1, 69-83.

Premoli, A., Francesco, D. and Prina, A., 1970, An empirical correlation for evaluating two phase mixture density under adiabatic conditions, Europ. Two-phase Flow Group Meet., Milan, Italy.

Rouhani, S.Z., 1969. Subcooled void fraction, AB Atomenergi Sweden, Internal Rept. AE-RTV841.

Sawai, T. and Kaji, M., 2001. Flow structure and pressure gradient in churn flow. In: Celata, G.P., Di Marco, P., Goulas, A., Mariani, A., (Eds.), Experimental Heat Transfer, Fluid Mechanics and Thermodynamics 2001, 2. Edizioni ETS, Pisa, pp. 1791–1796.

Sawai, T., Kaji, M., Kasugai, T., Nakashima, H., Mori, T., 2004. Gas-liquid interfacial structure and pressure drop characteristics of churn flow. Experimental Thermal and Fluid Science 28, 597-606.

Schwartz, W., Harnisch, J., 2003. Final Report on Establishing Leakage Rates of Mobile Air Conditioners, prepared for the European Commission (DG Environment).

Shearer, C.J. and Davidson, J.F., The investigation of a standing wave due to gas blowing upwards over a liquid film; its relation to flooding in wetted-wall columns. J. Fluid Mech. 22, 321–335 (1965).

Stephan, K., Abdelsalam, M., 1980. Heat-transfer correlation for natural convection boiling, International Journal of Heat and Mass Transfer 23, 73-87.

Taborek, J., 1983. Shell-and-tube heat exchangers: single phase flow (Chapter 3.3), HEDH, Hemisphere P. Corporation.

Taitel, Y., Barnea, D., Dukler, A.E., 1980. Modelling of flow pattern transitions for steady upward gas-liquid flow in vertical tubes. AlChE J. 26, 345-354.

Wallis, G.B., 1962. The onset of droplet entrainment in annular gas–liquid flows. General Electric Report No.62GL127.

Watson, M.J. and Hewitt, G.F., 1999. Pressure effects on the slug to churn transition. Int. J. Multiphase Flow 25, 1225–1241.

Whalley, P.B., 1987. Boiling, condensation and gas-liquid flow, Oxford University Press.

Wilcox, D.C., 1998, Turbulence modeling for CFD, DCW Industries, Inc., La Canada, California.

Yang, Z., Peng, X.F., Ye, P., 2008. Numerical and experimental investigation of two phase flow during boiling in a coiled tube, International Journal of Heat and Mass Transfer 51, 1003-1016.

Youngs, D.L., 1982. Time-dependent multi-material flow with large fluid distortion. In: Morton, K.W., Baibnes, M.J. (Eds.), Numerical Methods for FluidDynamics. Academic Press, New York, p. 273.

Zambolin, E., 2007. Progetto di una pompa di calore a propano a carica ridotta. Tesi di laurea, Università di Padova, Dipartimento di Fisica Tecnica.

Zivi, S.M., 1963, Estimation of steady-state steam void-fraction by means of the principal of minimum entropy production, ASME reprint 63-HT-16, 6th Nat. Heat Transfer Conf., AIChE-ASME, Boston.

Nomenclature

A	total cross sectional area (m^2)
A^*	cross sectional area at the wave crest (m^2)
D	internal diameter (m)
Fr	Froude number = $\rho j^2(\rho_L-\rho_G)^{-1}g^{-1}D^{-1}$ (-)
g	gravity acceleration (m/s^2)
G	mass flux (kg m^{-2} s^{-1})
HTC	Heat Transfer Coefficient (W m^{-2} K^{-1})
IHX	Internal Heat Exchanger
j	superficial velocity (m/s)
k	turbulent kinetic energy (m^2/s^2)
Ku	Kutateladze number = $j\rho^{1/2}[g\sigma(\rho_L-\rho_G)]^{-1/4}$ (-)
n	surface normal
p	pressure (Pa)
Re_{LO}	all-liquid Reynolds number GD/μ_L (-)
t	time (s)
T	temperature (K)
$\vec{u}$	velocity vector (m/s)
U_G^*	dimensionless velocity = $Fr^{1/2}$ (-)
VOF	Volume Of Fluid
x	vapour quality (-)

Greek letters

α	dimensionless diametral occlusion (-)
Δp^*	dimensionless pressure gradient = $(dp/dz-\rho_G g)(\rho_L-\rho_G)^{-1}g^{-1}$ (-)
ε	turbulent kinetic energy dissipation rate (m^2/s^3)
κ	curvature of interface
μ	dynamic viscosity (Pa s)
μ_t	turbulent viscosity (Pa s)
ρ	density (kg/m^3)
σ	surface tension (N/m)
ω	turbulent kinetic specific dissipation rate (s^{-1})

Subscripts

G	gas/vapour phase
L	liquid phase

Acknowledgements

The study concerning the minichannel heat exchangers, the propane heat pump and the VOF simulation of churn flow has been carried out at the Dipartimento di Fisica Tecnica, Università degli Studi di Padova, under the direction of Prof. Alberto Cavallini and Ing. Davide Del Col.

The study concerning the VOF simulation of condensation inside minichannels has been carried out at the Cooling Technologies Research Center (CTRC) of the Purdue University, West Lafayette, Indiana, USA under the supervision of Prof. Suresh Garimella and Prof. Jayathi Murthy.

The author would like to acknowledge the support of the European project SHERHPA, co-funded by the European Commission within the Sixth Framework Programme (2002-2006).

Ing. Giuseppe Censi of Onda SpA and Ing. Mauro Mantovan of Hiref SpA are acknowledged for their collaboration in the design and realization of the minichannel heat exchangers and the heat pump, respectively.

Special thanks to Ing. Sandro Lazzarato and Ing. Enrico Zambolin for their helpful cooperation during the set-up and instrumentation of the heat pump facility and the collection of experimental data.